Folia
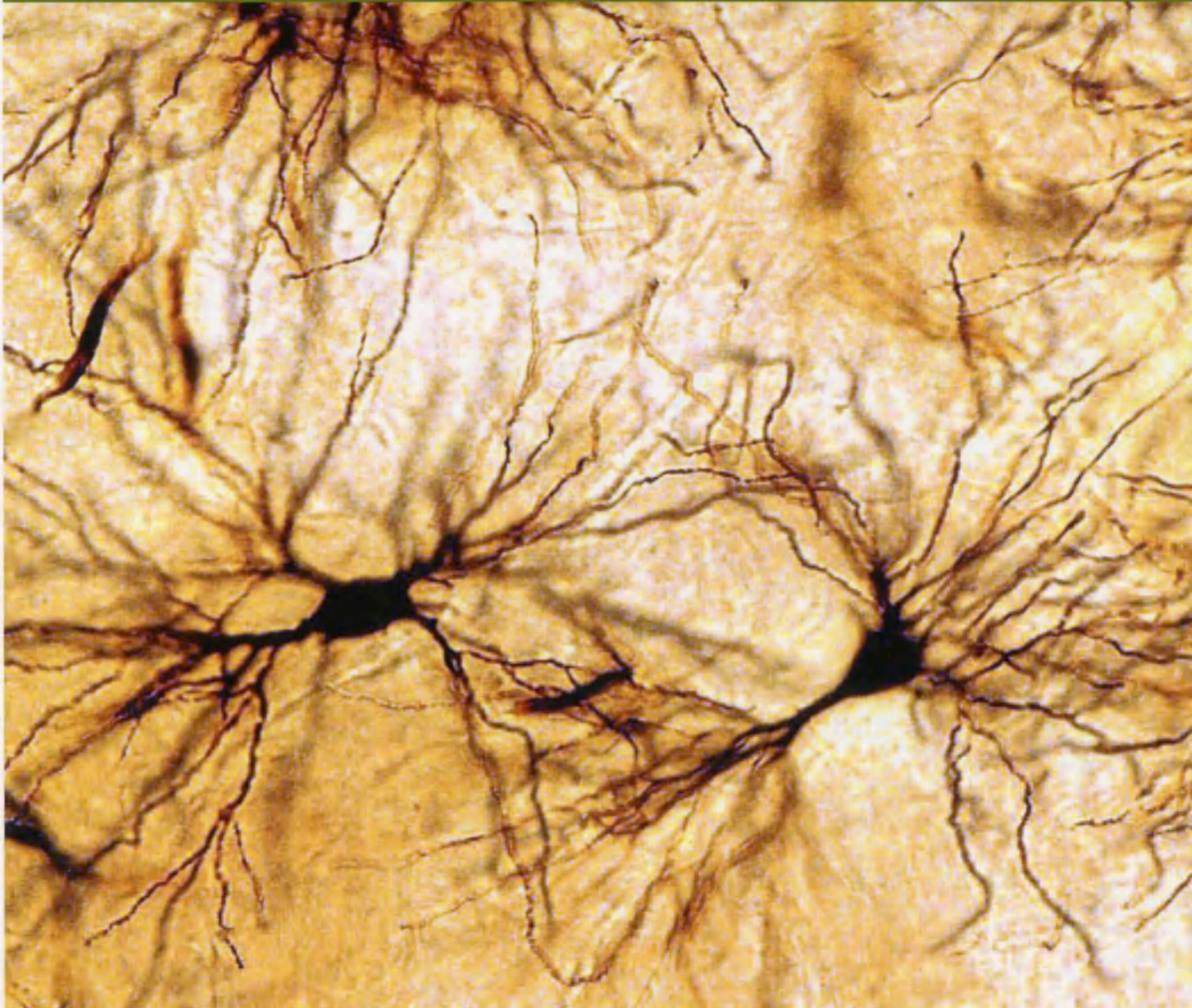
NEUROPATHOLOGICA

Official Journal of Mossakowski Medical Research Centre Polish Academy of Sciences and
Polish Association of Neuropathologists

Folia
Neuropathologica

TERMEDIA Publishing House

Folia
Neuropathologica
former *Neuropatologia Polska*

Contents

Biopathology of astrocytes in human traumatic and complicated brain injuries. Review and hypothesis

Orlando José Castejón

Biological Research Institute, Faculty of Medicine, Zulia University, Maracaibo, Venezuela

Abstract

The biopathology of astrocyte cells in severe human brain traumatic injuries complicated with subdural and epidural haematoma and hygroma is reviewed. Clear and dense oedematous and hypertrophic reactive astrocytes are distinguished in severe primary traumatic vasogenic and secondary cytotoxic brain oedema. Swollen perineuronal astrocytes appear compressing and indenting clear and dark degenerated pyramidal and non-pyramidal nerve cells, degenerated myelinated axons and synaptic contacts. Hypertrophic astrocytes display dense cytoplasm and contain numerous rosettes of alpha, beta- and gamma-type glycogen granules, swollen mitochondria, dilated smooth and rough endoplasmic reticulum, oedematous Golgi apparatus, microtubules, gliofilaments, intermediate filaments, lysosomes and liposomes. The perisynaptic astrocyte ensheathment of synaptic contacts, containing beta type-glycogen granules, can be traced in the neuropil, surrounding swollen, bead-shaped dendritic profiles, and degenerated myelinated axons. This perisynaptic glial layer is absent in severe oedematous regions. The glycogen-rich and glycogen-depleted perivascular astrocyte end-feet appear attached or dissociated from the capillary basement membrane. Phagocytic astrocytes can be seen engulfing degenerated synaptic contacts, necrotic membranes, degenerated myelinated axons, and myelin ovoids. Lipofuscin-rich astrocytes are also observed. The interastrocytary gap junctions appear either widened, fused or fragmented.

The key role of aquaporin in astrocyte swelling and brain oedema is emphasized. The findings are compared with those reported in experimental traumatic animal models, a large variety of pathogenetically related neuropathological conditions, and in vivo and in vitro experimental conditions. The contribution of pathological astrocytes to neurobehavioral disorders, such as loss of consciousness, neurological deficits and seizures is emphasized. Some hypotheses are postulated related to the dissociated or absent perisynaptic layer, neurobiology of glycogen-rich and glycogen-depleted perivascular astrocytes, the glio-basal dissociation process, abnormal astrocyte-neuronal unit, and astrocyte participation in seizures in patients with severe and complicated brain injuries.

Key words: *astrocytes, brain trauma, brain oedema, light microscopy, electron microscopy.*

Introduction

Astrocyte changes in traumatic brain injuries

Astrocyte reactions to traumatic brain injuries have been the topic of many studies and of much debate for almost a century. The current consent is that glial cells, mainly astrocyte cells, have a pivotal role in degeneration and regeneration of the gray matter, and that astrocyte changes are one of the hallmarks of the response of the central nervous system (CNS) to injury [1,8,12,15,17,44,58,65,68-70,74, 76,81,86,88,94-96,98,99,102,109,129,138]. The astrocyte cell changes in brain injuries have been widely

Communicating author:

Prof. Orlando José Castejón, MD, Biological Research Institute, Faculty of Medicine, Zulia University, Maracaibo, Venezuela,
fax: 58-261-7831611, e-mail: ocastejo@cantv.net

studied at light and electron microscope levels. Such earlier studies in human and experimental animals reported a wide spectrum of pathological changes, such as astrocyte swelling, division and proliferation (gliosis), gemistocytic astrocytes, a type of round to oval hypertrophic astrocyte cell with abundant cytoplasm containing glial filaments and an eccentric nucleus or two nuclei, clasmatodendrosis or astrocytes with breaking up of astrocytic protoplasmic expansions, active and reactive changes, accumulation of glial fibres and increased synthesis and expression of glial fibrillary acidic protein (GFAP), vimentin and glutamine synthetase, phagocytic properties, glycogen accumulation, intermediate filament gene expression, secretion of neurotrophic factors, migration, and down regulation of astrocyte glutamate transporter. An increased immunochemically detectable GFAP level was one of the earliest responses to specifically characterize CNS injuries [18, 21,51,52,54,60,65,68,77,81,125].

Castejón previously described astrocyte subtypes, morphological astrocytic changes and human neurobehavioral disorders in traumatic human oedematous cerebral cortex [27-32]. Ragaisis [120] found ischaemic swelling of astrocytes in brain contusion after increasing concentrations of potassium ion. Derugin *et al.* [45] and Fotheringham *et al.* [55] reported reactive astrocytes after transient middle cerebral artery occlusion. Del Bigio *et al.* [44] described astrocytic swelling and eosinophilia in human post-mortem brain indicative of plasma extravasation and brain oedema. According to Raivich *et al.* [119], damage to the CNS leads to cellular changes not only in the affected neurons but also in adjacent glial cells and endothelia, and frequently to recruitment of cells of the immune system. These cellular changes form a graded response which is a consistent feature in almost all forms of brain pathology. These authors provide evidence about the biological function of the neuroglial activation in the injured brain. Vajtr *et al.* [138] described in human cortical biopsies cytotoxic astrocyte oedema occurring during blood brain barrier damage after traumatic brain injury. According to Eng [52], GFA protein or GFAP is the major protein constituent of glial intermediate filaments in differentiated fibrous and protoplasmic astrocytes of the CNS. A putative function ascribed to glial filaments as a component of cytoskeletal substructures is defining and maintaining the shape of the astrocyte.

In the present review, I shall present the view supported by our light and electron microscopic laboratory data based on examinations of more than 60 human cortical biopsies immediately taken in the surgical room, and optimally fixed during the neurosurgical treatment. These studies have provided some insight into the subsets of astrocyte cells generated after severe and complicated traumatic brain injuries. A widely accepted view is that adult human CNS is inherently different from experimental animal models, and that astrocyte reactivity changes according to the aetiology or primary insult of human neuropathological conditions. Therefore, we characterize astrocyte pathological and heterogeneous populations in different cortical regions of patients with complicated and severe brain trauma associated with subdural, extradural haematoma or hygroma (a subdural body of cerebrospinal fluid (CSF), without blood, believed to be derived from chronic subdural haematomas). Additionally, we have compared the electron microscopic features of astrocyte subtypes in complicated human traumatic brain injuries with those reported in a large variety of nervous and mental diseases, and *in vivo* and *in vitro* experimental conditions, in an attempt to establish a link between basic and clinical neuroscience, and to gain a better insight into the real significance of heterogeneity of astrocytes that occur at the immediate site of severe and complicated human brain injuries. This comparative extrapolation of findings will allow us to explore new and common pathogenetic mechanisms, and to study new therapeutic strategies.

Light and electron microscopy fixation procedures for human cortical biopsies

Two to five mm thick cortical biopsies from the perifocal area of a traumatic lesion of the frontal and parietal region were taken by the neurosurgeon, and immediately fixed in the neurosurgical room in 4% glutaraldehyde-0.1 M phosphate or cacodylate buffer, pH 7.4, at 4°C, in order to avoid delay fixation. After 2 hours of the glutaraldehyde fixation period, the cortical biopsies were divided in our laboratory into approximately 1 mm slides, and observed under a stereoscopic microscope to check the quality of fixation of the sample, the glutaraldehyde diffusion rate, and the brownish coloration of the surface and deeper cortical regions, indicative of good glutaraldehyde fixation by the immersion technique. Immersion in fresh glutaraldehyde solution of 1 mm

http://rcin.org.pl

slices was secondarily done for 2 hours after eliminating the remaining blood from the cortical biopsy by washing in similar 0.1 M phosphate or cacodylate buffer, pH 7.4, to avoid oxidation of the primary fixative solution. Secondary fixation in 1% osmium tetroxide 0.1 M phosphate buffer, pH 7.4, was carried out for 1-2 hours at 4°C. Black staining of the cortical slices also was observed under a stereoscopic microscope to determine the osmium tetroxide diffusion rate and quality of secondary fixation. The samples were then rinsed for 5 to 10 minutes in phosphate or cacodylate buffer of similar composition to that used in the fixative solution, dehydrated in increasing concentrations of ethanol, and embedded in Araldite or Epon. For proper orientation during the electron microscope study and observation of cortical layers, approximately 0.1 to 1 μm thick sections were stained with toluidine blue and examined with a Zeiss photomicroscope. Light microscope study of neurons, glial cells, and blood-brain barriers was performed. Ultrathin sections, obtained with Porter-Blum and LKB ultramicrotomes, were stained with uranyl acetate and lead citrate, and observed in a JEOL 100B transmission electron microscope (TEM) at magnifications ranging from 20,000 to 90,000×. Approximately one hundred electron micrographs were taken of each cortical biopsy. Those cortical biopsies with delayed and poor fixation, due to inactivation of the primary fixative for the presence of tissue blood, were discarded. Since poor or delayed fixation of brain parenchyma exhibits features quite similar to those observed in an oedematous tissue, in each case we critically differentiate between true pathology and fixation artefacts. The different submicroscopic features that characterize moderate and severe brain oedema allowed us to discard fixation artefacts, mainly when analysing substructures such as the multilamellar arrangement of myelin layer [23]. To characterize a subpopulation of astrocytes we assemble a montage of serial electron micrographs to analyse the entire cell body and processes. A clear distinction between astrocytes and oligodendrocytes was made in each case examined.

Heterogeneity of astrocyte population after severe and complicated brain injuries

The following astrocyte populations are found at the light and electron microscopic levels in the oedematous human cerebral cortex associated with complicated brain trauma: reactive clear and dense swollen astrocytes, reactive hypertrophic astrocytes, lipofuscin-rich astrocytes, glycogen-rich and glycogen-depleted astrocytes, and phagocytic astrocytes [28,30,32].

Clear oedematous astrocytes in light and electron microscopy

Semithin plastic sections stained with toluidine blue show the presence of clear and dense notably swollen astrocytes at the perineuronal, interfascicular, and perivascular localizations. They appear surrounded by notably enlarged extracellular spaces (Fig. 1A), which feature the status spongiosus of brain parenchyma. Perineuronal astrocytes appear intimately applied to shrunken and ischaemic neuronal bodies (Fig. 1B). Binucleated and multinucleated astrocytes, indicating astrocyte proliferation, are also observed (Fig. 1C). Electron micrographs show the clear astrocytes characterized by an electron lucid cytoplasm matrix, widened rough endoplasmic reticulum, clear and swollen mitochondria with dislocated or fragmented cristae, lysosomes, phagolysosomes, and glycogen granules [24,26] (Fig. 1D).

Very severely oedematous clear astrocytes show lacunar or vacuolated enlargement of rough endoplasmic reticulum, an increased amount of glial filaments, fragmentation of Golgi apparatus, and numerous lysosomes (Fig. 2A).

Oedematous astrocyte were also reported by Ito *et al.* [67] in focal cortical infarction, and by Kuchiwaki *et al.* [79] in cytotoxic brain oedema.

These astrocytes are characterized by robust processes containing bundles of glial filaments (Fig. 2B).

Similar cable-like bundles of glial filaments were reported by Graeber and Kreutzberg in facial nerve axotomy [60].

Figures 2C and 2D show "control" electron micrographs of the apparently normal astrocyte cell body and processes from a patient with anomaly of the anterior cerebral artery. It is important to keep in mind that brain oedema is produced as soon as the brain is exposed to the air during neurosurgery following opening of the meningeal covering. The neighbouring neuropil shows the best ultrastructural preservation obtained with the immediate glutaraldehyde-osmium fixation procedure of cortical biopsies in the neurosurgical room. Note the integrity of subcellular structures of apparently normal nerve cell bodies and processes, the conti-

http://rcin.org.pl

Fig. 1. A) Brain trauma. Subdural haematoma. Left parietal cortex. Light microscopy of a toluidine blue stained semithin plastic section exhibiting notably swollen clear astrocytes (CA) surrounded by enlarged extracellular space (ES). A non-pyramidal neuron (NP), an ischaemic and dense perineuronal oligoden-droglial cell (PO) and degenerated myelinated axons (MA) are seen in the neighbouring neuropil. Note the status spongiosus of brain parenchyma. B) Similarly stained semithin plastic section showing swollen perineuronal (PA) and clear interfascicular astrocytes (CA) surrounding dense and ischaemic neurons (DN). A longitudinally sectioned capillary (C) also is noted. C) Semithin plastic section depicting a multinucleated astrocyte (MA). A dark neuron (DN), a clear non-pyramidal neuron, and a swollen clear astrocyte (CA) are distinguished. D) Electron micrograph of a swollen and clear astrocyte (CA) characterized by an electron lucid cytoplasmic matrix, dense mitochondria (M) with fragmented cristae, dilated rough endoplasmic retic-ulum (ER) and nuclear (N) envelope, glycogen granules (GG), and a phagolysosome (PL).

nuity of limiting plasma membrane profiles, glial filaments, and the membrane-to-membrane, 20 nm in width, non-dilated extracellular space separating nerve cell processes in the neuropil [24].

Brain trauma induces dense swollen reactive astrocytes

Dense, swollen astrocytes are easily identified by the higher electron density of their cytoplasmic matrix. They exhibit vacuolization of rough endoplas-mic reticulum, detachment of associated ribosomes, plasma membrane disruption, clear and swollen mitochondria with cristae fragmentation and dis-solution, and bundles of glial filaments extended toward the vacuolated astrocyte processes [28,29] (Figs. 3A and 3B).

Clear and dense astrocyte swelling also have been widely reported by Allen *et al.* [5] after high
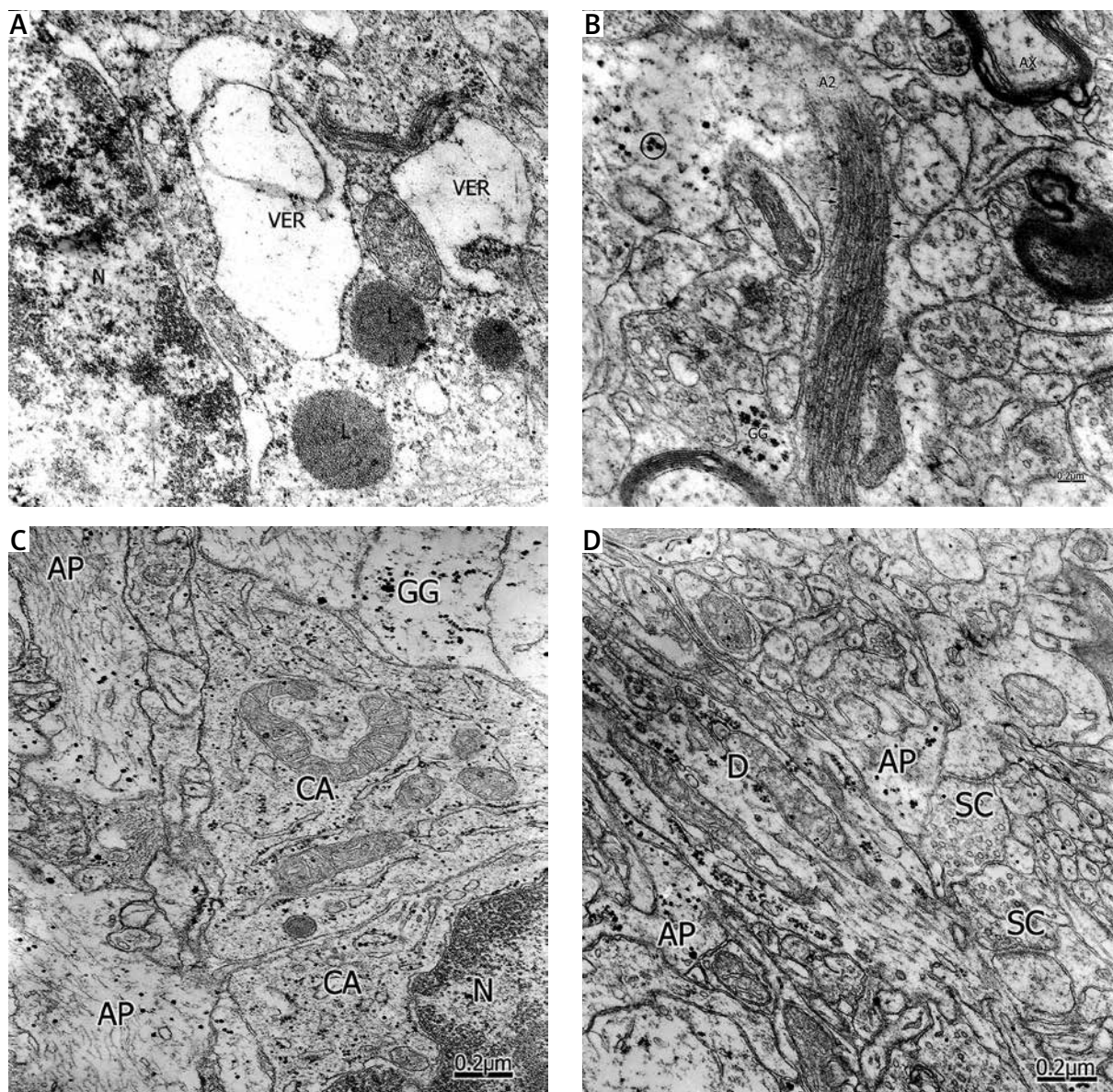
Fig. 2. A) Brain trauma. Subdural haematoma. Left parietal cortex. Clear and notably swollen astrocyte showing irregular enlargement of nuclear (N) envelope, vacuolated rough endoplasmic reticulum (RER), and lysosomes (L). **B)** Clear astrocyte (CA) showing alpha-type glycogen granules (circle), and a robust astrocyte process containing bundles of glial filaments (short arrows). A small astrocyte process, containing alpha-type glycogen granules (GG), is seen enveloping a degenerated myelinated axon. Another degenerated axon (AX) is seen at the upper right side of the figure. **C)** Electron micrograph of a "control" clear astrocyte cell body (CA) and processes (AP) of a cortical biopsy taken and fixed in the neurosurgical room from a patient with malformation of the anterior cerebral artery, and using the same glutaraldehyde-osmium fixation protocol employed in the cortical biopsies with traumatic brain injuries. Note better ultrastructural preservation of nuclear envelope, mitochondria, and bundles of glial filaments at the astrocyte processes. A glycogen-rich astrocyte process containing beta-type glycogen granules (GG) is also well preserved. **D)** "Control" neuropil of the same patient displaying optimal preservation of dendrites (D), astrocyte cytoplasm (A), and synaptic contacts (SC). Note the normal appearance of membrane-to-membrane spaces, and the absence of widened extracellular spaces.

http://rcin.org.pl
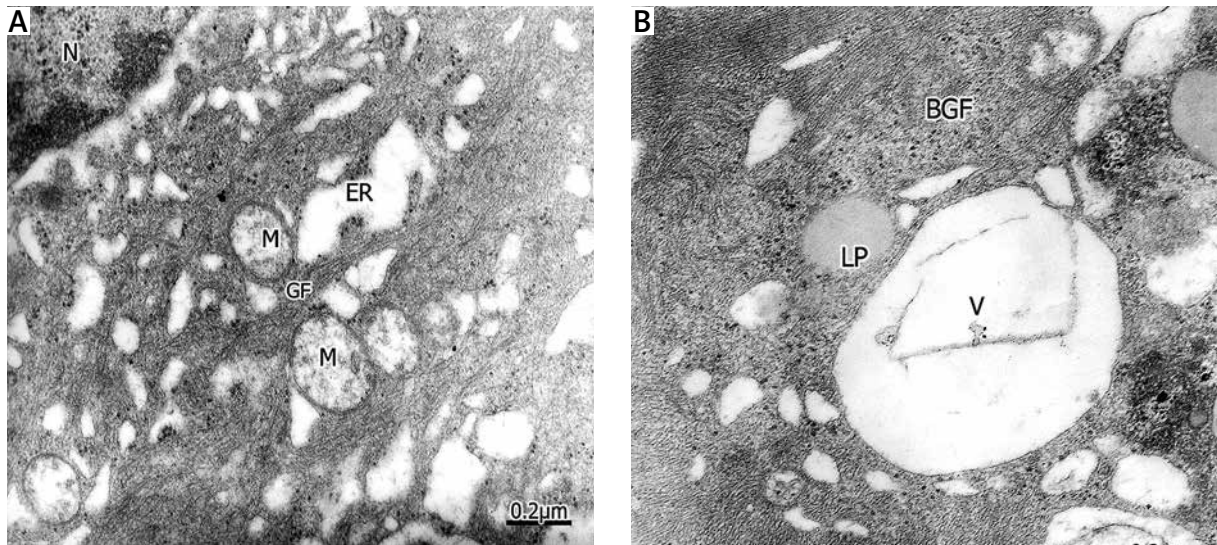
Fig. 3. A) Dense and swollen astrocyte displaying vacuolated rough endoplasmic reticulum (ER) with detachment of associated ribosomes, clear notably oedematous mitochondria (M) with granular disintegration of mitochondrial cristae, bundles of microfilaments, and notably enlarged nuclear (N) envelope. **B)** Dense astrocyte process containing bundles of glial filaments (BGF) at sublemmal localization, and sparse beta-type glycogen granules, large vacuoles (V), and low electron dense liposomes (LP).

velocity penetrating head injuries, Bullock *et al.* [15] following human cerebral contusion, Dietrich *et al.* [48] after fluid percussion brain injury, Fujisawa *et al.* [56] using a rat model of subdural haematoma, Mathew *et al.* [94] in an experimental model of contusion and focal cortical injury, Kuroiwa *et al.* [80] during early ischaemia, and by non-traumatic neuropathological conditions, such as Matyja *et al.* [96] in amyotrophic lateral sclerosis (ALS), a model of slow glutamate excitotoxicity. Similar findings have also been observed *in vitro* in a variety of experimental conditions, such as swelling-induced release of glutamate, aspartate, and taurine from astrocyte cultures, hypoosmotic media, high K$^+$, high glutamate, ethanol, free fatty acids, lacto-acidosis and acid-base exchange [7,73-75], and the role of Na$^+$, K$^+$ and Cl$^-$ cotransporters in brain ischaemia [39].

Interfascicular and swollen perisynaptic astrocyte processes

The clear and swollen astrocytic processes containing beta type-glycogen granules can be traced in the neuropil in moderate oedema far from the traumatic perifocal region, where they appear surrounding the synaptic contacts, swollen and bead-shaped dendritic profiles, and degenerated myelinated axons. These swollen astrocyte processes compress and indent the degenerated myelinated axons. At the level of this compression zone, the degenerated myelinated axons appear constricted with distorted and vacuolated myelin sheath [23] (Figs. 4A and 4B).

The presence of notably swollen astrocytes and degenerated myelinated axons has been described previously by Graeber and Kreutzberg [60] following facial nerve axotomy, by Gilmore *et al.* [59] after sciatic axotomy, and by Murray *et al.* [103] in dorsal root or peripheral nerve lesions.

In those patients with very severe brain oedema, located at the perifocal area, the haematogenous oedema fluid rejects the astrocyte perisynaptic cytoplasm, and the pre- and postsynaptic endings and the synaptic cleft appear in direct contact with the extracellular space [29,31] (Fig. 4C).

These findings indicate that astrocytes lost both the prime location to receive synaptic information from released neurotransmitters and the neurotransmitter receptor expression in response to injury [104]. Additionally, the diffusion of nerve impulse transmission to the extracellular space indicates loss of astrocyte modulation of extracellular space [6]. If we consider that the perisynaptic astrocyte should be viewed as an integral modulatory element of the tripartite synapse [6], we are really dealing with dissociated tripartite synapses.
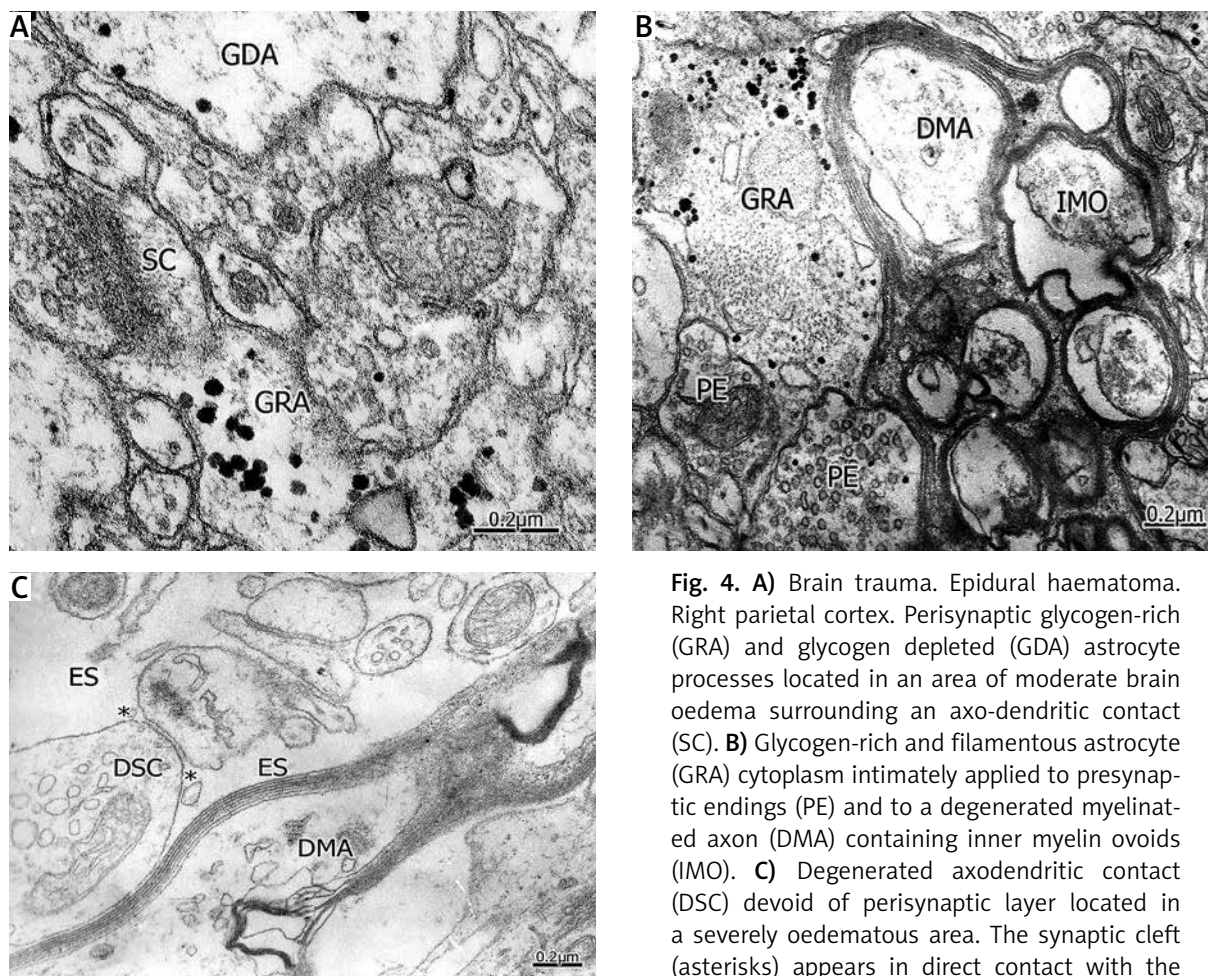
Fig. 4. A) Brain trauma. Epidural haematoma. Right parietal cortex. Perisynaptic glycogen-rich (GRA) and glycogen depleted (GDA) astrocyte processes located in an area of moderate brain oedema surrounding an axo-dendritic contact (SC). **B)** Glycogen-rich and filamentous astrocyte (GRA) cytoplasm intimately applied to presynaptic endings (PE) and to a degenerated myelinated axon (DMA) containing inner myelin ovoids (IMO). **C)** Degenerated axodendritic contact (DSC) devoid of perisynaptic layer located in a severely oedematous area. The synaptic cleft (asterisks) appears in direct contact with the enlarged and electron lucid extracellular space (ES) containing non-proteinaceous oedema fluid. Note the neighbouring and longitudinally section of a degenerated myelinated axon (DMA).

Hypothesis on the biopathological significance of absent perisynaptic astrocyte ensheathment

Our electron microscopic studies suggest that in the perisynaptic glial-synaptic contact dissociation process, the specific functions of astrocytes in synaptic transmission, such as the ability to take up and metabolize neurotransmitters, are disrupted – for example, glutamate uptake and glutamate release at the synapses that they envelop, to protect these synapses against inappropriate activation by excess transmitter released or regulate synaptic transmission [6], and also inactivate neurotransmitters [92]. Such modulatory regulation or inactivation is disrupted by traumatic brain oedema. The alteration of these specific functions would help to explain the contribution of pathological astrocytes to development of neurobehavioral disorders, such as loss of consciousness, neurological deficits, and

seizures [27,31]. In addition, Uranova *et al.* [137] have described ultrastructural alterations of both synaptic contacts and astrocytes in the postmortem caudate nucleus of schizophrenic patients, suggesting that perisynaptic ensheathment dissociation is not a specific finding of human traumatic brain injuries.

The glio-basal dissociation process in severe traumatic brain injuries

At the light microscopy level, clear and dense perivascular astrocytes appear mostly attached to the outer surface of the capillary basement membrane mainly in areas of moderate, and some regions of severe oedema located far from the traumatic perifocal region [25,37] (Fig. 5A and 5B).
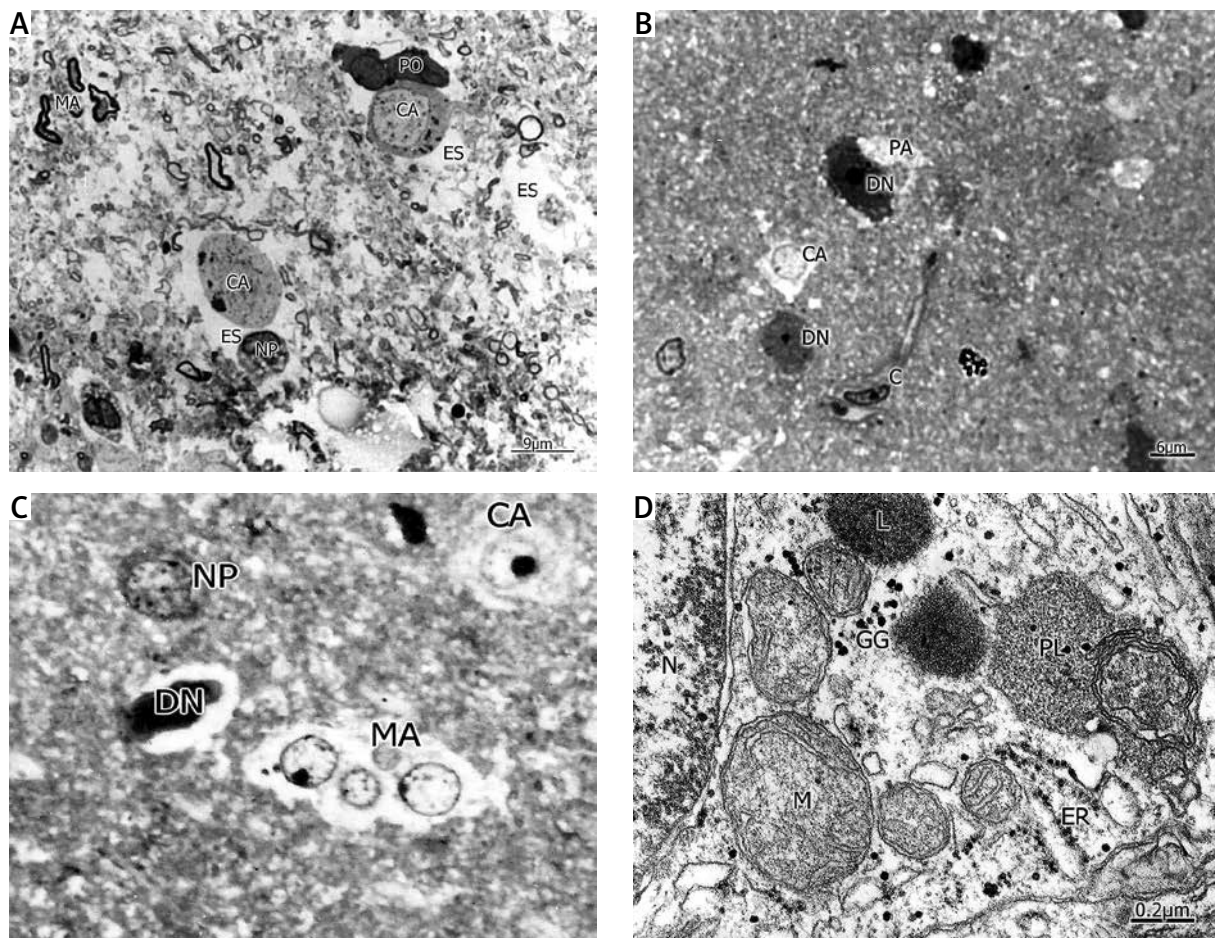
http://rcin.org.pl
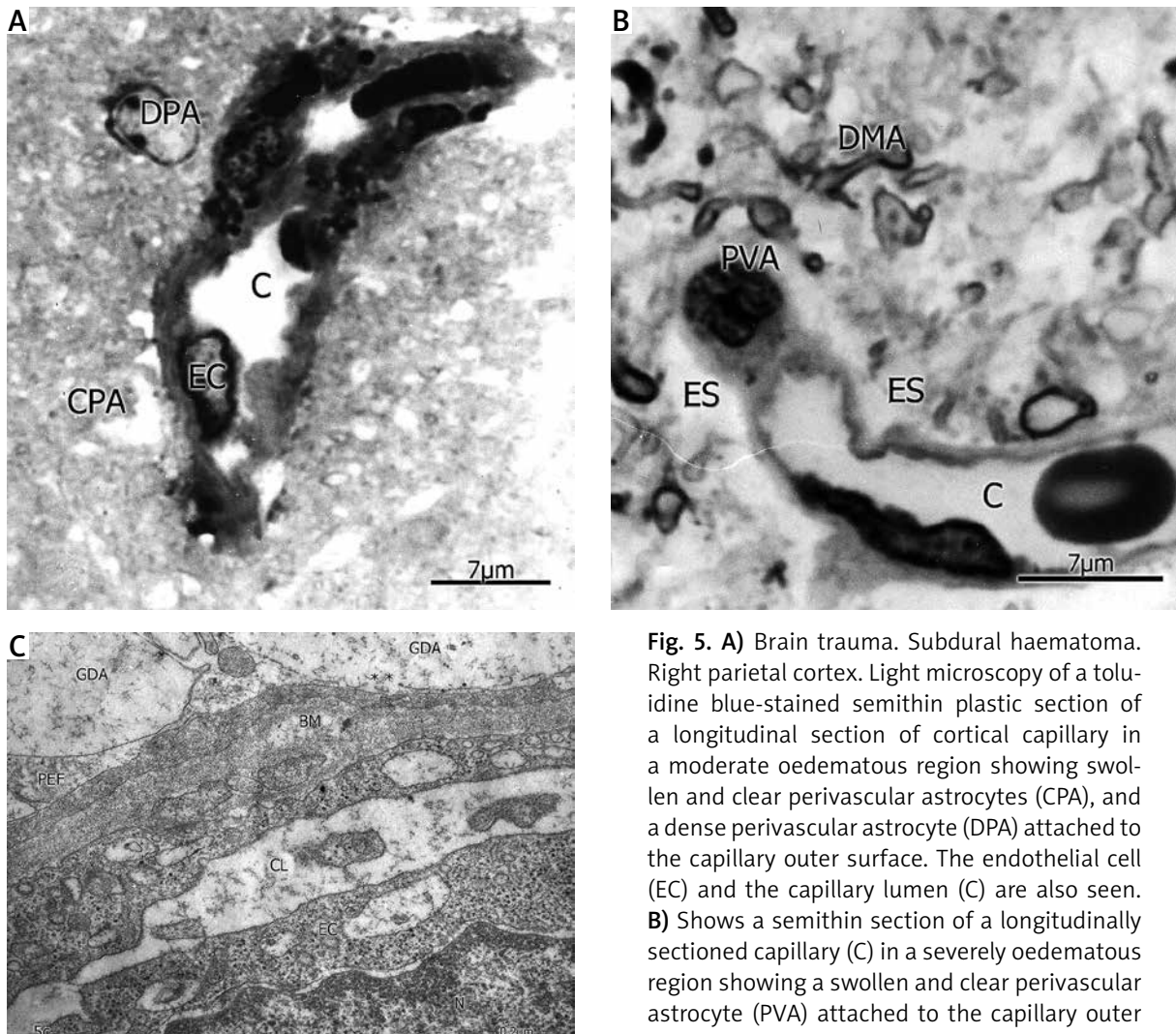
Fig. 5. A) Brain trauma. Subdural haematoma. Right parietal cortex. Light microscopy of a toluidine blue-stained semithin plastic section of a longitudinal section of cortical capillary in a moderate oedematous region showing swollen and clear perivascular astrocytes (CPA), and a dense perivascular astrocyte (DPA) attached to the capillary outer surface. The endothelial cell (EC) and the capillary lumen (C) are also seen. **B)** Shows a semithin section of a longitudinally sectioned capillary (C) in a severely oedematous region showing a swollen and clear perivascular astrocyte (PVA) attached to the capillary outer surface, and surrounded by large extracellular spaces (ES). Numerous degenerated myelinated axons (DMA) are also seen in the spongy neuropil. **C)** Electron micrograph of extremely swollen and glycogen-depleted perivascular astrocytic end-feet (GDA) localized in a severely oedematous area and dissociated from the thickened capillary basement membrane (BM) by proteinaceous oedema fluid (PEF) and a thin layer of dense astrocyte cytoplasm. Note the discontinuities of the limiting plasma membranes (asterisks). A swollen and vacuolated endothelial cell (EC) and the capillary lumen (CL) are also seen.

In severe and complicated brain injuries, a gliobasal dissociation process occurs and a separation of astrocyte end-foot limiting plasma membrane from the capillary basement membrane is observed (Fig. 5C). Additionally, the astrocyte perivascular end-feet are fragmented and remnants of their limiting plasma membranes are observed. Extensive areas of the capillary basement membrane devoid of astrocytic end-feet appear in direct contact with the enlarged extracellular space containing electron lucid or proteinaceous oedema. These findings demonstrate the absence of the glial cell component of the blood-brain barrier, and indicate the glial barrier dysfunction induced by the traumatic brain oedema [37], and interruption of the route between capillaries, astrocytes and the neuronal membranes by which metabolic substrates reach the neurons

[25,37,139]. Subsequently, vasogenic and cytotoxic oedema are superimposed, and degeneration and death of pyramidal and non-pyramidal nerve cells

http://rcin.org.pl
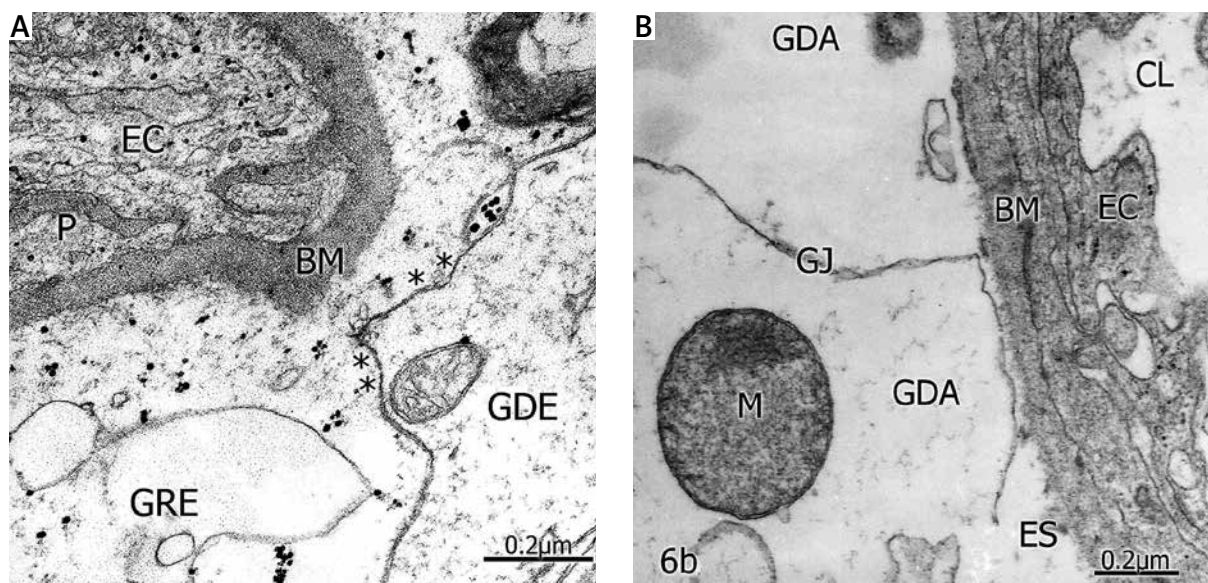
Fig. 6. A) Brain trauma. Subdural haematoma. Glycogen-depleted (GDE) and glycogen-rich (GRE) perivascular astrocytic end-feet appear applied to the outer surface of the capillary basement membrane (BM) in a moderate oedematous region. The GRE exhibits beta-type glycogen granules and vacuoles. The gap junction between both astrocyte end-feet shows areas of fused astrocyte confronted limiting membranes (asterisks) and absence of the intercalated extracellular space. A pericyte (P) and endothelial cell (EC) are also visualized. **B)** Extremely swollen glycogen-depleted perivascular astrocytic end-feet (GDA) dissociated from the capillary basement membrane (BM) by the oedema fluid and exhibiting discontinuities of the limiting membrane. A swollen and degenerated mitochondrion (M) is observed. Note the enlarged extracellular space (ES), and the denuded capillary basement membrane outer surface (BM). The gap junction (GJ) shows fused and disrupted confronted membranes. The vacuolated endothelial cells (EC), and the capillary lumen (CL) are also distinguished.

occur [25,37]. Similar findings were reported by Ito *et al.* [67] in experimental ischaemic brain oedema in gerbils.

Astrocytes' supply of substrates of glycogen metabolism to ischaemic neurons and oligodendroglial cells

Glycogen-rich and glycogen-depleted perivascular astrocyte end-feet are found in severe traumatic brain injuries [30]. The glycogen-rich perivascular astrocyte end-feet show enlarged vesicular and vacuolar profiles of endoplasmic reticulum, and beta- and alpha-type glycogen granules. In contrast, glycogen-depleted astrocyte end-feet are distinguished by a scarce amount or absent isolated beta- and gamma-type glycogen granules, characterized according to Drochman' s classification [49]. This classification allowed us to distinguish among beta or monogranular, alpha or in rosette clusters, and gamma or mini

type, according to glycogen granular size and degree of aggregation (Fig. 6A and 6B).

In physiological conditions there is no evidence for transfer of glycogen substrate energy from glial cell stores to neurons [42]. Our electron microscopic findings suggest that glycogen accumulation and breakdown are induced by the severity of traumatic brain injuries [30]. The fact that both glycogen-rich and glycogen-depleted astrocyte perivascular processes are simultaneously found strongly suggests the hypothesis that in human brain trauma astrocytes exert a neuroprotective action supplying substrates of glycogen metabolism for the survival of ischaemic neurons and oligodendroglial cells. In support of our hypothesis is the fact that glycogen accumulation after an initial decrease is a distinctive feature of astrocytes responding to injury [64]. According to Magistreti *et al.* [89], astrocytes may help neurons with their energy requirements during periods of activity.

Enlargement, fusion and disruption of interastrocytary gap junctions induced by the traumatic agent

At the level of interastrocytary gap junctions (gap junctions localized between two neighbouring astrocyte end-feet belonging to the same or to different clear or dark perivascular astrocytes), the severe traumatic injury induces widening of confronted astrocyte end-feet limiting membranes and enlargement of extracellular space between the astrocyte end-feet, or they appear either fused or disrupted by the notably swollen astrocyte end-feet [22,26] (Fig. 6A and 6B).

There is a relationship between swollen capillary endothelial cells and swollen perivascular astrocytes. The open endothelial junctions [35] and the increased transendothelial vacuolar and vesicular transport [32] discharge the brain oedema fluid into the thickened basement membrane, and into the astrocyte perivascular end feet [37].

These findings indicate blood brain barrier breakdown and the genesis of vasogenic brain oedema in severe human brain trauma. These findings also tend to demonstrate that in human traumatic brain oedema, the connecting hemichannels of each confronting astrocytic end-foot process forming the gap junctions [46,89,104,121] are set apart or damaged with subsequent disruption of connexin proteins. In normal physiological conditions, astrocytes *in vitro* modulate the blood-brain barrier permeability, but there is no correlation with alterations of tight junction protein from the cellular contacts. However, as previously demonstrated by Hossain *et al.* [66], astrocytes respond to an ischaemic insult reorganizing their gap junctions. Theriault *et al.* [133] described alteration of connexin 43 and astrocytic gap junctions after acute compression injury. Nerve cell injury causes large intracellular increase in intracellular K^+ and Ca^{2+}, which could lead to astrocytic uncoupling [108]. In addition, intracellular acidification mediated by lactate also results in irreversible astrocytic uncoupling [3]. Additionally, Li *et al.* [84] reported the phosphorylation status of gap junctions and connexin 43 in rat brain after cerebral focal ischaemia.

The above-mentioned findings on damaged astrocytic gap junctions suggest a whole alteration of the pan-glial syncytium postulated by Rash *et al.* [122] and Li *et al.* [84], or an interruption of the gap junction wiring described by Dermietzel *et al.* [46]. In addition,

it would mean an alteration of the coordinating role of gap junctions in motor behaviour [71].

Dense and reactive hypertrophic astrocytes

Hypertrophic astrocytes are observed at the interfascicular level at the neuropil and in perivascular localization. Their perivascular end-feet can be observed attached to the capillary basement membrane. They are characterized by increased cytoplasmic matrix density, distended rough endoplasmic reticulum profiles, swollen mitochondria, fragmentation of Golgi apparatus, and presence of alpha- and beta-glycogen particles. Close examination of the cytoplasm at higher magnification shows increased numbers of glial filaments, microtubules, and numerous round and lobulated lysosomes. They exhibit robust and extended processes in the neuropil containing compact bundles of glial filaments [26,28,29] (Fig. 7A).

These types of astrocytes have also been found by Kaur *et al.* [70] after a non-penetrative blast. However, hypertrophic astrocytes seem to be an unspecific population present in traumatic brain injuries since they have been described in a large variety of distinct human nerve pathological entities, and in experimental animal models, such as those reported by Ludowyk *et al.* [87] in chronic experimental autoimmune encephalitis in aged rats, Khurgel and Ivy [72] in kindling-induced seizures, Krsulovic *et al.* [78] in nerve cells of taiep rats, and by Harsan *et al.* [63] in dysmyelinated jimpy mouse brain. The mouse jimpy mutation of the X-linked proteolipid protein (Plp) gene causes dysmyelination and premature death of the mice. The established phenotype is characterized by severe hypomyelination, increased numbers of dead oligodendrocytes and astrocytosis. This astrocytosis exhibits similar features as in the case of the astrocytes described above. Therefore, dense and reactive hypertrophic astrocytes are not a subpopulation of astrocytes specifically induced by severe and complicated human brain injuries.

Dark astrocytes, which should be considered as a variety of hypertrophic astrocytes, have been found by Gallyas *et al.* [57], and by Tóth *et al.* [136] after compressive or concussive head injuries. These reactive astrocytes with dense processes are GFAP immunoreactive [51-53], and have been co-labelled by antibodies to GFAP and vimentin [54]. For further details the reader is referred to the elegant review of Malhotra *et al.* [91] on reactive astrocytes.

http://rcin.org.pl
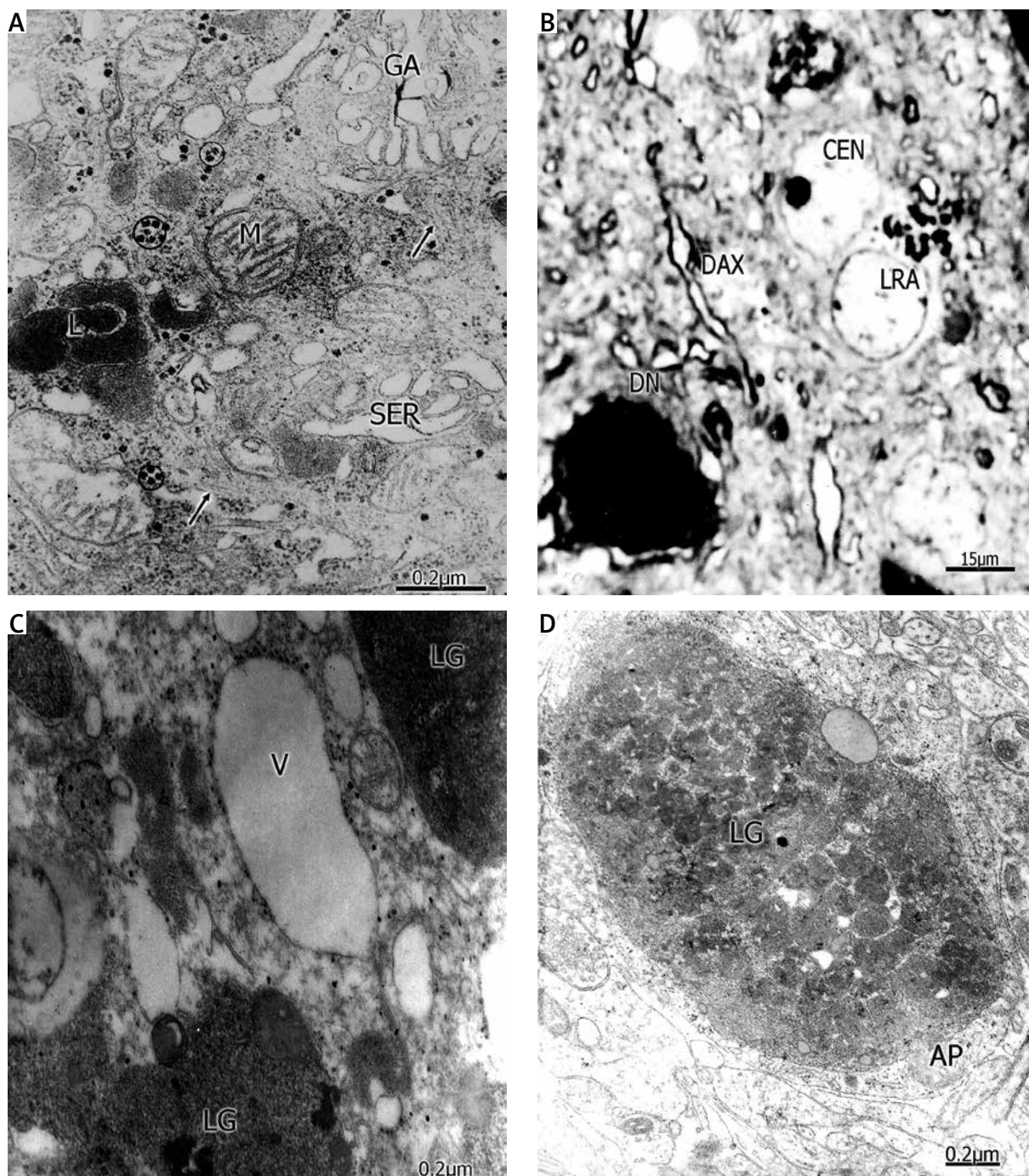
Fig. 7. A) Brain trauma. Subdural haematoma. Left parietal cortex. Electron micrograph of a dense hypertrophic astrocyte showing numerous canaliculi and vesicles of smooth endoplasmic reticulum (SER), multiple rosettes of multigranular or alpha-type glycogen particles (circle), clear and swollen mitochondria (M), lobulated lysosomes (L), fragmented Golgi apparatus (GA), and microfilaments (arrows). **B)** Brain trauma. Subdural haematoma. Frontal cortex. Light microscopy of a semithin section stained with toluidine blue showing a swollen and lipofuscin-rich clear astrocyte (LRA) surrounding a clear oedematous neuron (CEN). A dark ischaemic neuron (DN) and a degenerated myelinated axon (DAX) are also distinguished. **C)** Electron micrograph of a lipofuscin-rich astrocyte cytoplasm exhibiting lipofuscin granules (LG) and vacuoles (V). **D)** Lipofuscin-rich astrocyte process (AP) containing a huge lipofuscin granule (LP).

Lipofuscin-rich astrocytes favour the aging process and neuronal degeneration in traumatic brain injuries

In traumatic brain injuries, accumulation of lipofuscin granules has been found in the astrocyte body and processes [32] (Fig. 7B, 7C and 7D).

This lipofuscin accumulation has been widely reported in normal aging subjects [100]. Although age is considered an important factor reducing astrocyte reactivity, in aging patients with severe brain trauma, increased reactivity of astrocytes was observed characterized by a large amount of lipofuscin-rich astrocytes. The significance of lipofuscin accumulation for astrocyte biopathology is a subject that remains relatively poorly defined in the world literature. Our studies have demonstrated that lysosomes coexisting with an increased amount of lipofuscin granules are observed in young and adult patients with brain trauma, tumours and vascular anomalies, implicating a dysfunction of the endolysosomal system in astrocytes [32]. We have also reported lipofuscin granules in neonate and infant patients with congenital hydrocephalus [32], suggesting that lipofuscin formation is a life span process in immature and mature astrocytes, and not only due to the aging process, as it has been classically conceptualized. The neurodegeneration associated with lipofuscin accumulation may be caused by that accumulation, and induces astrocyte activation. Lipofuscin and ceroid are usually held responsible for impaired cellular performance, via oxidative damage and the irreversible accumulation of fluorescent products of lipid peroxidation. The participating evidence of free radical oxidative interactions in promoting astrocyte injury in such conditions as brain trauma, ischaemia, toxicity, and in neurodegenerative diseases such as Parkinson' s disease, Alzheimer' s dementia, multiple sclerosis, and lipofuscinosis, is growing and accumulating, and favouring the idea of an overall spectrum of an altered endosomal/lysosomal system. Accumulation of heterogeneous non-degraded macromolecules in dysfunctional lysosomes and autolysosomes ultimately leads to early-onset apoptotic death with subsequent activation of astrocytes [111]. The general hypothesis, as developed from chronic neurodegenerative diseases [14,16], is that astrocyte activation occurs in juvenile neuronal ceroid lipofuscinosis (JNLC) and Batten disease. Additionally,

the role of peroxy radicals or their products formed by lipoperoxidation of polyunsaturated fatty acids has also been implicated [13].

In spite of recent advances in immunohistochemical identification of biochemical markers, the ultrastructural identification of lipofuscinic pigments remains the gold standard to identify neuronal ceroid lipofuscinosis (NCL), together with the clinical aspects and respective gene defects [14]. Neuronal cell cultures offer a good model to study systematically lipofuscin' s impact on astrocyte biopathology.

Traumatically reactive astrocytes phagocytose synaptic contacts, myelinated axons and undifferentiated nerve cell debris

Clear and swollen dense perineuronal phagocytic astrocytes can be seen engulfing remnants of degenerated myelin sheath, myelin ovoids, degenerated myelinated axons, and entire degenerated axo-dendritic contacts, and fragments of nerve cell debris.

These two types of phagocytic astrocytes are frequently found in traumatic brain oedema: the clear type characterized by lamellar processes containing osmiophilic vesicles, as previously described by Gonatas et al. [62] (Fig. 8A), and a second type: the dark phagocytic astrocytes [26,28]. Figure 8B shows a clear phagocytic astrocyte cytoplasm with osmiophilic vesicles in the neuropil engulfing a presynaptic ending. These findings indicate the participation of phagocytic astrocytes in the removal of degenerated nerve cell substructures in the traumatic oedematous human cerebral cortex [28,29].

Table I below summarizes the features of astrocyte changes in moderate and severe oedema.

Traumatic brain oedema induces disruption of astrocyte plasma membrane and cytomembranes

The physical stress elicited by the intensity of the traumatic agent induces rupture of the astrocyte plasma membrane, nuclear membranes, cytomembranes and Golgi apparatus, and perivascular astrocyte end-feet exhibit membrane defects induced by decreased Na^+-K^+-ATPase activity exerted by the trauma [41], and changes in the extracellular ion Na^+ and K^+ concentrations [101]. Increased membrane tension could open stretch-activated ions chan-

nels in astrocyte cultures [73], and astrocyte amino acids could diffuse through these channels (swelling-induced release of amino acids from astrocytes). Mechanical injury alters the volume of activated ion channels [47]. As pointed out by Levi and Gallo [82], it is possible that the establishment of a vicious circle will cause self-potentiation of the pathological process. For example, the accumulation of extracellular glutamate and K^+ following the traumatic and ischaemic insults could induce astrocyte swelling with further glutamate and K^+ efflux, and consequent potentiation of swelling and excitotoxicity.

Astrocyte cell death types in severe and complicated traumatic brain injuries

In severe brain trauma complicated by subdural or epidural haematoma we found astrocyte cells exhibiting oncotic cell death type characterized by electron lucent and swollen cytoplasm and nucleoplasm, lobulated nucleus, presence of intranuclear inclusions, apparently intact and disrupted nuclear pore complex, numerous clear vacuoles, lysosomes, and numerous small dense bodies [33] (Fig. 9A).

The presence of typical apoptotic astrocyte cell death is characterized by chromatin condensation, a disrupted perinuclear cistern and the finding of apoptotic bodies in the nucleus and cytoplasm (Fig. 9B).

Other astrocytes display coexisting oncotic and apoptotic cell death, showing chromatin condensation, empty electron lucent and disrupted cytoplasm, and swollen degenerated mitochondria. Some of these astrocytes show postmortem morphological features of necrotic cell death, characterized by disorganized nuclear chromatin, clear or dense fibrillar and granular euchromatin, clear or dense nucleoplasm,
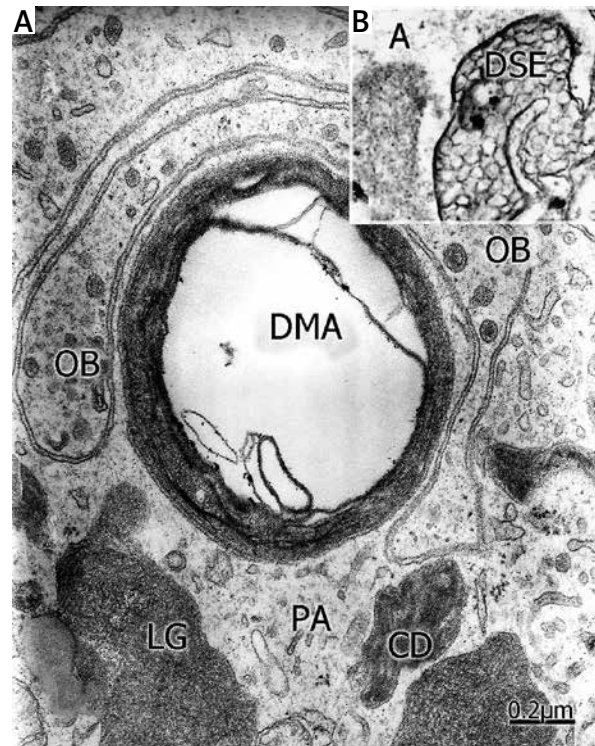
Fig. 8. A) Brain trauma. Subdural haematoma. Left parietal cortex. Phagocytic astrocyte (PA) exhibiting lamellar pseudopods containing osmiophilic bodies (OB) and vesicles, and engulfing a degenerated myelinated axon (DMA). The cytoplasm shows lipofuscin granules (LG) and remnants of nerve cell debris (CD). **B)** Insert showing a phagocytic astrocyte process (A) in the neuropil engulfing a degenerated presynaptic ending (DSE).

remnants of cytomembranes, small dense vesicles, massive vacuolar degeneration, plasma membrane fragmentation and degeneration, and dispersed,

Table I. Astrocyte changes in human severe traumatic brain injuries

	Moderate oedema	Severe oedema
Reactive clear swollen astrocytes	Dilated RER	Vacuolated RER
Reactive dense swollen astrocytes	Increased NF, Fragmented GA	Numerous L Oedematous GA
Astrocyte plasma membrane	Mostly preserved	Disrupted
Reactive hypertrophic astrocytes	Present	Present
Glycogen-rich and glycogen-depleted astrocytes	Present	Present
Phagocytic astrocytes	Present	Present
Lipofuscin-rich astrocytes	Present	Present
Astrocyte nerve cell death types (Oncosis, Apoptosis, Necrosis)	Present	Present

RER – endoplasmic reticulum, M – mitochondria, GA – Golgi apparatus, NF – neurofilaments, MT – microtubules, MA – myelinated axons, L – lysosomes, LG – lipofuscin granules

degenerated mitochondria at cytoplasmic and extra-cellular localizations [33] (Fig. 9C).

Ischaemic neuronal death influenced by astrocytes has been described by Swanson *et al.* [132]. Experimental brain injury induces regional distinct apoptosis during the acute and delayed post-traumatic period [43].

A continuum of increased oncosis, apoptosis and necrosis appeared to involve astrocytes and oligodendrocytes in traumatic human brain oedema [33], and in animals following blast exposure [139]. In patients with higher brain dysfunction after mild traumatic brain injury, diagnostic imaging showed cortical neuron loss in the frontal lobes, using single-photon emission computed tomography (SPECT) with I-iomazenil, as a radioligand for the central benzodiazepine receptor [105]. Swanson and Kauppinen [132] have recently examined the influences of astrocytes on ischaemic neuronal death.

The key role of aquaporin in traumatic astrocyte swelling

Aquaporins (AQPs) play pivotal roles in cerebral water movement as essential mediators during oedema and fluid accumulation. Aquaporin 4 (AQP4), a water channel protein located at the blood-brain barrier, might facilitate the removal of this excess of water from the parenchyma into the blood. Aquaporin 4 was first located on astrocyte end-feet but later on the whole membrane of astrocytes that became hypertrophic in the most severe traumatic brain injuries [130]. The key role of aquaporin in astrocyte swelling and traumatic brain oedema has been emphasized by several investigators [61,130,131]. More recent studies indicate a key role of aquaporin in astrocyte swelling, ischaemia and brain oedema [2,85,106,107,113,141]. According to some of these studies, AQP4 expression follows an adaptive profile to the severity of traumatic brain oedema, which is probably a protective response mechanism. A very important avenue for future work in traumatic brain injuries and brain oedema is to study aquaporin as a target for pharmaceutical treatment.

The dissociated astrocyte-neuronal unit in human traumatic brain injuries

As mentioned above, normal neuronal-astrocyte cooperation is important for signalling, energy metabolism, extracellular ion homeostasis, volume regula-

tion, and neuroprotection [10]. The findings described above in traumatic and complicated human brain injuries in the oedematous cerebral cortex reveal a structural alteration of the astrocyte-neuronal unit. Swollen and ischaemic neurons and swollen perineuronal astrocytes should be considered an abnormal metabolic cooperation of the astrocyte-neuronal unit. This dissociation would mean an altered astrocyte response to chemical signals from damaged neurons, which would send back other messages in the form of neuroactive and neurotrophic substances. These alterations would include not only those classical neurotransmitters and neuromodulators, but also growth factors, cytokines and prostanoids [50,97].

Swollen astrocytes could be responsible for the degeneration of damaged neurons, not only for the exerted outer surface physical stress due to the notably swollen astrocyte soma, but in addition, for the establishment of high extracellular levels of glutamate released during severe traumatic brain injuries (glutamate excitotoxicity) [28,29,73-75].

These findings have led to the prevalent hypothesis that excitatory amino acid efflux is a major contributor to the development of neuronal damage subsequent to traumatic injury. Obrenovitch *et al.* [110] ask an interesting question related to the role of glutamate excitotoxicity in traumatic brain injuries.

Hypothesis of astrocyte responsibility for production of seizures

Astrocyte mitochondrial matrix swelling and loss of cristae [34], and early inactivation of cytochrome oxidase, have been reported after injury [41]. Since astrocyte glutamine synthesis requires ATP, it is rational to argue that in human brain trauma due to mitochondrial swelling, astrocytes would not be able to convert accumulated glutamate to glutamine. If we consider that glutamine is also a quantitatively important precursor of GABA [9], we could infer that a disturbance of the GABA-glutamine cycle and glutamate excitotoxicity could explain the seizures observed in some patients studied in our laboratory [27]. An impairment of glutamate-inactivating ability of astrocytes in human brain trauma [92] could be important in increasing the excitotoxic effect of glutamate on neurons. This hypothesis should be considered in explaining the degeneration of pyramidal and non-pyramidal nerve cells leading to nerve cell death.
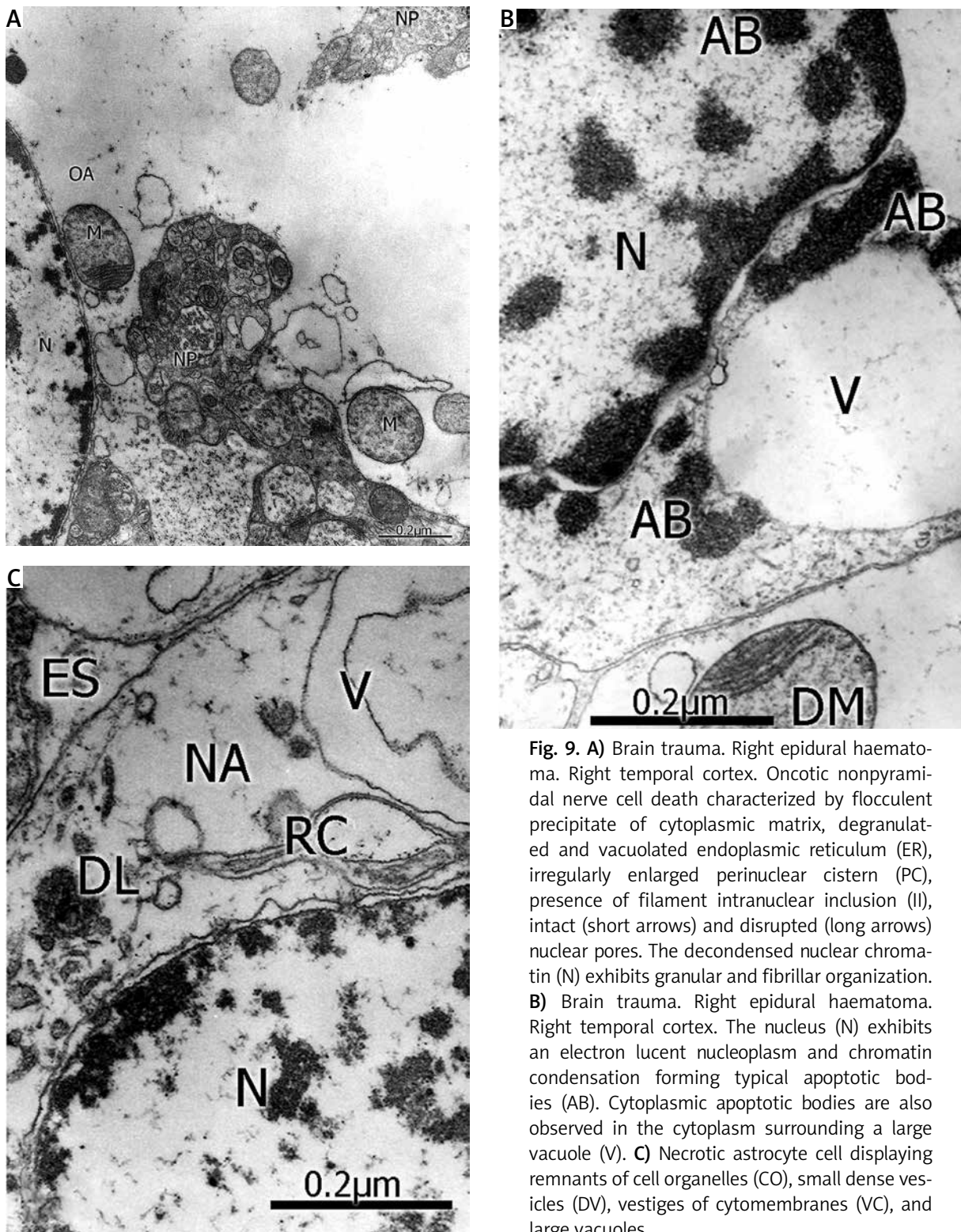
Fig. 9. A) Brain trauma. Right epidural haematoma. Right temporal cortex. Oncotic nonpyramidal nerve cell death characterized by flocculent precipitate of cytoplasmic matrix, degranulated and vacuolated endoplasmic reticulum (ER), irregularly enlarged perinuclear cistern (PC), presence of filament intranuclear inclusion (II), intact (short arrows) and disrupted (long arrows) nuclear pores. The decondensed nuclear chromatin (N) exhibits granular and fibrillar organization. **B)** Brain trauma. Right epidural haematoma. Right temporal cortex. The nucleus (N) exhibits an electron lucent nucleoplasm and chromatin condensation forming typical apoptotic bodies (AB). Cytoplasmic apoptotic bodies are also observed in the cytoplasm surrounding a large vacuole (V). **C)** Necrotic astrocyte cell displaying remnants of cell organelles (CO), small dense vesicles (DV), vestiges of cytomembranes (VC), and large vacuoles.

Table II. Altered astrocyte-neuronal unit

	Moderate oedema	Severe oedema
Perisynaptic astrocyte	Preserved	Absent
Astrocytes supply substrates of glycogen metabolism	Increased	Increased
Glio-basal dissociation process	Preserved	Dissociated
Gap junction alteration	Present	Dissociated
Glutamate cytotoxicity	Increased	Increased

Table II summarizes the abnormal astrocyte-neuronal unit in traumatic moderate and severe oedema.

Concluding remarks

Severe and complicated traumatic human brain injuries induce notably swollen astrocytes and numerous subpopulations of astrocyte subtypes, such as clear and dense oedematous astrocytes, hypertrophic reactive astrocytes, glycogen-rich and glycogen-depleted astrocytes, lipofuscin-rich astrocyte, and phagocytic astrocytes. Swollen clear and dense perineuronal astrocytes appear compressing and indenting dark, ischaemic nerve cells, degenerated myelinated axons, and synaptic contacts. At the level of the neuropil, in areas of moderate brain oedema, the perisynaptic astrocyte cytoplasmic layer appears covering axodendritic synaptic contacts, dendrites and myelinated axons. In severe oedematous regions the perisynaptic astrocytic glial ensheathment is rejected and lost by the brain oedema fluid deposited in the enlarged extracellular space. The synaptic contacts appear in direct continuity with the extracellular space impairing neurotransmission.

Glycogen-rich and glycogen-depleted perivascular astrocyte end-feet are found applied or dissociated from the capillary basement membrane. The interastrocytary gap junctions appear separated, fused and fragmented. Reactive hypertrophic astrocytes exhibit dense cytoplasmic matrix, increased amounts of dilated smooth and rough endoplasmic reticulum, microtubules, gliofilaments, and vacuolization and fragmentation of Golgi apparatus. Lipofuscin-rich astrocytes and phagocytic astrocytes are also frequently observed, induced by lipid peroxidation, and an overall spectrum of altered endosomal/lysosomal system. Some hypotheses are raised related to the absence of the perisynaptic layer, the neurobiological significance of glycogen-rich and glycogen-depleted astrocytes, the abnormal astrocyte-neuron unit, and the astrocyte responsibility for production of seizures. The results are compared with those described in experimental brain trauma, related neuropathological conditions, ischaemic processes, and *in vivo* and *in vitro* experimental conditions, in an attempt to establish a link between basic and clinical neuroscience, and to design new therapeutic strategies.

Acknowledgements

Disclosure

Authors report no conflict of interest.

References

1. Adams RD. Implications of the biology of the neuroglia and microglia cells for clinical neuropathology. In: Windle WF (ed.). Biology of Neuroglia. Oxford University Press, Springfield 1958; pp. 245-263.
2. Amiry-Moghaddam M, Ottersen OP. The molecular basis of water transport in the brain. Nat Rev Neurosci 2003; 4: 991-1001.
3. Anders JJ. Lactic acidification of GAP junctional communication in "in vitro" astrocytes as measured by fluorescence recovery after laser photobleaching. Glia 1988; 1: 371-379.
4. Al-Ali SY, al-Hussain SM. An ultrastructural study of the phagocytic activity of astrocytes in adult rat brain. J Anat 1996; 188: 257-262.
5. Allen IV, Kirk J, Maynard RL, Cooper GK, Scott R, Crockard A. Experimental penetrating head injury: some aspects of light microscopical and ultrastructural abnormalities. Acta Neurochir Suppl (Wien) 1983; 32: 99-104.
6. Araque A, Sanzgiri RP, Purpura V, Haydon PG. Astrocyte-induced modulation of synaptic transmission. Can J Physiol Pharmacol 1999; 77: 699-706.
7. Ballanyi K. Modulation of glial potassium, sodium and chloride activities by the extracellular milieu. In: Neuroglia. Kettenmann H, Ransom B.(eds.). Oxford University Press, New York 1995; pp. 289-298.

8. Barron KD, Dentinger MP, Kimelberg HK, Nelson LR, Bourke RS, Keegan S, Mankes R, Kragoe EJ Jr. Ultrastructural features of a brain injury model in cat. I. Vascular and neuroglial changes and the prevention of astroglial swelling by a fluorenyl (aryloxy) alkanoic acid derivative. Acta Neuropathol 1988; 75: 295-307.

9. Bataglioni G, Martin DL. GABA synthesis in brain slices in dependent on glutamine produced in astrocytes. Neurochem Res 1991; 16: 151-156.

10. Benarroch EE. Neuron-astrocyte interactions: partnership for normal function and disease in the central nervous system. Mayo Clin Proc 2005; 80: 1326-1338.

11. Bignami A, Ralston HJ. The cellular reaction to Wallerian degeneration in the central nervous system of the cat. Brain Res 1969; 13: 444-461.

12. Bignami A, Dahl D. In: Gliosis. Neuroglia. Kettenmann H, Ransen B (eds.). Oxford University Press, New York 1995; pp. 843-858.

13. Boehme DH, Leonberg SC, Varagiannis E, Marks N. On the neurochemistry of an adult form of ceroid lipofuscinosis (Kuf's disease). Prog Clin Biol Res 1980; 39: 305-314.

14. Boldrini R, Biselli R, Santorelli FM, Bosman C. Neuronal ceroid lipofuscinosis: an ultrastructural, genetic, and clinical study report. Ultrastruct Pathol 2001; 25: 51-58.

15. Bullock R, Maxwell WL, Graham DI, Teasdale GM, Adams JH. Glial swelling following human cerebral contusion: an ultrastructural study. J Neurosurg Psychiatr 1991; 54: 427-434.

16. Burkovetskaya M, Karpuk N, Xiong J, Bosch M, Boska MD, Takeuchi H, Suzumura A, Kielian T. Evidence for aberrant astrocyte hemichannel activity in Juvenile Neuronal Ceroid Lipofuscinosis (JNCL). PLoS One 2014; 9: e95023.

17. Butt AM, Kirvell S. Glial cells in transected optic nerves of immature rats. II. An immunohistochemical study. J Neurocytol 1996; 25: 381-392.

18. Calvo JL, Carbonell AL, Boya J. Coexpression of glial fibrillary acidic protein and vimentin in reactive astrocyte following brain injury in rats. Brain Res 1991; 566: 333-336.

19. Cammermayer J. Astroglial changes during retrograde atrophy of the nucleus facials in mice. J Comp Neurol 1955; 102: 133-150.

20. Canady KS, Hyson RL, Rubel EW. The astrocytic response to afferent activity blockade in chick nucleus magnocellularis is independent of synaptic activation, age, and neuronal survival. J Neurosci 1994; 14: 5973-5985.

21. Cancilla PA, Breedy J, Berliner J, Sharifi-Nia H, Toga AW, Santony EM, Scully S, Devellis J. Expression of MRNA for glial fibrillary acidic protein after experimental brain injury. J Neuropathol Exp Neurol 1992; 51: 560-565.

22. Castejón OJ. Electron microscopic study of capillary wall in human cerebral edema. J Neuropathol Exp Neurol 1980; 39: 296-328.

23. Castejón OJ. Electron microscopic study of central axonal degeneration in traumatic human brain edema. J Submicrosc Cytol 1985; 17: 703-718.

24. Castejón OJ, Valero C, Díaz, M. Light and electron microscope study of nerve cells in traumatic edematous human cerebral cortex. Brain Injury 1997; 11: 363-388.

25. Castejón OJ. Ultrastructural alterations of human cortical capillary basement membrane in perifocal brain edema. J Submicrosc Cytol Pathol 1988; 20: 519-536.

26. Castejón OJ. Morphological astrocytic changes in complicated human brain trauma. A light and electron microscopic study. Brain Injury 1998; 12: 409-427.

27. Castejón OJ. Electron microscopic analysis of cortical biopsies in patients with traumatic brain injuries and dysfunction of neuro-behavioural system. J Submicrosc Cytol Pathol 1998; 30: 145-156.

28. Castejón OJ. Astrocyte subtypes in the gray matter of injured human cerebral cortex. A transmission electron microscopic study. Brain Injury 1999; 13: 291-304.

29. Castejón OJ, Castejón HV, Diaz M, Castellano A. Consecutive light microscopy, scanning-transmission electron microscopy and transmission electron microscopy of traumatic human brain oedema and ischaemic brain damage. Histol Histopathol 2001; 16: 1117-1134.

30. Castejón OJ, Díaz M, Castejón HV, Castellano A. Glycogen-rich and glycogen-depleted astrocytes in the oedematous human cerebral cortex associated with brain trauma, tumours and congenital malformations: an electron microscopy study. Brain Injury 2002; 116: 109-132.

31. Castejón OJ, Castejón HV, Díaz M, Sánchez M, Zavala M. A light and electron microscoy study of edematous human cerebral cortex in two patients with post-traumatic seizures. Brain Injury 2002; 16: 331-346.

32. Castejón OJ. Lysosome abnormalities and lipofucsin content of nerve cells of edematous cerebral cortex. J Submicrosc Cytol Pathol 2004; 36: 263-271.

33. Castejón OJ, Arismendi G. Nerve cell death types in the edematous human cerebral cortex. J Submicrosc Cytol Pathol 2006; 38: 21-36.

34. Castejón OJ. Structural pattern of injured mitochondria in oedematous human cerebellar cortex. Brain Injury 2004; 18: 1107-1126.

35. Castejón OJ. Ultrastructural pathology of endothelial tight junctions in human brain oedema. Folia Neuropathol 2012; 50: 118-129.

36. Castejón OJ. Increased vesicular and vacuolar transendothelial transport in traumatic human brain oedema. A review. Folia Neuropathol 2013; 51: 93-102.

37. Castejón OJ. Ultrastructural alterations of human cortical capillary basement membrane in perifocal brain edema. Folia Neuropathol 2014; 52: 1-9.

38. Cervós-Navarro J. Brain edema due to ionizing radiation. In: Brain Edema. Klatzo Y, Seitelberger F (eds.). Springer-Verlag, New York 1967; pp. 632-638.

39. Chen H, Sun D. The role of Na-K-Cl co-transporter in cerebral ischemia. Neurol Res 2005; 27: 280-286.

40. Chen S, Pickard JD, Harris NG. Time course of cellular pathology after controlled cortical impact injury. Exp Neurol 2003; 182: 87-102.

41. Clendenon NR, Allen N. Organelle and membrane defects: Lysosomes, mitochondria and cell membranes. In: Neural Trauma. Seminars in Neurological Surgery. Popp A, Bowoke RS, Nelson LR, Kimelberg HK (eds.). Raven Press, New York 1979; pp. 115-129.

42. Coles JA. Glial cells and the supplement of substrates of energy metabolism to neurons. In: Neuroglia. Kettenmann H, Ranson H (eds.). Oxford University Press, New York 1995; pp. 793-804.

http://rcin.org.pl

43. Conti AC, Raghupathi R, Trojanowski JQ, Mcintosh TK. Experimental brain injury induces regionally distinct apoptosisduring the acute and delayed post-traumatic period. J Neurosci 1998; 18: 5663-5672.

44. Del Bigio MR, Deck JH, Davidson GS. Glial swelling with eosinophilia in human post-mortem brains: a change indicative of plasma extravasation. Acta Neuropathol 2000; 100: 688-694.

45. Derugin N, Wendland M, Muramatsu K, Roberts TP, Gregory G, Ferreiro DM, Vexler ZS. Evolution of brain injury after transient middle cerebral artery occlusion in neonatal rats. Stroke 2000; 31: 1752-1761.

46. Dermietzel R. Gap junction wiring: a 'new' principle in cell-to-cell communication in the nervous system? Brain Res Brain Res Rev 1998; 26: 176-183.

47. Di X, Goforth PB, Bullock R, Ellis E, Satin L. Mechanical injury alters volume of activated ion channels in cortical astrocytes. Acta Neurochir (Suppl) 2000; 76: 379-383.

48. Dietrich WD, Alonso O, Halley M, Busto R. Delayed posttraumatic brain hyperthermia worsens outcome after fluid percussion brain injury: a light and electron microscopic study in rats. Neurosurgery 1996; 38: 533-541.

49. Drochman P. Morphologie du glycogène. Étude au microscopie électronique de colorations négatives du glycogènes. J Ultrastruct Res 1962; 6: 141-163.

50. Eddleston M, Mucke L. Molecular profile of reactive astrocytes implications for their role in neurologic disease. Neuroscience 1993; 54: 15-36.

51. Eng LF, Shiurba RA. Glial fibrillary acidic protein: a review of structure, function, and clinical application. In: Neuronal and Glial Proteins: Structure, Function and Clinical Application. Vol. 2. Marangos PJ, Campbell I, Cohen RM (eds.). Academic Press, New York 1988; pp. 339-359.

52. Eng LF. Glial fibrillary acidic protein: the major protein of glial intermediate filaments in differentiated astrocytes. J Neuroimmunol 1985; 8: 203-205.

53. Eng LF. Astrocyte response to injury. In: Current Issues in Neural Regeneration Research. Reir PJ, Bunge J, Seil J (eds.). Alan R Liss, New York 1988; pp. 220-230.

54. Farooque M, Badonic T, Olsson Y, Holtz A. Astrocytic reaction after graded spinal cord compression in rats: immunohistochemical studies on glial fibrillary acidic protein and vimentin. J Neurotrauma 1995; 12: 41-52.

55. Fotheringham AP, Davies CA, Davies I. Oedema and glial cell involvement in the aged mouse brain after permanent focal ischaemia. Neuropathol Appl Neurobiol 2000; 26: 412-423.

56. Fujisawa H, Maxwell WL, Graham DI, Reasdale GM, Bullock R. Focal microvascular occlusion after acute subdural haematoma in the rat: a mechanism for ischaemic damage and brain swelling? Acta Neurochir (Suppl) 1994; 60: 193-196.

57. Gallyas F, Horváth Z, Dávid K, Liposits Z. An immediate morphopathologic response of a subpopulation of astrocytes to electroshock: "dark" astrocytes. Neurobiology 1994; 2: 245-253.

58. García JH, Lossinsky AS, Nishimoto K, Klatzo Y, Lightfoote Jr. W. Cerebral microvasculature in ischemia. In: Advances in Neurology. Cervós-Navarro J (ed.). Raven Press, New York 1978; pp. 141-148.

59. Gilmore SA, Sims TJ, Leiting JE. Astrocyte reactions in spinal gray matter following sciatic axotomy. Glia 1990; 3: 342-349.

60. Graeber MB, Kreutzberg W. Delayed astrocyte reaction following facial nerve axotomy. J Neurocytol 1988; 17: 209-220.

61. Ghabriel MN, Thomas A, Vink R. Magnesium restores altered aquaporin-4 immunoreativity following traumatic brain injury to a pre-injury state. Acta Neurochir (Suppl) 2006; 96: 402-406.

62. Gonatas NK, Martin J, Evangelista I. The osmiophilic particles of astrocytes. Viruses, lipid droplets or products of secretion? J Neuropathol Exp Neurol 1967; 26: 369-376.

63. Harsan LA, Poulet P, Guignard B, Parizel N, Skoff RP, Ghandour MS. Astrocyte hypertrophy in dysmielination influences the diffusion anisotropy of white matter. J Neurosci Res 2007; 85: 935-944.

64. Haymaker W, Miguel J, Ibrahim MZM. Glycogen accumulation following brain trauma. Top Probl Psychiatr Neurol 1970; 10: 71-87.

65. Höke A, Silver J. Heterogeneity of astrocytes in reactive gliosis. Perspect Dev Neurobiol 1994; 2: 269-274.

66. Hossain MZ, Peeling J, Sutherland R, Hertzberg EL, Nagy JI. Ischemia-induced cellular redistribution of the astrocytic gap junctional protein connexin43 in rat brain. Brain Res 1994; 652: 311-322.

67. Ito U, Kuroiwa T, Hanyu S, Hakamata Y, Kawakami E, Nakano I, Oyanigi K. Temporal profile of experimental ischemic edema after threshold amount of insult to induce infarction, ultrastructure, gravimetry and Evans' blue extravasation. Acta Neurochir (Suppl) 2003; 86: 131-135.

68. Janeczko K. The proliferative response of astrocytes to injure in neonatal brain: A combined immunocytochemical and autorradiographic study. Brain Res 1988; 456: 280-285.

69. Kamyrio T, López MB, Kassell NF, Steiner L, Lee KS. Radiosurgery-induced microvascular alterations precede necrosis of the brain neuropil. Neurosurgery 2001; 49: 409-414.

70. Kaur C, Slingh J, Lim MK, Ng BL, Yap EP, Ling EA. Ultrastructural changes of macroglial cells in the rat brain following an exposure to a non-penetrative blast. Ann Acad Med (Singapore) 1997; 26: 27-29.

71. Kiehn O, Tresch MC. Gap junctions and motor behaviour. Trends Neurosci 2002; 25: 108-115.

72. Khurgel M, Ivy GO. Astrocytes in kindling: relevance to epileptogenesis. Epilepsy Res 1996; 26: 163-175.

73. Kimelberg HK, Goderic SK, Higman S, Pang S, Warriewski RA. Swelling-induced release of glutamate, aspartate, and taurine from astrocyte cultures. J Neurosci 1990; 10: 1583-1591.

74. Kimelberg HK. Astrocytic edema in CNS trauma. J Neurotrauma (Suppl) 1992; 1: S71-S81.

75. Kimelberg HK. Brain Edema. In: Neuroglia. Kettenmann H, Ramson BR (eds.). Oxford University Press, New York 1995; pp. 919-935.

76. Klatzo I. Neuropathological aspect of brain edema. J Neuropathol Exper Neurol 1967; 26: 1-14.

77. Kost-Micucki SA, Oblinger MM. Changes in glial fibrillary acidic protein mRNA expression after corticospinal axotomy in the adult hamster. J Neurosci Res 1991; 28: 182-188.

78. Krsulovic J, Couve E, Roncagiolo M. Dysmelination, demyelination and reactive astrogliosis in the optic nerve of the taiep rat. Biol Res 1999; 32: 253-262.

79. Kuchiwaki H, Takada S, Itoh J, Nagasaka M, Kageyama N. Distribution andconstitutional changes of edema fluid in cyto-

http://rcin.org.pl

toxic brain edema analyzed by electron microscopy and differential scanning calorimetry. No To Shinkei 1987; 39: 463-470.

80. Kuroiwa T, Nagaoka T, Ueki M, Yamada I, Miyasaka N, Akimoto H. Different apparent diffusion coefficient: water content correlations of gray and white matter during early ischemia. Stroke 1998; 29: 859-865.

81. Latov N, Nilavev G, Zimmerman EA, Johnson WG, Silverman AJ, Defendim R, Cote L. Fibrillary astrocytes proliferate in response to brain injury: A study combining immunoperoxidase technique for glial fibrillary acidic protein and radioautography of tritiated thymidine. Dev Biol 1979; 72: 381-384.

82. Levi G, Gallo V. Release of neuroactive aminoacids from glia. In: Neuroglia. Kettenman H, Ransom BR (eds.). Oxford University Press, New York 1995; pp. 815-826.

83. Lehmann GL, Gradilone SA, Marinelli RA. Aquaporin water channels in central nervous system. Curr Neurovasc Res 2004; 1: 293-303.

84. Li WE, Ochalski PA, Hertzberg EL, Nagy JI. Immunorecognition, ultrastructure and phosphylation status of astrocytic gap junctions and connexin43 in rat brain after cerebral focal ischaemia. Eur J Neurosci 1998; 10: 2444-2463.

85. Lo AC, Chen AY, Hung VK, Yaw LP, Fung MK, Ho MC, Tsang MC, Chung SS, Chung SK. Endothelin-1 overexpression leads to further water accumulation and brain edema after middle cerebral artery occlusion via aquaporin 4 expression in astrocytic end-feet. J Cerebr Blood Flow Metab 2005; 25: 998-1011.

86. Long DM, Hartman JF, French L. The ultrastructure of human cerebral edema. J Neuropathol Exp Neurol 1966; 25: 373-395.

87. Ludowyk PA, Hughes W, Hugh A, Willenborg DO, Rockett K, Parish CR. Astrocytic hypetrophy: an import pathological feature of chronic experimental autoimmune encephalitis in aged rats. J Neuroimmunol 1993; 48: 121-134.

88. Maeda M, Akai F, Yanagihara T. Neuronal integrity and astrocytic reaction in cold injury: an immunohistochemical investigation. Acta Neuropathol 1997; 94: 116-123.

89. Magistreti PJ, Hoff PR, Martin JL. Adenosine stimulates glycogenolisis in mouse cerebral cortex: A possible coupling mechanism between neuronal activity and energy metabolism. J Neurosci 1986; 6: 2558-2562.

90. Makowski L, Caspar DLD, Phillips WC, Goodenough DA. Gap junction structures. J Cell Biol 1974; 74: 629-645.

91. Malhotra SK, Shnitka TK, Elbrink J. Reactive astrocytes: A review. Cytobios 1990; 61: 133-160.

92. Martin D. The role of glia in the inactivation of neurotransmitter. In: Neuroglia. Kettenmann H, Ransom BR (eds.). Oxford University Press, New York 1995; pp. 732-745.

93. Mázló M, Gasz B, Szigeti A, Zsombok A, Gallyas F. Debris of "dark" (compacted) neurons are removed from an otherwise undamaged environment mainly by astrocytes via blood vessels. J Neurocytol 2004; 33: 557-567.

94. Mathew P, Bullock R, Graham DI, Maxwell WL, Teasdale GM, Mc Cullock J. A new experimental model of contusion in the rat. Histopathological analysis and temporal patterns of cerebral blood flow disturbance. J Neurosurg 1996; 85: 860-870.

95. Mathewson AJ, Berry. Observations on the astrocyte response to a cerebral stab wound in adult rat. Brain Res 1985; 327: 61-69.

96. Matyja E, Taraszewska A, Naganska E, Rafalowska J, Gebarowska J. Astroglial alterations in amyotrophic lateral sclerosis (ALS) model of slow glutamate excitotoxicity in vitro. Folia Neuropathol 2006; 44: 183-190.

97. Merryl JE. Lymphokines, morokines and glial cells. In: Volume Transmission in the Brain: Novel Mechanism for Neural Transmission. Fuxe K, Agnati LF (eds.). Raven Press, New York 1991; pp. 267-277.

98. Miyake T, Hallory T, Fukuda M, Kitamura T, Fujita S. Quantitative studies on proliferative changes of reactive astrocytes in mouse cerebral cortex. Brain Res 1988; 451: 133-138.

99. Miyake T, Okada M, Kitamura T. Reactive proliferation of astrocytes studied by immunohistochemistry for proliferating cell nuclear antigen. Brain Res 1992; 590: 300-302.

100. Monteiro RAF, Rocha E, Marini-Abreu MO. Age-related morphometric changes occurring in the somata of astrocytes of the granular layer of rat neocerebellar cortex (Crus I and Crus II). Histol Histopathol 1992; 7: 427-444.

101. Mori K, Miyazaki M, Iwase H, Maeda M. Temporal profile of change in brain tissue extracellular space and extracellular ion (Na (+), K (+)) concentrations after cerebral ischemia and the effects in mild cerebral hypothermia. J Neurotrauma 2002; 19: 1261-1270.

102. Moumdjian RA, Antel JP, Yong VW. Origin of contralateral reactive gliosis in surgically injured rat cerebral cortex. Brain Res 1991; 547: 223-228.

103. Murray M, Wang SD, Goldberger ME, Levitt P. Modification of astrocytes in the spinal cord following dorsal root or peripheral nerve lesions. Exp Neurol 1990; 110: 248-257.

104. Nagy JI, Ochalski PA, Li J, Hertzberg EL. Evidence for the co-localization of another connexin with connexin-43 at astrocytic gapjunctions in rat brain. Neuroscience 1997; 78: 533-548.

105. Nakagawara J, Kamiyama K, Takahashi M, Nakamura H. Cortical neuron loss in post-traumatic higher brain dysfunction using (123)I-iomazenil SPECT. Acta Neurochir (Suppl) 2013; 118: 245-250.

106. Nicchia GP, Frigeri A, Liuzzi GM, Svelto M. Inhibition of aquaporin-4 expression in astrocytes by RNAi determines alteration in cell morphology, growth, and water transport and induces changes in ischemia-related genes. FASEB J 2003; 17: 1508-1510.

107. Nicchia GP, Nico B, Camassa LM, Mola MG, Loh N, Dermietzel R, Spray DC, Svelto M, Frigeri A. The role of aquaporin-4 in the blood-brain barrier development and integrity: studies in animal and cell culture models. Neuroscience 2004; 129: 935-945.

108. Nillson P, Hillered L, Olson L, Sheardown MJ, Hansen AJ. Regional changes in interstitial K+ and Ca2+ levels following cortical compression trauma in rats. Cerebr Blood Flow Metab 1963; 13: 183-192.

109. Oblinger MM, Singh LD. Reactive astrocytes in neonate brain upregulate intermediate filament gene expression in response to axonal injury. Int J Dev Neurosci 1993; 11: 149-156.

110. Obrenovitch TP, Urenjak J. Is high extracellular glutamate the key to excitotoxicity in traumatic brain injury? J Neurotrauma 1997; 14: 677-698.

111. Oswald MJ, Palmer DN, Kay GW, Shemilt SJ, Rezaie P, Cooper JD. Glial activation spreads from specific cerebral foci and pre-

http://rcin.org.pl

cedes neurodegeneration in presymptomatic ovine neuronal ceroid lipofuscinosis (CLN6). Neurobiol Dis 2005; 20: 49-63.

112. Palmer DN, Oswald MJ, Westlake VJ, Kay GW. The origin of fluorescence in the neuronal ceroid lipofuscinoses (Batten disease) and neuron cultures from affected sheep for studies of neurodegeneration. Arch Gerontol Geriatr 2002; 34: 343-357.

113. Papadopoulos MC, Manley GT, Krishna S, Verkman AS. Aquaporin-4 facilitates reabsorption of excess fluid in vasogenic brain edema. FASEB J 2004; 18: 1291-1293.

114. Persson LI, Rosengren LE, Hansson HA. Ultrastructural studies on blood-brain barrier dysfunction around cerebral stab wounds, aggravated by acute ethanol intoxication. Acta Neurol Scandinav 1978; 57: 405-417.

115. Plesnila N, Ringel F, Chang RC, Staub F, Baethmann A. Relevance of calcium homeostasis in glial cell swelling from acidosis. Acta Neurochir (Suppl) 1998; 71: 203-205.

116. Porter JT, Mc Carthy KD. Astrocyte neurotransmitter receptors in in situ and in vivo. Progr Neurobiol 1997; 51: 439-455.

117. Povlishock JT, Becker DP, Sullivan HG, Miller JD. Vascular permeability alterations to horseradish peroxidase in experimental brain injury. Brain Res 1978; 153: 223-239.

118. Povlishock JT. The morphopathological responses in head injuries of varying severity. Central Nervous System Trauma: Status Report. In: Becker DP, Povlishock JT (eds.). NINCDS, Washington 1985; pp. 443-455.

119. Raivich G, Bohatschek M, Kloss CU, Werner A, Jones LL, Kreutzberg GW. Neuroglial activation repertoire in the injured brain: graded response, molecular mechanisms and cues to physiological function. Brain Res Rev 2002; 30: 77-105.

120. Ragaisis V. Brain contusion: morphology pathogenesis and treatment. Medicina (Kaunas) 2002; 38: 243-249.

121. Ranson B. Gap junctions. Neuroglia. In: Kettenmann H, Ranson BR (eds.). Oxford University Press, New York 1995; pp. 299-318.

122. Rash JE, Duffy HS, Dudek FE, Bilhartz BL, Whalen LR, Yasumura T. Grid-mapped freeze-fracture analysis of gap junctions in gray and white matter of adult rat central nervous system, with evidence for a "panglial syncytium" that is not coupled to neurons. J Comp Neurol 1997; 388: 265-292.

123. Reier PJ. Gliosis following CNS injury: The anatomy of astrocyte scars and their influences on axonal elongation. Astrocytes. Vol. 3. In: Fedoroff S, Vernakadi A (eds.). Academic Press, New York 1986; pp. 263-324.

124. Rio Hortega PD, Penfield W. Cerebral cicatrix: the reaction of neuroglia and microglia to brain wounds. Johns Hopkins Hosp Bull 1927; 41: 278-303.

125. Roesmann V, Gambetti P. Pathological reaction of astrocytes in perinatal brain injury: immunohistochemical study. Acta Neuropathol (Berl) 1986; 70: 302-307.

126. Salahuddin TC, Johansson BB, Kalimo H, Olsson Y. Structural changes in the rat brain after carotid infusions of hyperosmolar solutions. An electron microscopic study. Acta Neuropathol 1988; 77: 5-13.

127. Sasaki S, Ferzt R, Cervós Navarro J. Transendothelial vesicular transport of protein in brain edema induced by ultraviolet irradiation. Acta Neuropathol 1977; 40: 207-212.

128. Schousboe A. Transport and metabolism of glutamate and GABA in neurons and glial cells. Int Rev Neurobiol 1981; 22: 1-45.

129. Sims TJ, Gilmore SA. Glial response to dorsal root lesion in the irradiated spinal cord. Glia 1992; 6: 96-107.

130. Sobue K, Asai K, Katsuya H. Aquaporin water channels in the brain and molecular mechanism of brain edema. Nippon Rinsho 2006; 64: 1181-1189.

131. Suzuki R, Okuda M, Asai J, Nagashima G, Itokawa H, Matsunaga A, Fujimoto T, Suzuki T. Astrocytes co-express aquaporin-1, -4, and vascular endothelial growth factor in brain edema tissue associated with brain contusion. Acta Neurochirurg (Suppl) 2006; 96: 398-401.

132. Swanson RA, Ing W, Kauppinen TM. Astrocyte influences on ischemic neuronal death. Curr Mol Med 2004; 4: 193-205.

133. Theriault E, Frankenstein UN, Hertzberg EL, Nagy JI. Connexin43 and astrocytic gap junctions in the rat spinal cord after acute compression injury. J Comp Neurol 1997; 382: 199-214.

134. Thiel HJ, Hammersen F, Sauer R. Histochemical and ultrastructural studies on the anti-edema and radiation-protective effects of 0-(beta-hydroxyethyl)-rutosides in the rat brain after single-dose irradiation. 1. Electron microscopy study of terminal blood circulation. Strahlenther Onkol 1988; 164: 544-552.

135. Tomas-Camardiel M, Venero JL, Herrera AJ, De Deblos RM, Pintor-Toro JA, Machado A, Cano J. Blood-brain barrier disruption highly induces aquaporin-4 mRNA and protein in perivascular and parenchymal astrocytes: protective effect by estradiol treatment in ovariectomized animals. J Neurosci Res 2005; 80: 235-246.

136. Tóth Z, Séress L, Tóth P, Ribak CE, Gallyas F. A common morphological response of astrocytes to various injuries: "dark" astrocytes. A light and electron microscopic analysis. J Hirnforsch 1997; 38: 173-186.

137. Uranova NA. Brain synaptic plasticity in schizophrenia. Vestn Ross Akad Med Nauk 1996; 4: 23-29.

138. Vajtr D, Benada O, Kukacka J, Průsa R, Houstava L, Toupalík P, Kizek R. Correlation of ultrastructural changes of endothelial cells and astrocytes occurring during blood brain barrier damage after traumatic brain injury with biochemical markers of BBB leakage and inflammatory response. Physiol Res 2009; 58: 263-268.

139. Vise WN, Liss L, Yashow D, Hunt WE. Astrocytic process: A route between vessels and neurons following brain barrier injury. J Neuropathol Exp Neurol 1975; 34: 324-334.

140. Yarnell AM, Shaughness MC, Barry ES, Ahlers ST, McCarron RM, Grunberg NE. Blast traumatic brain injury in the rat using a blast overpressure model. Curr Protoc Neurosci 2013; 9: 9-41.

141. Zhao J, Moore AN, Clifton GL, Dash PK. Sulforaphane enhances aquaporin-4 expression and decreases cerebral edema following traumatic brain injury. J Neurons Res 2005; 82: 499-506.

http://rcin.org.pl

Folia
Neuropathologica

Quantitative pathological changes in the cerebellum of multiple system atrophy

Richard A. Armstrong

Vision Sciences, Aston University, Birmingham, UK

Abstract

Multiple system atrophy (MSA) is a rare neurodegenerative disorder associated with parkinsonism, ataxia, and auto-nomic dysfunction. Its pathology is primarily subcortical comprising vacuolation, neuronal loss, gliosis, and α-synuclein-immunoreactive glial cytoplasmic inclusions (GCI). To quantify cerebellar pathology in MSA, the density and spatial pattern of the pathological changes were studied in α-synuclein-immunolabelled sections of the cerebellar hemisphere in 10 MSA and 10 control cases. In MSA, densities of Purkinje cells (PC) were decreased and vacuoles in the granule cell layer (GL) increased compared with controls. In six MSA cases, GCI were present in cerebellar white matter. In the molec-ular layer (ML) and GL of MSA, vacuoles were clustered, the clusters exhibiting a regular distribution parallel to the edge of the folia. Purkinje cells were randomly or regularly distributed with large gaps between surviving cells. Densities of glial cells and surviving neurons in the ML and surviving cells and vacuoles in the GL were negatively correlated consis-tent with gliosis and vacuolation in response to neuronal loss. Principal components analysis (PCA) suggested vacuole densities in the ML and vacuole density and cell losses in the GL were the main source of neuropathological variation among cases. The data suggest that: (1) cell losses and vacuolation of the GCL and loss of PC were the most significant pathological changes in the cases studied, (2) pathological changes were topographically distributed, and (3) cerebellar pathology could influence cerebral function in MSA via the cerebello-dentato-thalamic tract.

Key words: *multiple system atrophy, cerebellum, vacuolation, α-synuclein, spatial pattern.*

Introduction

Multiple system atrophy (MSA) is a rare, largely sporadic neurodegenerative disorder, associated with varying degrees of parkinsonism, ataxia, and auto-nomic dysfunction [25]. The average annual incidence of the disorder is 3.0/100,000 of the population and median survival time is 8.5 years [12]. Symptoms of MSA begin early in the fifth decade and the dis-order is slightly more common in males than in fe-males (male : female 1.3 : 1) [37]. Two main subtypes

of the disease are recognised: the cerebellar subtype (MSA-C) and the parkinsonian subtype (MSA-C) [19-21]. A third subtype, viz. Shy-Drager syndrome, in which the symptoms are primarily autonomic, is not currently included as a subtype of MSA [21].

The neuropathology of MSA largely affects sub-cortical grey matter including the substantia nigra, striatum, inferior olivary nucleus, pontine nuclei, and cerebellum [8,9,17,25]. In some cases, there is a pro-gressive cerebral atrophy affecting the frontal lobes [22] and the motor/premotor areas [36]. Histological-

Communicating author:

Dr Richard A. Armstrong, Vision Sciences, Aston University, Birmingham B4 7ET, UK, phone: 0121-204-4102, fax: 0121-204-4048, e-mail: R.A.Armstrong@aston.ac.uk

ly, MSA is characterised by selective neuronal loss, gliosis, and myelin pathology [25], the 'signature' pathological lesion being the glial cytoplasmic inclusion (GCI) found mainly in oligodendrocytes [28]. The GCI are composed of argyrophilic 10-15 nm diameter coated filaments immunoreactive for ubiquitin and α-synuclein, but glial fibrillar acid protein (GFAP) reactivity is absent [34]. α-Synuclein-immunoreactive neuronal cytoplasmic inclusions (NCI) have also been observed in MSA but at significantly lower densities [8,16,17,29]. α-Synuclein is a small pre-synaptic protein that regulates the normal functioning of dopamine transporter and tyrosine hydroxylase [24]. It normally exists in a relatively unfolded state and is highly soluble, but in synucleinopathies such as MSA it, undergoes a conformational change to insoluble amyloid fibrils that form a major component of the GCI.

Cerebellar pathology has been reported in previous studies of MSA [18,20,27] including loss of Purkinje cells (PC) [26] and the presence of α-synuclein-immunoreactive cellular inclusions in the molecular layer (ML) [31,33]. Cerebellar pathology could influence a variety of brain functions in MSA including motor function, the fine timing of events, sensory analysis, feeding behaviour, the modulation of cognition, and the regulation of emotion [22]. Hence, to quantify cerebellar pathology in MSA and identify the anatomical pathways likely to be affected, the density and spatial pattern of vacuoles, surviving neurons, glial cell nuclei, and glial cytoplasmic inclusions (GCI) were studied in α-synuclein-immu-

nolabelled sections of the cerebellar hemisphere in 10 MSA and 10 control cases. The specific objectives were: (1) to quantify and compare pathological changes in the cerebellar hemisphere in MSA and cognitively normal brain, (2) to determine the spatial topography of the pathological changes within each layer, (3) to examine the spatial correlations between the vacuoles, glial cell nuclei, and GCI both within and between layers, (4) to investigate pathological differences among cases, and (5) to consider how cerebellar pathology might affect cerebral function in MSA.

Material and methods
Cases

Ten cases of MSA (details in Table I) and 10 control cases (50-80 years of age) were obtained from the Brain Bank, Department of Neuropathology, Institute of Psychiatry, King's College London, UK. Control cases had no neurological or psychiatric histories and were matched as closely as possible for gender and age to the MSA cases. Multiple system atrophy cases were diagnosed according to the Minneapolis Consensus Criteria [19-21] and subsequently neuropathologically verified. All cases had GCI in subcortical grey matter, including the striatum, substantia nigra, pontine nuclei, and medulla [8]. The major clinical features of the 10 cases are shown in Table II. Four cases were diagnosed as the MSA-C subtype and two as the MSA-P subtype. Four cases had a more complex pathology, exhibiting both

Table I. Subtypes, demographic data, and brain weights (BW) of the multiple system atrophy (MSA) cases studied

Case	Subtype	Sex	Onset (years)	Death (years)	Duration (years)	BW (gm)
A	MSA-P	F	73	77	4	1274
B	M	Ma	69	76	7	1290
C	MSA-C	Ma	63	65	2	1276
D	MSA-C	Ma	65	67	2	1309
E	MSA-C	F	70	81	11	817
F	MSA-P	Ma	66	78	12	1400
G	MSA-C	Ma	69	72	3	1035
H	M	F	61	63	2	1283
I	M	Ma	63	73	10	NA
J	M	Ma	NA	53	NA	NA

MSA-P – Parkinsonian subtype, MSA-C – cerebellar subtype, M – mixed pathology, i.e. cases with features of more than one subtype, Ma – male, F – female, NA – data not available

Table II. Clinical features of the multiple system atrophy cases studied

Case	Clinical features
A	Rigidity and akinesia. No cerebellar ataxia. Nocturnal sweating, salivation, and frequent urination. Cognition preserved. Perseveration of speech
B	Minimal parkinsonism. Balance problems. Impotence, urination and swallowing difficulties, impaired blinking. Cognition preserved. Depression
C	Minimal parkinsonism. Restricted mobility and falls. Cerebellar ataxia. Urination difficulty. Cognition preserved. Dysarthria
D	Some tremor of hands. Significant cerebellar ataxia. Dysarthria
E	Minimal parkinsonism. Significant cerebellar ataxia affecting limbs and trunk. Memory impairment
F	Significant parkinsonism with tremor and cogwheel rigidity. Urination and swallowing difficulties. Cognition preserved
G	Minimal parkinsonism. Significant cerebellar ataxia. Confusion
H	Significant parkinsonism and cerebellar ataxia. Cognition preserved
I	Some rigidity. Significant cerebellar ataxia. Swallowing difficulties. Cognition preserved. Dysarthria
J	Significant parkinsonism and cerebellar ataxia. Dysphagia. Cognition preserved.

parkinsonism and cerebellar clinical signs, and could not easily be assigned to either the MSA-C or MSA-P subtypes. Hence, the two MSA-P cases exhibited significant parkinsonism but no cerebellar ataxia, the four MSA-C cases showed significant cerebellar ataxia but with minimum parkinsonism, while the four 'mixed' cases exhibited a combination of cerebellar and parkinsonian symptoms. Only cases of the MSA-C subtype exhibited evidence of cognitive impairment including memory impairment and confusion.

Histological methods

After death, consent of the next of kin was obtained for brain removal following local Ethical Committee procedure and the 1964 Declaration of Helsinki (as revised in Edinburgh, 2000). A block of the right cerebellar cortex was taken from each case at the level of the superior cerebellar peduncle. Tissue was fixed in 10% phosphate-buffered formal-saline and embedded in paraffin wax. For quantitative analysis, sequential coronal 7-µm sections were stained with haematoxylin and eosin (H/E) or immunohistochemistry (IHC) was performed using a non-phosphorylated polyclonal rabbit antibody (a116), after formic acid pretreatment, and at a dilution 1/3000, against the 116-131 amino acid sequence of α-synuclein (kindly supplied by Dr D. Hanger). This type of antibody is regarded as one of the most efficient available, especially for revealing the GCI, and is particularly recommended for diagnostic use [15].

The secondary antibody was biotinylated anti-rabbit antibody (DAKO diagnostics, Germany), used at a concentration of 1/200, which binds to the avidin-peroxidase complex. Chromogen 3,3-diaminobenzidine tetrahydrochloride was used to reveal the GCI. Immunolabelled sections were also stained with haematoxylin.

Morphometric methods

Variations in density of histological features were measured parallel to the edge of randomly selected
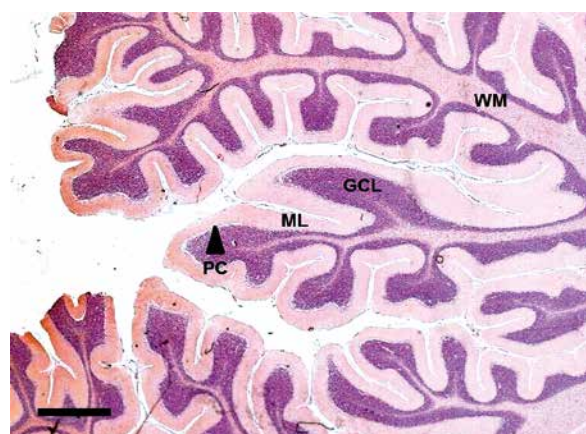
Fig. 1. Section of cerebellar hemisphere in a case of multiple system atrophy (MSA) (α-synuclein immunohistochemistry, haematoxylin; Magnification bar = 1 mm). GCL – granule cell layer, ML – molecular layer, PC – Purkinje cell layer, WM – white matter.

http://rcin.org.pl
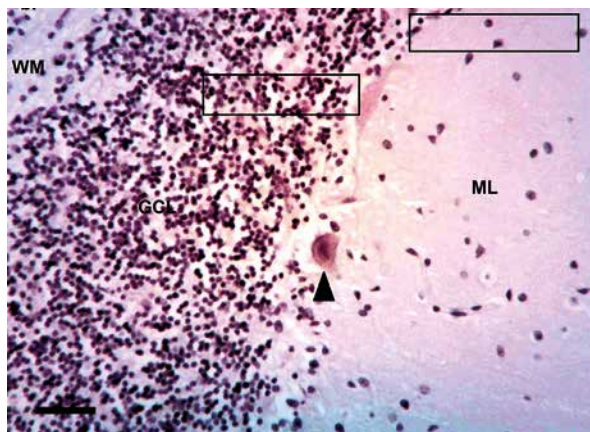
Fig. 2. Quantitative method of sampling the cerebellum hemisphere in multiple system atrophy (MSA) showing the 50 × 250 mm plots. (α-synuclein immunohistochemistry, haematoxylin; Magnification bar = 50 mm). Arrow indicates surviving Purkinje cell. GCL – granule cell layer, ML – molecular layer, PC – Purkinje cell layer.

folia within each case (Fig. 1). Within each folium, a strip of cerebellar cortex 3200 to 4800 μm in length, starting at a randomly determined location, was studied with 64-96, 50 × 250 μm sample fields arranged contiguously (Fig. 2) [3]. First, the sample field was positioned with the shorter dimension aligned along the upper edge of the GL at the base of the PC layer to quantify the density of PC and the pathology of the inner region of the ML. In each sam-

ple field, the number of PC, distinct vacuoles greater than 5 μm in diameter, neurons, glial cell nuclei, and α-synuclein-immunoreactive inclusions were counted. Second, at the same position, the field was moved to sample the outer region of the GL, the short edge of the field aligned with the edge of the granule cells (Fig. 2). It was not possible in these preparations to differentiate between different cell types in the GL, e.g. granule cells, Golgi type II cells, glia, and a single count of cell density was made. Third, at the same location, the number of vacuoles, glial cell nuclei, and GCI (Fig. 3 and 4) were counted in sample fields arranged along the white matter, the upper short edge of the sample field being aligned with the lower edge of the GL (Fig. 2).

Data analysis

Data analysis was carried out using STATISTICA software (Statsoft Inc., 2300 East 14th St, Tulsa, Ok, 74104, USA). First, densities of histological features in the ML, GL, and white matter were compared in MSA and control subjects using a 't' test. Second, the spatial pattern of a histological feature, i.e. whether the feature was distributed randomly, regularly, or in clusters, was determined using the variance/mean (V/M) method described previously [1,2,5,6]. Third, spatial correlations between histological features along the folia were tested in each case using Pearson's correlation coefficient ('r') [4]. Fourth, to study pathological variation among cases, the data were

Fig. 3. Vacuolation in a case of multiple system atrophy (MSA) (α-synuclein immunohistochemistry, haematoxylin; magnification bar = 20 mm). GCL – granule cell layer, ML – molecular layer, PC – Purkinje cell layer.
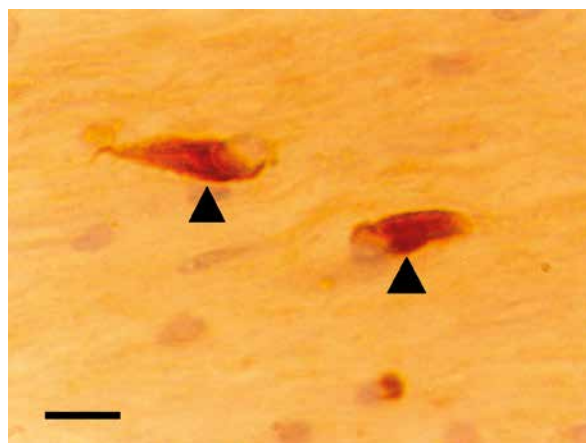
**Fig. 4.** High-power view of glial cytoplasmic inclusions (GCI) (arrows) in the white matter of the cerebellum of a case of multiple system atrophy (MSA) (α-synuclein immunohistochemistry, haematoxylin; magnification bar = 6 mm).

analysed using principal components analysis (PCA) [11]. The result of a PCA is a plot of the ten MSA cases in relation to the extracted PC in which distance between cases reflects their pathological similarity or dissimilarity. To correlate the location of a case on a PC axis with the numerical density of a specific histological feature, correlations (Pearson's 'r') were calculated between the densities of each histological feature and the factor loadings of cases on PC1 and PC2. Clinical features were also plotted onto the PCA to determine if cases were segregated according to clinical symptoms in relation to PC1 and PC2.

Results

Pathological features observed in MSA included: (1) modest vacuolation of the ML in some cases and more extensive vacuolation of the GL, (2) loss of PC, and (3) GCI in white matter (Fig. 1-4). No α-synuclein-immunoreactive GCI or NCI were observed in the ML or GL. Mean density of vacuoles in the GL was significantly increased ($t = 2.57$, $p < 0.05$) and PC was decreased ($t = 7.65$, $p < 0.001$), in MSA compared with controls (Fig. 5). In addition, the mean density of vacuoles was significantly greater in the GCL compared with the ML ($t = 3.52$, $p < 0.01$) but was similar to vacuole density in adjacent white matter ($t = 2.01$, $p > 0.05$).

Examples of the spatial patterns of histological features along the folia are shown in Fig. 6. The V/M of the PC was not significantly different to unity at any field size, suggesting a random distribution. The V/M of the vacuolation in the ML, however, revealed significant peaks at field sizes 100 mm and 400 mm, suggesting clustering at two scales in the tissue, i.e. vacuoles were clustered, the mean dimension of the clusters being equal to 100 mm, and they were regularly distributed along the folium, the smaller clusters being aggregated into larger clusters, 400 mm in diameter.

The spatial patterns of all histological features in each case are shown in Table III. Vacuoles were clustered in the ML in the majority of cases, regular spaced clustering of vacuoles along the folia being present in 4/10 (40%) cases. Similarly, neurons in the ML were clustered, a regular distribution of clusters being present in 6/10 (60%) cases. By contrast, glial cell nuclei in the ML were randomly or regularly distributed. In the majority of cases, PCs were randomly or regularly distributed and there were large gaps between surviving cells. In the GL, the vacuoles

and cell nuclei were clustered, a regular distribution of clusters being present. In the white matter, large clusters of vacuoles were present and the GCI and glial cell nuclei exhibited a regular distribution of clusters along the folia. The frequency of the different types of spatial pattern was similar in the different layers ($\chi^2 = 5.28$, 6DF, $p > 0.05$).
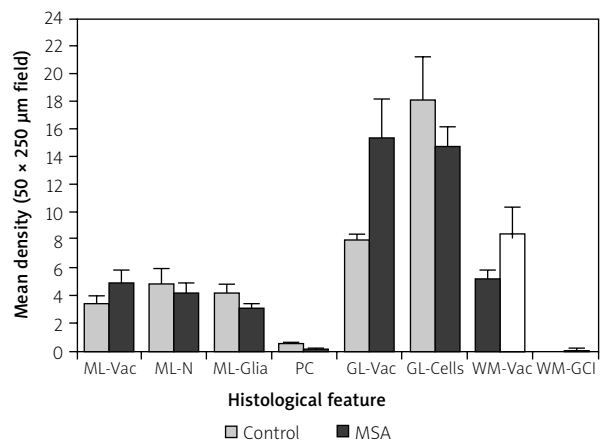
Fig. 5. Mean densities (50 × 250 mm field, standard error of mean in parentheses) of histological features (Vac – vacuolation, PC – Purkinje cells, GCI – glial cytoplasmic inclusions) in various layers of the cerebellar cortex (ML – molecular layer, PC – Purkinje cell layer, GL – granule cell layer, WM – white matter) in ten cases of multiple system atrophy (MSA) and ten control cases.
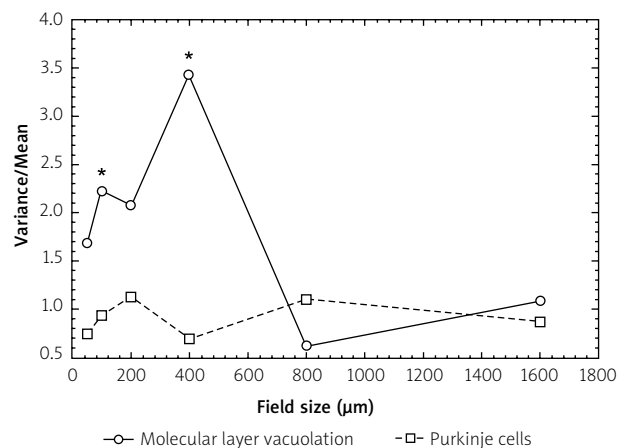
Fig. 6. Examples of the topographical patterns of the vacuolation and glial cell nuclei in the cerebellum in a case of multiple system atrophy (MSA) (Case A). *Significant variance/mean peaks.

http://rcin.org.pl

Table III. Spatial patterns of histological features in various layers of the cerebellar cortex in 10 cases of multiple system atrophy

Case	Molecular layer (ML)			Granule cell layer (GL)			White matter (WM)		
	Vac	SN	G	PC	Vac	SC	Vac	GCI	G
A	100, 400	R	Reg	R	200	200	R	–	Reg
B	50, 400	R	Reg	R	> 800	R	400	–	200
C	R	200	R	Reg	> 800	400	> 800	Reg	400
D	> 800	> 400	> 400	Reg	> 400	> 800	> 400	100	> 40
E	200	50, 400	R	Reg	100	R	> 800	–	R
F	> 800	400	> 800	Reg	400	Reg	200	–	40
G	> 400	> 400	R	–	> 400	> 400	> 400	R	> 400
H	100, 400	400	400	R	> 800	100	R	–	R
I	R	50, 200	200	R	Reg	200	400	–	400
J	R	50	> 800	R	Reg	> 800	> 800	100	50, 400

Comparison of spatial patterns (χ² contingency table): ML vs. GL vs. WM, c² = 5.28 (6DF, p > 0.05)
Vac – vacuolation, SN – surviving neurons, G – glial cell nuclei, PC – Purkinje cells, SC – surviving cells, GCI – glial cytoplasmic inclusions

Table IV. Frequency of correlations (Pearson's 'r') between histological features within and between layers of the cerebellum in multiple system atrophy. Figures indicate the number of cases in which a positive (+) or negative (–) correlation was recorded

	X variable								
Y	MLV	MLN	MLG	PC	GLV	GLC	WMV	WMGCI	WMG
MLV	–	2(+)	–	3(–)	1(–)	–	–	–	1(+)
MLN		–	5(–)	1(+)	1(+)	–	1(+)	1(+)	1(+)
MLG			–	1(–)	–	–	1(+)	–	–
PC				–	1(+)	–	–	–	1(+)
GLV					–	5(–)	–	1(+)	2(+)
GLC						–	1(+)2(–)	–	–
WMV							–	–	1(+)2(–)
WMGCI								–	1(+)
WMG									–

MLV – molecular layer vacuoles, MLN – molecular layer neurons, MLG – molecular layer glia, PC – Purkinje cells, GLV – granular layer vacuoles, GLC – granular layer cells, WMV – white matter vacuoles, WMGCI – white matter glial cytoplasmic inclusions, WMG – white matter glia

Spatial correlations among histological features within and between layers are summarised in Table IV. The most notable correlations were: (1) in the ML of 5 cases, a negative spatial correlation between glial cell nuclei and neurons, (2) in the GL of 5 cases, a negative spatial correlation between cells and vacuolation, and (3) in the PC layer of 3 cases, a negative spatial correlation between PC and vacuoles. Histological features in different layers of the cerebellar cortex were not spatially correlated.

http://rcin.org.pl

A PCA of the data resulted in the extraction of two PC accounting in total for 87% of the total variance (PC1 = 72%, PC2 = 15%). A plot of the 10 cases in relation to PC1 and PC2 is shown in Fig. 7. MSA-C cases were located at the upper right of the plot and the MSA-P and cases of mixed pathology to the left of the plot. In addition: (1) PC1 was negatively correlated with the density of vacuoles in the ML ($r = -0.66$, $p < 0.05$) and (2) PC2 was negatively correlated with the density of cells in the GL ($r = -0.81$, $p < 0.05$) and positively correlated with the density of vacuoles in the GL ($r = 0.82$, $p < 0.001$). In addition, cases to the right of the plot exhibited significant cerebellar ataxia but with minimum parkinsonism while those to the left of the plot exhibited a greater degree of parkinsonism, i.e. rigidity, akinesia, tremor, and less cerebellar ataxia.

Discussion

In the 10 MSA cases studied, a significant loss of PC and vacuolation of the GL were the most consistent pathological changes compared with controls [26,30,37]. Some vacuolation was also evident in the ML and white matter but at significantly lower levels than the GCL, and it did not differ quantitatively from controls. No α-synuclein-immunoreactive inclusions were observed in control cases or in the grey matter of any MSA case, but such structures have been reported previously in the ML located into GFAP-immunoreactive radial processes of Bergmann glia [30,32]. α-Synuclein-immunoreactive GCI were present in white matter, but not in all cases. GCI have been observed in other subcortical white matter tracts in MSA, including the external and internal capsules and central tegmental tract [9].

The vacuoles and surviving neurons were frequently clustered, and in some cases the clusters were regularly distributed relative to the edge of the folia, a pattern evident in both ML and GL. In addition, significant gaps were observed between PC perikarya, surviving PC often being regularly distributed, which suggests loss of clusters of PC. These results are consistent with a topographic pattern of the cerebellar pathology in MSA, which has also been observed in the cerebellum in the sporadic [7] and variant subtypes of Creutzfeldt-Jakob disease (CJD) [10]. A topographic loss of PC may also occur in Niemann-Pick type C disease, in which there is a complex pattern of cell loss in the cerebellum, with surviving PC being aligned in strips [32]. Further loss
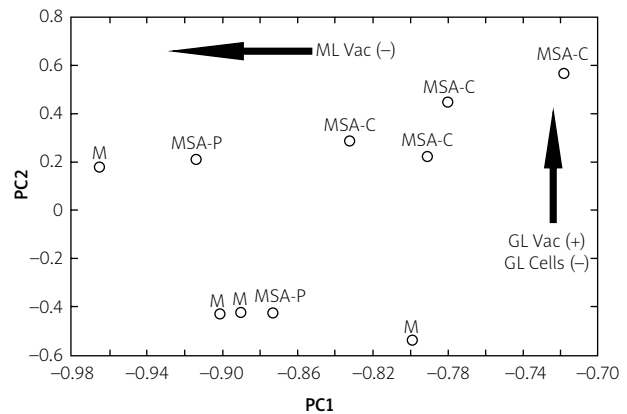
Fig. 7. Principal components analysis (PCA) of ten cases of multiple system atrophy (MSA) based on the densities of all histological features in the cerebellum. A plot of the cases in relation to PC1 and PC2 (MSA-C – cerebellar subtype, MSA-P – Parkinsonian subtype, M – mixed pathology). Arrows PC1 was negatively correlated with the density of vacuoles in the molecular layer (ML Vac) and PC2 negatively correlated with the density of cells in the granule cell layer (GL Cells –) and positively correlated with the density of vacuoles in the GL (GL Vac +).

of PC then occurs as the disease develops, resulting in large gaps between surviving cells similar to those observed in MSA.

There was a negative correlation between cells and vacuoles in the GL suggesting that vacuolation replaces lost neurons. Furthermore, there was a negative correlation between the densities of neuronal perikarya in the ML and glial cell nuclei consistent with gliosis. A negative spatial correlation was also observed between individual PCs and clusters of vacuoles in the ML of three MSA-C cases, which could represent a more specific cerebellar pathology in MSA. These vacuoles may have developed in relation to the dendritic trees of the PC, which branch in a plane perpendicular to that of the section, the climbing fibres that ramify over individual PC, or the parallel fibres that ramify in the plane of the section and which are in contact with many adjacent PCs [10].

Although the number of cases of MSA is small, the PCA suggested some variations in quantitative pathology among cases. First, PC1 was negatively correlated with the density of vacuoles in the ML. Although there was no significantly increased vacuole density overall in the MSA cases, the vacuolation in the ML did vary among cases with more significant

http://rcin.org.pl

vacuolation in cases that exhibited more significant parkinsonism compared with those with cerebellar ataxia. Second, PC2 was negatively correlated with cell density and positively correlated with vacuole density in the GL. This result suggests that increased vacuolation and cell loss in the GL may be a more significant feature of the MSA-C subtype.

The cerebellum receives input from several sources (Fig. 8): (1) the spinal cord (posterior spino-cerebellar tract), reticular formation nuclei (reticulo-cerebellar tract), and pontine nuclei (ponto-cerebellar tract), which relay signals to the cerebellum, via the inferior and superior cerebellar peduncles, to the large diameter, rapidly conducting mossy fibres, the synaptic endings terminating in complex glomeruli; (2) climbing fibres that originate in the inferior olive (olivo-cerebellar tract) and which synapse directly on to the PC; and (3) fibres from the white matter which enter the GL and course parallel to the pia mater before synapsing with the PC [14]. α-Synuclein-immunoreactive GCIs have been observed in white and grey matter regions, which provide these inputs to the cerebellum in MSA, e.g. the ponto-cerebellar and reticulo-cerebellar tracts [13], and in the present study they were also observed in cerebellar white matter. This pathology has also been observed in motor tracts providing both the input and output pathways of the cerebellum, e.g., the cortico-pontine, cortical bulbar, cortico-spinal, and spino-reticular tracts. In addition, significant densities of inclusions have been observed in pre-cerebellar nuclei such as the inferior olivary nucleus [8], lateral reticular nucleus, interfascicular nucleus, and the nucleus of Roller in MSA [13].

Hence, α-synuclein pathology spreading via cerebellar connections [35] could result in: (1) cell loss-
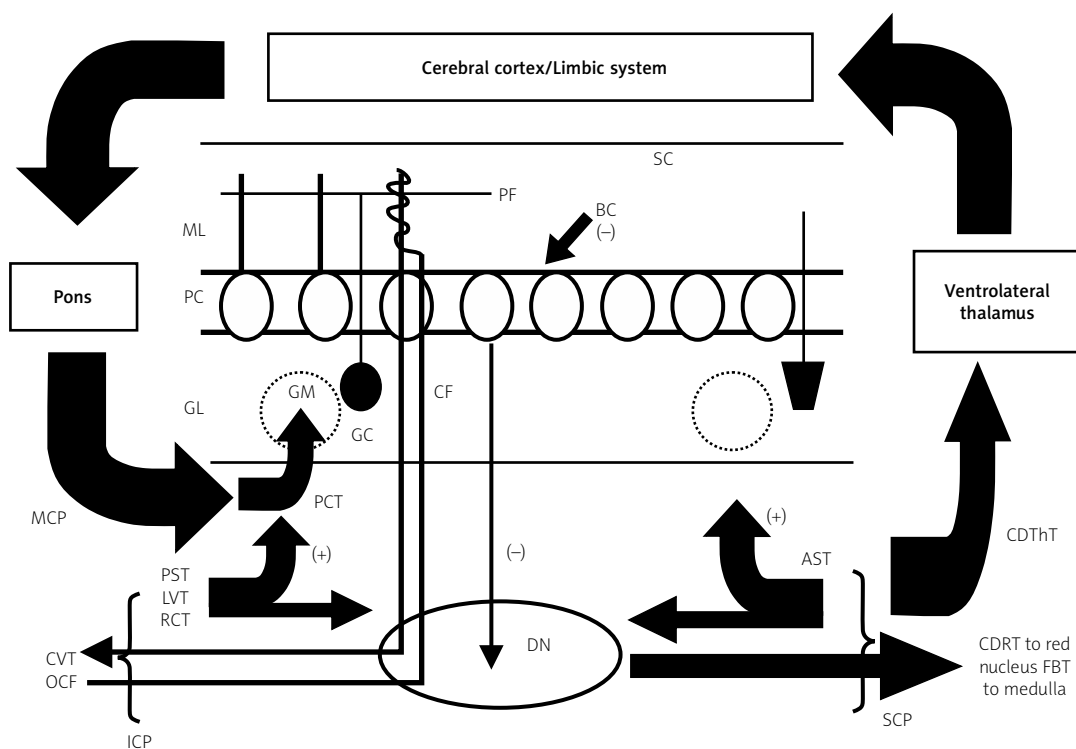
Fig. 8. Input and output pathways of the cerebellar cortex (ICP – inferior cerebellar peduncle, MCP – middle cerebellar peduncle, SCP – superior cerebellar peduncle, PF – parallel fibres, CF – climbing fibres, GM – glomerulus, BC – basket cell, GC – granule cell, SC – stellate cell, ML – molecular layer, PC – Purkinje cell layer, GL – granule cell layer, DN – dentate nucleus, ASCT – anterior spino-cerebellar tract, CDthT – cerebello-dentato-thalamic tract, CDRT – cerebello-dentato-rubral tract, FBT – fastigio-bulbar tract, PCT – ponto-cerebellar tract, PST – posterior spino-cerebellar tract, LVT – lateral vestibular tract, RCT – reticulo-cerebellar tract, CVT – cerebello-vestibular tract, OCF – olivo-cerebellar tract (+ excitatory influence, – inhibitory influence).

es and vacuolation in the GL, (2) loss of parallel and climbing fibres, (3) a reduction in the degree of facilitation of surviving PC, (4) a reduction in the degree of inhibitory control by PC of the dentate nucleus (DN), and (5) a reduction of fine tuning of the cerebral output via the cerebello-dentato-thalamic tract, which leaves the cerebellum as the superior cerebellar peduncle and connects the cerebellum to various regions such as the red nucleus (cerebello-dentato-rubral tract), medulla (fastigio-bulbar tract), and the cerebral cortex/limbic system, the latter- via the ventro-lateral thalamus. This pathology could potentially influence a variety of clinical symptoms reported in MSA, including dysfunction of motor activity, the fine timing of events, sensory analysis, feeding behaviour, the modulation of cognition, and in the regulation of emotions [22].

Conclusions

Cerebellar pathology in MSA may affect all layers of the cerebellar hemisphere, but cell losses and vacuolation in the GL and loss of PC were the most significant pathological changes in the cases studied. There was evidence of a topographic distribution of pathological change, which could reflect the spread of α-synuclein pathology via anatomical connections. Cerebellar pathology may ultimately influence a variety of clinical symptoms in MSA, especially in the MSA-C subtype. Nevertheless, only 10 cases of this rare disorder were studied quantitatively, and these observations should be repeated on a larger series of well-characterised MSA cases.

Acknowledgements

Disclosure

Authors report no conflict of interest.

References

1. Armstrong RA. The usefulness of spatial pattern analysis in understanding the pathogenesis of neurodegenerative disorders, with particular reference to plaque formation in Alzheimer's disease. Neurodegeneration 1993; 2: 73-80.
2. Armstrong RA. Analysis of spatial patterns in histological sections of brain tissue. J Neurosci Meth 1997; 73: 141-147.
3. Armstrong RA. Quantifying the pathology of neurodegenerative disorders: quantitative measurements, sampling strategies and data analysis. Histopathology 2003; 42: 521-529.
4. Armstrong RA. Measuring the degree of spatial correlation between histological features in thin sections of brain tissue. Neuropathology 2003; 23: 245-253.
5. Armstrong RA. Methods of studying the planar distribution of objects in histological sections of brain tissue. J Microsc (Oxf) 2006; 221: 153-158.
6. Armstrong RA. Measuring the spatial arrangement patterns of pathological lesions in histological sections of brain tissue. Folia Neuropathol 2007; 44: 229-237.
7. Armstrong RA, Cairns NJ. Spatial patterns of the pathological changes in the cerebellar cortex in sporadic Creutzfeldt-Jakob disease (sCJD). Folia Neuropathol 2003; 41: 183-189.
8. Armstrong RA, Lantos PL, Cairns NJ. A quantitative study of the pathological changes in ten patients with multiple system atrophy (MSA). J Neural Transm 2004; 111: 485-495.
9. Armstrong RA, Cairns NJ, Lantos PL. A quantitative study of the pathological changes in white matter in multiple system atrophy. Neuropathology 2007; 27: 221-227.
10. Armstrong RA, Ironside JW, Lantos PL, Cairns NJ. A quantitative study of the pathological changes in the cerebellum in 15 cases of variant Creutzfeldt-Jakob disease (vCJD). Neuropathol Appl Neurobiol 2009; 35: 36-45.
11. Armstrong RA, Ellis W, Hamilton RL, Mackenzie IRA, Hedreen J, Gearing M, Montine T, Vonsattel J-P, Head E, Lieberman AP, Cairns NJ. Neuropathological heterogeneity in frontotemporal lobar degeneration with TDP-43 proteinopathy: a quantitative study of 94 cases using principal components analysis. J Neural Transm 2010; 117: 227-239.
12. Bower JH, Maraganore DM, McDonnell K, Rocca WA. Incidence of progressive supranuclear palsy and multiple system atrophy in Olmstead County, Minnesota, 1976-1990. Neurology 1997; 49: 1284-1288.
13. Braak H, Rub U, Del Tredici K. Involvement of pre-cerebellar nuclei in multiple system atrophy. Neuropathol Appl Neurobiol 2003; 29: 60-76.
14. Brodal A. Neurological anatomy. 3rd ed. Oxford University Press, New York, Oxford 1981.
15. Croisier E, Mres DE, Deprez K, Goldring K, dexter DT, Pearce RKB, Graeber MB, Roncaroli F. Comparative study of commercially available anti-α-synuclein antibodies. Neuropath Appl Neurobiol 2006; 32: 351-356.
16. Dickson DW, Liu WL, Liu WK, Yen SH. Multiple system atrophy: a sporadic synucleinopathy. Brain Pathol 1995; 9: 721-732.
17. Dickson DW, Liu WK, Hardy J, Farrar M, Mehta N, Uitti R, Mark M, Zimmerman T, Golbe L, Sage J, Sima A, d'Amato C, Albin R, Gilman S, Yen SH. Widespread alterations of alpha-synuclein in multiple system atrophy. Am J Pathol 1999; 155: 1241-1251.
18. Ehot V, Brieger P, Broich K, Marneros A. Psychotic symptoms as initial manifestation of a multiple system atrophy. Fortshritte der Neurol Psych 1999; 67: 104-107.
19. Gilman S, Low PA, Quinn N, Albanese A, Ben-Schlomo Y, Fowler CJ, Kaufmann H, Klockgether T, Lang AE, Lantos PL, Livan I, Mathias CJ, Oliver E, Roberstson D, Schatz I, Wenning GK. Con-

http://rcin.org.pl

sensus statement on the diagnosis of multiple system atrophy. J Auto Nerv Syst 1998; 74: 189-192.

20. Gilman S, Low PA, Quinn N, Albanese A, Ben-Schlomo Y, Fowler CJ, Kaufman H, Klockgether T, Lang AE, Lantos PL, Litvan I, Mathias CJ, Oliver E, Robertson D, Schatz I, Wenning GK. Consensus statement on the diagnosis of multiple system atrophy. J Neurol Sci 1999; 163: 94-98.

21. Gilman S, Wenning GJK, Low PA, Brooks DJ, Mattias CJ, Trojanowski JQ, Wood NW, Colosima C, Durr A, Fowler CJ, Kaufmann H, Klockgether T, Lees A, Poese W, Quinn N, Revesz T, Robertson D, Sandroni T, Seppi K, Vidailhet M. Second consensus statement on the diagnosis of multiple system atrophy. Neurology 2008; 71: 670-676.

22. Ioannides AA, Fenwick PBC. Imaging cerebellum activity in real time with magnetoencephalographic data. In: Creating Coordination in the Cerebellum. Prog in Brain Res 2005; 148: 139-150.

23. Konogaya M, Sakai M, Matsuoka Y. Konogaya Y, Hashzume Y. Multiple system atrophy with remarkable frontal lobe atrophy. Acta Neuropathol 1999; 97: 423-428.

24. Kovacs GG, Milenkovic IJ, Preusser M, Budka H. Nigral burden of alpha-synuclein correlates with striatal dopamine deficit. Move Disord 2008; 23: 1608-1612.

25. Lantos PL. Cellular pathology of multiple system atrophy: a review. J Neurol Neurosurg Psychiatr 1994; 57: 129-133.

26. Mori F, Piao YS, Hayashi S, Fujiwara H, Hasegawa M, Yoshimoto M, Iwatsubo T, Takahashi H, Wakabayashi K. Alpha-synuclein accumulates in Purkinje cells in Lewy body disease but not in multiple system atrophy. J Neuropathol Exp Neurol 2003; 62: 812-819.

27. Oertel WH, Bandmann O. Multiple system atrophy. J Neural Transm (Suppl) 1999; 56: 155-164.

28. Papp MI, Kahn JE, Lantos PL. Glial cytoplasmic inclusions in the CNS of patients with multiple system atrophy (striatonigral degeneration, olivopontocerebellar atrophy and Shy-Drager syndrome). J Neurol Sci 1989; 94: 79-100.

29. Papp MI, Lantos PL. The distribution of oligodendroglial inclusions in multiple system atrophy and its relevance to clinical symptomology. Brain 1994; 117: 235-243.

30. Park SH, Becker-Catania S, Gatti RA, Crandall BF, Emelin JK, Vinters HV. Congenital olivopontocerebellar atrophy: report of two siblings with paleo and neocerebellar atrophy. Acta Neuropathol 1998; 96: 315-321.

31. Piao YS, Mori F, Hayashi S, Tanji K, Yoshimoto M, Kakita A, Wakabayashi K, Takahashi H. Alpha-synuclein pathology affecting Bergmann glia of the cerebellum in patients with alpha-synucleinopathies. Acta Neuropathol 2003; 105: 403-409.

32. Sarna JR, Larouche M, Marzban H, Sillitoe RV, Rancourt DE, Hawkes R. Patterned Purkinje cell degeneration in mouse models of Niemann-Pick type C disease. J Comp Neurol 2003; 456: 279-291.

33. Sebeo J, Hof PR, Perl DP. Occurrence of alpha-synuclein pathology in the cerebellum of Guamanian patients with parkinsonism dementia complex. Acta Neuropathol 2004; 107: 497-503.

34. Spillantini MG, Crowther RA, Jakes R, Cairns NJ, Lantos PL, Goedert M. Filamentous α-synuclein inclusions link multiple system atrophy with Parkinson's disease and dementia with Lewy bodies. Neurosci Lett 1998; 251: 205-208.

35. Steiner JA, Angot E, Brunden P. A deadly spread: cellular mechanisms of α-synuclein transfer. Cell Death and Differ 2011; 18: 1425-1433.

36. Wakabayashi K, Ikeuchi T, Ishikawa A, Takahashi H. Multiple system atrophy with severe involvement of the motor cortical areas and cerebral white matter. J Neurol Sci 1998; 156: 114-117.

37. Wenning GK, Tison F, Ben-Shlomo Y, Daniel SE, Quinn NP. Multiple system atrophy: a review of 203 pathologically proven cases. Move Disord 1997; 12: 133-147.

Folia
Neuropathologica

Ganglion cell tumours in the sella turcica in close morphological connection with pituitary adenomas

Ewa Matyja[1,2], Maria Maksymowicz[3], Wiesława Grajkowska[4,5], Grzegorz Zieliński[6], Jacek Kunicki[2], Wiesław Bonicki[2], Przemysław Witek[7], Ewa Naganska[4]

[1]Mossakowski Medical Research Centre, Polish Academy of Sciences, Warsaw, [2]Department of Neurosurgery, M. Sklodowska-Curie Memorial Cancer Centre and Institute of Oncology, Warsaw, [3]Department of Pathology and Laboratory Diagnostic, M. Sklodowska-Curie Memorial Cancer Center and Institute of Oncology, Warsaw, [4]Department of Experimental and Clinical Neuropathology, Mossakowski Medical Research Centre, Polish Academy of Sciences, Warsaw, [5]Department of Pathology, The Children's Memorial Health Institute, Warsaw, [6]Department of Neurosurgery, Military Institute of Medicine, Warsaw, [7]Department of Endocrinology and Isotope Therapy, Military Institute of Medicine, Warsaw, Poland

Abstract

Ganglion cell tumours in the sellar region are uncommon. They are usually associated with pituitary adenomas, while isolated ganglion cell neoplasms are extremely rare. We report the clinicopathological studies of five cases diagnosed as ganglion cell tumours located in the intrasellar region: four mixed/collision tumours composed of gangliocytoma and pituitary adenoma, and one isolated ganglioglioma unrelated to adenoma. Clinically, two patients presented with acromegaly, while three others were initially diagnosed as non-functioning adenomas. In four cases, the histopathological examination of surgical specimens revealed intermixed lesions composed of pituitary adenoma and ganglion cell elements. The adenomas appeared to secrete growth hormone. Electron microscopy enabled identification of the sparsely granulated somatotroph cells. Neoplastic neuronal lesions were composed of mature ganglion cells, including binucleate or multinucleate cells. In all cases, boundaries between adenomatous and gangliocytic components were not clearly demarcated, and numerous gangliocytic cells were closely intermingled with adenomatous tissue. One case lacked endocrine symptoms, and no pituitary adenoma was identified in the surgically excised material; it was finally diagnosed as low-grade ganglioglioma. The etiopathogenesis of ganglion cell neoplasms in the sellar region is not clearly defined. Our study revealed that if ganglion cell neoplasms were combined with adenoma, both neoplastic components were closely related to each other, and numerous neuronal elements were strictly intermingled with adenoma cells. Such a tissue pattern indicates that these neoplastic changes, including their common respective etiopathogeneses, are closely related. The identification of both components in sellar regions may have some nosological implications.

Key words: *ganglion cell tumour, gangliocytoma, ganglioglioma, sellar tumours, pituitary adenoma.*

Communicating author:

Prof. Ewa Matyja, Mossakowski Medical Research Centre, Polish Academy of Sciences, 5 Pawinskiego St., 02-106 Warsaw, Poland, e-mail: ematyja@imdik.pan.pl

Ewa Matyja, Maria Maksymowicz, Wiesława Grajkowska, Grzegorz Zieliński, Jacek Kunicki, Wiesław Bonicki, Przemysław Witek, Ewa Naganska

Introduction

Gangliocytic neoplasms in the sella turcica and parasellar region are uncommon. Ganglion cell tumours in this location are usually associated with functioning or nonfunctioning pituitary adenomas or pituitary cell hyperplasia. Such neoplasms occur without evidence of adjacent adenoma only occasionally. The majority of ganglion cell tumours appear in association with growth hormone-secreting pituitary adenoma presenting with acromegaly [2,4-6,12,17-19,23,25,32,38,40,42]. They appear less often with adrenocorticotropic hormone-producing adenomas with clinical presentation of Cushing's disease [25,36,40].

We present the clinicopathological features of five cases of intrasellar ganglion cell tumours: four mixed/collision tumours composed of gangliocytoma and pituitary adenoma, and one isolated ganglioglioma. Clinically, two patients presented with acromegaly, while three others were initially diagnosed with non-functioning adenomas.

Material and methods

The biopsy tissues from neurosurgery procedure were fixed in 10% formalin, embedded in paraffin and stained with hematoxylin and eosin (H&E). Immunohistochemical staining was performed on paraffin-embedded specimens, according to the labelled EnVision Flex Visualization System (Dako, K8000) with DAB as chromogen, using antibodies against anterior pituitary hormones: prolactin (PRL, 1 : 200), growth hormone (GH, 1 : 500), adrenocorticotrophic hormone (ACTH, 1 : 500), thyroid-stimulating hormone (β-TSH, 1 : 500), follicle-stimulating hormone (β-FSH, 1 : 500), luteinizing hormone (β-LH, 1 : 500) all antibodies from Thermo Scientific Lab Vision Corp., andglycoprotein α-subunit (1 : 100) from Novocastra. The antibodies against CAM5,2 from Cell Marque and: cytokeratins AE1/AE3 (CK), chromogranin A, glial fibrillary acidic protein (GFAP), S100 protein, synaptophysin, neurofilaments (NF) and Ki-67 (MIB-1) from Dako (all antibodies ready to use) were also used.

For electron microscopic study, the tissue was fixed in 2.5% glutaraldehyde, postfixed in 1% osmium tetroxide, dehydrated in graded alcohols and embedded in Epon 812. Ultrathin sections were counterstained with uranyl acetate and lead citrate and examined in a Philips CM 120 BioTWIN electron microscope.

Report of cases

Case 1

A 51-year-old woman who presented with acromegaly was admitted to the Department of Neurosurgery. Changes in this patient's facial features has developed slowly over the last several years, and included nasal dysmorphism and skin changes. Growth in the acral parts of limbs had been observed, with increases noted in her foot and finger sizes. The patient had been complaining of headaches, significant perspiration, and fatigue for many years. She denied any visual problems. She also had diabetes mellitus and menstrual irregularities. There was no family history of pituitary or brain tumours. Magnetic resonance imaging (MRI) of the brain revealed a homogenously enhanced, large pituitary mass with sellar floor destruction and suprasellar and infrasellar extension (Fig. 1A-C). The tumour diameter was approximately 2.5 cm. Tumour growth had resulted in mild compression of the optic chiasm and invasion of the right cavernous sinus (Knosp III°). The pituitary gland appeared normal, but was displaced to the medial wall of the left cavernous sinus and diaphragm sellae. Endocrine laboratory tests revealed elevated GH (8.1 μg/ml). The PRL level, measured several times, ranged from 57.3 to 189.1 ng/ml; β-TSH and free thyroxine (free T4) were 0.119 mIU/l and 11.88 pmol/l, respectively; serum cortisol was 85.9 ng/ml at 8:00 AM and 27.3 ng/ml at 8:00 PM. The patient received 8 months of pretreatment with somatostatin analogue (sandostatin, LAR 30 mg), which resulted in tumour regression on neuroimaging studies. Surgery was conducted using a trans-sphenoidal microsurgical approach with tumour resection. Transitional postoperative hypopituitarism was observed. At follow-up, this patient had persistent acromegaly caused by tumour remnants in the right cavernous sinus. She was referred for a radiosurgical procedure.

Histopathology

Histological examination of the resected specimens revealed two different neoplastic components: pituitary adenoma and ganglion cell neoplasm (Fig. 2A). The ganglion cell lesion was composed of large neoplastic neuronal cells scattered in a fibrillar, eosinophilic background (Fig. 2B). Numerous ganglion cells exhibited irregular cytoplasmic outlines

Fig. 1. Case 1: **A)** A coronal, post-contrast, T1-weighted MRI depicts an invasive sellar mass with moderate heterogeneous enhancement and invasion of the right cavernous sinus. **B)** A sagittal T2-weighted MRI shows an isointense tumour with sellar enlargement, moderate suprasellar extension, and slight compression of the optic chiasm. **C)** A sagittal, post-contrast, T1-weighted MRI depicts the sellar tumour with moderate enhancement and remnants of pituitary.

and aggregates of Nissl granules at the cell body periphery. Immunohistochemistry revealed diffuse immunoreactivity for NF (Fig. 2C) and intense synaptophysin expression (Fig. 2D). The lesion lacked any astroglial component positive for GFAP.

Immunostaining for pituitary hormones demonstrated GH-positive adenoma cells in the adenomatous part (Fig. 2E). The intermingled neurons themselves did not express GH immunoreactivity. Other pituitary hormones were not detected. The pituitary tumour cells were immunopositive for CK, chromogranin A, and synaptophysin. The boundaries between adenomatous and gangliocytic components were not clearly demarcated, and clusters of small adenoma cells were intermingled with neuronal elements.

Ultrastructural features documented a sparsely granulated somatotroph adenoma (SG-GH) composed of medium-sized, round cells. Some cells contained typical globular fibrous bodies of intermediate filaments and sparse, small, electron-dense secretory granules (Fig. 2F).

The final histopathological diagnosis was established as sparsely granulated somatotroph pituitary adenoma combined with gangliocytoma.

Case 2

A 59-year-old man with a history of headaches and visual disturbances for the past few weeks was admitted to the Department of Neurosurgery. The patient did not present clinical symptoms typical of acromegaly or Cushing's syndrome. His levels of PRL

and other pituitary hormones were within normal ranges. An MRI revealed a large sellar-suprasellar mass with moderate heterogenous enhancement after gadolinium administration. On T1-weighted sequences, a rim of compressed anterior pituitary tissue was observed. The tumour caused enlargement of the *sella turcica* and invaded the left cavernous sinus and sellar floor, with submucosal extension to the left sphenoid sinus (Fig. 3A,B). Its maximal cranio-caudal diameter was 36 mm. The clinical diagnosis was a nonfunctioning invasive macroadenoma.

The patient underwent two consecutive surgeries with an endoscopic trans-sphenoidal approach. The initial surgery was a subtotal resection that left tumour remnants invading the left cavernous sinus and the diaphragm of the sella. Intraoperatively, the tumour displayed a biphasic appearance, with predominant yellow-whitish fibrous tissue and an admixture of pink-white foci; it resembled a typical intraoperative view of pituitary adenoma. The procedure was ceased because of bradycardia and suspicion of acute coronary syndrome. The postoperative course was uneventful, with significant visual improvement.

Eight months later, the residual sellar tumour was resected through the same operating access. The sellar floor was reconstructed with an autologous fat tissue graft, titanium micro-mesh, and fibrin glue. The postoperative MRI revealed minimal tissue remnants within the left cavernous sinus. The postoperative course was uneventful, with no visual

http://rcin.org.pl

Ewa Matyja, Maria Maksymowicz, Wiesława Grajkowska, Grzegorz Zieliński, Jacek Kunicki, Wiesław Bonicki, Przemysław Witek, Ewa Naganska
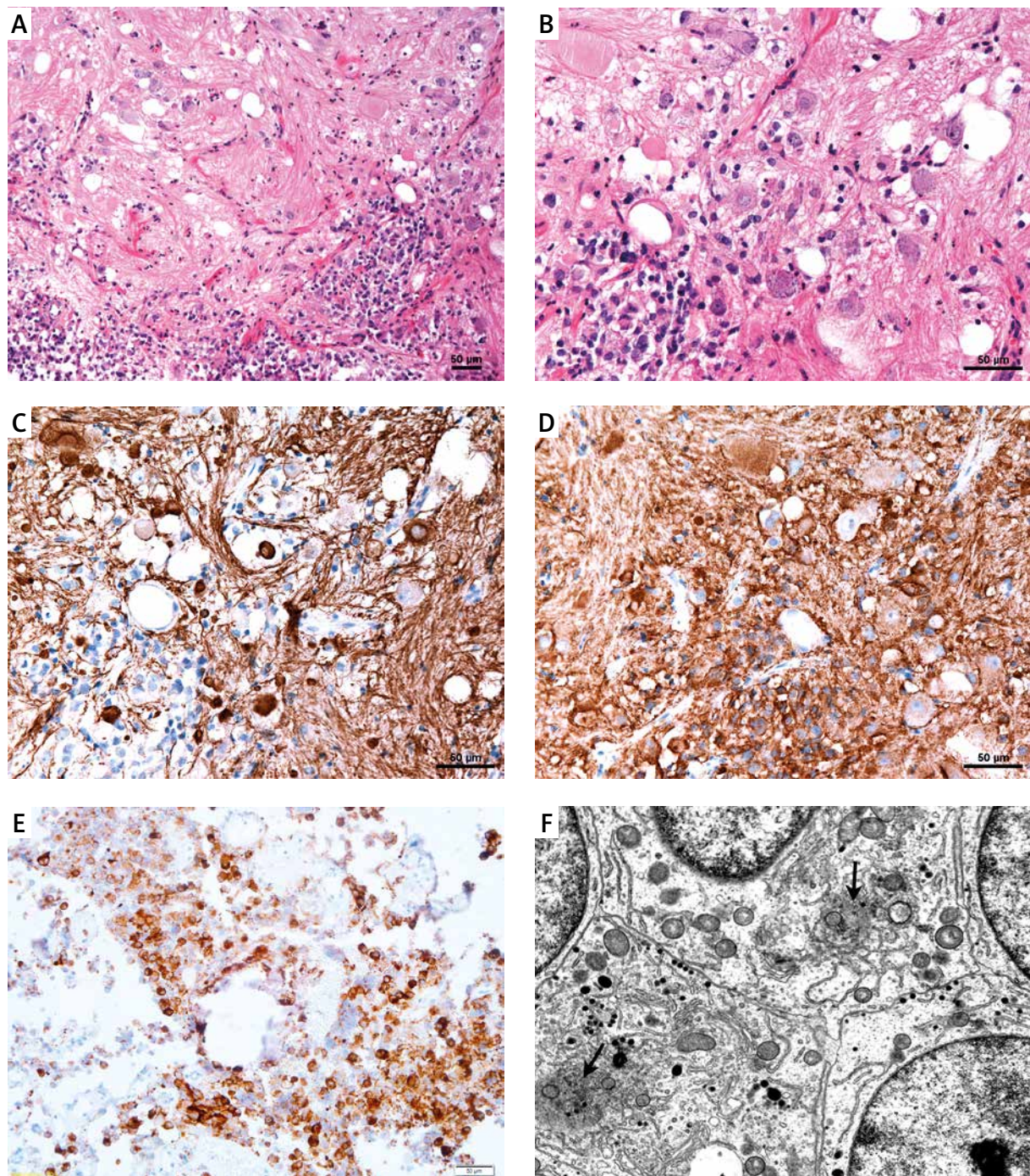
Fig. 2. Case 1: **A)** This sellar tumour is composed of small, round, adenoma cells and a lesion of gangliocytic cells with a fibrillar, eosinophilic background, H&E. **B)** Large neoplastic ganglion cells are closely intermixed with adenoma cells, H&E. Note the gangliocytic part of the tumour exhibits strong expression of NF **(C)** and synaptophysin **(D)**. **E)** Adenoma cells are immunoreactive for GH. **F)** Ultrastructural features of sparsely granulated somatotroph adenoma with polygonal cells, containing abundant cytoplasm and characteristic fibrous bodies (arrows). Secretory granules are sparse and small. Original magnification 9700×.
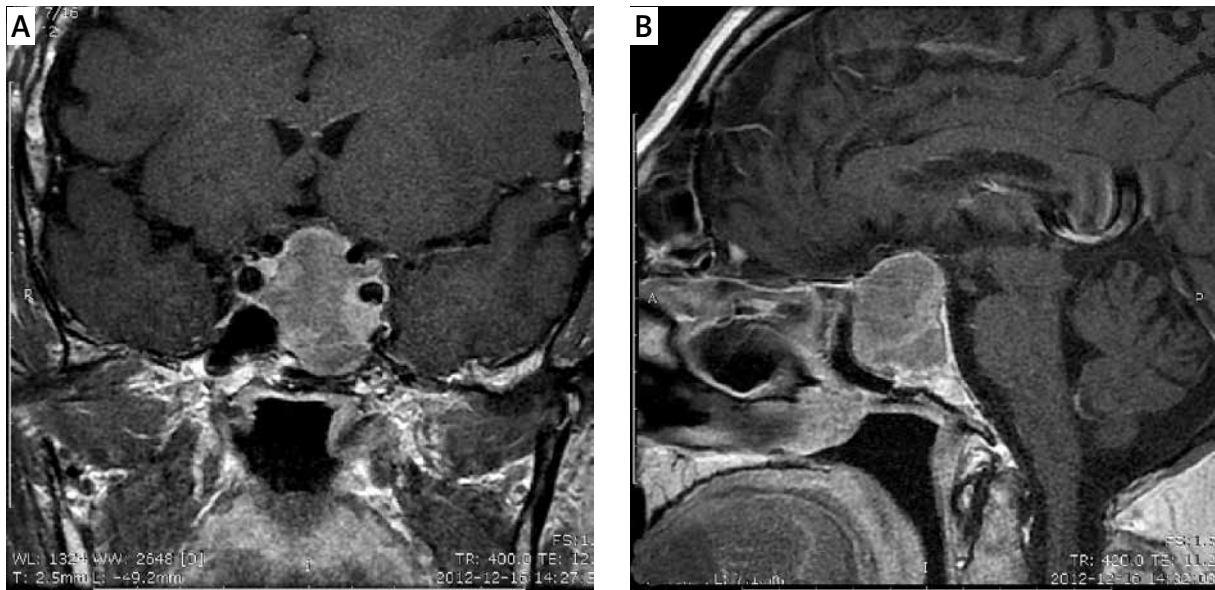
Fig. 3. Case 2: Coronal post-contrast **(A)** and axial T1-weighted **(B)** MRI reveal a hyperintense tumour of the sellar region with erosion of the sellar floor, invasion of the left cavernous sinus, and moderate suprasellar extension with optic chiasm compression.

symptoms. The GH level was below 1 ng/ml, with some minimal elevation of insulin-like growth factor 1 (363 ng/ml; N: 144-286). The patient did not require any hormone replacement therapy.

Histopathology

At both surgeries, the tumours were composed of pituitary adenoma combined with a ganglion cell component (Fig. 4A). The large part of the lesion was composed of clusters of randomly distributed ganglionic cells exhibiting abundant cytoplasm, large vesicular nuclei with prominent nucleoli, and aggregates of Nissl granules. Binucleate or multinucleate neoplastic neuronal cells were present. Immunohistochemistry revealed intense synaptophysin expression outlining the cell borders (Fig. 4B) and NF in the ganglion cell bodies and their processes (Fig. 4C). The gangliocytic component correlated closely with pituitary adenoma, and numerous ganglion cells were intermixed with adenomatous tissue. The pituitary adenoma cells were strongly positive for chromogranin A and cytokeratin. The adenomatous cells revealed GH immunoexpression (Fig. 4D), but were negative for other anterior pituitary hormones.

Electron microscopy revealed ultrastructural features of sparsely granulated somatotroph adenoma, composed of round, medium-sized cells with typical cytoplasmic fibrous bodies (Fig. 4E). The ganglion cells were characterized by the presence of a large nucleus or nuclei, with prominent nucleoli. We also observed binucleate neuronal cells (Fig. 4F). The cytoplasm of neuronal cells contained abundant mitochondria, well-developed endoplasmic reticulum, neurofilaments, and dense core neurosecretory granules. The neuronal processes contained microtubules and dense core neurosecretory granules. Ultrastructural studies provided evidence of a close relationship between neuronal and adenomatous elements. Silent sparsely granulated somatotroph pituitary adenoma and gangliocytoma was the final pathological diagnosis.

Case 3

A 58-year-old, post-menopausal woman with a 3-month history of headache and diplopia was admitted to the Department of Neurosurgery. At admission, neuro-ophthalmological examination revealed a decrease of visual acuity to 0.9 in both eyes and diplopia with not restriction of the visual field. There was a limitation of abduction on the right side. The color and shape of optic discs were normal. Apart from the visual impairment, the neurological examination did not reveal any focal

http://rcin.org.pl

Ewa Matyja, Maria Maksymowicz, Wiesława Grajkowska, Grzegorz Zieliński, Jacek Kunicki, Wiesław Bonicki, Przemysław Witek, Ewa Naganska
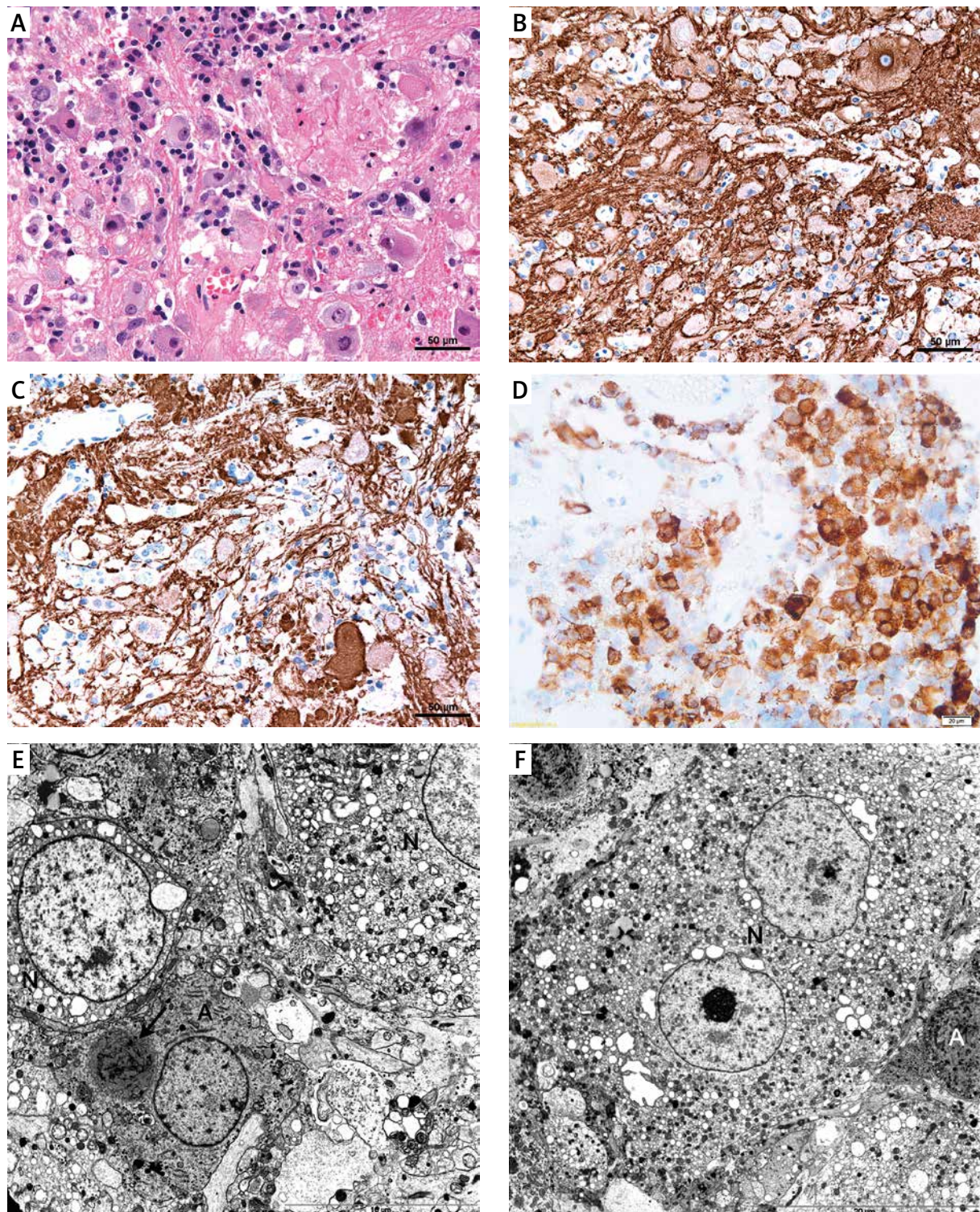
Fig. 4. Case 2: **A)** A mixed sellar tumour composed of an adenomatous component and large ganglion cells, H&E. **B)** The gangliocytic component, with strong immunostaining for synaptophysin. **C)** Ganglion cells and dense neuronal processes are strongly immunoreactive for NF. **D)** GH-secreting adenoma cells. **E)** Ultrastructure of gangliocytoma admixed with sparsely granulated somatotroph adenoma. Large ganglion cells (N) with abundant cytoplasm are surrounded by bands of axons and polygonal cells of somatotroph adenoma, with characteristic fibrous bodies (arrow); original magnification 4200×. **F)** The large binucleate neuronal cell (N) with a prominent nucleolus and abundant cytoplasm, contains numerous mitochondria, vacuoles, and neurofilaments, as well as small adenomatous cells (A); original magnification 2500×.

Table I. Preoperative hormonal results (Case 3)

GH	IGF-1	TSH	fT4	PRL	FSH	LH	Cortisol
0.93 µg/l	197 µg/ml	0.233 µlU/ml	19.42 pmol/l	6.9 ng/ml	34.33 lU/l	15.05 lU/l	16.6 µg/dl

deficits of cranial nerves. There were no symptoms of raised intracranial pressure. Other than obesity, the patient did not present typical Cushing's syndrome features. Acromegaly was not observed. Pituitary hormone levels were within normal limits, and there were no signs of diabetes insipidus (Table I).

MRI revealed an aggressive pituitary tumour measuring 14 × 13 × 15 mm, with right cavernous sinus invasion, partial encasement of the right cavernous carotid artery, and sellar floor erosion (Fig. 5A,B). Microsurgery was performed using a trans-sphenoidal approach. The tumour was removed subtotally owing to invasion of the cavernous sinus. The pituitary gland was displaced to the left side of the sella. The postoperative course was uneventful. Based on the patient's postoperative early morning serum cortisol level, insufficiency of the adrenal cortex was excluded. There were no postoperative indications of diabetes insipidus or water-electrolyte disturbance (e.g., hyponatremia). This patient was discharged from the Neuro-surgical Department in good general condition and transferred to the outpatient clinic.

Histopathology

Microscopically distinct neoplastic components composed of pituitary adenoma and ganglion cell neoplasm were found (Fig. 6A). The gangliocytic component was composed of pure neoplastic ganglion cells distributed within a neuropil-like background, without any glial component. The majority of ganglion neoplastic cells were large, some of them binucleate or multinucleate, and were closely intermixed with small adenoma cells (Fig. 6B). Immunohistochemistry revealed fairy dense granular reactivity for synaptophysin (Fig. 6C) and reactivity for NF. The adenomatous part of the tumour was composed of GH-positive adenoma cells (Fig. 6D). There was no immune reactivity against any other pituitary hormones. The pituitary tumour cells expressed chromogranin A, and synaptophysin. Electron microscopy was not performed but immunoreaction for Cam
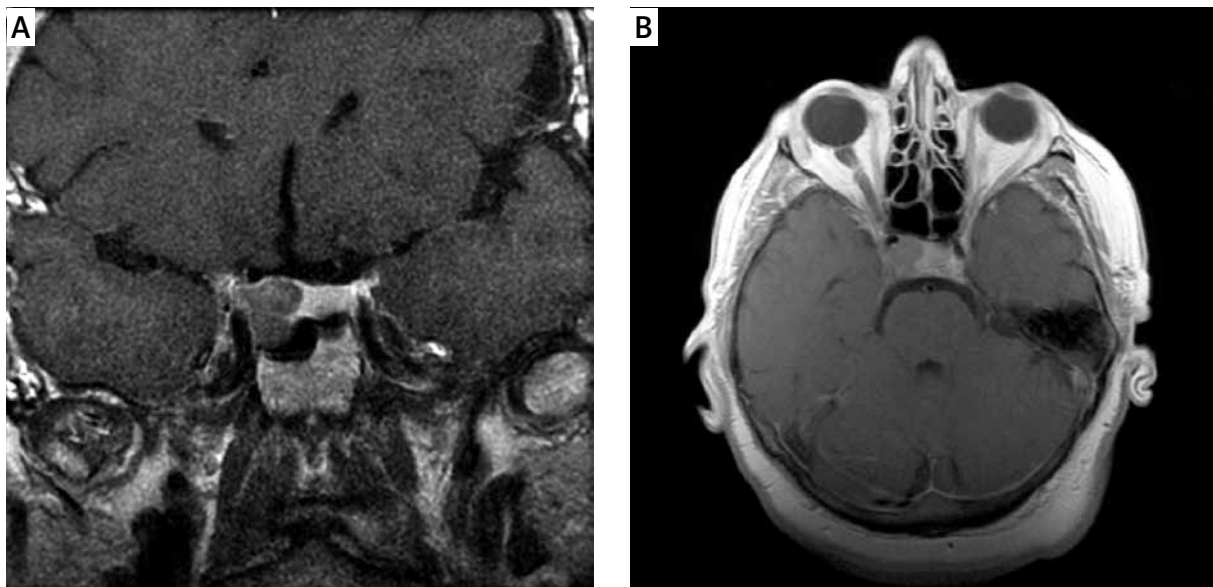
Fig. 5. Case 3: Coronal **(A)** and axial **(B)** T1-weighted, post-Gd-DTPA MRI depict an aggressive pituitary tumour with invasion of the right cavernous sinus (Knosp III°), partial encasement of the right cavernous carotid artery, and sellar floor erosion.

Ewa Matyja, Maria Maksymowicz, Wiesława Grajkowska, Grzegorz Zieliński, Jacek Kunicki, Wiesław Bonicki, Przemysław Witek, Ewa Naganska
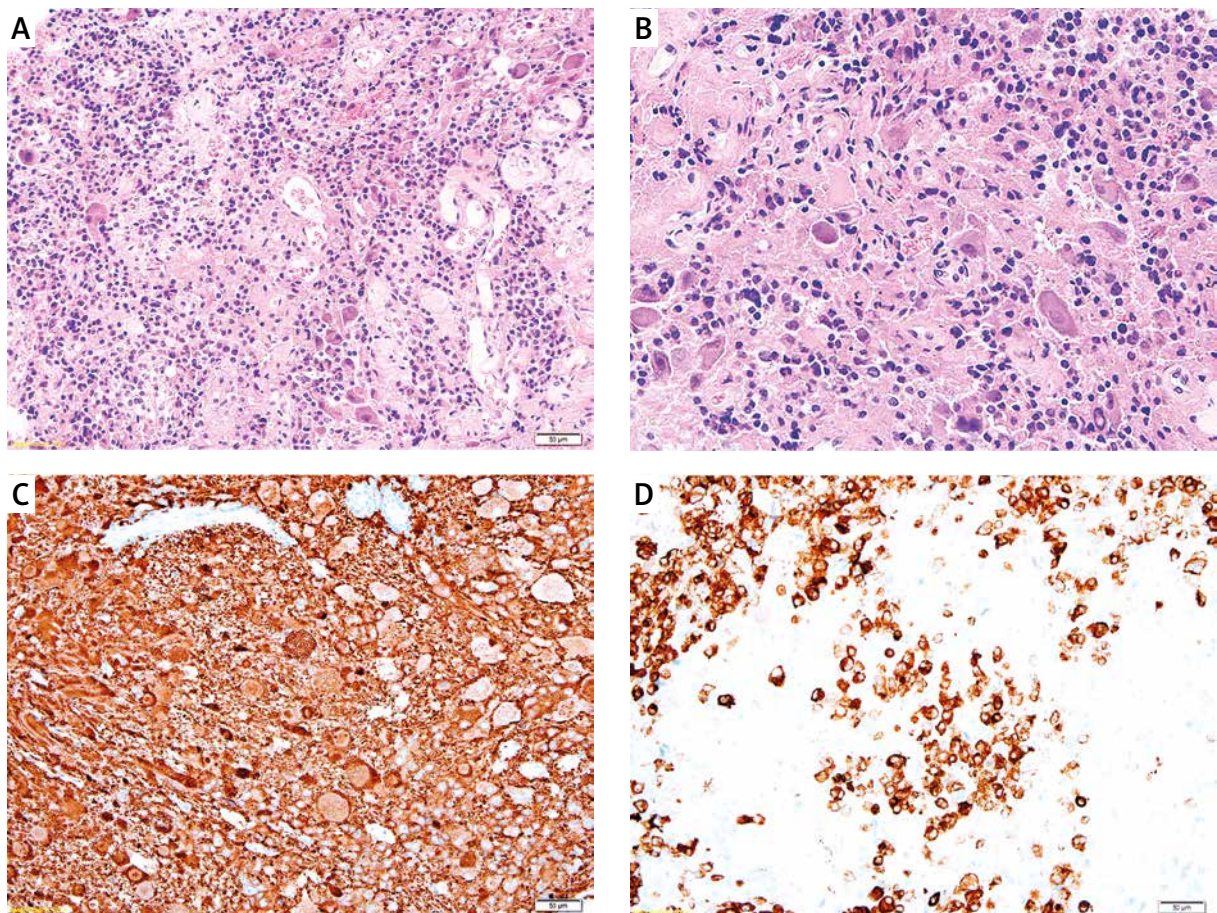
Fig. 6. Case 3: **(A)** A mixed sellar lesion composed of gangliocytic cells and adenoma, H&E. **B)** The majority of ganglion tumour cells were large and closely intermixed with small adenoma cells, H&E. **C)** Dense granular immunoreactivity for synaptophysin. **D)** GH-positive adenoma cells in the adenomatous part of the tumour.

5.2 supported the diagnosis of sparsely granulated somatotroph pituitary adenoma.

The final histopathological diagnosis was silent sparsely granulated somatotroph pituitary adenoma and gangliocytoma.

Case 4

A 63-year-old woman was admitted to the Department of Neurosurgery with typical clinical features of acromegaly lasting 6 years. Her presenting symptoms were progressive headaches and sleep apnea syndrome. The patient was under general medical care because of arterial hypertension and diabetes mellitus. Neurological examination showed no impairment of visual acuity or visual fields. The function of other cranial nerves was also intact. Fundoscopic examination revealed no optic nerve atro-

phy. The patient had no family history of pituitary adenoma or multiple endocrine neoplasia. Endocrine investigation revealed elevated basal serum levels of GH and somatomedin-C, with an abnormal oral glucose tolerance test. The serum levels of other pituitary hormones were within normal limits (Table II).

MRI of the sellar region revealed a homogenic tumour mass (12 × 15 × 16 mm) with intrasellar extension and invasion of the left cavernous sinus (Knosp I°) on coronal and sagittal T1-weighted images before and after the administration of Gd-DTPA (Fig. 7A,B).

The patient underwent trans-sphenoidal surgery. During the procedure, a yellowish, fibrous, compact tumour was separated from the pituitary gland and completely excised. There were no signs of cavernous sinus invasion. The postoperative period was

Table II. Preoperative hormonal results (Case 4)

GH	IGF-1	IGF BP3	TSH	fT4	PRL	FSH	LH	Cortisol
3.88 µg/l 60' 5.14 µg/l 120' 3.81 µg/l	976 ng/ml	9.40 µg/ml	1.05 µIU/ml	20.41 pmol/l	5.67 ng/ml	86.21 IU/l	21.11 IU/l	8.00 – 8.26 µg/dl 20.00 – 1.81 µg/dl
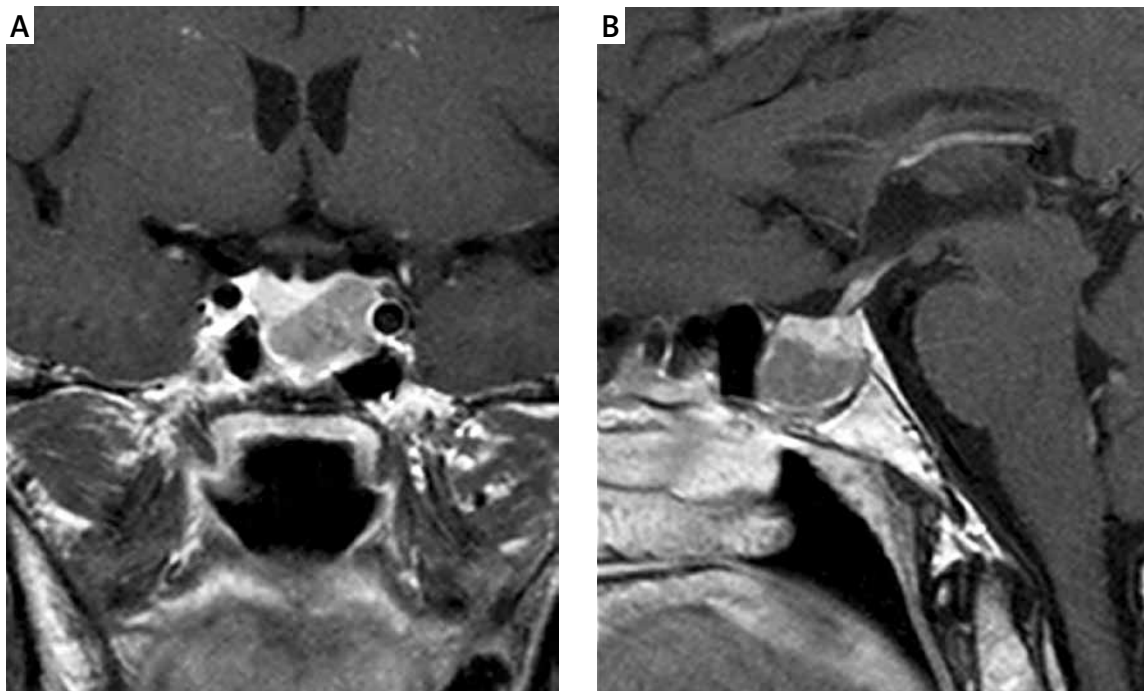
Fig. 7. Case 4: MRI of the sellar region. Coronal **(A)** and sagittal **(B)** T1-weighted images before and after Gd-DTPA administration reveal a homogenic tumour mass with intrasellar extension and invasion of the left cavernous sinus (Knosp I°).

uneventful. There were no postoperative indications of diabetes insipidus or water-electrolyte disturbance (e.g., hyponatremia). The patient was discharged from the Neurosurgical Department in good general condition and transferred to the endocrinological outpatient clinic.

Histopathology

The tumour comprised mixed pituitary adenoma and gangliocytoma (Fig. 8A). Both neoplastic components were closely intermingled. The gangliocytic part exhibited clusters of large neuronal cells within a fibrillar background. Large binucleate or multinucleate ganglion cells were often seen (Fig. 8B). Immunohistochemistry documented strong NF expression (Fig. 8C). In the adenomatous part of the lesion, a few small (probably adenoma) cells and short pro-

cesses also exhibited NF immune reactivity (Fig. 8D). Both tumour components strongly expressed synaptophysin (Fig. 8E). Tumour cells were negative for GFAP and S-100 protein. The pituitary adenoma cells were immunoreactive for GH (Fig. 8F), and negative for other anterior pituitary hormones. The Ki-67 labeling index was low.

Electron microscopy revealed ultrastructural features of sparsely granulated somatotroph adenoma combined with the ganglion cell component. The final histopathological diagnosis was sparsely granulated somatotroph pituitary adenoma combined with gangliocytoma.

Case 5

A 26-year-old man was referred to the Department of Neurosurgery with persistent, distending

http://rcin.org.pl

Ewa Matyja, Maria Maksymowicz, Wiesława Grajkowska, Grzegorz Zieliński, Jacek Kunicki, Wiesław Bonicki, Przemysław Witek, Ewa Naganska
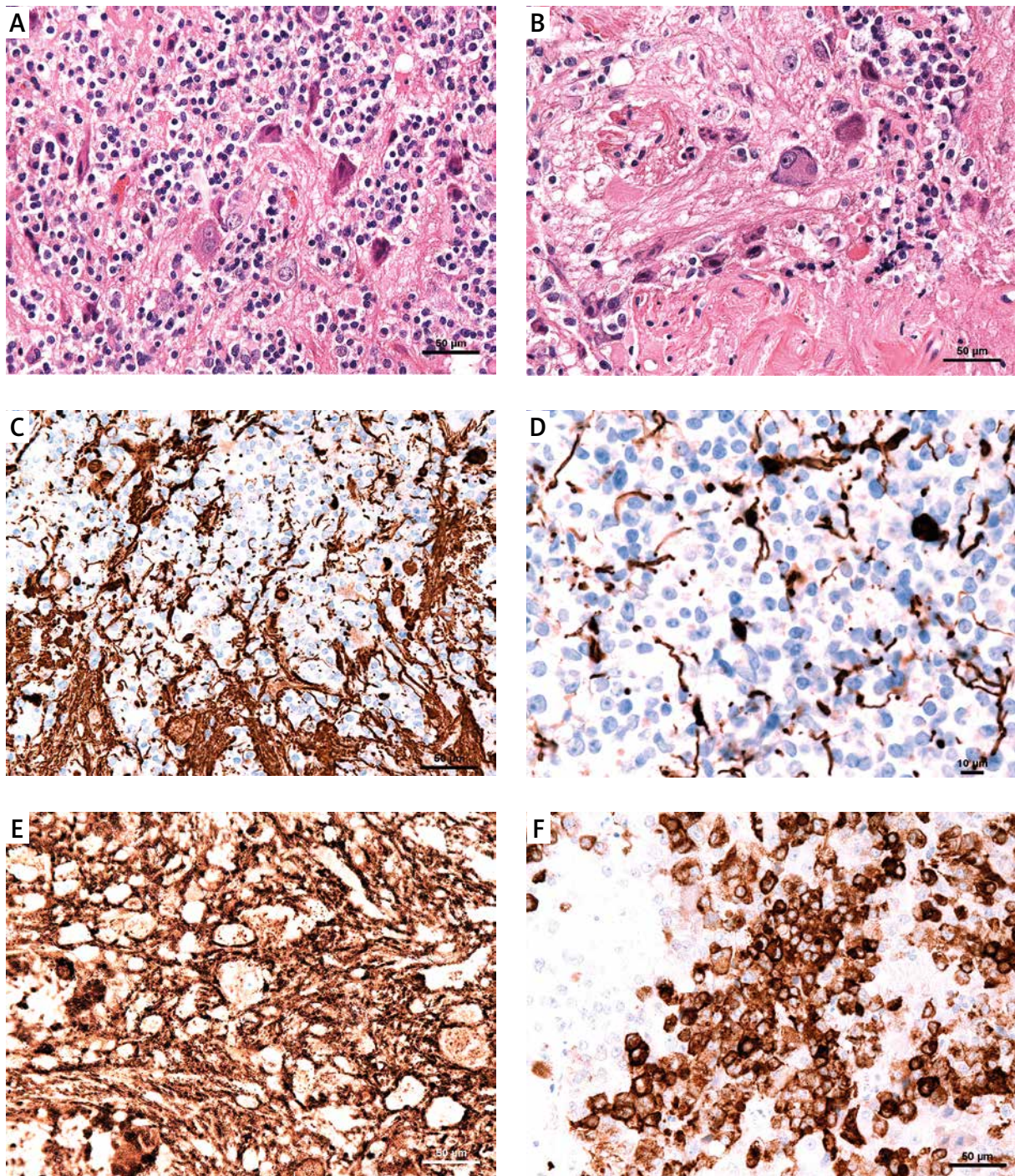
Fig. 8. Case 4: **A)** A mixed sellar lesion composed of gangliocytic cells intermingled with adenoma, H&E. **B)** Large ganglion cells, including binucleate or trinucleate cells, H&E. **C)** Immunoreactivity for NF. **D)** A few small, likely adenoma cells and short processes exhibiting NF immunoreactivity. **E)** Strong synaptophysin expression. **F)** Immunoreactivity for GH in pituitary adenoma cells.

headache and dizziness that had lasted approximately 3 months prior to admission. The patient had suffered from progressive visual impairment for the last 6 weeks before admission. Two weeks prior to admission, MRI had revealed a skull base tumour with extension of the lateral ventricles. Coronal (Fig. 9A) and sagittal (Fig. 9C) T1-weighted MRI after Gd-DTPA and coronal T2-weighted MRI (Fig. 9B) revealed a giant, invasive skull base tumour measuring 42 × 29 × 49 mm. The mass lesion originated from the sella turcica, with invasion of the hypothalamus and brain stem, encasement of the arteries of the circle of Willis, and compression of the pituitary gland. Treatment with steroids (dexamethasone 12 mg *p.o.* daily) was initiated. After admission, the patient was conscious, but confused and drowsy. The ophthalmological examination revealed a decrease of visual acuity to 0.5 in both eyes, as well as bilateral temporal field restriction without diplopia. The optic discs were pale and without papilloedema. Neurological examination demonstrated no obvious clinical signs. We measured this patient's hormone levels in order to assess pituitary function, and the results confirmed secondary adrenal insufficiency. Anterior pituitary insufficiency was diagnosed based on the obtained results (Table III).

The patient underwent subtotal tumour resection through a right-side temporal craniotomy. In the course of this treatment, the visual abnormalities resolved, but third cranial nerve paresis occurred.

The postoperative control axial computed tomography scan revealed lateral ventricle extension. The patient's neurological state improved gradually after a ventriculo-peritoneal shunt was implanted. The patient was finally discharged on the 23rd day of his hospital stay, and was administered replacement hormonal therapy (hydrocortisone, 30 mg once daily; levothyroxine supplementation, 100 µg/day). Three months after surgery, the patient died during complementary radiotherapy.

Histopathology

Microscopically, the sellar lesion appeared to be a mixed glioneuronal tumour composed of large, often multipolar neurons of various size and neoplastic astroglial elements (Fig. 10A). The ganglion-like cells displayed conspicuous nucleus and abundant cytoplasm, with aggregated Nissl granules at the perikarion periphery. The glial component was composed of bipolar, elongated, pilocytic-like astroglial cells within a fibrillar background. The lesion lacked
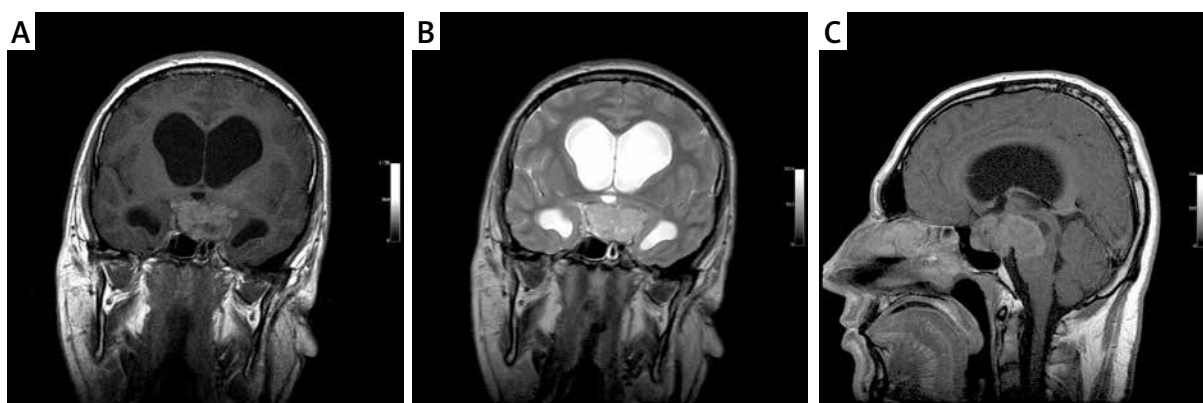
Fig. 9. Case 5: Coronal **(A, B)** and sagittal **(C)** T1-weighted MRI depict a homogenously enhanced, huge intrasellar and suprasellar mass with sellar floor destruction. Note the involvement of the optic chiasm, floor of the third ventricle, and midbrain, with compression of the aqueductus mesencephali and resultant hydrocephalus.

Table III. Preoperative hormonal results (Case 5)

GH	ACTH	TSH	fT4	PRL	FSH	LH	Testosterone
0.42 µg/l	7 pg/ml (during steroids therapy)	0.93 µIU/ml	6.21 pmol/l	21 ng/ml	1.2 IU/l	0.93 IU/l	0.41 ng/ml

http://rcin.org.pl

Ewa Matyja, Maria Maksymowicz, Wiesława Grajkowska, Grzegorz Zieliński, Jacek Kunicki, Wiesław Bonicki, Przemysław Witek, Ewa Naganska
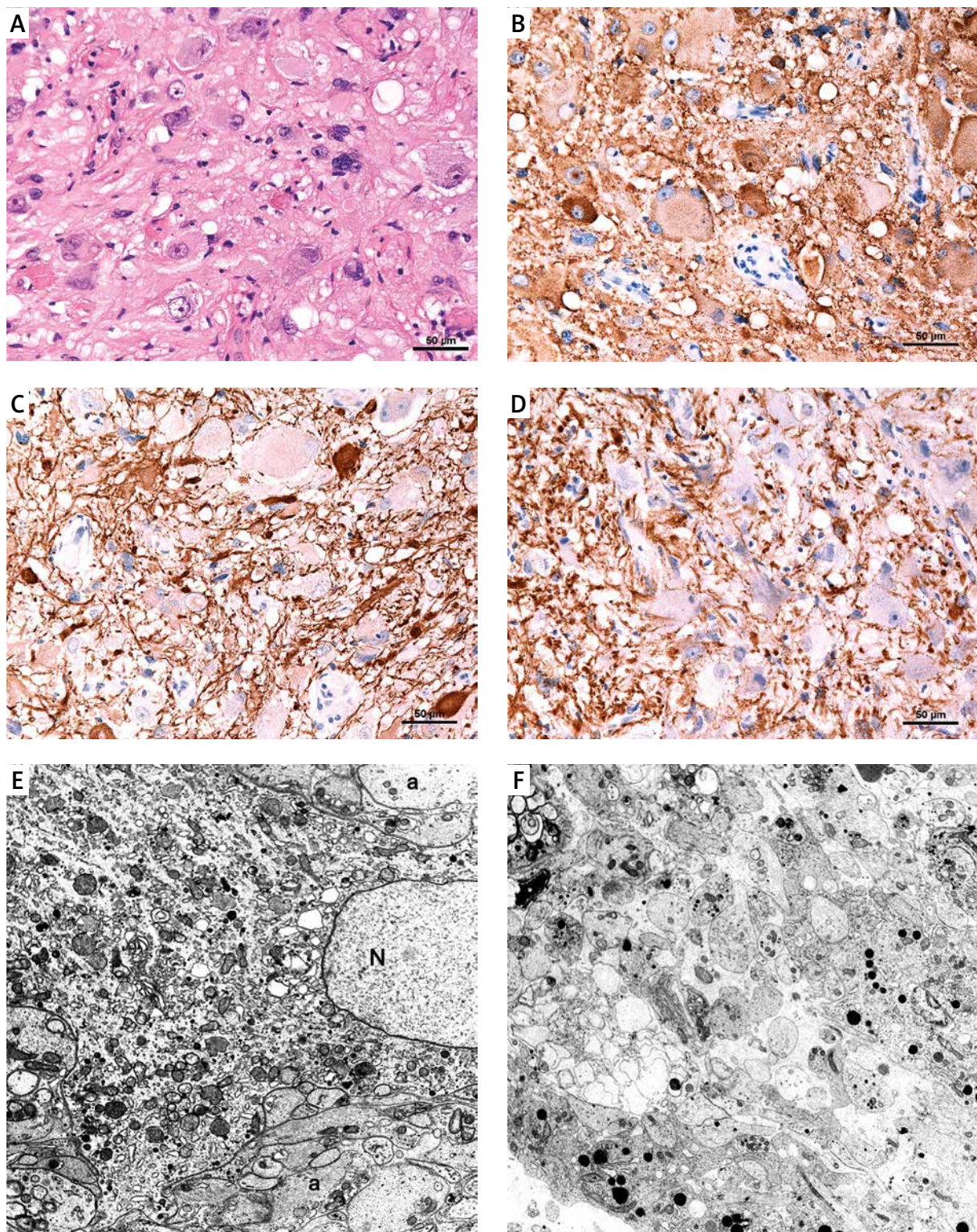
Fig. 10. Case 5: Ganglioglioma of the sellar region. **A)** Ganglion cells combined with neoplastic astrocytes, H&E. **B)** Synaptophysin immunoreactivity at the surface of ganglion cells. **C)** NF expression in ganglion cell processes and cell bodies. **D)** GFAP-positive astroglial neoplastic cells surrounding immunonegative neuro-nal cells. **E)** Ultrastructure of a large ganglion cell (N) with abundant cytoplasm filled with numerous organelles. Glial processes were identified in the surrounding neuropil. Original magnification 7400×. **F)** Neuropil with numerous neuronal and glial processes. Original magnification 4200×.

mitotic figures and signs of vascular hyperplasia or necrosis. Immunohistochemistry supported the biphasic nature of tumours expressing of both neuronal and glial markers. The neuronal cells exhibited strong surface and/or cytoplasmic synaptophysin reactivity (Fig. 10B). The presence of NF was documented in ganglion cell bodies and neuronal processes (Fig. 10C). Astroglial cells were immunoreactive for GFAP (Fig. 10D) and S-100 protein. The Ki-67 labeling index was below 1%. There was no adenomatous tissue or normal pituitary gland in the surgically excised material.

Ultrastructural studies revealed large ganglion cells with abundant cytoplasm filled with numerous organelles (Fig. 10E). Numerous neuronal and glial processes were identified in the surrounding neuropil (Fig. 10F). The histopathological diagnosis was established as a low-grade ganglioglioma, WHO GI.

Discussion

Various malignancies arise in the intrasellar or parasellar region, including pituitary adenomas, craniopharyngiomas, and glial and neuronal neoplasms. However, these tumours rarely occur together. The most common tumours of the sellar and suprasellar region are pituitary adenomas and craniopharyngiomas, which have occasionally been reported in collision [15,20,33]. Mixed pituitary adenomas and craniopharyngiomas usually display a close commixture of both neoplastic components. They are called "hybrid" cells and exhibit features of both pituitary adenoma and craniopharyngioma [15]. Such cells contain small, dense secretory granules, bundles of cytoplasmic filaments, and desmosomes.

Glial neoplasms, which are occasionally found in the sellar region, include pilocytic astrocytoma, diffuse astrocytoma, pilomyxoid astrocytoma, oligoastrocytoma, and mixed glio-neuronal tumours. The clinical presentation and imaging features of these lesions differ from those of craniopharyngiomas. These tumours can cause visual disturbances, GH deficiencies, cystic changes, and calcification [13]. However, glial neoplasms are only occasionally combined with pituitary adenomas.

The neurohypophysis is also a rare site of ganglion cell tumours. The majority of ganglionic tumours at this location occur in association with pituitary pathology; less often, they appear as isolated lesions. Sellar gangliocytomas may cause hypersecretion of pituitary hormone and enlargement of the sella turcica. Sometimes, they are separable from the pituitary gland, stalk, and hypothalamus, and may be successfully removed without further endocrine deficit [16]. Most sellar ganglion cell lesions are related to functioning or nonfunctioning pituitary adenomas or pituitary cell hyperplasia. However, independent of such relationship, they can cause a variety of clinical symptoms that reflect mass effect or their own endocrine activity. Occasionally, pure ganglion cell tumours are themselves hormonally active [35]. An unique case of ganglioglioma of the neurohypophysis associated with syndrome of inappropriate antidiuretic hormone secretion (SIADH) has been reported [14].

A few studies describing a larger series of cases with sellar ganglion cell tumours, classified as ganglioneuromas or gangliocytomas, have been published [7,35,46]. In earlier reports, the different terminology was used to describe ganglion cells lesions, including pituitary adenoma with neuronal choristoma (PANCH) [34,38,42,43], hypothalamic hamartomas, and hamartomatous gangliocytomas [22]. Such a diverse classification may cause nosological confusion. Typical pituitary gangliocytomas located within the sella turcica are not connected with hypothalamus, and the distinction between gangliocytoma and choristoma at a hypothalamic location is not reasonable [43].

Ganglion cell tumours, considered gangliocytomas and gangliogliomas, are usually benign, slow-growing neoplasms; they constitute only 0.4% of all central nervous system tumours and 1.3% of all brain tumours [28]. They are composed of mature ganglion cells with or without a glial component. Gangliocytomas of the pituitary gland are exceptionally rare and usually coexist with a pituitary adenoma, most commonly a GH-secreting adenoma, with the clinical manifestation of acromegaly [4-6,12,17,23,27,32,35,39,44,46]; less often, they are associated with ACTH-producing adenomas, and present with Cushing's disease [25,36,40].

Only in exceptional cases has the coexisting adenoma been endocrinologically silent. Occasionally, gangliocytic lesions of the pituitary gland arise without pituitary adenoma; however, these might themselves produce corticotrophin-releasing factor and display clinical signs of Cushing's disease [3,8]. Thus far, few cases of Cushing's syndrome associated

http://rcin.org.pl

Ewa Matyja, Maria Maksymowicz, Wiesława Grajkowska, Grzegorz Zieliński, Jacek Kunicki, Wiesław Bonicki, Przemysław Witek, Ewa Naganska

with intrasellar ganglion cell lesions, including isolated ganglion lesions, have been described [35,46].

Isolated sellar gangliocytoma without adenoma may also manifest as acromegaly (or, occasionally, diabetes insipidus or hypopituitarism). One case of mixed ACTH adenoma-gangliocytoma with an opportunistic infection has been described [10]. A very rare case of combined gangliocytoma and PRL-producing adenoma (prolactinoma) of the pituitary gland has also been reported [9,30,45].

In the presented cases, the histopathological examination of surgical specimens from four patients (two cases of acromegaly and two cases of clinically nonfunctioning pituitary tumours) revealed pituitary adenomas closely intermingled with neoplastic ganglion cells. The adenomatous contribution appeared to be a GH-secreting adenoma on immunohistochemistry, and sparsely granulated somatotroph adenoma on electron microscopy. In all cases, the neuronal contribution was diagnosed as a purely gangliocytic lesion composed exclusively of groups of neoplastic mature ganglion cells. The two components were close together and in some places intermingled with each other. The close relationship of both neoplastic components suggests that they share a common origin. The neoplastic ganglion cells lacked pituitary hormone expression. The fifth case had no endocrine symptoms, and there was no adenoma or normal pituitary gland in the surgically excised material. The sellar lesion appeared to be a mixed glio-neuronal tumour composed of large, ganglioid, often multipolar neurons and neoplastic astroglial elements. Immunohistochemistry supported a biphasic pattern of neoplastic tissue with expression of both neuronal and glial markers, and the lesion was diagnosed as low-grade ganglioglioma.

The etiopathogenesis of pituitary lesions composed of neuronal and adenomatous components remains controversial. The majority of studies have confirmed the common origin of neuronal and adenomatous elements from the same stem/progenitor cells. The presence of focal differentiation of ganglion cells within a neuropil-like background has been documented [23,43]. Whether such composite lesions are collision tumours that arise from cells of different histogenesis or the two components are derived from the same cell is a matter of debate. The stem/progenitor cells of normal pituitary, which possess the ability of multidirectional differentiation, are the most likely cells of tumour origin.

Based on these facts, two hypotheses have been put forward. The first reasonable speculation is that the majority of ganglion cell tumours arise as a result of neuronal differentiation within conventional pituitary adenomas, mainly sparsely granulated GH cell adenoma [18,21,46]. This suggestion was confirmed by morphological findings, which demonstrated significant intermixing of adenomatous and gangliocytic elements. Histopathological and immunohistochemical findings documented the presence of cells that exhibit intermediate features between ganglion and GH or PRL adenoma cells [4,18,30]. A close relationship between neurons and adenomatous GH cells was also confirmed by electron microscopy [3]. Moreover, pituitary hormones have been detected within the neuronal element of some gangliocytic pituitary lesions [25]. Towfighi *et al.* [46] explained that the transformation of pituitary adenoma cells into mature ganglion cells was a result of their common origin from the same embryonic pituitary cell; their explanation rests on the fact that the cells exhibit features that place them on an intermediate developmental axis between neurons and adenohypophyseal cells. *In vitro* studies indicated that adenohypophyseal cells cultured in collagen gels might transform spontaneously into neuronal cells [29]. The opposite etiopathogenetic hypothesis suggests that the primary gangliocytoma, which produces GH-releasing hormone (GHRH), is able to stimulate the adenomatous transformation of the adjacent normal pituitary gland. It has been suggested that the intrasellar gangliocytoma might promote the growth of a pituitary adenoma through chronic overstimulation resulting from excess GHRH production [23].

Considering the common molecular background of pituitary adenoma and ganglion cell tumours, the activation of the mammalian target of rapamycin (mTOR) intracellular pathway and its two main regulators, Akt and Erk, appears to be important. Increased mTOR activity was observed in pituitary adenomas, with the highest frequency in GH-secreting pituitary adenomas. The regulation of mTOR activity was implicated in the treatment of malignant pituitary adenomas and carcinomas [31,41]. Recently, the upregulation of mitogen-activated protein kinase has also been reported in gangliogliomas [37]. Moreover, when the methylation status of O(6)-methylguanine DNA methyltransferase (MGMT) was examined in pituitary adenomas, the degree of MGMT expression appeared to be related

to therapeutic responses to temozolomide [1,24,26]. MGMT protein expression was also implicated as a prognostic factor for patients with low-grade ganglingliomas [11].

Sellar lesions of double morphology, composed of adenoma and ganglion cells, ought to be classified as a mixed/collision pituitary adenoma-gangliocytoma. Our cases document the close morphological relationship between ganglion cells and adenomatous GH-secreting cellular elements. It was suggested recently that in the cases in which the gangliocytic component is closely intermingled with adenoma, the term "pituitary adenoma with gangliocytic component" best emphasizes the clinical importance of the adenomatous parts of the lesion [7].

Conclusions

Ganglion cell tumours rarely appear in the sellar/parasellar region, either alone or in combination with pituitary adenoma. A tight mixture of neuronal and adenomatous components is commonly observed. Although the pathogenesis of tumours of such intermingled morphology remains unclear, their origin from the stem/progenitor cells that engender normal pituitary tissue is speculated. Distinguishing both components in sellar lesions as precisely defined individual neoplastic elements may determine the prognosis and direct therapeutic management.

Disclosure

Authors report no conflict of interest.

References

1. Arya S, Majaid MA, Shwetha SD, Sravani K, Arivazhagan A, Sampath S, Santosh V. Implications of MGMT methylation status in pituitary adenoma. Pathol Res Pract 2014; 210: 407-411.
2. Asa SL, Bilbao JM, Kovacs K, Linfoot JA. Hypothalamic neuronal hamartoma associated with pituitary growth hormone cell adenoma and acromegaly. Acta Neuropathol 1980; 52: 231-234.
3. Asa SL, Kovacs K, Tindall GT, Barrow DL, Horvath E, Vecsei P. Cushing's disease associated with an intrasellar gangliocytoma producing corticotrophin-releasing factor. Ann Intern Med 1984; 101: 789-793.
4. Asa SL, Scheithauer BW, Bilbao JM, Horvath E, Ryan N, Kovacs K, Randall RV, Laws ER, Jr., Singer W, Linfoot JA, et al. A case for hypothalamic acromegaly: a clinicopathological study of six patients with hypothalamic gangliocytomas producing growth hormone-releasing factor. J Clin Endocrinol Metab 1984; 58: 796-803.
5. Asada H, Otani M, Furuhata S, Inoue H, Toya S, Ogawa Y. Mixed pituitary adenoma and gangliocytoma associated with acromegaly – case report. Neurol Med Chir (Tokyo) 1990; 30: 628-632.
6. Azarpira N, Pakbaz S, Torabineghad S, Musavi J, Rakei M. Acromegaly associated with mixed pituitary adenoma-gangliocytoma and Rathke's cleft cyst. Turk Neurosurg 2013; 23: 527-530.
7. Balci S, Saglam A, Oruckaptan H, Erbas T, Soylemezoglu F. Pituitary adenoma with gangliocytic component: report of 5 cases with focus on immunoprofile of gangliocytic component. Pituitary 2015; 18: 23-30.
8. Baysefer A, Gezen F, Kayali H, Erdogan E, Timurkaynak E, Celasun B. Intrasellar gangliocytoma resembling pituitary adenoma. Minim Invasive Neurosurg 1997; 40: 107-109.
9. Bodi I, Martin AJ, Connor SE, Thomas NW, Lantos PL. Mixed pituitary gangliocytoma/adenoma (prolactinoma) with histogenetic implications. Neuropathol Appl Neurobiol 2002; 28: 252-255.
10. Bridenstine M, Kerr JM, Lillehei KO, Kleinschmidt-DeMasters BK. Cushing's disease due to mixed pituitary adenoma-gangliocytoma of the posterior pituitary gland presenting with Aspergillus sp. sinus infection. Clin Neuropathol 2013; 32: 377-383.
11. Chang IW, Hsu CT, Lin JW, Hung CH. The prognostic impact of MGMT expression on low-grade gangliogliomas: a clinicopathological and immunohistochemical study. Folia Neuropathol 2013; 51: 275-282.
12. Crowley RK, Al-Derazi Y, Lynch K, Rawluk D, Thompson CJ, Farrell M, Agha A. Acromegaly associated with gangliocytoma. Ir J Med Sci 2012; 181: 353-355.
13. Deng S, Li Y, Guan Y, Xu S, Chen J, Zhao G. Gliomas in the Sellar Turcica Region: A Retrospective Study Including Adult Cases and Comparison with Craniopharyngioma. Eur Neurol 2014; 73: 135-143.
14. Fehn M, Lohmann F, Ludecke DK, Rudorff KH, Saeger W. Ganglioglioma of the neurohypophysis with secretion of vasopressin. Exp Clin Endocrinol Diabetes 1998; 106: 425-430.
15. Finzi G, Cerati M, Marando A, Zoia C, Ferreli F, Tomei G, Castelnuovo P, La Rosa S, Capella C. Mixed pituitary adenoma/craniopharyngioma: clinical, morphological, immunohistochemical and ultrastructural study of a case, review of the literature, and pathogenetic and nosological considerations. Pituitary 2014; 17: 53-59.
16. Fischer EG, Morris JH, Kettyle WM. Intrasellar gangliocytoma and syndromes of pituitary hypersecretion. Case report. J Neurosurg 1983; 59: 1071-1075.
17. Geddes JF, Jansen GH, Robinson SF, Gomori E, Holton JL, Monson JP, Besser GM, Revesz T. 'Gangliocytomas' of the pituitary: a heterogeneous group of lesions with differing histogenesis. Am J Surg Pathol 2000; 24: 607-613.
18. Horvath E, Kovacs K, Scheithauer BW, Lloyd RV, Smyth HS. Pituitary adenoma with neuronal choristoma (PANCH): composite lesion or lineage infidelity? Ultrastruct Pathol 1994; 18: 565-574.
19. Iwase T, Nishizawa S, Baba S, Hinokuma K, Sugimura H, Nakamura S, Uemura K, Shirasawa H, Kino I. Intrasellar neuronal choristoma associated with growth hormone-producing pituitary adenoma containing amyloid deposits. Hum Pathol 1995; 26: 925-928.

http://rcin.org.pl

Ewa Matyja, Maria Maksymowicz, Wiesława Grajkowska, Grzegorz Zieliński, Jacek Kunicki, Wiesław Bonicki, Przemysław Witek, Ewa Naganska

20. Jin G, Hao S, Xie J, Mi R, Liu F. Collision tumors of the sella: coexistence of pituitary adenoma and craniopharyngioma in the sellar region. World J Surg Oncol 2013; 11: 178.

21. Kontogeorgos G, Mourouti G, Kyrodimou E, Liapi-Avgeri G, Parasi E. Ganglion cell containing pituitary adenomas: signs of neuronal differentiation in adenoma cells. Acta Neuropathol 2006; 112: 21-28.

22. Kudo M. Hypothalamic gangliocytoma. Selective appearance of neurofibrillary changes, granulovacuolar degeneration, and argentophilic bodies. Acta Pathol Jpn 1986; 36: 1225-1229.

23. Kurosaki M, Saeger W, Ludecke DK. Intrasellar gangliocytomas associated with acromegaly. Brain Tumor Pathol 2002; 19: 63-67.

24. Lau Q, Scheithauer B, Kovacs K, Horvath E, Syro LV, Lloyd R. MGMT immunoexpression in aggressive pituitary adenoma and carcinoma. Pituitary 2010; 13: 367-379.

25. Li JY, Racadot O, Kujas M, Kouadri M, Peillon F, Racadot J. Immunocytochemistry of four mixed pituitary adenomas and intrasellar gangliocytomas associated with different clinical syndromes: acromegaly, amenorrhea-galactorrhea, Cushing's disease and isolated tumoral syndrome. Acta Neuropathol 1989; 77: 320-328.

26. Liu JK, Patel J, Eloy JA. The role of temozolomide in the treatment of aggressive pituitary tumors. J Clin Neurosci 2015; 22: 923-929.

27. Luna V, Morales F, Luengo LM, Sanz A, Diaz J. Pituitary gangliocytoma-adenoma presenting with acromegaly: response to treatment. Arch Intern Med 2001; 161: 1010-1011.

28. Luyken C, Blumcke I, Fimmers R, Urbach H, Wiestler OD, Schramm J. Supratentorial gangliogliomas: histopathologic grading and tumor recurrence in 184 patients with a median follow-up of 8 years. Cancer 2004; 101: 146-155.

29. Martinez-Campos A, Dannies PS. A possible differentiation of anterior pituitary cells in collagen gels into neurons. Cell Tissue Res 1986; 244: 21-26.

30. Mikami S, Kameyama K, Takahashi S, Yoshida K, Kawase T, Sano T, Mukai M. Combined gangliocytoma and prolactinoma of the pituitary gland. Endocr Pathol 2008; 19: 117-121.

31. Monsalves E, Juraschka K, Tateno T, Agnihotri S, Asa SL, Ezzat S, Zadeh G. The PI3K/AKT/mTOR pathway in the pathophysiology and treatment of pituitary adenomas. Endocr Relat Cancer 2014; 21: R331-344.

32. Morikawa M, Tamaki N, Kokunai T, Imai Y. Intrasellar pituitary gangliocyto-adenoma presenting with acromegaly: case report. Neurosurgery 1997; 40: 611-614; discussion 614-615.

33. Moshkin O, Scheithauer BW, Syro LV, Velasquez A, Horvath E, Kovacs K. Collision tumors of the sella: craniopharyngioma and silent pituitary adenoma subtype 3: case report. Endocr Pathol 2009; 20: 50-55.

34. Nishizawa H, Fukuoka H, Iguchi G, Inoshita N, Yamada S, Takahashi Y. AIP mutation identified in a patient with acromegaly caused by pituitary somatotroph adenoma with neuronal choristoma. Exp Clin Endocrinol Diabetes 2013; 121: 295-299.

35. Puchner MJ, Ludecke DK, Saeger W, Riedel M, Asa SL. Gangliocytomas of the sellar region – a review. Exp Clin Endocrinol Diabetes 1995; 103: 129-149.

36. Puchner MJ, Ludecke DK, Valdueza JM, Saeger W, Willig RP, Stalla GK, Odink RJ. Cushing's disease in a child caused by a corticotropin-releasing hormone-secreting intrasellar gangliocytoma associated with an adrenocorticotropic hormone-secreting pituitary adenoma. Neurosurgery 1993; 33: 920-924; discussion 924-925.

37. Rak B, Szlufik S, Grajkowska W, Perek D, Dembowska-Baginska B, Filipek I, Daszkiewicz P, Wlodarski P, Jozwiak J. Upregulation of mitogen-activated protein kinase in ganglioglioma. Folia Neuropathol 2013; 51: 283-289.

38. Rhodes RH, Dusseau JJ, Boyd AS, Jr., Knigge KM. Intrasellar neural-adenohypophyseal choristoma. A morphological and immunocytochemical study. J Neuropathol Exp Neurol 1982; 41: 267-280.

39. Sabel MC, Hans VH, Reifenberger G. Mixed gangliocytoma/pituitary adenoma. Arch Neurol 2000; 57: 587-588.

40. Saeger W, Puchner MJ, Ludecke DK. Combined sellar gangliocytoma and pituitary adenoma in acromegaly or Cushing's disease. A report of 3 cases. Virchows Arch 1994; 425: 93-99.

41. Sajjad EA, Zielinski G, Maksymowicz M, Hutnik L, Bednarczuk T, Wlodarski P. mTOR is frequently active in GH-secreting pituitary adenomas without influencing their morphopathological features. Endocr Pathol 2013; 24: 11-19.

42. Sato Y, Wada T, Nishikawa Y, Yoshida K, Kurose A, Ogawa A, Ogasawara K. Growth hormone-producing pituitary adenoma regrowing as pituitary adenoma with neuronal choristoma 14 years after tumor removal. World Neurosurg 2013; 80: 436.e11-33.

43. Scheithauer BW, Kovacs K, Randall RV, Horvath E, Okazaki H, Laws ER, Jr. Hypothalamic neuronal hamartoma and adenohypophyseal neuronal choristoma: their association with growth hormone adenoma of the pituitary gland. J Neuropathol Exp Neurol 1983; 42: 648-663.

44. Syro LV, Horvath E, Kovacs K. Double adenoma of the pituitary: a somatotroph adenoma colliding with a gonadotroph adenoma. J Endocrinol Invest 2000; 23: 37-41.

45. Thodou E, Kontogeorgos G, Horvath E, Kovacs K. Prolactin-producing pituitary adenoma with incomplete neuronal transformation: an intermediate adenoma-neuronal tumor. Acta Neuropathol 2004; 108: 115-120.

46. Towfighi J, Salam MM, McLendon RE, Powers S, Page RB. Ganglion cell-containing tumors of the pituitary gland. Arch Pathol Lab Med 1996; 120: 369-377.

Folia
Neuropathologica

The effect of neurosphere culture conditions on the cellular metabolism of glioma cells

Ulf Dietrich Kahlert[1,2], Katharina Koch[2], Abigail Kora Suwala[2], Rudolf Hartmann[3], Menglin Cheng[4], Donata Maciaczyk[2], Dieter Willbold[3,5], Charles G. Eberhart[1], Kristine Glunde[4], Jarek Maciaczyk[2]

[1]Department of Pathology, Division of Neuropathology, Johns Hopkins Hospital, Baltimore, USA, [2]Department of Neurosurgery, University Medical Center Düsseldorf, Germany, [3]Institute of Complex Systems ICS-6, Research Center Jülich, Germany, [4]Division of Cancer Imaging Research, Russell H. Morgan Department of Radiology and Radiological Science, Johns Hopkins Hospital, Baltimore, USA, [5]Institute of Physical Biology, Heinrich-Heine-University Düsseldorf, Germany

Abstract

Malignant gliomas, with an average survival time of 16-19 months after initial diagnosis, account for one of the most lethal tumours overall. Current standards in patient care provide only unsatisfying strategies in diagnostic and treatment for high-grade gliomas. Here we describe metabolic phenomena in the choline and glycine network associated with stem cell culture conditions in the classical glioma cell line U87. Using high-resolution proton magnetic resonance spectroscopy of cell culture metabolic extracts we compare the metabolic composition of U87 chronically propagated as adherent culture in medium supplemented with serum to serum-free neurosphere growth. We found that the switch to neurosphere growth, besides the increase of cells expressing the putative glioma stem cell marker CD133, modulated a number of intracellular metabolites including choline, creatine, glycine, and myo-inositol that have been previously reported as potential diagnostic markers in various tumours.

These findings highlight the critical influence of culture conditions on glioma cell metabolism, and therefore particular caution should be drawn to the use of in vitro system research in order to investigate cancer metabolism.

Key words: *glioma, metabolism, neurosphere, CD133, choline, creatine, glycine, myo-inositol.*

Introduction

Glioblastoma (GBM) is the most common and lethal adult glial brain tumour, with a mean overall survival of 16-19 months after primary diagnosis under the current standard-of-care treatment scheme [26]. Despite enormous research efforts towards early diagnosis and more efficient treatment, the prognosis of GBMs remains dismal.

The influence of culture conditions has been widely investigated in the field of glioma research, suggest-ing that neurosphere cultures, compared to adherent growth, more closely resemble the original patient's tumour [29] showing high stem cell compartment [1] and therefore are more suitable for testing of novel therapeutic spectras approaches [30]. In this report we describe altered relative concentrations of the cholines, creatine, myo-inositol, and glycine in the human GBM cell line U87 propagated under stem cell conditions as compared to classical monolayer culture. Furthermore, U87 neurospheres showed significant high-

Communicating author:
Jarek Maciaczyk, PD, Department of Neurosurgery, University Medical Center Düsseldorf, Germany,
e-mail: Jaroslaw.Maciaczyk@med.uni-duesseldorf.de

Ulf Dietrich Kahlert, Katharina Koch, Abigail Kora Suwala, Rudolf Hartmann, Menglin Cheng, Donata Maciaczyk, Dieter Willbold, Charles G. Eberhart, Kristine Glunde, Jarek Maciaczyk

er levels of the putative GBM stem cell marker CD133 as their serum-propagated counterparts. Detection and targeting of miss-regulated choline-, myo-inositol-, creatine-, and glycine-metabolism has been described to have potential utility in the diagnosis and treatment of malignant gliomas [2-4,13,16,19].

This is, to our knowledge, the hitherto first link of changes in those oncometabolites [4,25] to variations in cell culture conditions of glioma cells. Inter-spectral co-analysis of metabolite concentrations under the two propagation conditions identified reductions in ratios of phosphocholine to glycerophosphocholine (PC/GPC) and glycine to total choline (Gly/tCho) but increases in the quotient of total choline to total creatine (tCho/tCre) and PC/tCre, as well as Gly/myo-inositol (Gly/myo). This work should draw the attention of the scientific community on possible *in vitro* artefacts and on the need for appropriate models most closely resembling the *in vivo* biology of investigated tumours.

Material and methods

Cell culture

U87 cell line was purchased from American Type Cell Culture bank (www.ATCC.com) and propagated either as adherent culture in Dulbecco's modified Eagle's medium (DMEM, Life Technologies) containing 20% foetal calf serum or as neurospheres (stem cell culture) in DMEM/F12 (3 : 1, both Life Technologies) medium supplemented with B27 (Life Technologies), 20 ng/ml recombinant human basic fibroblast growth factor (bFGF, Peprotech), 20 ng/ml recombinant human epidermal growth factor (EGF, Peprotech), Anti-Anti (Life Technologies), and 5 μg/ml heparin (Sigma-Aldrich), as described before [12]. Cells were passaged at least eight times in each culture condition before they were subjected to experimental analysis.

Cell line identity was confirmed by analysis of nine tandem repeats plus a gender-determining marker, Amelogenin, using the StemElite kit (Promega, Supporting Information File).

Metabolic extractions of *in vitro* cultures, proton nuclear magnetic resonance spectroscopy (^{1}H-NMR) and metabolite quantification.

A minimum of 7×10^6 cells were collected for each extraction (each condition $n = 3$). A methanol-chloroform-water (1/1/1, v/v/v) dual phase cell lyses protocol was applied to extract water and lipid-soluble metabolites as described before [9]. In this study we only assessed content of the water-soluble extracts. The lyophilised water-soluble extracts were resolved in 20 mM phosphate buffer pH 7 (10% v/v D_2O, Sigma-Aldrich, MO, USA) supplemented with sodium (2,2-dimethyl-2-silapentane-5-sulfonate) (DSS; Euriso-top, internal NMR-standard, STD) for the scans at the Research Centre in Jülich (Germany), and in D_2O containing 0.24* μmol 3-(trimethylsilyl) propionic-2,2,3,3,-d$_4$ acid (Sigma-Aldrich, internal concentration standard, STD) at John Hopkins Hospital. The spectras were acquired at 25°C on a Bruker Avance 500 spectrometer operating at 11.7 T using a 5-mm HX inverse probe, as previously described [9], at the Department of Radiology in the John Hopkins Hospital, and a Bruker Avance III HD 600 spectrometer operating at 14.1 T using a 5-mm TXI-cryo-probe at the Institute of Complex Systems (ICS-6) in the Research Centre in Jülich (Germany). Water suppression was achieved by applying a pulse-sequence using excitation sculpting with gradients. The fully relaxed 1H-NMR data were processed, and the signal integrals listed below were measured using Mestrenova V10 software (Mestrelab). All metabolite concentrations were quantified through peak integration after standardised performed phase correction and baseline fitting. The respective concentration standard served as intra-spectral normalisation for each 1H-NMR spectra, and metabolite concentrations within the same spectra were co-analysed and presented as means plus SDs.

FACS-based assessment of CD133+ cell population

Cells were stained for cell surface antigen CD133 (AC133-PE, #130-098-826, Miltenyi Biotec) according to the manufacturer's protocols, as described before [11]. AC133-antibody without a fluorescent dye (AC133-pure, #130-090-422, Miltenyi Biotec) was used as control. Fluorescence activated cell sorting (FACS) was performed on an Accuri C6 cytometer (BD Biosciences, Franklin Lakes, NJ) whereas for post-processing data analysis FlowJo v10 software (FlowJo, Tree Star Inc, Ashland, OR) was applied.

Cell apoptosis assays

Cultures were dissociated to single cell suspension and viable cells were quantified using the MUSE

Count & Viability Assay Kit (#MCH100102, Merck KGaA, Darmstadt on a Muse Cell Analyser [#0500-3115, Merck KGaA]). Apoptotic cells were quantified using the AnnexinV & Dead Cell Kit (#MCH100105, Merck KGaA, Darmstadt, Germany) on the Muse Cell Analyser, according to the manufacturer's protocol. A minimum of 2000 gated events were acquired.

Statistical evaluation

Statistical evaluation was performed using Students *t*-test in Statistica (Statsoft, OK, USA) and presented as means plus respective standard deviations.

Results

Modification of the culture condition alters the relative concentration of choline, creatine glycine, and myo-inositol in U87 glioma cells.

High-resolution ^{1}H-NMR spectra were obtained as described above, and a representative spectrum is shown in Figure 1A. The most prominent metabolites were annotated and quantified, including adenine (Ade), myo-inositol (myo), glycine (Gly), phosphocholine (PC), glycerophosphocholine (GPC), free choline (fCho), total choline (tCho = fCho + PC + GPC), total creatine (tCre), glutathione (GSH), glutamine (Gln), glutamate (Glu), N-acetylaspartylglutamate (NAAG), alanine (Ala), lactate (Lac), threonine (Thr), and valine/isoleucine (Val/Iso). Due to the previously described importance in glioma biology we focused our quantitative analysis on choline, creatine, glycine, and myo-inositol ratios (Fig. 1B).

The switch to neurosphere media decreased the ratio of PC/GPC (40%) and significantly diminished the Gly/tCho concentration (70%). In contrast, we detected an increase in the ratios of Gly/myo (65%), tCho/tCre (300%), and PC/tCre (280%), reaching statistical significance for the latter two.

Neurosphere assay condition increases the expression of cell surface marker CD133

U87 culture in classical serum-containing growth medium expressed very low levels of CD133$^+$ cells (about the amount of the negative control, 1% CD133$^+$ cells on average, Fig. 1C). Following their transfer into stem cell conditions, the CD133$^-$ population was increased to 18.5% (*p*-value ≤ 0.001, Fig. 2A). Similar results of CD133$^+$ U87 cells in free-floating culture conditions have been published previously [6,21].

U87 neurosphere cultures exhibit a higher fraction of apoptotic cells

We identified increased levels of apoptosis and cell death in cells propagated under neurosphere growth conditions compared to their adherent counterparts as assessed by AnnexinV/Propiodium iodide-based quantification (Fig. 2B).

Discussion

In this work we analysed the changes of U87 cell metabolism depending on whether a monolayer or 3D *in vitro* propagation has been applied. Our study of this human glioma cell line confirms the accumulation or preferential selection of CD133$^+$ cells, a putative brain tumour stem cell marker [15], under prolonged stem cell culture conditions compared to propagation in serum-containing media. Recent studies addressing the effect of different culture conditions in *in vitro* mouse models of GBM described the robust enhancement of stem cell marker expression and self-renewal capacity of cells transferred from adherent growth to spheroid culture [1]. Moreover, neurosphere cultures are suggested to more closely resemble the original patient's tumour [29] and therefore are more suitable for testing novel therapeutic approaches [30].

Using high-resolution magnetic resonance spectroscopy (^{1}H-NMR) in extracts of cells chronically propagated under serum-free neurosphere growth, we identified several alterations in metabolite concentrations with proposed diagnostic utility as a response to changed growth stimuli.

Phosphocholine (PC), glycerophosphocholine (GPC), and free choline (fCho) all play an important role in the membrane phospholipid household that accompanies cell cycle progression [10]. Moreover, dysregulated choline metabolism has already been proposed as an underlying molecular event during cancerous malformation in a variety of cancers [7], including GBM [2]. Interestingly, we found that U87 glioma neurospheres exhibit a reduced PC/GPC ratio, although it is not statistically significant. The PC/GPC ratio has been shown to be elevated in aggressive breast cancer cells [8], however, the diagnostic impact of this parameter in brain cancers has been challenged [18]. The tCho/tCre quotient is a historically established diagnostic biomarker in brain tumours, which increases with progression of malignancy [20,23,24]. Concordant with this data we revealed that the tCho/

http://rcin.org.pl

Ulf Dietrich Kahlert, Katharina Koch, Abigail Kora Suwala, Rudolf Hartmann, Menglin Cheng, Donata Maciaczyk, Dieter Willbold, Charles G. Eberhart, Kristine Glunde, Jarek Maciaczyk
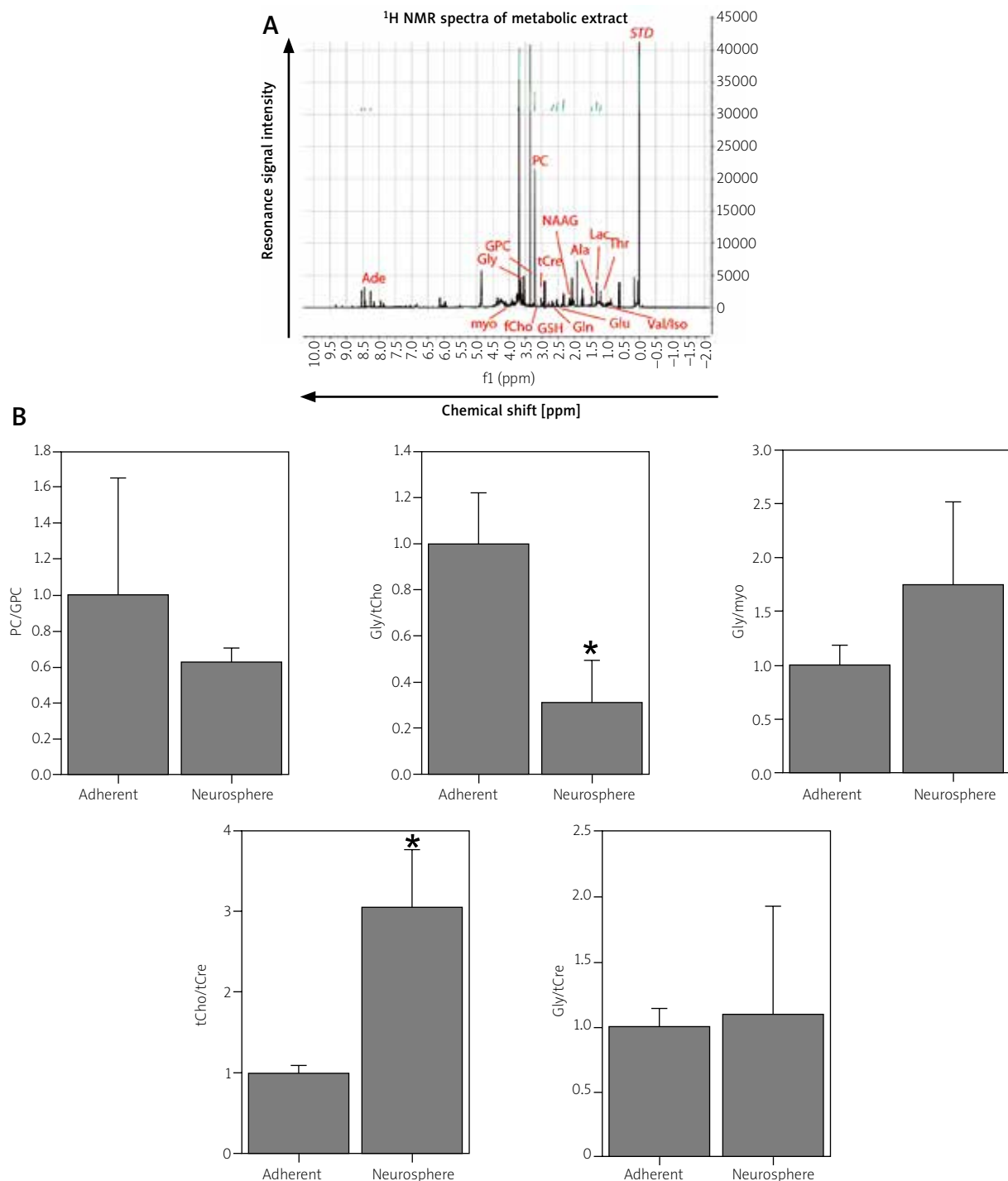
Fig. 1. Global metabolic profiling of U87 glioma cells under adherent and suspension growth: Representative ^{1}H NMR spectra of the intracellular metabolites of U87 glioma cells with annotated adenine (Ade), myo-inositol (myo), glycine (Gly), phosphocholine (PC), glycerophosphocholine (GPC), free choline (fCho), total choline (tCho = fCho + PC + GPC), total creatine (tCre), glutathione (GSH), glutamine (Gln), glutamate (Glu), N-acetylaspartylglutamate (NAAG), alanine (Ala), lactate (Lac), threonine (Thr) as well as valine/iso-leucine (Val/Iso) plus internal concentration standard (STD). **A)** Relative quantification of phosphocholine, glycerophosphocholine, glycine, creatine, and myo-inositol revealed altered metabolism after transfer of U87 cells into neurosphere growth conditions: reduction of PC/GPC and Gly/tCho whereas Gly/myo and tCho/tCre ratios were increased (**B**), $p = 0.05$.
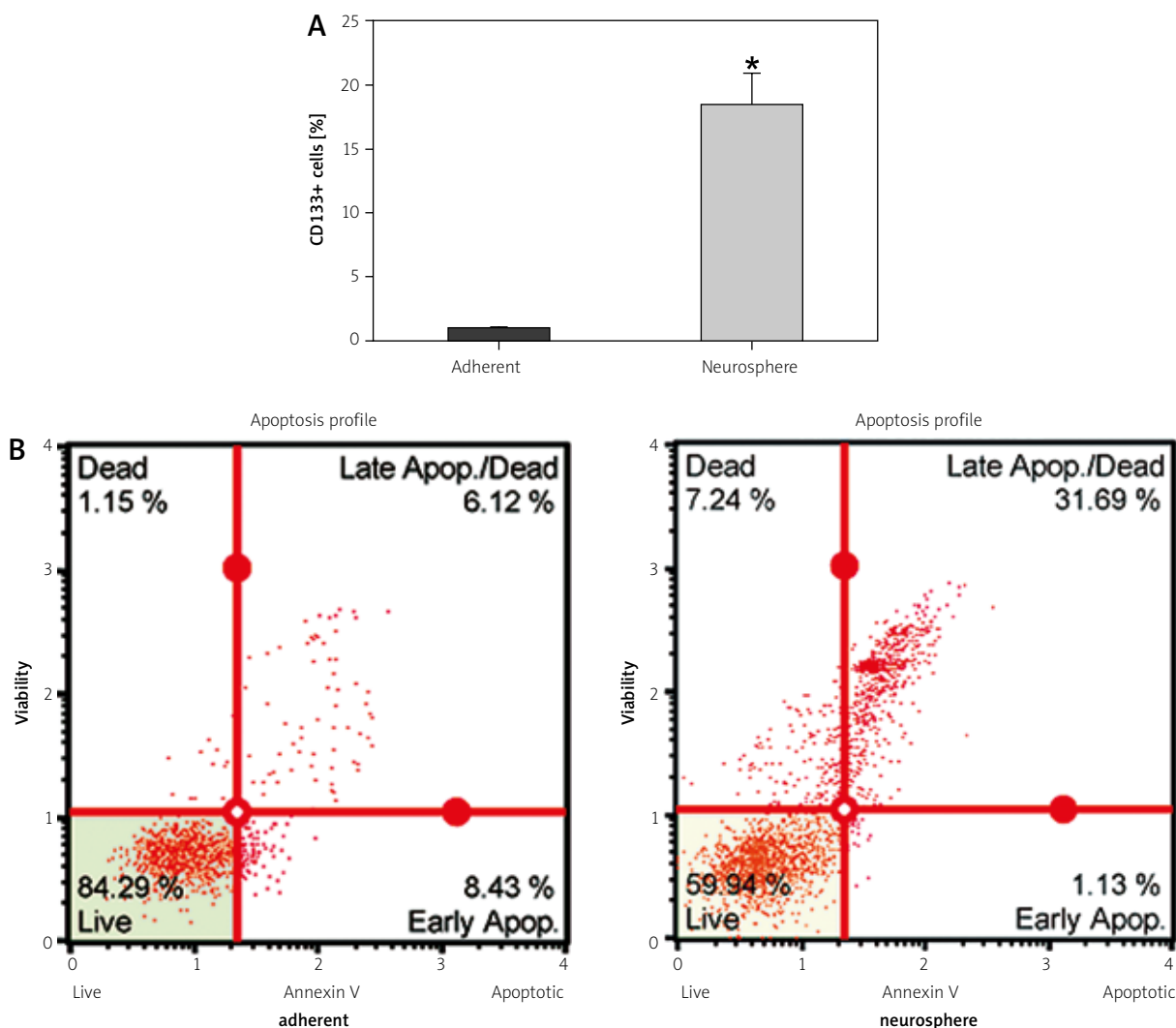
Fig. 2. U87 neurosphere cells compared to monolayer cells show an increased population of cells expressing the cell surface marker CD133 (**A**) (*p*-value ≤ 0.001) and are characterised by a higher number of apoptotic cells (**B**).

tCre ratio is significantly increased in cells cultivated as neurospheres.

Glycine (Gly), a currently intensively studied metabolite with oncogenic potential, has been reported to be directly correlated with glioma malignancy [4]. Hypoxic glioma cells, which are known to contain a population of cells with high stem-like signature [11], are highly susceptible to glycine metabolism [13]. In addition, efforts using ^{1}H-NMR-spectroscopy to grade brain tumour malignancy based on their cellular metabolism suggested glycine as a negative prognostic biomarker [5,17,22]. The Gly/tCre ratio is thought to be a suitable parameter for grading of gliomas and for their distinction from brain metastasis [14]. Interestingly, we did not notice differenc-

es in Gly/tCre between the two growth conditions. Therefore, we performed co-analyses with additional metabolites, including myo-inositol (myo) – a metabolite reported to be reduced in high-grade as compared to low-grade brain tumours [3,19]. We could detect that the Gly/myo ratio, reported to be a valid marker for high-grade gliomas including GBM [22], is increased in suspension cells, indicating either the increase of Gly or the reduction of myo in neurospheres, as compared to adherent cells. An important route for the synthesis of glycine involves the degradation of choline [28]. We therefore sought to compare their relative concentrations in the two culture conditions and found the Gly/tCho ratio significantly diminished (about 75% decrease)

Ulf Dietrich Kahlert, Katharina Koch, Abigail Kora Suwala, Rudolf Hartmann, Menglin Cheng, Donata Maciaczyk, Dieter Willbold, Charles G. Eberhart, Kristine Glunde, Jarek Maciaczyk

in neurosphere cells. The reduction of Gly/tCho could potentially be due to elevated concentrations of tCho in stem-like neurospheres, as increased tCho is an accepted marker for high-grade brain tumour malignancy [27].

Conclusions

In summary, we conclude that switching the cell culture conditions for U87 cells effectively alters their cellular metabolism, influencing a variety of metabolites with reported importance in glioma and glioma stem cell progression. Cells propagated in suspension and adherent growth can dramatically alter their cellular proliferation and apoptosis rate due to alterations in environmental stimuli. We confirm increased apoptosis in U87 neurosphere cells compared to cells grown as a monolayer. We cannot preclude, that the described metabolic differences might, at least partially, be due to the increased cell death.

Therefore, particular caution has to be used interpreting the results of studies on cancer metabolism in the context of the *in vitro* model. As reported here, substantial variations in intracellular levels of metabolites might be a consequence of different culture conditions, precluding the formulation of general conclusions.

Acknowledgements

Disclosure

Authors report no conflict of interest.

References

1. Ahmad M, Frei K, Willscher E, Stefanski A, Kaulich K, Roth P, Stühler K, Reifenberger G, Binder H, Weller M. How stemlike are sphere cultures from long-term cancer cell lines? Lessons from mouse glioma models. J Neuropathol Exp Neurol 2014; 73: 1062-1077.

2. Bianchi L, De Micheli E, Bricolo A, Ballini C, Fattori M, Venturi C, Pedata F, Tipton KF, Della Corte L. Extracellular levels of amino acids and choline in human high grade gliomas: an intraoperative microdialysis study. Neurochem Res 2004; 29: 325-334.

3. Castillo M, Smith JK, Kwock L. Correlation of myo-inositol levels and grading of cerebral astrocytomas. Am J Neuroradiol 2000; 21: 1645-1649.

4. Chinnaiyan P, Kensicki E, Bloom G, Prabhu A, Sarcar B, Kahali S, Eschrich S, Qu X, Forsyth P, Gillies R. The metabolomic signature of malignant glioma reflects accelerated anabolic metabolism. Cancer Res 2012; 72: 5878-5888.

5. Choi C, Ganji SK, Madan A, Hulsey KM, An Z, Zhang S, Pinho MC, Deberardinis RJ, Bachoo RM, Maher EA. In vivo detection of citrate in brain tumors by (1) H magnetic resonance spectroscopy at 3T. Magn Reson Med Off J Soc Magn Reson Med Soc Magn Reson Med 2014; 72: 316-323.

6. Christensen K, Aaberg-Jessen C, Andersen C, Goplen D, Bjerkvig R, Kristensen BW. Immunohistochemical expression of stem cell, endothelial cell, and chemosensitivity markers in primary glioma spheroids cultured in serum-containing and serum-free medium. Neurosurgery 2010; 66: 933-947.

7. Glunde K, Bhujwalla ZM, Ronen SM. Choline metabolism in malignant transformation. Nat Rev Cancer 2011; 11: 835-848.

8. Glunde K, Jie C, Bhujwalla ZM. Molecular causes of the aberrant choline phospholipid metabolism in breast cancer. Cancer Res 2004; 64: 4270-4276.

9. Glunde K, Shah T, Winnard PT, Raman V, Takagi T, Vesuna F, Artemov D, Bhujwalla ZM. Hypoxia regulates choline kinase expression through hypoxia-inducible factor-1 alpha signaling in a human prostate cancer model. Cancer Res 2008; 68: 172-180.

10. Jackowski S. Cell cycle regulation of membrane phospholipid metabolism. J Biol Chem 1996; 271: 20219-20222.

11. Kahlert UD, Maciaczyk D, Dai F, Claus R, Firat E, Doostkam S, Bogiel T, Carro MS, Döbrössy M, Herold-Mende C, Niedermann G, Prinz M, Nikkhah G, Maciaczyk J. Resistance to hypoxia-induced, BNIP3-mediated cell death contributes to an increase in a CD133-positive cell population in human glioblastomas in vitro. J Neuropathol Exp Neurol 2012; 71: 1086-1099.

12. Kahlert UD, Maciaczyk D, Doostkam S, Orr BA, Simons B, Bogiel T, Reithmeier T, Prinz M, Schubert J, Niedermann G, Brabletz T, Eberhart CG, Nikkhah G, Maciaczyk J. Activation of canonical WNT/β–catenin signaling enhances in vitro motility of glioblastoma cells by activation of ZEB1 and other activators of epithelial-to-mesenchymal transition. Cancer Lett 2012; 325: 42-53.

13. Kim D, Fiske BP, Birsoy K, Freinkman E, Kami K, Possemato RL, Chudnovsky Y, Pacold ME, Chen WW, Cantor JR, Shelton LM, Gui DY, Kwon M, Ramkissoon SH, Ligon KL, Kang SW, Snuderl M, Vander Heiden MG, Sabatini DM. SHMT2 drives glioma cell survival in ischaemia but imposes a dependence on glycine clearance. Nature 2015; 520: 363-367.

14. Kinoshita Y, Kajiwara H, Yokota A, Koga Y. Proton magnetic resonance spectroscopy of astrocytic tumors: an in vitro study. Neurol Med Chir (Tokyo) 1993; 33: 350-359.

15. Li Z. CD133: a stem cell biomarker and beyond. Exp Hematol Oncol 2013; 2: 17.

16. Liao CL, Herman MM, Bensch KG. Prolongation of G1 and S phase in C-6 glioma cells treated with maple syrup urine disease metabolits. Morphologic and cell cycle studies. Lab Investig J Tech Methods Pathol 1978; 38: 122-133.

17. Maudsley AA, Gupta RK, Stoyanova R, Parra NA, Roy B, Sheriff S, Hussain N, Behari S. Mapping of glycine distributions in gliomas. AJNR Am J Neuroradiol 2014; 35 (6 Suppl): S31-36.

18. McKnight TR, Smith KJ, Chu PW, Chiu KS, Cloyd CP, Chang SM, Phillips JJ, Berger MS. Choline metabolism, proliferation, and angiogenesis in nonenhancing grades 2 and 3 astrocytoma. J Magn Reson Imaging 2011; 33: 808-816.

19. Metwally LIA, El-din SE, Abdelaziz O, Hamdy IM, Elsamman AK, Abdelalim AM. Predicting grade of cerebral gliomas using Myo-inositol/Creatine ratio. Egypt J Radiol Nucl Med 2014; 45: 211-217.

20. Ott D, Hennig J, Ernst T. Human brain tumors: assessment with in vivo proton MR spectroscopy. Radiology 1993; 186: 745-752.

21. Platet N, Liu SY, Atifi ME, Oliver L, Vallette FM, Berger F, Wion D. Influence of oxygen tension on CD133 phenotype in human glioma cell cultures. Cancer Lett 2007; 258: 286-290.

22. Righi V, Andronesi OC, Mintzopoulos D, Black PM, Tzika AA. High-resolution magic angle spinning magnetic resonance spectroscopy detects glycine as a biomarker in brain tumors. Int J Oncol 2010; 36: 301-306.

23. Sabatier J, Gilard V, Malet-Martino M, Ranjeva JP, Terral C, Breil S, Delisle MB, Manelfe C, Tremoulet M, Berry I. Characterization of choline compounds with in vitro 1H magnetic resonance spectroscopy for the discrimination of primary brain tumors. Invest Radiol 1999; 34: 230-235.

24. Segebarth CM, Balériaux DF, Luyten PR, den Hollander JA. Detection of metabolic heterogeneity of human intracranial tumors in vivo by 1H NMR spectroscopic imaging. Magn Reson Med 1990; 13: 62-76.

25. Shao W, Gu J, Huang C, Liu D, Huang H, Huang Z, Lin Z, Yang W, Liu K, Lin D, Ji T. Malignancy-associated metabolic profiling of human glioma cell lines using 1H NMR spectroscopy. Mol Cancer 2014; 13: 197.

26. Stupp R, Mason WP, van den Bent MJ, Weller M, Fisher B, Taphoorn MJ, Belanger K, Brandes AA, Marosi C, Bogdahn U, Curschmann J, Janzer RC, Ludwin SK, Gorlia T, Allgeier A, Lacombe D, Cairncross JG, Eisenhauer E, Mirimanoff RO; European Organisation for Research and Treatment of Cancer Brain Tumor and Radiotherapy Groups; National Cancer Institute of Canada Clinical Trials Group. Radiotherapy plus concomitant and adjuvant temozolomide for glioblastoma. N Engl J Med 2005; 352: 987-996.

27. Tedeschi G, Lundbom N, Raman R, Bonavita S, Duyn JH, Alger JR, Di Chiro G. Increased choline signal coinciding with malignant degeneration of cerebral gliomas: a serial proton magnetic resonance spectroscopy imaging study. J Neurosurg 1997; 87: 516-524.

28. Wang W, Wu Z, Dai Z, Yang Y, Wang J, Wu G. Glycine metabolism in animals and humans: implications for nutrition and health. Amino Acids 2013; 45: 463-477.

29. De Witt Hamer PC, Van Tilborg AA, Eijk PP, Sminia P, Troost D, Van Noorden CJ, Ylstra B, Leenstra S. The genomic profile of human malignant glioma is altered early in primary cell culture and preserved in spheroid spectras s. Oncogene 2008; 27: 2091-2096.

30. Witusik-Perkowska M, Rieske P, Hułas-Bigoszewska K, Zakrzewska M, Stawski R, Kulczycka-Wojdala D, Bieńkowski M, Stoczyńska-Fidelus E, Grešner SM, Piaskowski S, Jaskólski DJ, Papierz W, Zakrzewski K, Kolasa M, Ironside JW, Liberski PP. Glioblastoma-derived spheroid cultures as an experimental model for analysis of EGFR anomalies. J Neurooncol 2011; 102: 395-407.

http://rcin.org.pl

Ciliary neurotrophic factor protects SH-SY5Y neuroblastoma cells against Aβ$_{1-42}$-induced neurotoxicity via activating the JAK2/STAT3 axis

Ke Wang[1], Minhao Xie[1], Ling Zhu[2], Xue Zhu[1], Kai Zhang[1], Fanfan Zhou[3]

[1]Key Laboratory of Nuclear Medicine, Ministry of Health, Jiangsu Key Laboratory of Molecular Nuclear Medicine, Jiangsu Institute of Nuclear Medicine, Wuxi 214063, Jiangsu Province, China, [2]Save Sight Institute, University of Sydney, NSW 2000, Australia, [3]Faculty of Pharmacy, University of Sydney, NSW 2006, Australia

Abstract

The neurotoxicity of aggregated amyloid beta (Aβ) has been implicated as a critical cause in the pathogenesis of Alzheimer's disease (AD), which leads to neuronal cell damage by inducing oxidative stress and consequently triggering cell apoptosis. Recently, Aβ-dependent inactivation of the Janus tyrosine kinase 2/signal transducer and activator of transcription 3 (JAK2/STAT3) signaling pathway was found to play a critical role in the memory impairment related to AD. Previous research indicated that JAK2/STAT3 axis inactivation might be the result of aberrant reactive oxygen species (ROS) generation induced by Aβ in neurons. As the JAK2/STAT3 axis is a major transducer of ciliary neurotrophic factor (CNTF)-mediated neuroprotective activity, this study extensively evaluated whether activation of the JAK2/STAT3 axis by CNTF was responsible for the neuroprotective effect of this protein against Aβ$_{1-42}$-induced cytotoxicity, oxidative injury and cell apoptosis in human SH-SY5Y neuroblastoma cells. Our data showed that CNTF could attenuate or restore cell injury induced by Aβ$_{1-42}$ in human SH-SY5Y neuroblastoma cells through activating the JAK2/STAT3 signaling pathway. Furthermore, CNTF strikingly prevented Aβ$_{1-42}$-induced mitochondrial dysfunction and activation of mitogen-activated protein kinases (MAPKs), an effect that could be potently attenuated by the specific JAK2 inhibitor AG490. In summary, this study confirmed the detailed mechanism accounting for CNTF's protective effect against Aβ$_{1-42}$-induced cytotoxic events in human SH-SY5Y neuroblastoma cells – information which might significantly contribute to better understanding of the mechanism of action of CNTF as well as providing a novel target in AD therapy.

Key words: *Alzheimer's disease, Aβ1-42, ciliary neurotrophic factor, JAK2/STAT3.*

Introduction

Alzheimer's disease (AD) is the leading cause of dementia in aging adults, which currently has about 36 million cases worldwide [1,3,14]. Alzheimer's disease causes a large loss in brain weight and volume and affects some brain regions and neuronal populations [24,36]. Although the pathogenesis of AD

Communicating author:

Minhao Xie, Key Laboratory of Nuclear Medicine, Ministry of Health, Jiangsu Key Laboratory of Molecular Nuclear Medicine, Jiangsu Institute of Nuclear Medicine, Wuxi 214063, Jiangsu Province, China, phone: +86-510-85514482; fax: +86-510-85514482, e-mail: nypd0723@gmail.com

remains unclear, the key event appears to be the formation of a peptide known as amyloid beta (Aβ), with two major forms, $A\beta_{1-40}$ and $A\beta_{1-42}$ [2,16,26]. Amyloid β clusters into amyloid plaques on the blood vessels and the outer surface of neurons of the brain, leading to the killing of neurons [10]. The mechanism of Aβ-induced neurotoxicity is inconclusive. New evidence suggests that Aβ-dependent inactivation of the Janus tyrosine kinase 2/signal transducer and activator of transcription 3 (JAK2/STAT3) axis in hippocampal neurons causes cholinergic dysfunction via pre- and post-synaptic mechanisms, which leads to memory impairment related to AD [7,8]. However, intracellular events accounting for the mechanism of this action in neurons remain elusive.

Oxidative stress is the redox state resulting from an imbalance between the generation and detoxification of reactive oxygen species (ROS) [33]. Increased cellular oxidative stress has been implicated in the pathogenesis of several neurodegenerative diseases, including Alzheimer's disease [27]. Aβ peptides are key stimuli of ROS generation, which could infuse into the brain through microdialysis probes and increase ROS production in an NMDA receptor- and nitric oxide-dependent manner [4]. A previous study indicated that aberrant activation of ROS generation might block activation of the JAK2/STAT3 axis in neurons, consequently disrupting the effect of neurotrophic factor and inducing neuronal damage in neurodegenerative diseases [19]. Thus, activation of the JAK2/STAT3 axis might induce a protective effect against oxidative stress induced by Aβ.

The major role of neurotrophic factors (NTFs) in synapse function along with evidence that synaptic failure is a critical early event in AD has put NTFs at the forefront of neuroprotective strategies for AD [32]. Ciliary neurotrophic factor (CNTF), a classic member of the NTFs, was first described as a growth factor that supports survival of chick ciliary ganglion neurons. Later, it was shown to be an important factor in the central and peripheral neurons of the nervous system [30]. CNTF binds to its α-receptor and two signal-transducing transmembrane subunits, LIFRβ and gp130, specifically activating the JAK2/STAT3 signaling pathway and thus preventing neuron death and facilitating axonal regeneration after nerve injury [4,28]. The neuroprotective effect of CNTF in AD has been previously reported; it might be mediated through modulating brain plasticity by promoting neurogenesis [12]. However, the precise cellular and molecular mechanisms underpinning such a neuroprotective effect remain far from clear.

In this study, we aimed to elucidate the role of the JAK2/STAT3 axis during the neuroprotective effect of CNTF against $A\beta_{1-42}$-induced oxidative injury in human SH-SY5Y neuroblastoma cells, which has been widely used as a typical model for AD [17,38]. Furthermore, we also elucidated the molecular events of both the upstream and downstream signaling pathways involved in this cellular process.

Material and methods

Materials and chemicals

Recombinant human CNTF was produced in *Escherichia coli* by our laboratory [37]. All cell culture reagents were purchased from Gibco (NY, USA). $A\beta_{1-42}$, AG490, 3-(4,5-dimethylthiazol-2-yl)-2,5-diphenyltetrazolium bromide (MTT) and 2, 7-dichlorodihydrofluorescein diacetate (DCFH-DA) were purchased from Sigma-Aldrich (MO, USA). The Annexin V-FITC and PI double staining kit was obtained from BD Biosciences (CA, USA). Dimethyl sulfoxide (DMSO), RNase A, PVDF membranes and the enhanced chemiluminescence (ECL) detection kit were purchased from Beyotime (Nantong, China). Antibodies against Bcl-2, Bcl-xL and β-actin were obtained from Santa Cruz Biotechnology (CA, USA). Antibodies against JAK2, STAT3, phospho-JAK2, phospho-STAT3, JNK, ERK, p38, phospho-JNK, phospho-ERK and phospho-p38 were purchased from Abcam (MA, USA). Caspase-3 and caspase-9 fluorometric assay kits were obtained from BioVision (SF, USA). All other chemicals and reagents were of analytical grade.

Cell culture and treatment

The human neuroblastoma cell line (SH-SY5Y) was obtained from Shanghai Institute of Cell Biology, Chinese Academy of Sciences (Shanghai, China). SH-SY5Y cells were cultured in flasks at 37°C under an atmosphere of 5% CO_2/95% air in Dulbecco's Modified Eagle Medium (DMEM) supplemented with 10% fetal bovine serum (FBS) and 1% penicillin-streptomycin. Before the experiments, $A\beta_{1-42}$ peptide was diluted to the desired concentrations and maintained for 3 days at 37°C for oligomerization. For the experiments, the cells were detached, re-seeded on plates and then incubated with or without drugs for the indicated time.

http://rcin.org.pl

Ke Wang, Minhao Xie, Ling Zhu, Xue Zhu, Kai Zhang, Fanfan Zhou

Cell growth assay

Cell proliferation was measured by the MTT assay as described before [22,43]. Briefly, 10 µl of MTT stock solution (5 mg/ml) was added to each well and incubated for 4 h at 37°C. The culture medium was then removed and 100 µl of DMSO was added to dissolve the formazan crystals. After mixing, absorbance was measured at 570 nm with an ELISA reader (Bio-Rad, CA, USA). Cell viability was also analyzed by the trypan blue exclusion assay. After treatment with the indicated drugs, cells were washed with phosphate buffer saline (PBS) twice at the end of the incubation period and trypsinized. The cells were re-suspended and subjected to trypan blue staining and then cell counting. Cell viability was expressed as a percentage value in relation to that of the control.

Cell apoptosis assay

Apoptosis of cells was examined by double staining with Annexin V-FITC and PI. After treatment, cells were washed twice with ice-cold PBS and re-suspended in 300 µl of binding buffer (Annexin V-FITC kit, Becton-Dickinson, CA, USA) containing 10 µl of Annexin V-FITC stock and 10 µl of PI. After 15 min incubation at room temperature in the dark, the samples were analyzed by flow cytometry. The Annexin V$^+$/PI$^-$ cells were considered as apoptotic cells, the percentage of which was calculated by CellQuest software (Becton-Dickinson, CA, USA).

Reactive oxygen species detection

Reactive oxygen species (ROS) production was measured by flow cytometry using DCFH-DA staining. DCFH-DA is cleaved intracellularly by nonspecific esterases and transforms to highly fluorescent 2',7'-dichlorofluorescein (DCF) in the presence of ROS. Briefly, after treatment, the cells were incubated with DCFH-DA (20 µM) for 30 min at 37°C in the dark. After washing twice with PBS, the fluorescence intensity was measured by the microplate reader (Molecular Devices, CA, USA) at an excitation wavelength of 485 nm and an emission wavelength of 538 nm. The level of ROS was expressed as a percentage value in relation to the control.

Western blot analysis

The treated cells were collected and lysed in ice-cold RIPA buffer (50 mM Tris-HCl, 150 mM NaCl,

1 mM ethylene glycol tetraacetic acid (EGTA), 1 mM ethylene diamine tetraacetic acid (EDTA), 20 mM NaF, 100 mM Na_3VO_4, 1% Nonidet P-40 (NP-40), 1% Triton X-100, 1 mM phenylmethylsulfonyl fluoride (PMSF), 10 mg/ml aprotinin and 10 mg/ml leupeptin) for 30 min. After centrifugation, protein concentration was determined by the Bradford method [21]. Cell lysates were separated by electrophoresis on 15% SDS-polyacrylamide gel (SDS-PAGE) and transferred onto PVDF membrane. After blocking with 5% bovine serum albumin (BSA) in the mixture of Tris-buffered saline and Tween-20 (TBST) for 1 h, membranes were incubated with primary antibody (diluted in 1 : 500) overnight and followed by incubation with secondary antibody (diluted in 1 : 1000) for 1 h at room temperature. Protein bands were visualized using the ECL assay kit (Beyotime, Nantong, China). The density of each band was normalized to the expression of β-actin.

Caspase activity assay

Caspase activity was assessed by fluorometric assay [38]. Cells were collected and lysed in caspase assay buffer containing 50 mM Tris-HCl (pH 7.4), 1 mM EDTA, 10 mM EGTA, 10 mM digitonin and 2 mM dithiothreitol (DTT). Protein was separated by centrifugation, the concentration of which was determined as previously described [21]. An equal amount of protein from each sample was incubated with caspase-3 substrate DEVD-AFC or caspase-9 substrate LEHD-AFC for 30 min at 37°C. The caspase activity was assessed by a spectrofluorometer (Molecular Devices, CA, USA) with an excitation wavelength of 400 nm and an emission wavelength of 505 nm.

Statistical analysis

Biostatistical analyses were conducted with the Prism 5.0 and SPSS 16.0 software packages. Data were represented as mean ± SEM. Comparisons between experimental and control groups were performed by one-way ANOVA and differences were considered to be statistically significant when p value was less than 0.05.

Results

CNTF induces JAK2/STAT3 activation in Aβ$_{1-42}$-treated SH-SY5Y cells

It is known that CNTF prevents neuronal cell death and facilitates axonal regeneration after nerve injury

http://rcin.org.pl
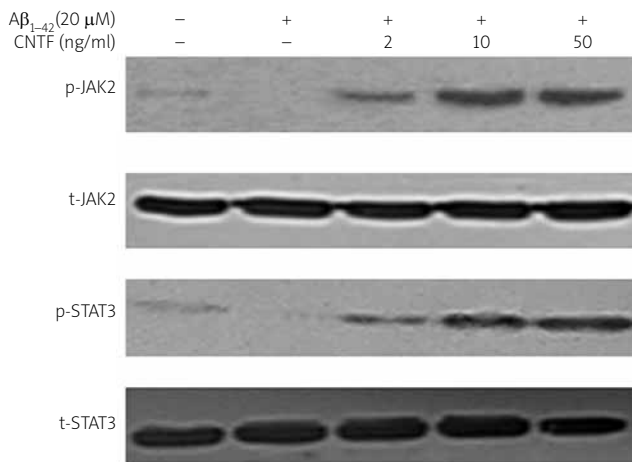
Fig. 1. The effect of CNTF on JAK2/STAT3 pathway activation in $A\beta_{1-42}$-treated SH-SY5Y cells. Cells were pretreated with or without $A\beta_{1-42}$ (20 μM) for 24 h and then exposed to the indicated concentrations of CNTF (2, 10, 50 ng/ml) for another 2 h. After treatment, the phosphorylation of JAK2 and STAT3 was evaluated by western blotting.

directly via activating the JAK2/STAT3 signaling pathway [28]. To test whether JAK2/STAT3 pathway was activated by CNTF in $A\beta_{1-42}$-treated human SH-SY5Y neuroblastoma cells, cells were pre-incubated with $A\beta_{1-42}$ (20 μM) for 24 h and then exposed to the indicated concentrations of CNTF (0, 2, 10, 50 ng/ml) for another 2 h. As shown in Fig. 1, treatment with $A\beta_{1-42}$ alone could inactivate the JAK2/STAT3 pathway, whereas co-treatment with CNTF significantly stimulated the phosphorylation of JAK2 and STAT3 in a dose-dependent manner. Our data indicated that CNTF potently induced the activation of the JAK2/STAT3 pathway in $A\beta_{1-42}$-treated human SH-SY5Y neuroblastoma cells.

CNTF protects SH-SY5Y cells from $A\beta_{1-42}$-induced cytotoxicity

$A\beta_{1-42}$ impairing neuronal cells has been considered as one of the major causes of AD [31]; therefore, in this study, $A\beta_{1-42}$ was employed as a neurotoxicant. The neuroprotective effect of CNTF against $A\beta_{1-42}$-induced cytotoxicity was evaluated as the viability of SH-SY5Y cells using the MTT assay and trypan blue exclusion assay. As shown in Fig. 2, $A\beta_{1-42}$ (20 μM) exhibited a remarkable inhibitory effect on

Fig. 2. The effect of CNTF on $A\beta_{1-42}$-induced cytotoxicity in SH-SY5Y cells. Cells were treated with $A\beta_{1-42}$ (20 μM) in the absence or presence of CNTF (10 ng/ml) and AG490 (10 μM) for 24 h. The viability of SH-SY5Y cells was assessed by MTT assay **(A)** and trypan blue exclusion assay **(B)**. Results are shown as mean ± SEM of three experiments with each including triplicate sets. a: $p < 0.05$ vs. control, b: $p < 0.05$ vs. $A\beta_{1-42}$, c: $p < 0.05$ vs. $A\beta_{1-42}$ + CNTF.

the growth of SH-SY5Y cells. However, this cytotoxic effect was attenuated by co-treatment with CNTF (10 ng/ml). To investigate the involvement of JAK2/STAT3 signaling in the protective effect of CNTF against $A\beta_{1-42}$ induced cytotoxicity, we assessed cell viability with the co-treatment of the JAK2 inhibitor AG490 in the presence of both CNTF and $A\beta_{1-42}$. Our results indicated that the suppressive effect of CNTF on $A\beta_{1-42}$-induced cytotoxicity was significantly diminished in the presence of AG490 in human SH-SY5Y neuroblastoma cells.

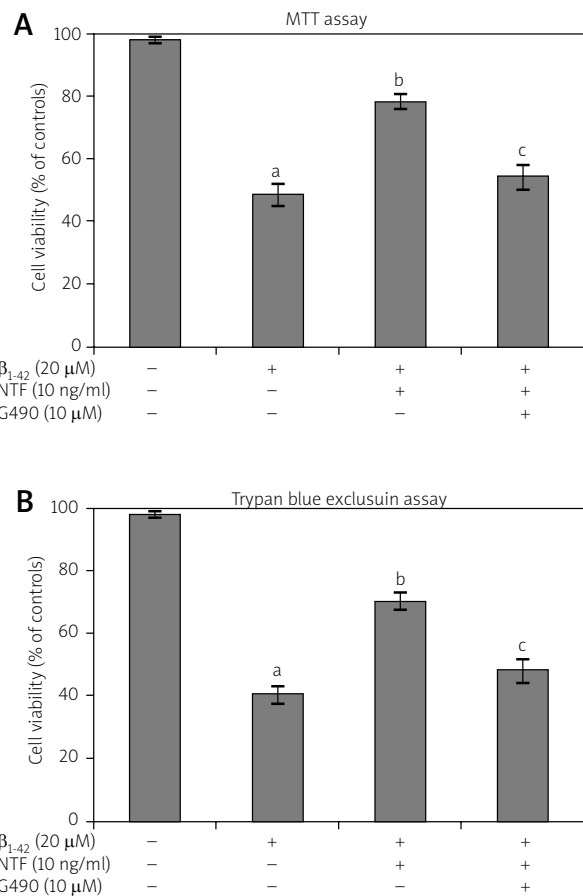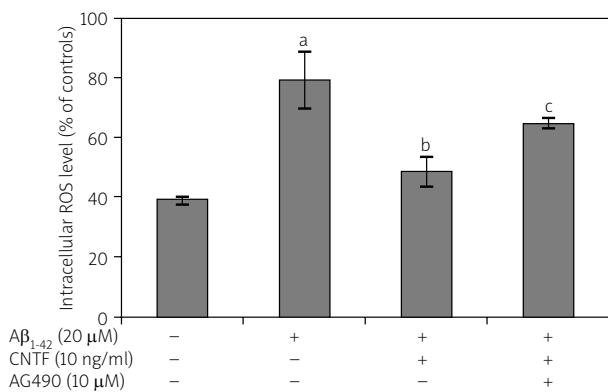**Fig. 3.** The effect of CNTF on $A\beta_{1-42}$-induced oxidative stress in SH-SY5Y cells. Cells were treated with $A\beta_{1-42}$ (20 µM) in the absence or presence of CNTF (10 ng/ml) and AG490 (10 µM) for 6 h. Oxidative stress was assessed as the intracellular ROS level. Results are shown as mean ± SEM of three experiments with each including triplicate sets. a: $p < 0.05$ vs. control, b: $p < 0.05$ vs. $A\beta_{1-42}$, c: $p < 0.05$ vs. $A\beta_{1-42}$ + CNTF.

CNTF protects SH-SY5Y cells from $A\beta_{1-42}$-induced oxidative injury

$A\beta_{1-42}$-induced oxidative stress was considered as crucial to the pathophysiology of AD [6]. In this study, oxidative stress was assessed by measuring the intracellular ROS level using the ROS-sensitive fluorescence probe DCF. As shown in Fig. 3, after exposure to $A\beta_{1-42}$ (20 µM) for 6 h, the intracellular ROS level was significantly increased (198.5% of the control), which suggested induced oxidative stress in SH-SY5Y cells. After co-treatment with CNTF (10 ng/ml), the intracellular ROS level was significantly decreased compared to that of $A\beta_{1-42}$ treatment alone (122.3% of the control). In addition, AG490 inhibited the protective effect of CNTF on $A\beta_{1-42}$-induced oxidative injury in SH-SY5Y cells. Our results suggested that CNTF could prevent $A\beta_{1-42}$-induced oxidative injury in human SH-SY5Y neuroblastoma cells, possibly via activating the JAK2/STAT3 signaling pathway.

CNTF protects SH-SY5Y cells from $A\beta_{1-42}$-induced apoptosis

$A\beta_{1-42}$-induced neuronal apoptosis in the brain and primary neuronal culture might be responsible in part for the cognitive decline found in AD [16].

Apoptosis of SH-SY5Y cells with or without treatment was evaluated by dual-staining with Annexin V-FITC/PI. As shown in Fig. 4, treatment with $A\beta_{1-42}$ (20 µM) remarkably increased the percentage of early apoptotic cells, while co-treatment with CNTF (10 ng/ml) resulted in decreased cell apoptosis from 38.67 ± 6.43% to 11.28 ± 2.62%. The addition of AG490 reversed the protective effect of CNTF, increasing the percentage of apoptosis to 24.77 ± 4.15%. These data suggest that CNTF could prevent $A\beta_{1-42}$-induced cell apoptosis in human SH-SY5Y neuroblastoma cells, an effect which was also closely connected with activation of the JAK2/STAT3 pathway.

CNTF inhibits $A\beta_{1-42}$-induced mitochondrial dysfunction

Mitochondrial dysfunction is an early event of cell apoptosis [39]. Increasing evidence indicates that $A\beta$ induces oxidative injury and neuronal apoptosis through mediating mitochondrial dysfunction [25]. To investigate the effect of CNTF on $A\beta_{1-42}$-induced mitochondrial dysfunction, the expression of anti-apoptotic members (Bcl-xL and Bcl-2) and activity of caspases were assessed, these genes being downstream targets of the JAK2/STAT3 pathway. As shown in Fig. 5, $A\beta_{1-42}$ (20 µM) treatment significantly down-regulated the expression of Bcl-xL and Bcl-2 and up-regulated the activity of initiator caspase-9 and effector caspase-3. However, CNTF (10 ng/ml) co-treatment substantially reversed the regulatory effect of $A\beta_{1-42}$. In addition, AG490 attenuated the protective effect of CNTF on $A\beta_{1-42}$-induced mitochondrial dysfunction in human SH-SY5Y neuroblastoma cells.

CNTF inhibits $A\beta_{1-42}$-induced JNK and ERK activation

Accumulating evidence has suggested that the MAPK signaling pathway plays an important role in neuronal death in AD [42]. $A\beta_{1-42}$-induced oxidative stress influences the decision of susceptible neurons to undergo either apoptosis or proliferation, a process which is likely mediated through the MAPK signaling pathway [34]. In this study, the phosphorylation of JNK, ERK and p38, the most extensively studied vertebrate MAPKs, was assessed by western blot analysis. As shown in Fig. 6, $A\beta_{1-42}$ (20 µM) treatment significantly induced the phosphorylation of JNK and ERK but not p38 (data not shown), an effect that was inhibited by CNTF (10 ng/ml). Again, the
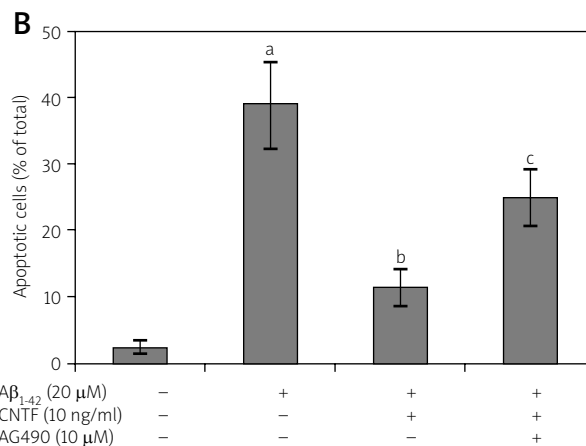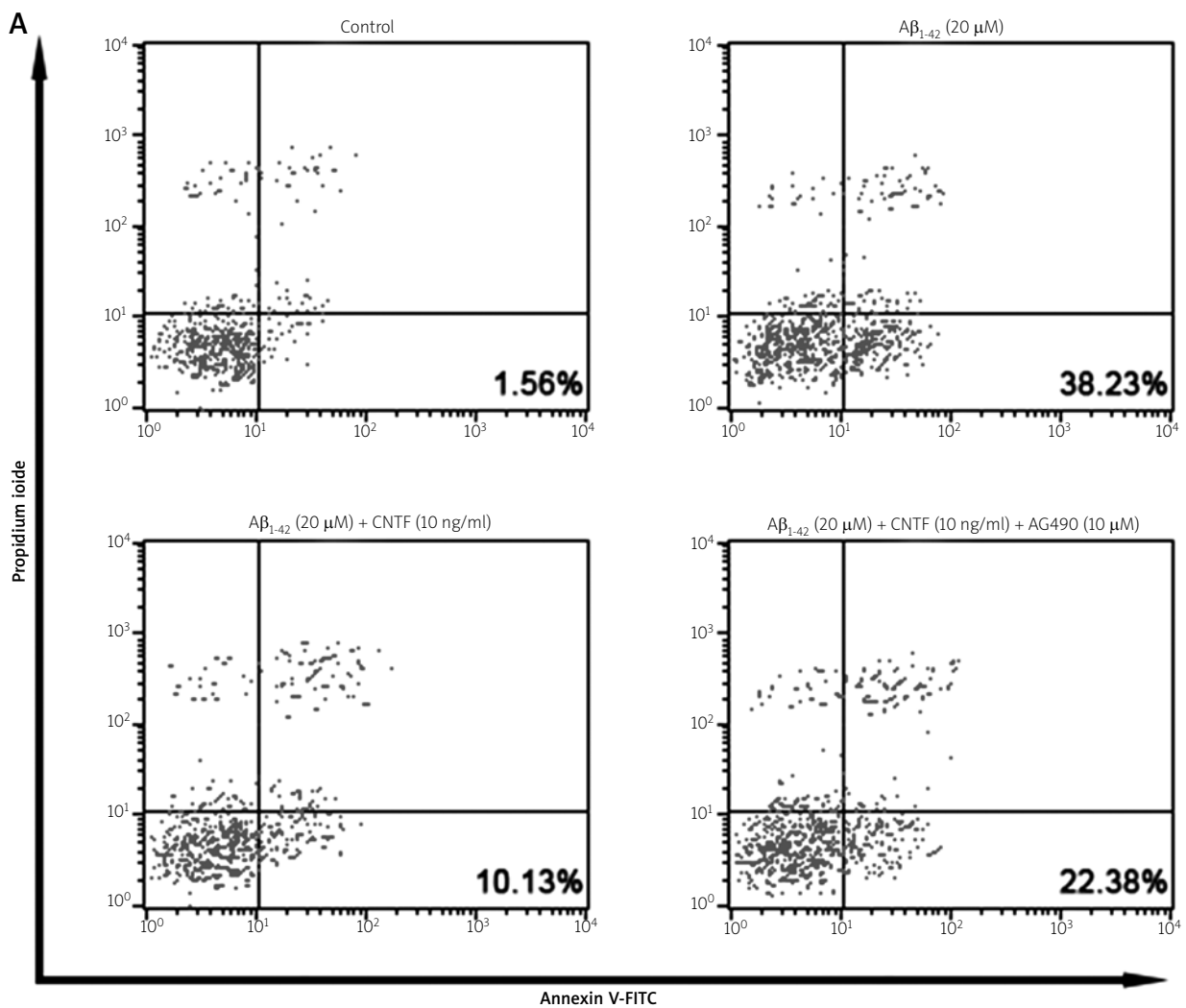
Fig. 4. The effect of CNTF on $A\beta_{1-42}$-induced apoptosis in SH-SY5Y cells. Cells were treated with $A\beta_{1-42}$ (20 μM) in the absence or presence of CNTF (10 ng/ml) and AG490 (10 μM) for 24 h. Cell apoptosis was evaluated by flow cytometry. **(A)** Flow cytometry analysis of cell apoptosis using Annexin V-FITC/PI dual staining. **(B)** Percentage distribution of apoptotic cells. Results are shown as mean ± SEM of three experiments with each including triplicate sets. a: $p < 0.05$ vs. control, b: $p < 0.05$ vs. $A\beta_{1-42}$, c: $p < 0.05$ vs. $A\beta_{1-42}$ + CNTF.

http://rcin.org.pl

Ke Wang, Minhao Xie, Ling Zhu, Xue Zhu, Kai Zhang, Fanfan Zhou

$A\beta_{1-42}$ (20 µM)	–	+	+	+
CNTF (ng/ml)	–	–	+	+
AG490 (10 µM)	–	–	–	+

Bcl-xL

Bcl-2

β-actin
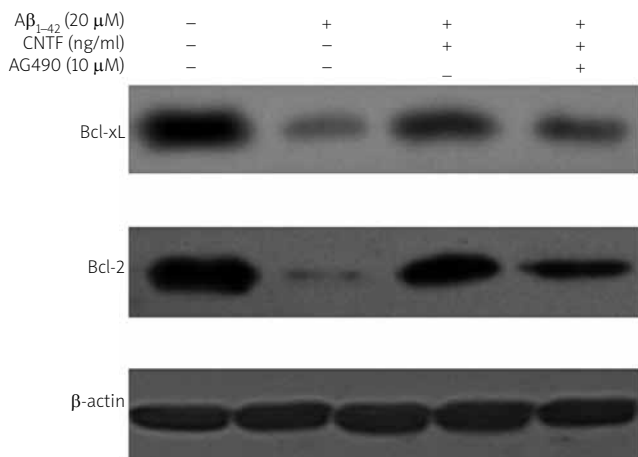
Fig. 5. The effect of CNTF on $A\beta_{1-42}$-induced mitochondrial dysfunction in SH-SY5Y cells. Cells were treated with $A\beta_{1-42}$ (20 µM) in the absence or presence of CNTF (10 ng/ml) and AG490 (10 µM) for 24 h. **(A)** Expression of Bcl-xL and Bcl-2 was assessed by western blotting. **(B)** Activity of caspase-3 and -9 was determined by fluorometric assay. Results are shown as mean ± SEM of three experiments with each including triplicate sets. a: $p < 0.05$ vs. control, b: $p < 0.05$ vs. $A\beta_{1-42}$, c: $p < 0.05$ vs. $A\beta_{1-42}$ + CNTF.

effect of CNTF on $A\beta_{1-42}$-induced JNK and ERK activation was abolished by co-treatment with AG490 in human SH-SY5Y neuroblastoma cells.

Discussion

Alzheimer's disease is the most common neurodegenerative dementia in the elderly, affecting cognition, behavior and functioning due to neuron loss [35]. Neurodegeneration possibly results from the abnormal accumulation of extracellular Aβ; therefore, Aβ is a promising therapeutic target of AD [20]. CNTF is a pleiotropic cytokine with neurotrophic properties for a number of neurons *in vitro* and *in vivo*. It is also one of the most active neurotrophic factors widely studied in promoting neurogenesis [15,23]. Previous studies reported that treatment of CNTF in two AD mice models prevented Aβ oligomer-induced neuronal damage and neurobehavioral impairments [29]; however, the molecular mechanism underpinning this effect was largely unknown. Consistently, we confirmed the protective effect of CNTF on $A\beta_{1-42}$-induced cytotoxicity in human SH-SY5Y neuroblastoma cells in the current study.

$A\beta_{1-42}$ (20 µM)	–	+	+	+
CNTF (ng/ml)	–	–	+	+
AG490 (10 µM)	–	–	–	+

p-JNK

JNK

p-ERK1/2

ERK1/2

β-actin
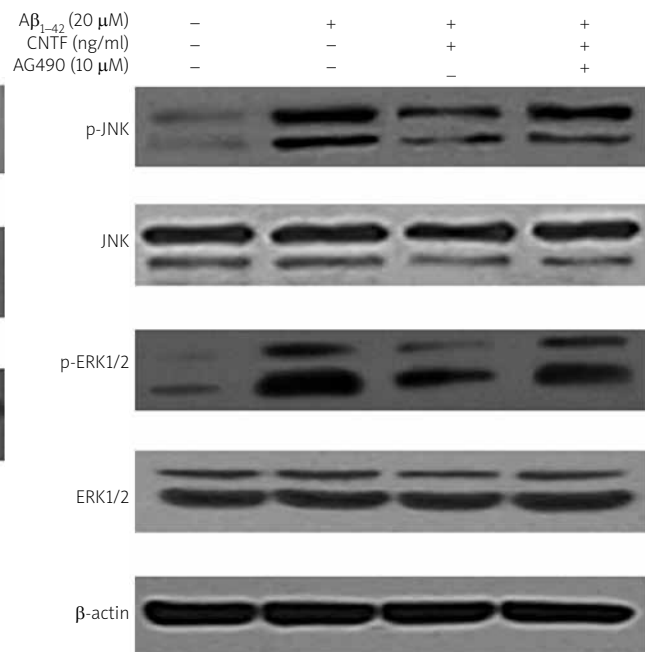
Fig. 6. The effect of CNTF on $A\beta_{1-42}$-induced JNK and ERK activation in SH-SY5Y cells. Cells were treated with $A\beta_{1-42}$ (20 µM) in the absence or presence of CNTF (10 ng/ml) and AG490 (10 µM) for 6 h. Expression of JNK and ERK was assessed by western blotting.

Furthermore, we elucidated the involvement of the critical signaling pathway in the molecular response of CNTF.

CNTF belongs to the IL-6 family of cytokines, signaling of which is mainly mediated through activation of the receptor-associated JAK2/STAT3 pathway [18]. Recent studies have demonstrated that the JAK2/STAT3 pathway is involved in multiple physiological processes of the nervous system [11, 41]. Chiba *et al.* reported that Aβ-dependent inactivation of the JAK2/STAT3 axis could lead to memory loss through cholinergic dysfunction [9]. In the current study, our results demonstrated that the JAK2/STAT3 pathway was inactivated upon the treatment with $A\beta_{1-42}$ in human SH-SY5Y neuroblastoma cells, whereas the further co-treatment with CNTF significantly stimulated the phosphorylation of JAK2 and STAT3 in a dose-dependent manner and protected cells against $A\beta_{1-42}$-induced cytotoxicity. Additionally, the JAK2 inhibitor AG490 largely attenuated the protective effect of CNTF on $A\beta_{1-42}$-induced toxicity in human SH-SY5Y neuroblastoma cells. Our study
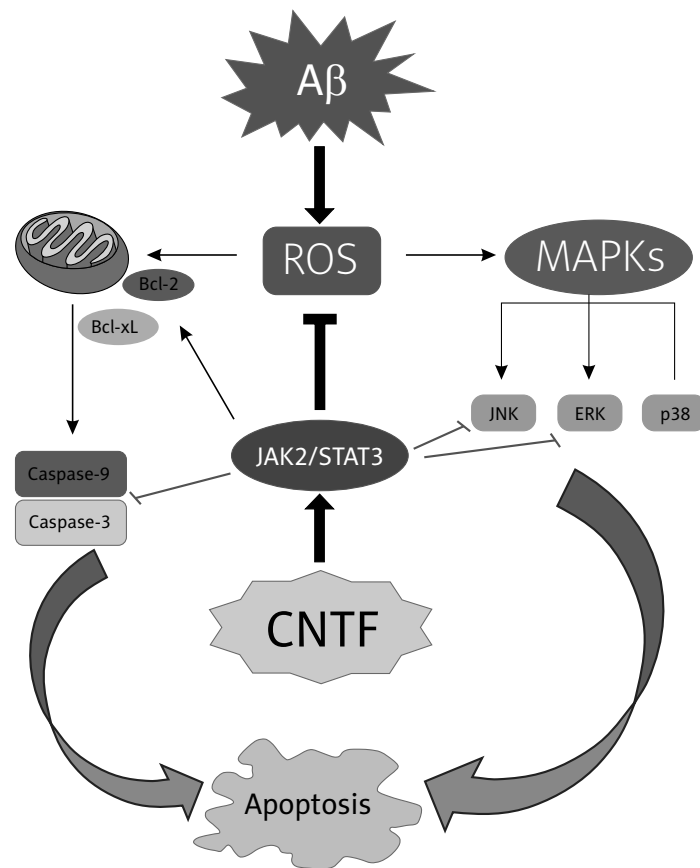
Fig. 7. The proposed model of CNTF neuroprotective effect against $A\beta_{1-42}$-induced cytotoxicity in human SH-SY5Y neuroblastoma cells.

suggested that the JAK2/STAT3 pathway might be the major transducer of CNTF-mediated neuroprotective activity.

Oxidative stress is one of the early events in AD, and is also implicated as an important mediator of the onset, progression and pathogenesis of AD. Several studies have suggested that oxidative stress plays a key role in Aβ-mediated neuronal cytotoxicity by triggering or facilitating neurodegeneration through a wide range of molecular events that eventually lead to neuronal cell loss [6]. In our study, after exposure of SH-SY5Y cells to $A\beta_{1-42}$ for 6 h, the intracellular ROS level was significantly increased; however, co-treatment with CNTF potently inhibited this effect, suggesting that CNTF could prevent $A\beta_{1-42}$-induced oxidative injury in SH-SY5Y cells. Recent studies demonstrated that the JAK2/STAT3 pathway was involved in regulating oxidative stress in certain types of neurons. We also confirmed that activation of the

JAK2/STAT3 pathway was involved in the protective effect of CNTF against $A\beta_{1-42}$-induced oxidative injury.

To further investigate the molecular mechanisms underlying this neuroprotective effect, the ROS-related downstream signaling pathways including the mitochondrial pathway and MAPK cascades were monitored. Zhao *et al.* showed that the JAK2/STAT3 pathway could modulate the expression of anti-apoptotic members (Bcl-xL and Bcl-2) and activity of caspases [40]. Our present study also proved that activation of the JAK2/STAT3 pathway could reverse the decreased expression of Bcl-xL and Bcl-2 as well as activation of caspases induced by $A\beta_{1-42}$ in human SH-SY5Y neuroblastoma cells. Oxidative stress is one of the major stimuli of MAPK cascades, pathways widely involved in apoptotic signal transduction. Ghribi *et al.* reported that administration of $A\beta_{1-42}$ into rabbit brain induced apoptosis accompanied with activation of JNK and ERK, but not p38 [13]. Our study showed that treatment with $A\beta_{1-42}$ significantly induced the phos-

http://rcin.org.pl

Ke Wang, Minhao Xie, Ling Zhu, Xue Zhu, Kai Zhang, Fanfan Zhou

phorylation of JNK and ERK in human SH-SY5Y neu-roblastoma cells, an effect that could be abolished by co-treatment with CNTF. JNK and ERK pathways are also targets of the JAK2/STAT3 axis, and co-treatment with AG490 inhibited the effect of CNTF on $A\beta_{1-42}$-in-duced JNK and ERK activation. Our data suggested that CNTF could inhibit $A\beta_{1-42}$-induced mitochondrial dysfunction and MAPK activation via activating the JAK2/STAT3 pathway in human SH-SY5Y neuroblasto-ma cells.

In conclusion, our study extensively evaluated the protective effect of CNTF against $A\beta_{1-42}$-induced neurotoxicity in human SH-SY5Y neuroblastoma cells. More importantly, we provided evidence that such a neuroprotective effect of CNTF was largely medi-ated through activation of the JAK2/STAT3 signaling pathway (Fig. 7). Our findings might significantly con-tribute to better understanding of the mechanism of action of CNTF and constitute a basis for future devel-opment of neuronal growth factors as potential drugs for the treatment of AD.

Acknowledgements

Disclosure

Authors report no conflict of interest.

References

1. Alzheimer's Association. Alzheimer's Association report. 2013 Alzheimer's disease facts and figures. Alzheimers Dement 2013; 9: 208-245.
2. Armstrong RA. What causes alzheimer's disease? Folia Neuro-pathol 2013; 51: 169-188.
3. Armstrong RA. A critical analysis of the 'amyloid cascade hypothesis'. Folia Neuropathol 2014; 52: 211-225.
4. Bonni A, Frank DA, Schindler C, Greenberg ME. Characteriza-tion of a pathway for ciliary neurotrophic factor signaling to the nucleus. Science 1993; 262: 1575-1579.
5. Butterfield AD. Amyloid β-peptide (1-42)-induced Oxidative Stress and Neurotoxicity: Implications for Neurodegeneration in Alzheimer's Disease Brain. A Review. Free Radic Res 2002; 36: 1307-1313.
6. Butterfield DA, Swomley AM, Sultana R. Amyloid β-peptide (1-42)-induced oxidative stress in Alzheimer disease: Impor-tance in disease pathogenesis and progression. Antioxid Redox Signal 2013; 19: 823-835.
7. Chiba T, Yamada M, Aiso S. Targeting the JAK2/STAT3 axis in Alz-heimer's disease. Expert Opin Ther Targets 2009; 10: 1155-1167
8. Chiba T, Yamada M, Sasabe J, Terashita K, Shimoda M, Mat-suoka M, Aiso S. Amyloid-β causes memory impairment by disturbing the JAK2/STAT3 axis in hippocampal neurons. Mol Psychiatry 2008; 14: 206-222.
9. Chiba T, Yamada M, Sasabe J, Terashita K, Shimoda M, Mat-suoka M, Aiso S. Amyloid-β causes memory impairment by disturbing the JAK2/STAT3 axis in hippocampal neurons. Mol Psychiatry 2009; 14: 206-222.
10. Crews L, Masliah E. Molecular mechanisms of neurodegenera-tion in Alzheimer's disease. Hum Mol Genet 2010; 19: R12-R20.
11. Dominguez E, Rivat C, Pommier B, Mauborgne A, Pohl M. JAK/STAT3 pathway is activated in spinal cord microglia after peripheral nerve injury and contributes to neuropathic pain development in rat. J Neurochem 2008; 107: 50-60.
12. Garcia P, Youssef I, Utvik JK, Florent-Béchard S, Barthélémy V, Malaplate-Armand C, Kriem B, Stenger C, Koziel V, Olivier J-L. Ciliary neurotrophic factor cell-based delivery prevents synap-tic impairment and improves memory in mouse models of Alz-heimer's disease.J Neurosci 2010; 30: 7516-7527.
13. Ghribi O, Prammonjago P, Herman MM, Spaulding NK, Savory J. Aβ (1–42)-induced JNK and ERK activation in rabbit hippocam-pus is differentially regulated by lithium but is not involved in the phosphorylation of tau. Mol Brain Res 2003; 119: 201-206.
14. Hampel H, Prvulovic D, Teipel S, Jessen F, Luckhaus C, Frölich L, Riepe MW, Dodel R, Leyhe T, Bertram L. The future of Alz-heimer's disease: the next 10 years. Prog Neurobiol 2011; 95: 718-728.
15. Ip N, Li Y, Van de Stadt I, Panayotatos N, Alderson R, Lindsay R. Ciliary neurotrophic factor enhances neuronal survival in embryonic rat hippocampal cultures. J Neurosci 1991; 11: 3124-3134.
16. Ittner LM, Götz J. Amyloid-β and tau – a toxic pas de deux in Alzheimer's disease. Nat Rev Neurosci 2011; 12: 67-72.
17. Jämsä A, Hasslund K, Cowburn RF, Bäckström A, Vasänge M. The retinoic acid and brain-derived neurotrophic factor dif-ferentiated SH-SY5Y cell line as a model for Alzheimer's dis-ease-like tau phosphorylation. Biochem Biophys Res Commun 2004; 319: 993-1000.
18. Kaur N, Kim IJ, Higgins D, Halvorsen SW. Induction of an inter-feron-gamma Stat3 response in nerve cells by pre-treatment with gp130 cytokines. J Neurochem 2003; 87: 437-447.
19. Kaur N, Lu B, Ward S, Halvorsen S. Inducers of oxidative stress block ciliary neurotrophic factor activation of Jak/STAT signal-ing in neurons. J Neurochem 2005; 92: 1521-1530.
20. Klein WL, Krafft GA, Finch CE. Targeting small Aβ oligomers: the solution to an Alzheimer's disease conundrum? Trends Neuro-sci 2001; 24: 219-224.
21. Kruger NJ. The Bradford method for protein quantitation. Methods Mol Biol 1994; 32: 9-15.
22. Li J, Ji X, Zhang J, Shi G, Zhu X, Wang K. Paeoniflorin attenuates Abeta25-35-induced neurotoxicity in PC12 cells by preventing mitochondrial dysfunction. Folia Neuropathol 2014; 52: 285-290.

23. Li P, Wang Z, Yan J, Li Z, Jiang C, Ni X, Yang Y, Liu F, Lu C. Neuro-protective effects of CNTF on hippocampal neurons via an unknown signal transduction pathway. Chin Sci Bull 2006; 51: 48-53.

24. Mavroudis IA, Manani MG, Petrides F, Petsoglou C, Njau SN, Costa VG, Baloyannis SJ. Dendritic and spinal alterations of neurons from Edinger-Westphal nucleus in Alzheimer's disease. Folia Neuropathol 2014; 52: 197-204.

25. Onyango IG, Khan SM. Oxidative Stress, Mitochondrial Dysfunction, and Stress Signaling in Alzheimers Disease. Curr Alzheimer Res 2006; 3: 339-349.

26. Palop JJ, Mucke L. Amyloid-[beta]-induced neuronal dysfunction in Alzheimer's disease: from synapses toward neural networks. Nat Neurosci 2010; 13: 812-818.

27. Perry G, Cash AD, Smith MA. Alzheimer disease and oxidative stress. J BioMed Biotechnol 2002; 2: 120-123.

28. Peterson WM, Wang Q, Tzekova R, Wiegand SJ. Ciliary neurotrophic factor and stress stimuli activate the Jak-STAT pathway in retinal neurons and glia. J Neurosci 2000; 20: 4081-4090.

29. Qu HY, Zhang T, Li XL, Zhou JP, Zhao BQ, Li Q, Sun MJ. Transducible P11-CNTF rescues the learning and memory impairments induced by amyloid-beta peptide in mice. Eur J Pharmacol 2008; 594: 93-100.

30. Richardson P. Ciliary neurotrophic factor: a review. Pharmacol Ther 1994; 63: 187-198.

31. Roher AE, Lowenson JD, Clarke S, Woods AS, Cotter RJ, Gowing E, Ball MJ. Beta-amyloid-(1-42) is a major component of cerebrovascular amyloid deposits: implications for the pathology of Alzheimer disease. Proc Nat Acad Sci USA 1993; 90: 10836-10840.

32. Schindowski K, Belarbi K, Buee L. Neurotrophic factors in Alzheimer's disease: role of axonal transport. Genes Brain Behav 2008; 7: 43-56.

33. Sies H. Oxidative stress. Academic Press, London 1985.

34. Son Y, Cheong Y-K, Kim N-H, Chung H-T, Kang DG, Pae H-O. Mitogen-activated protein kinases and reactive oxygen species: how can ROS activate MAPK pathways? J Signal Transduct 2011; 2011:792639.

35. Sonkusare S, Kaul C, Ramarao P. Dementia of Alzheimer's disease and other neurodegenerative disorders – memantine, a new hope. Pharmacol Res 2005; 51: 1-17.

36. Sperling RA, Dickerson BC, Pihlajamaki M, Vannini P, LaViolette PS, Vitolo OV, Hedden T, Becker JA, Rentz DM, Selkoe DJ. Functional alterations in memory networks in early Alzheimer's disease. Neuromolecular Med 2010; 12: 27-43.

37. Wang K, Zhou F, Zhu L, Zhu X, Zhang K, Zhu L. High level soluble expression, purification, and characterization of human ciliary neuronotrophic factor in Escherichia coli by single protein production system. Protein Expr Purif 2014; 96: 8-13.

38. Wang K, Zhu L, Zhu X, Zhang K, Huang B, Zhang J, Zhang Y, Zhu L, Zhou B, Zhou F. Protective Effect of Paeoniflorin on Aβ25–35-Induced SH-SY5Y Cell Injury by Preventing Mitochondrial Dysfunction. Cell Mol Neurobiol 2014; 34: 227-234.

39. Wang X. The expanding role of mitochondria in apoptosis. Genes Dev 2001; 15:2922-2933.

40. Zhao J, Li G, Zhang Y, Su X, Hang C. The potential role of JAK2/STAT3 pathway on the anti-apoptotic effect of recombinant human erythropoietin (rhEPO) after experimental traumatic brain injury of rats. Cytokine 2011; 56: 343-350.

41. Zhong Z, Wen Z, Darnell J. Stat3: a STAT family member activated by tyrosine phosphorylation in response to epidermal growth factor and interleukin-6. Science 1994; 264: 95-98.

42. Zhu X, Lee H-G, Raina AK, Perry G, Smith MA. The role of mitogen-activated protein kinase pathways in Alzheimer's disease. Neurosignals 2002; 11: 270-281.

43. Zhu X, Wang K, Zhang K, Zhu L, Zhou F. Ziyuglycoside II induces cell cycle arrest and apoptosis through activation of ROS/JNK pathway in human breast cancer cells. Toxicol Lett 2014; 227: 65-73.

http://rcin.org.pl

Folia
Neuropathologica

MicroRNA-210 regulates cell proliferation and apoptosis by targeting regulator of differentiation 1 in glioblastoma cells

Shuai Zhang[1], Niansheng Lai[2], Keman Liao[1], Jun Sun[1], Yuchang Lin[1]

[1]Department of Neurosurgery, Wuxi Second Hospital Affiliated to Nanjing Medical University, Wuxi City, [2]Department of Neurosurgery, the First Affiliated Hospital of Wannan Medical College, Wuhu, China

Abstract

MicroRNAs (miRNAs) are small noncoding RNAs that negatively regulate protein biosynthesis and participate in the pathogenesis of various tumours. Previous studies have shown that miR-210 is highly expressed in different types of human cancers, including glioblastoma multiforme (GBM). However, the role that miR-210 plays in GBM remains unclear. Here, we detected the expression and examined the function of miRNA-210 in GBM cells. Furthermore, we investigated the possible molecular mechanisms by which miRNA-210 mediates cell proliferation and apoptosis. Fifteen GBM and five normal brain tissues, in addition to the U87MG and U251 GBM cell lines, were analysed in this study. We found that miR-210 was upregulated in GBM tissues and cell lines when compared to normal brain tissue. Cell counting and flow cytometric assay results demonstrated that upregulation of miR-210 induced cell proliferation and decreased cell apoptosis, respectively. In addition, downregulation of miR-210 inhibited cell proliferation and induced apoptosis. We also detected a miR-210 target, regulator of differentiation 1 (ROD1), which is involved in GBM progression. Knockdown of ROD1 reversed the growth arrest and apoptosis that were originally induced by miR-210 inhibition. We propose that miR-210 regulates cell proliferation and apoptosis in GBM cells by targeting ROD1. Our findings may provide a new potential therapeutic target for the treatment of GBM.

Key words: microRNA-210, glioblastoma, ROD1, proliferation, apoptosis.

Introduction

Glioblastoma multiforme (GBM) is the most common malignant brain tumour, accounting for 45.2% of all central nervous system tumours. Glioblastoma multiforme often infiltrates diffusely into normal tissue, making it difficult to completely eliminate via traditional surgery and radiotherapy. This leads to a poor outcome, with a five-year survival rate of less than 5% and an average survival time of only 10-14 months post-diagnosis [11,16]. Hence, it is import-

ant to determine the mechanisms involved in the development of GBM and find more effective therapies to treat this deadly disease.

Research examining microRNAs (miRNAs) has grown exponentially since they were first discovered in 1993. MicroRNAs are non-coding RNAs that are 18-25 nucleotides in length, and they represent 1% to 2% of the eukaryotic transcriptome [2]. MiRNAs can lead to translational repression and/or mRNA degradation of their targets. Many miRNAs have

been reported to be correlated with various carcinomas and have emerged as vital regulators in certain biological processes, including cell proliferation, migration, differentiation, apoptosis, and angiogenesis. For example, down-regulation of miR-150 inhibits cell proliferation and induces apoptosis in non-small-cell lung cancer (NSCLC) cells in culture. As another example, miR-27a suppression inhibits cell proliferation and migration by targeting mitogen activated protein kinase kinase 4 (MAP2K4) in human osteosarcoma cells [6,12]. These studies explored the expression and molecular mechanisms of miRNAs in specific tumour types, and determined that these small RNAs are novel biomarkers and therapeutic targets for anti-tumour treatments.

Previously, we found that miRNA-210, one of the most significantly upregulated miRNAs in hypoxic cells, is highly expressed in human gliomas and confers a poor prognosis in glioma patients [10]. Furthermore, an increase in miR-210 expression directly correlated with the histopathological grade of astrocytic tumours [9]. In the current study, we investigated the expression of miR-210 in GBM tissues and cell lines. Moreover, we explored its function in the regulation of proliferation and apoptosis, and determined that the regulator of differentiation 1 (ROD1), a protein also known as polypyrimidine trace binding protein 3 (PTBP3), is probably the target of miRNA-210 in GBM cells.

Material and methods

Tissue samples

A total of 15 GBM tissues and five normal tissues were obtained from surgical resection at the Wuxi Second Hospital affiliated to Nanjing Medical University. Tissue samples from nine men and six women (mean age: 59.9 ± 7.7 years; age range: 46-72 years) were included in the study. Pathological information was obtained after surgery and glioma stage and grade were determined based on the 2007 World Health Organization (WHO) Classification System. Five normal brain tissue samples were obtained from adult patients with craniocerebral injuries. A partial resection of brain tissue was required as decompression treatment to reduce intracranial pressure in these patients. Specimens were snap-frozen in liquid nitrogen and stored at $-80^{\circ}C$. Patient permission was obtained for the collection and examination of all

samples, and this study was approved by the Ethics Committee of Nanjing Medical University.

Cell culture

The U87MG and U251 cell lines were obtained from the Cell Resource Centre, Peking Union Medical College, which is the headquarters of the National Infrastructure of Cell Line Resources, National Science & Technology Infrastructure (NSTI). The NSTI determined that the cell lines were free of mycoplasma contamination via polymerase chain reaction (PCR) analysis, and confirmed the species of origin for the two cell lines by PCR. All of the results from these tests can be viewed on the following website: http://cellresource.cn. Cells were grown in Dulbecco's modified Eagle's medium (DMEM; Hyclone, USA) supplemented with 10% foetal bovine serum (FBS; Gibco, USA) and 1% penicillin-streptomycin. Cells were incubated at 37°C in a saturated humidity atmosphere containing 5% CO_2. For all experiments, the cells were detached and one third of the cells were re-seeded in plates. All the cells used in this study were at passage 20. The medium was changed on the cells every three days.

Oligonucleotide transfection

The miR-210 inhibitor and mimic and the ROD1 siRNA were chemically synthesised by Genepharma (Genepharma, China). The miR-210 inhibitor, a small, modified, single-stranded RNA molecule, was used to downregulate miR-210 expression, whereas the miR-210 mimic, a small, modified, double-stranded RNA molecule, was used to upregulate miR-210 expression. The siRNA was utilised to block the expression of ROD1. Scramble oligonucleotide sequences were used as negative controls. Relative sequences were as follows: hsa-miR-210 inhibitor: 5'-UCAGCCGCUGU-CACACGCACAG-3'; negative control oligonucleotide for the inhibitor: 5'-CAGUACUUUUGUGUAGUACAA-3'; hsa-miR-210 mimic: 5'-CUGUGCGUGUGACAGCGGCU-GAAGCCGCUGUCACACGCACAGUU-3'; negative control oligonucleotide for the mimic: 5'-UUCUCCGAAC-GUGUCACGUUACGUGACACGUUCGGAGAATT-3'. The transfection efficiency of the cells was identified via SYBR Green quantitative real-time reverse transcriptase polymerase chain reaction (qRT-PCR). Transfections were carried out using Lipofectamine 2000 (Invitrogen, USA) according to the manufacturer's protocol.

http://rcin.org.pl

Total RNA isolation, reverse transcription, and quantitative real-time RT-PCR

Total RNA, including miRNA, was extracted from the tissues or cells using Trizol reagent (Invitrogen) following the manufacturer's instructions. For ROD1, qRT-PCR was performed using ImProm-IITM reverse transcriptase (Promega, USA) and the QuantiFast SYBR Green PCR Kit (Qiagen, Germany). Detection was performed with the ABI7500 Real-time PCR system instrument (Applied Biosystems, USA). Relative primers were as follows: ROD1 forward: 5'-AAGGAA-ATGAATGGGCAGCCGTTAG-3'; ROD1 reverse: 5'-CATG-TAGTTGAGGTCAATGAAGGGGTC-3; glyceraldehyde-3-phosphate dehydrogenase (GAPDH) forward: 5'-GCT-CTCTGCTCCTCCTGTTC-3'; GAPDH reverse: 5'-GACT-CCGACCTTCACCTTCC-3'. Hairpin-it^{TM} miRNAs RT-PCR Quantitation Kit (Genepharma) was utilised to determine miR-210 expression, and the U6 small nuclear RNA (snRNA) Real-time RT-PCR Normalisation Kit (Genepharma) was used as the control.

The expression levels of ROD1 and miR-210 were calculated by the $2^{-\Delta\Delta Ct}$ analysis method and were normalised to the controls.

Western blot analysis

The primary antibodies used in this study were anti-ROD1 (Santa Cruz, USA) and anti-GAPDH (Beyotime, China). Equal amounts of protein samples were mixed with equal amounts of sodium dodecyl sulphate (SDS) sample buffer and separated via 12% SDS-polyacrylamide gel electrophoresis (PAGE). Gels were run for one hour, and the separated proteins were transferred to polyvinylidene fluoride (PVDF) membranes. The membranes were then blocked with 5% nonfat powdered milk in tris-buffered saline with 10% Tween-20 (TBST) for one hour. Membranes were incubated with primary antibody at 4°C overnight. Secondary antibody incubations were conducted using a goat anti-mouse antibody conjugated to horseradish peroxidase. Visualisation was performed using chemiluminescence.

Cell proliferation assays

Post-transfection, cells were seeded in 96-well plates at a density of 5000 cells per well for 12, 24, 36, 48, and 72 hours. Cell Count Kit-8 (CCK8; Dojindo, Japan) was used to measure cell proliferation according to the manufacturer's protocol. 10 µl of CCK8 solution was added into the medium of each well and incubated for 1.5 hours. The absorbance was read at 450 nm via a microplate system.

Cell apoptosis assays

Cells were seeded in six-well plates. After 48 hours the cells were washed with cold PBS and subsequently treated with Annexin V and propidium iodide (PI) using Alexa Fluor 488 annexin V/Dead Cell Apoptosis Kit (Invitrogen) to determine the cell apoptosis according to the protocol and then analysed by a flow cytometer (Beckman Coulter, USA).

Statistical analysis

All data were analysed using SPSS 11.0 for Windows (SPSS Inc., USA). Statistical significance was determined using the Student's t-test. Differences were considered significant when $p < 0.05$.

Results

Expression of miR-210 in glioblastoma multiforme tissues and cell lines

To examine the expression of miR-210 in GBM tissue compared to normal tissue, we detected miR-210 levels via qRT-PCR in GBM and normal brain tissue. Fifteen specimens diagnosed as GBM were examined, and five normal brain tissues were utilised as controls. In addition, miR-210 expression in the U87MG and U251 GBM cell lines was detected and compared to miR-210 expression in normal brain tissue. The expression levels were normalised to U6 RNA levels in the cells/tissues. As shown in Fig. 1A, miR-210 expression in the GBM tissues was significantly higher when compared to normal brain tissues ($p < 0.001$). Additionally, miR-210 expression in the U87MG and U251 GBM cell lines was higher than in normal brain tissue, as shown in Fig. 1B ($p < 0.05$).

Upregulation of miR-210 promotes cell proliferation and inhibits cell apoptosis in glioblastoma multiforme cells

To decipher the biological significance of miR-210 in GBM, the chemically synthesised miR-210 mimic and inhibitor were transfected into the U87MG and U251 GBM cell lines to upregulate and downregulate miR-210 expression, respectively. Transfection efficiency was evaluated via qRT-PCR and is shown in Fig. 2A and 2B. The U87MG cell line exhibited higher
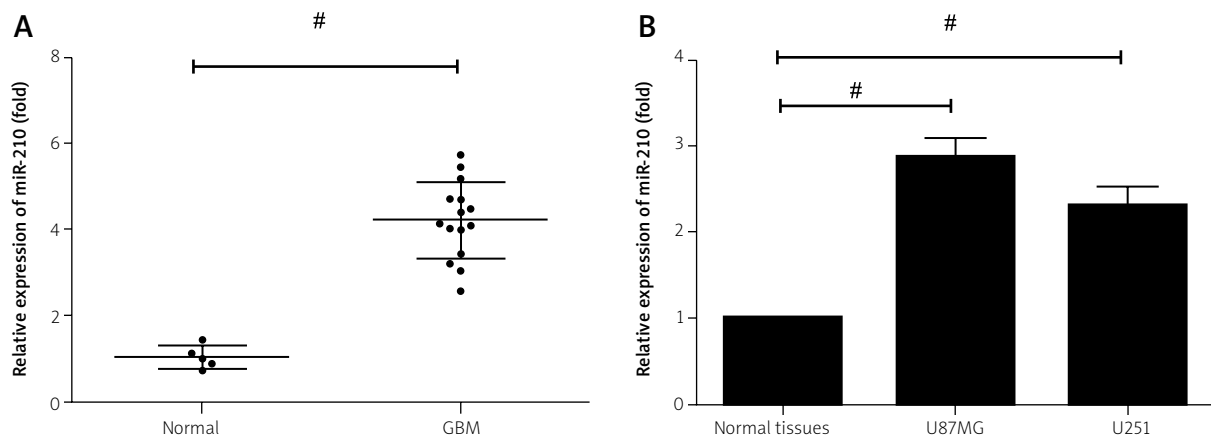
Fig. 1. A) Fifteen glioblastoma multiforme (GBM) and five normal brain tissue samples were utilised to examine miR-210 expression. Quantitative real-time reverse transcriptase PCR (qRT-PCR) was performed, and the relative expression between the groups is shown (#p < 0.05). **B)** The relative expression levels of miR-210 in the U87MG and U251 GBM cell lines compared to normal brain tissue were measured by qRT-PCR (#p < 0.05).

transfection efficiency than U251 cells; therefore, all of our experiments in this study were conducted in the U87MG cell line. To investigate the effect miR-210 has on proliferation in GBM cells, we performed CCK8 assays on the transfected U87MG cells. These cell proliferation assays revealed that mimic-induced miR-210 overexpression led to a statistically significant increase in U87MG cell proliferation compared to the negative control cells (Fig. 2C, p < 0.05). Conversely, the proliferation rate of the U87MG cells treated with the miR-210 inhibitor was decreased when compared to control cells (Fig. 2D, p < 0.05).

Next, we analysed apoptosis in the transfected GBM cells via flow cytometry. As shown in Fig. 3, U87MG cells transfected with the miR-210 inhibitor demonstrated a statistically significant increase in apoptotic rate when compared to controls, while the cells transfected with the miR-210 mimic exhibited a decrease in apoptosis (p < 0.05). Thus, miR-210 expression may be upregulated in GBM cells and tissues because expression of this microRNA promotes proliferation and regulates apoptosis in GBM cells.

Regulator of differentiation 1 as a potential target of miR-210 in glioblastoma multiforme

Because ROD1 has been identified as a miR-210 target in HEK293 cells, we next sought to investigate ROD1 as a potential miR-210 target in GBM cells. First, ROD1 expression was examined in GBM tissues at both the mRNA and protein levels. We found that

expression of ROD1 was significantly lower in GBM tissues than in normal tissues (Fig. 4A, p < 0.001 and Fig. 4B). To examine whether ROD1 is a likely target of miR-210 in GBM cells, we observed ROD1 expression in U87MG cells transfected with the miR-210 mimic or inhibitor. The miR-210 mimic effectively reduced ROD1 expression as detected by western blot analysis, whereas the miR-210 inhibitor led to an increase in ROD1 expression (Fig. 4C). This data indicates that ROD1 is probably a target of miR-210 in GBM cells.

Knockdown of regulator of differentiation 1 reverses the cell proliferation and apoptosis induced by miR-210

Since we demonstrated that downregulation of miR-210 via a specific inhibitor could suppress cell proliferation and induce cell apoptosis in GBM cells (Fig. 2), we then wanted to determine whether ROD1 is directly involved in miR-210 regulation of GBM cell activity. Cell proliferation and apoptosis assays were performed on GBM cells transfected with a miR-210 inhibitor or co-transfected with the miR-210 inhibitor and siRNA to knockdown ROD1. Regulator of differentiation 1 expression was remarkably reduced by the siRNA as detected via western blot (Fig. 5A). Additionally, cell proliferation analysed by the CCK8 assay demonstrated that the proliferation of GBM cells induced by miR-210 was abrogated by the knockdown of ROD1 (Fig. 5B, p < 0.001). Furthermore, cell apoptosis analysis detected by flow

http://rcin.org.pl
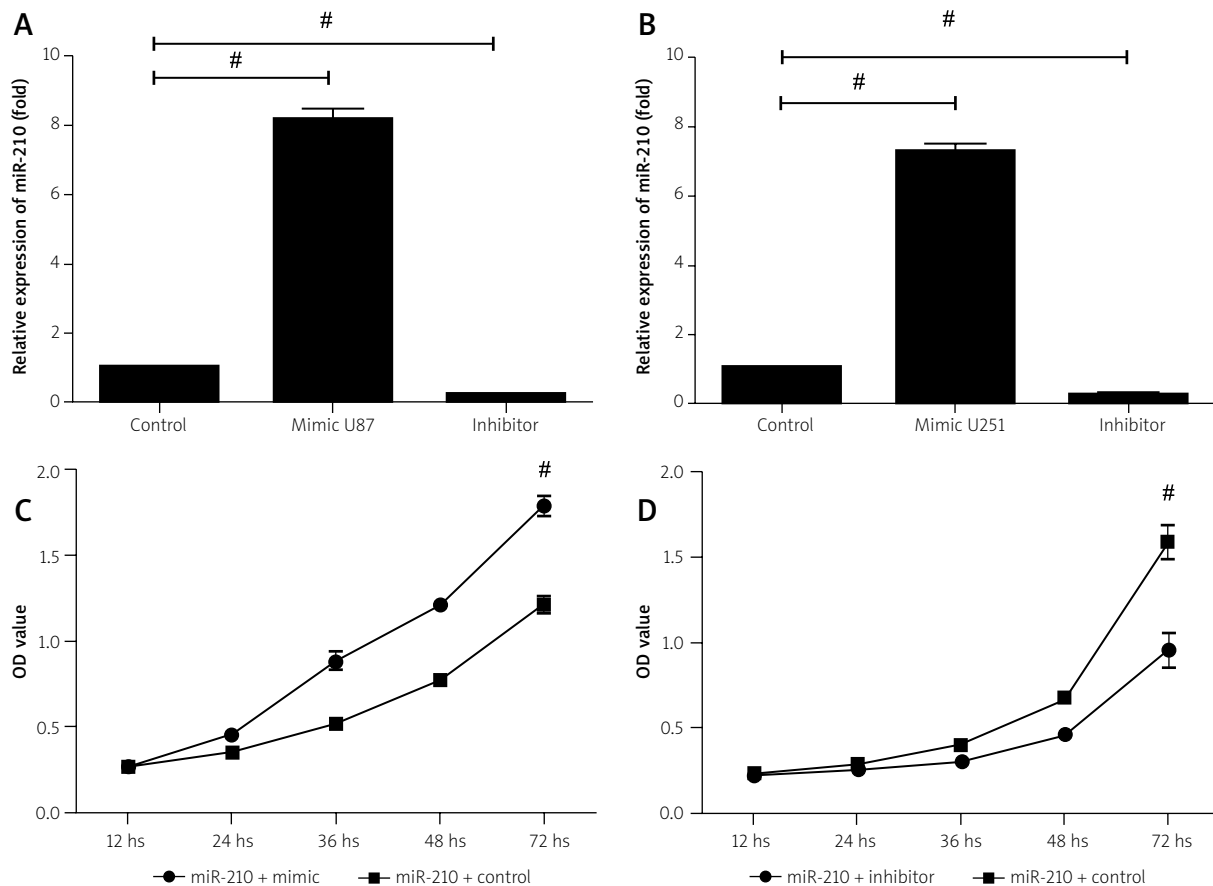
Fig. 2. A, B) The U87MG and U251 glioblastoma multiforme (GBM) cell lines were transfected with the miR-210 mimic or inhibitor. Forty-eight hours post-transfection, the cells were harvested and samples were prepared for quantitative real-time reverse transcriptase polymerase chain reaction (qRT-PCR). MiR-210 levels in the U87MG and U251 GBM cell lines were measured and compared to the non-transfected control group. MiR-210 was significantly upregulated in the cells expressing the mimic and significantly downregulated in the cells transfected with the inhibitor ($^{\#}p < 0.05$). The U87MG cells exhibited higher transfection efficiency than the U251 cells. **C)** Cell proliferation of U87MG cells transfected with the miR-210 mimic was measured by CCK8 analysis ($^{\#}p < 0.05$). **D)** U87MG cells transfected with the miR-210 inhibitor were analysed for cell proliferation via CCK8 analysis ($^{\#}p < 0.05$).
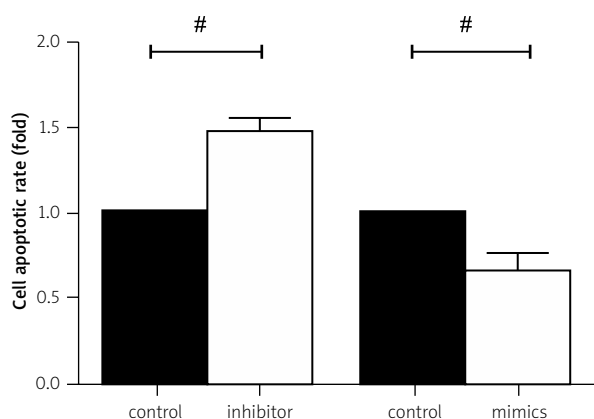
Fig. 3. After transfection with the miR-210 mimic or inhibitor, U87MG cell apoptosis was measured by flow cytometry ($^{\#}p < 0.05$).

cytometry revealed that the decrease in apoptosis observed after miR-210 expression was abolished by the knockdown of ROD1 (Fig. 5C, $p < 0.05$). The above results indicate that knockdown of ROD1 expression rescues the growth arrest and apoptosis that was observed when the GBM cells were treated with the miR-210 inhibitor.

Discussion

Accumulating studies have demonstrated that miRNAs play crucial roles in the occurrence and progression of malignant tumours. MiRNA dysregulation can be observed in diseased tissues or body fluids such as plasma, urine, tears, and cerebrospinal fluid [21]. Specific miRNA expression and/or levels of

http://rcin.org.pl
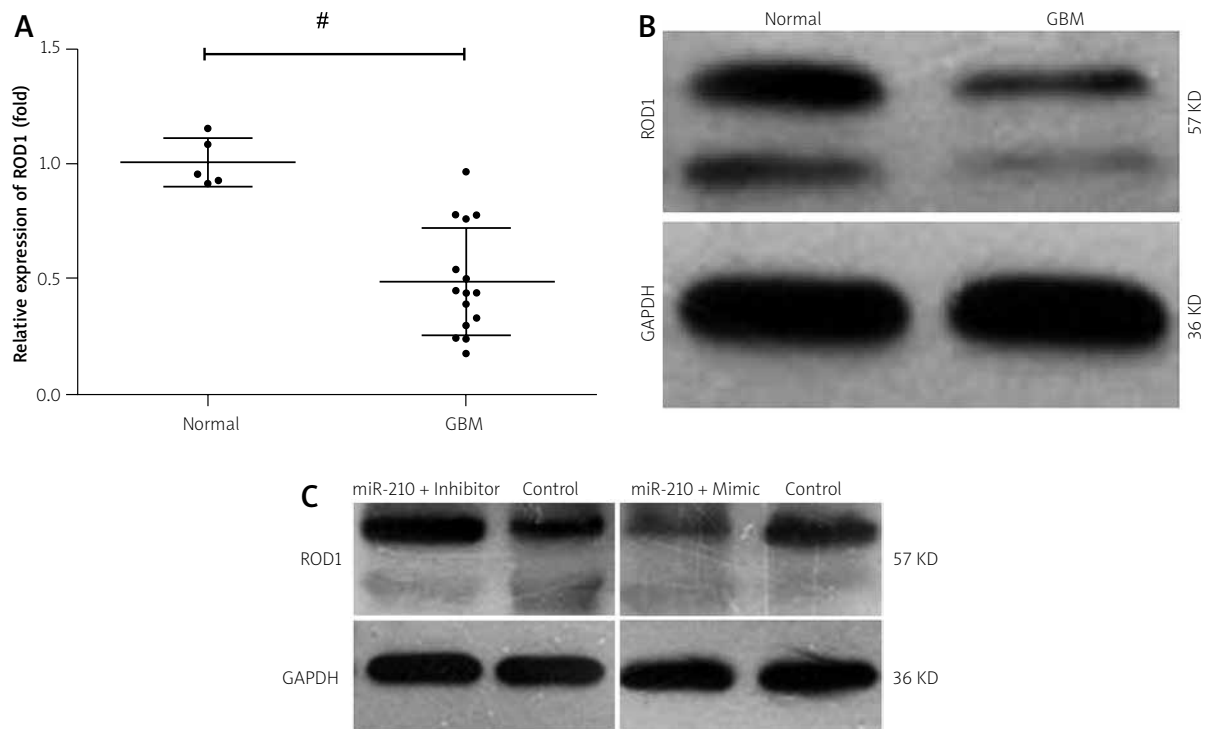
Fig. 4. A) Regulator of differentiation 1 (ROD1) expression was measured via real-time polymerase chain reaction (RT-PCR) in fifteen glioblastoma multiforme (GBM) and five normal brain tissue samples ($^{\#}p < 0.05$). **B)** Regulator of differentiation 1 protein expression in GBM and normal brain tissue was measured by western blot analysis. According to the instructions of the ROD1 antibody, the upper band is considered to be ROD1 with an apparent molecular weight of 57KD. **C)** U87MG cells were transfected with the miR-210 inhibitor or mimic and 48 hours post-transfection were analysed for ROD1 expression via immunoblot.

expression in particular tissues may predict certain diseases. Thus, these miRNAs can be selected as candidate biomarkers for the diagnosis and prognosis of various tumours [20,22,24]. The expression and function of various miRNAs have been reported in glioma [17,25,26]. In the current study, we determined the expression and function of miR-210 in GBM cells.

The stem-loop of miR-210 is located in an intron of a noncoding RNA that is transcribed from AK123483 on chromosome 11p15.5 [13]. AK123483 is regarded as the pri-miR-210, which is then processed to the pre- and then the mature miR-210. Most studies conclude that miR-210 is a specific target of hypoxia inducible factor-1 (HIF-1), whereby HIF-1 directly binds to a hypoxia-responsive element (HRE) in the proximal miR-210 promoter. The HRE is responsible for the hypoxic induction of AK123483 and may coordinate the expression of genes downstream of miR-210 [7]. MiR-210 is upregulated by hypoxia in multiple cell lines. Hypoxic conditions are also a common feature of the tumour microenviron-

ment. MiR-210 expression is increased in most solid tumours, and its expression correlates with a negative prognosis [3]. MiR-210 has been shown to be involved in angiogenesis, DNA damage response, invasion, proliferation, apoptosis, and the cell cycle. Anton *et al.* [1] reported that miR-210 is upregulated in preeclamptic placentas, and that it regulates cell viability. MiR-210 overexpression was shown to reduce trophoblast invasion, while miR-210 inhibition promoted invasion. The authors concluded that miR-210 is a novel predictive serum biomarker for preeclampsia. Wang *et al.* [18] reported expression of miR-210 in neural progenitor cells, whereby they identified Bcl-2 adenovirus E1B 19 kDa-interacting protein 3 (BNIP3), which is regulated by HIF-1α and promotes cell death, as a direct functional target of miR-210. MiR-210 directly suppressed BNIP3 expression, which subsequently reduced cell death.

Our previous report showed that oligodendroglial tumours exhibit a significantly reduced level of miR-210 as compared to normal brain tissue. In
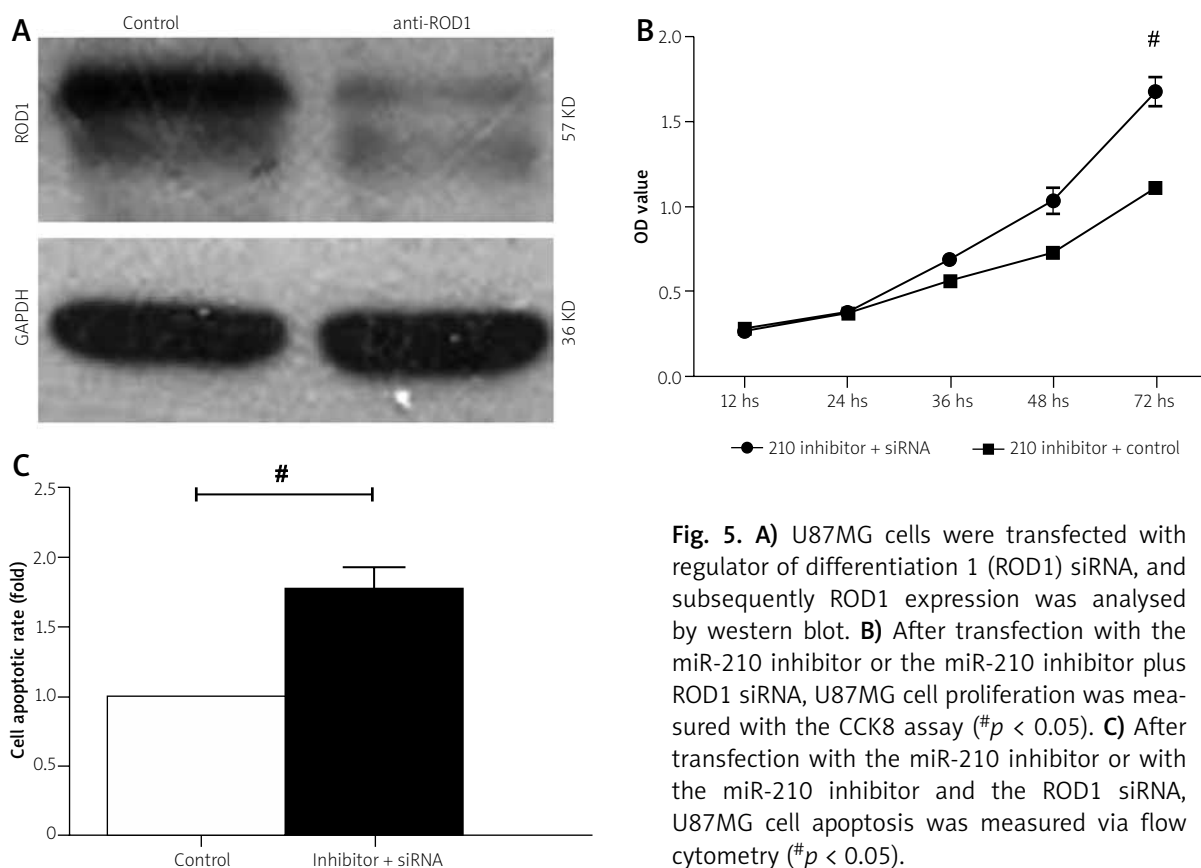
Fig. 5. A) U87MG cells were transfected with regulator of differentiation 1 (ROD1) siRNA, and subsequently ROD1 expression was analysed by western blot. B) After transfection with the miR-210 inhibitor or the miR-210 inhibitor plus ROD1 siRNA, U87MG cell proliferation was measured with the CCK8 assay ($^{\#}p < 0.05$). C) After transfection with the miR-210 inhibitor or with the miR-210 inhibitor and the ROD1 siRNA, U87MG cell apoptosis was measured via flow cytometry ($^{\#}p < 0.05$).

contrast, astrocytic tumours demonstrate significantly increased levels of miR-210. Furthermore, the expression of miR-210 positively correlates with the grade of astrocytic tumours. Thus, miR-210 could be a novel candidate biomarker for glioma diagnosis and prognosis [9,10]. In the study presented here, we determined that miR-210 expression is increased in GBM tissue and cells when compared to normal brain tissue, and that miR-210 could potentially modulate tumour progress by affecting cell growth and viability. Our finding that miR-210 is upregulated in GBM could have enhanced significance since recent studies have shown that miRNAs expressed in the brain have relatively short half-lives and can be rapidly degraded [8,14,19]. Functional analyses were performed to examine the affect that miR-210 expression has on proliferation and apoptosis in GBM cells. CCK8 cell proliferation analysis and flow cytometric assays examining apoptosis indicated that introduction of a miR-210 inhibitor into GBM cells significantly suppressed cell number and induced apoptosis, respectively. Moreover, transfection of the miR-210 mimic significantly promoted cell growth.

These findings suggest that miR-210 plays a critical role in the proliferation and apoptosis potential of GBM cells.

We then explored ROD1, also known as PTBP3, as a potential target of miR-210 in GBM cells. ROD1 has been confirmed as a direct but seedless target of miR-210 in HEK293 cells [4]. Immuno-precipitation analysis performed by Fasanaro et al. [5] identified ROD1 as a miR-210-seedless transcript enriched in miR-210-containing RNA-induced silencing complexes. In both the presence and absence of hypoxic conditions, expression of ROD1 inhibited cell proliferation and induced cell apoptosis. This same study also found two well-established miR-210 targets, ephrin-A3 and RAD52 homolog, indicating the reliability of the experiment. Furthermore, Rna22 prediction, thermodynamic stability analysis, and luciferase activity all indicated that ROD1 is a direct target of miR-210 in HEK293 cells. Taken together with our findings in GBM, it is likely that miR-210 directly targets ROD1 in GBM and could affect the biological activity of GBM cells. ROD1, a member of the PTBP family of proteins [15], is a repressive splicing regula-

tor expressed in various cell types. Regulator of differentiation 1 was reported to be primarily expressed in haematopoietic cells in rats [23], thus the role that ROD1 plays in differentiation was examined in mammalian cells. Overexpression of ROD1 was found to inhibit 12-O-tetradecanoylphorbol-13-acetate (TPA)-induced megakaryocytic differentiation and sodium butyrate-induced erythroid differentiation in the pluripotent human hematopoietic leukaemia cell line K562 [23]. Our research demonstrated that ROD1 is expressed in human brain tissues, and may play an important role in the development of GBM via regulation by miR-210. Our results show that overexpression of miR-210 decreased ROD1 levels; and ROD1 inhibition abolishes the anti-tumour effects observed in GBM cells treated with the miR-210 inhibitor. Thus, miR-210 could be a candidate biomarker and an important factor in GBM through the targeting ROD1.

In summary, we demonstrated that miR-210 is overexpressed in GBM tissues, and that miR-210 may function as an oncogene in GBM cells. Based on our observations and previous findings by other groups, we conclude that miR-210 could be a novel biomarker for GBM, and it probably regulates tumour progression through the targeting of ROD1. Since GBM is a form of cancer that progresses and spreads quickly, traditional therapies such as surgery and chemoradiotherapy have only limited effectiveness in treating this aggressive disease. Therefore, new approaches such as molecular targets would be highly beneficial in the therapeutic treatment of GBM. Targeting miR-210 may provide a new therapeutic option in the treatment of this deadly disease.

Acknowledgments

Disclosure

Authors report no conflict of interest.

References

1. Anton L, Olarerin-George AO, Schwartz N, Srinivas S, Bastek J, Hogenesch JB, Elovitz MA. miR-210 inhibits trophoblast invasion and is a serum biomarker for preeclampsia. Am J Pathol 2013; 183: 1437-1445.

2. Dalmay T, Edwards DR. MicroRNAs and the hallmarks of cancer. Oncogene 2006; 25: 6170-6175.

3. Fasanaro P, D'Alessandra Y, Di Stefano V, Melchionna R, Romani S, Pompilio G, Capogrossi MC, Martelli F. MicroRNA-210 modulates endothelial cell response to hypoxia and inhibits the receptor tyrosine kinase ligand Ephrin-A3. J Biol Chem 2008; 283: 15878-15883.

4. Fasanaro P, Greco S, Lorenzi M, Pescatori M, Brioschi M, Kulshreshtha R, Banfi C, Stubbs A, Calin GA, Ivan M, Capogrossi MC, Martelli F. An integrated approach for experimental target identification of hypoxia-induced miR-210. J Biol Chem 2009; 284: 35134-35143.

5. Fasanaro P, Romani S, Voellenkle C, Maimone B, Capogrossi MC, Martelli F. ROD1 is a seedless target gene of hypoxia-induced miR-210. PLoS One 2012; 7: e44651.

6. Gu XY, Wang J, Luo YZ, Du Q, Li RR, Shi H, Yu TP. Down-regulation of miR-150 induces cell proliferation inhibition and apoptosis in non-small-cell lung cancer by targeting BAK1 in vitro. Tumour Biol 2014; 35: 5287-5293.

7. Huang X, Le QT, Giaccia AJ. MiR-210 – micromanager of the hypoxia pathway. Trends Mol Med 2010; 16: 230-237.

8. Krol J, Busskamp V, Markiewicz I, Stadler MB, Ribi S, Richter J, Duebel J, Bicker S, Fehling HJ, Schubeler D, Oertner TG, Schratt G, Bibel M, Roska B, Filipowicz W. Characterizing light-regulated retinal microRNAs reveals rapid turnover as a common property of neuronal microRNAs. Cell 2010; 141: 618-631.

9. Lai N, Zhu H, Chen Y, Zhang S, Zhao X, Lin Y. Differential expression of microRNA-210 in gliomas of variable cell origin and correlation between increased expression levels and disease progression in astrocytic tumours. Folia Neuropathol 2014; 52: 79-85.

10. Lai NS, Dong QS, Ding H, Miao ZL, Lin YC. MicroRNA-210 overexpression predicts poorer prognosis in glioma patients. J Clin Neurosci 2014; 21: 755-760.

11. Ostrom QT, Gittleman H, Farah P, Ondracek A, Chen Y, Wolinsky Y, Stroup NE, Kruchko C, Barnholtz-Sloan JS. CBTRUS statistical report: Primary brain and central nervous system tumors diagnosed in the United States in 2006-2010. Neuro Oncol 2013; 15 Suppl 2: ii1-56.

12. Pan W, Wang H, Jianwei R, Ye Z. MicroRNA-27a Promotes Proliferation, Migration and Invasion by Targeting MAP2K4 in Human Osteosarcoma Cells. Cell Physiol Biochem 2014; 33: 402-412.

13. Saini HK, Griffiths-Jones S, Enright AJ. Genomic analysis of human microRNA transcripts. Proc Natl Acad Sci U S A 2007; 104: 17719-17724.

14. Sethi P, Lukiw WJ. Micro-RNA abundance and stability in human brain: specific alterations in Alzheimer's disease temporal lobe neocortex. Neurosci Lett 2009; 459: 100-104.

15. Spellman R, Llorian M, Smith CW. Crossregulation and functional redundancy between the splicing regulator PTB and its paralogs nPTB and ROD1. Mol Cell 2007; 27: 420-434.

16. Van Meir EG, Hadjipanayis CG, Norden AD, Shu HK, Wen PY, Olson JJ. Exciting new advances in neuro-oncology: the avenue to a cure for malignant glioma. CA Cancer J Clin 2010; 60: 166-193.

17. Wan X, Cheng Q, Peng R, Ma Z, Chen Z, Cao Y, Jiang B. ROCK1, a novel target of miR-145, promotes glioma cell invasion. Mol Med Rep 2014; 9: 1877-1882.

18. Wang F, Xiong L, Huang X, Zhao T, Wu LY, Liu ZH, Ding X, Liu S, Wu Y, Zhao Y, Wu K, Zhu LL, Fan M. miR-210 suppresses BNIP3 to

http://rcin.org.pl

protect against the apoptosis of neural progenitor cells. Stem Cell Res 2013; 11: 657-667.

19. Wang H, Chiu M, Xie Z, Chiu M, Liu Z, Chen P, Liu S, Byrd JC, Muthusamy N, Garzon R, Croce CM, Marcucci G, Chan KK. Synthetic microRNA cassette dosing: pharmacokinetics, tissue distribution and bioactivity. Mol Pharm 2012; 9: 1638-1644.

20. Wang X, Meng X, Li H, Liu W, Shen S, Gao Z. MicroRNA-25 expression level is an independent prognostic factor in epithelial ovarian cancer. Clin Transl Oncol 2014; 16: 954-958.

21. Weber JA, Baxter DH, Zhang S, Huang DY, Huang KH, Lee MJ, Galas DJ, Wang K. The microRNA spectrum in 12 body fluids. Clin Chem 2010; 56: 1733-1741.

22. Wu CW, Ng SC, Dong Y, Tian L, Ng SS, Leung WW, Law WT, Yau TO, Chan FK, Sung JJ, Yu J. Identification of microRNA-135b in stool as a potential noninvasive biomarker for colorectal cancer and adenoma. Clin Cancer Res 2014; 20: 2994-3002.

23. Yamamoto H, Tsukahara K, Kanaoka Y, Jinno S, Okayama H. Isolation of a mammalian homologue of a fission yeast differentiation regulator. Mol Cell Biol 1999; 19: 3829-3841.

24. Zhao J, Lu Q, Zhu J, Fu J, Chen YX. Prognostic value of miR-96 in patients with acute myeloid leukemia. Diagn Pathol 2014; 9: 76.

25. Zhong Q, Wang T, Lu P, Zhang R, Zou J, Yuan S. miR-193b promotes cell proliferation by targeting Smad3 in human glioma. J Neurosci Res 2014; 92: 619-626.

26. Zhou J, Wang W, Gao Z, Peng X, Chen X, Chen W, Xu W, Xu H, Lin MC, Jiang S. MicroRNA-155 promotes glioma cell proliferation via the regulation of MXI1. PLoS One 2013; 8: e83055.

Folia
Neuropathologica

Occurrence of spontaneous and audiogenic seizures following global brain ischaemia due to cardiac arrest

Marzena Ułamek-Kozioł[1], Janusz Kocki[2], Anna Bogucka-Kocka[3], Sławomir Januszewski[1], Stanisław J. Czuczwar[4,5], Ryszard Pluta[1]

[1]Laboratory of Ischaemic and Neurodegenerative Brain Research, Mossakowski Medical Research Centre, Polish Academy of Sciences, Warsaw, [2]Department of Clinical Genetics, Medical University of Lublin, Lublin, [3]Department of Pharmaceutical Botany, Medical University of Lublin, Lublin, [4]Department of Pathophysiology, Medical University of Lublin, Lublin, [5]Department of Physiopathology, Institute of Rural Health, Lublin, Poland

Abstract

Transient cardiac arrest due to cardiac vessel bundle occlusion was used to produce a rat model of spontaneous and audiogenic seizures. Among the rats, spontaneous seizures were present in 64%, and audiogenic seizures could be evoked in 86%, during two weeks of survival after cardiac arrest, by exposure to a loud sound produced by rattling keys, beginning one day after the post-ischaemic injury. Data from literature suggested a key role for GABA-ergic system widespread dysfunction especially in the hippocampus in post-cardiac arrest onset of audiogenic seizures. Reduced GABA inhibition in the hippocampus seems responsible for audiogenic seizures following cardiac arrest. In summary it may be considered that the occurrence of audiogenic seizures following cardiac arrest is determined not only by a neuronal loss, especially in the hippocampus, but also by a condition of synapse modification by a regenerative phenomenon. Data from our study clearly indicate that global brain ischaemia due to cardiac arrest may induce the susceptibility to spontaneous and audiogenic seizures, but this effect is transient.

Key words: cardiac arrest, audiogenic seizures, spontaneous seizures, global brain ischaemia.

Introduction

Due to the rapid improvement in lifestyle and better of healthcare systems, especially in developed countries, the relative amount of aged people is growing rapidly [12]. With aging, arterial and venous vessel dysfunction occurs, which causes different diseases such as hypertension and/or heart coronary artery disease, which can cause cardiac arrest [3]. Thus, there is the push for a better under-

standing of the mechanisms underlying cardiac arrest development and cardiac arrest-related diseases. Cardiac arrest frequently occurs with aging, is a leading cause of death, and plays a crucial role in occurrence of global brain ischaemia and dementia [3,11,13,29,30].

It is reasonable to remark that the brain essentially ages the equivalent of several years within the few minutes taken to resuscitate a patient (or animal) from cardiac arrest. With reference to the natu-

Communicating author:
Prof. Ryszard Pluta, MD, PhD, Laboratory of Ischaemic and Neurodegenerative Brain Research, Mossakowski Medical Research Centre, Polish Academy of Sciences, 5 Pawińskiego St., 02-106 Warsaw, Poland, phone: +48 22 608 65 40 or 608 64 69, fax: +48 22 668 55 32, e-mail: pluta@imdik.pan.pl

Marzena Ułamek-Kozioł, Janusz Kocki, Anna Bogucka-Kocka, Sławomir Januszewski, Stanisław J. Czuczwar, Ryszard Pluta

ral rate of neuronal loss in brain aging, the post-ischaemic brain ages 3.6 years each hour without therapy [27]. In each hour, 120 million neuronal cells, 830 billion synapses, and 714 km of myelinated fibres are lost [27]. The above abnormalities can be part of the cause of the death of ischaemia-susceptible neurons in areas such as the hippocampus and dysfunction of other, e.g. cortical, neurons also contributing to dysfunction of the neural network. Secondary pathology in the hippocampus in humans and after experimental global cerebral ischaemia due to cardiac arrest occurs with several features similar to Alzheimer's disease [10,20,21,23,24]. The most important similarity is the accumulation of amyloid precursor protein or its fragments, e.g. β-amyloid peptide, in intra- and extracellular space in the hippocampus in humans and rats subjected to transient global brain ischaemia [10,20,26]. The progression of neuronal impairment and cell death, observed during cardiac arrest and following post-arrest, is very fast; however, processes involved in progression are unknown fully. A wide variety of brain lesions and injuries are associated with increased risk for development of seizures. The biggest risk factor are cerebrovascular pathologies, at around 21% [4]. Post-ischaemic acute symptomatic seizures occur at between 3 and 15% (c. 11%), more commonly in animals and humans with severe brain injury [4]. Seizures, especially after cardiac arrest, are of increasing importance as the population ages and are a growing contribution to symptomatic epilepsies. Post-cardiac arrest seizures are less well characterised and are good targets for clinical trials of seizure prevention. Despite differences between humans and animals, and the time courses, mechanistic information gained from studying the experimental cardiac arrest conditions could be harnessed to synergistically advance both groups and to develop treatments targeting specific components in these neurodegenerative pathways to provide more robust protection of patients from neurocognitive impairment and/or death [29]. However, little is known about cardiac arrest-related diseases or induced brain dysfunction resulting because of the occurrence of seizures.

Experimental data indicate that cardiac arrest induces a susceptibility to audiogenic seizures in previously unsusceptible rats [7]. In view of the importance of cardiac arrest in human and its increasing occurrence in the world, as well as its frequent association with seizures, an experimental cardiac arrest model was used in the present investigations. Consequently, the present study was aimed at elucidating whether cardiac arrest in rats could induce audiogenic seizure susceptibility in Wistar rats that were not susceptible to audiogenic stimulation.

Material and methods

The cardiac arrest was induced by a method described previously by Pluta et al. [16]. Female Wistar rats were used (150-170 g, 3 months old). In animals under anaesthesia [7], a blunt-ended, hook-like, metal probe with the distal end bent at 90° was placed inside the rats' chest cavity after midline skin incision [16]. The hook was inserted through the right parasternal line and third intercostal space into the mediastinum. The hook was gently positioned under the heart vessel bundle and was then moved up and, at the same time, finger pressure (index and middle) was applied from outside. Blood flow in both arterial and venous heart blood vessels was stopped. The device was removed after 3.5 minutes. The animals remained in a state similar to clinical death for 10 minutes. Next the resuscitation procedure was initiated with external heart massage and artificial ventilation with room air (7025 Rodent Ventilator, Ugo Basile, Italy). The procedure was continued until spontaneous heart activity and respiration were resumed. After cardiac arrest the rats ($n = 50$) survived for one month. Audiogenic seizures were triggered by using the rattling sound of keys (sound intensity 90-100 dB, frequency > 4,000 Hz), according to Kawai et al. [7]. The sound stimulus was set until rats started to have seizures. Audiogenic seizure test was performed 24 hours after cardiac arrest, once daily for one month. The rats were kept in plastic cages with free access to food and tap water under standardised housing conditions (natural light/dark cycle, temperature of 24 ± 2°C, relative humidity 55 ± 5%). Procedures involving animals and their care were conducted in accordance with the guide for the care and use of laboratory animals as adopted and promulgated by the National Institutes of Health. The experimental protocols and procedures described here were approved by the First Local Ethical Committee in Warsaw.

Results

Following 10 minutes of cardiac arrest, spontaneous heart activity was restored after 82.7 ± 16.5

http://rcin.org.pl

seconds (mean ± SD) and respiratory activity within 8.4 ± 1.3 minutes. The pain reaction reappeared at 15.8 ± 3.0 minutes and the corneal reflex at 28.5 ± 4.3 minutes following cardiac arrest. After reanimation procedure taking about one hour the rats were placed onto one side of a cage. After 24 hours the animals resumed a normal posture without paralysis of legs. Following that, the animals began to feed themselves and became restless. All animals after 10-minute cardiac arrest were alert and had no motor deficits at one day of survival, which is in accordance with other data [7,8]. As already shown, the rats' survival up to one month after reanimation did not exhibit any neurological or somatic deficits during the whole period of observation [8]. After successful resuscitation, during a one-month period all of the animals survived following cardiac arrest.

Animals after cardiac arrest showed spontaneous (64% [n = 32 out of 50]) and induced (by rattling keys) audiogenic (86% [n = 43 out of 50]) susceptibility to seizures with manifestation of the behaviours presented below. The spontaneous sensitivity and induced-by-rattling-key audiogenic seizures became manifest on the first day following reanimation, just after the animals had resumed their normal posture. At that time the animals appeared to be hyperreactive. Spontaneous and sound-triggered seizures started with an episode of locomotor automatism and vocalisation. They always reacted with bouncing or jumping (startle myoclonus) when one loud rattling key stimulation was given. After a few seconds, the rats suddenly started instantaneous and wild continuous running without any attempts to avoid obstacles and/or directional change. The running was completely uncontrolled. The animals bumped into the wall of the cage and/or its cover. With the end of this furious running, the animals presented brief tonic extension of the trunk and all four limbs; this was followed by clonic movements – bouncing or jumping, involving the whole body. At the end of the above episode, the rats tended to fall onto one side and the clonic movements suddenly disappeared. After that, postictal irritability was observed, e.g. for touch as effect they started again running, jumping with vocalisation. Finally, all of the rats had postictal depression characterised by a catatonic posture and immobility. This state of activity lasted from a few to several seconds. The occurrence of spontaneous and audiogenic seizures was observed only for a period of two weeks, following cardiac arrest. The sham-op-

erated rats (n = 5; with surgery but without the cardiac arrest) were also observed for one month for the possible occurrence of seizure activity. However, neither spontaneous nor audiogenic seizure activity was noted.

Discussion

Seizures following transient global brain ischaemia due to cardiac arrest are of increasing importance as the population ages, and may be considered as a growing contribution to symptomatic epilepsies. An association of acute brain ischaemia due to cardiac arrest with seizures has been regarded as indicator of severe ischaemic brain injury. In clinical conditions, the appearance of seizures following cardiac arrest seems a predictor of poor outcome [9,29]. In our study, regular onset of audiogenic seizures was noted one day after cardiac arrest, which is in accordance with the observations by Kawai *et al.* [7]. In our model, audiogenic seizures occured in the first two weeks of survival after acute transient global brain ischaemia, and after a particular period of time completely disappeared.

Available evidence indicates that one of the consequences of cardiac arrest in humans may be seizure activity or myoclonic status epilepticus [2]. Generally, the prognosis for resuscitated patients seems to be poor and only a small proportion of them recover without serious neurological deficits [2]. The pathogenesic pathways are incompletely understood, but they may include alterations in the energy metabolism [4] and blood-brain barrier functioning [17,25], intracellular Ca^{2+} overload [15], release of excitotoxic glutamate [15], neuroinflammation [28], free radical changes [23], and the presence of brain parenchyma haemorrhages [14]. Kawai *et al.* [5] observed remarkable neuronal changes, affecting predominantly GABA-ergic neurons in different areas, immediately following cardiac arrest. Observations by Kawai *et al.* [7] suggested a key role for GABA-ergic system widespread dysfunction especially in the hippocampus in post-cardiac arrest onset of audiogenic seizures. A reduced GABA inhibition in the hippocampus seems responsible for audiogenic seizures following cardiac arrest. However, data are available, showing that GABA-egric deficit seems largely reversible as a sign of some plastic modifications/regenerations such as sprouting of inhibitory terminals from surviving interneuron [7]. According to previous inves-

http://rcin.org.pl

Marzena Ułamek-Kozioł, Janusz Kocki, Anna Bogucka-Kocka, Sławomir Januszewski, Stanisław J. Czuczwar, Ryszard Pluta

tigations, regenerative sprouting of GABA-ergic terminals coincides with cessation of the appearance of audiogenic seizures following cardiac arrest [6]. Interestingly, animals after global brain ischaemia lasting in the range of five minutes did not develop any susceptibility to audiogenic stimulation [7]. When the mean duration of ischaemia reached circa nine minutes, which is slightly less than our experimental conditions, 65% of rats responded with audiogenic seizures [7]. Our recent data also indicate that cardiac arrest rats show an increased susceptibility to pentylenetetrazol-induced clonic seizure activity after one month but not after two months, and this effect is probably also associated with a transient deficit in central GABA-ergic neurotransmission [1].

Two days after cardiac arrest, small areas of neuronal disappearance were noted in the selectively vulnerable hippocampus CA1 region [18,20,21]. At 7-14 days, in ischaemic hippocampus neuronal loss was almost complete in CA1 area with single and scattered damaged pyramidal neurons [8,18,20,21]. But in areas not selectively vulnerable, such as CA2, CA3, and CA4 sectors of the hippocampus, alterations were of a nature characteristic of the acute ischaemic phase [20-22]. In different periods following ischaemia, regions of neuronal loss were replaced by proliferating and hypertrophic astrocytes with staining for β-amyloid peptide and microglia [18,19]. The above pathology was localised in layers 3, 5, and 6 of the neocortex and the striatum. The ischaemic neuronal changes are identified as progressive acute and chronic degeneration processes of neuronal cells in the brain, taking place during the whole period of recirculation. Recently it has been identified that degenerative machinery in post-ischaemic neuronal cells continues outside the acute period of the ischaemic episode [18-20]. Evidence indicates that post-ischaemic brain injury, regardless of the time of survival after ischaemia, is followed by acute neuronal damage as a "burning phenomenon" in areas of the brain belonging or not to selectively vulnerable regions [18-22].

In summary, it may be considered that the occurrence of audiogenic seizures following cardiac arrest is determined not only by neuronal loss, especially in the hippocampus, but also by a condition of synapse modification by regenerative phenomenon. Data from our study clearly indicate that global brain ischaemia due to cardiac arrest may trigger suscep-

tibility to spontaneous and audiogenic seizures, but this effect is transient.

Acknowledgments

Disclosure

Authors report no conflict of interest.

References

1. Dudra-Jastrzebska M, Ułamek-Kozioł M, Andres-Mach M, Luszczki JJ, Januszewski S, Czuczwar SJ, Pluta R. Seizure susceptibility to electroconvulsions or pentylenetetrazol after complete cerebral ischaemia in rats due to cardiac arrest. Pharmacol Rep 2015; 67: 417-420.

2. Geri G, Mongardon N, Daviaud F, Empana JP, Dumas F, Cariou A. Neurological consequences of cardiac arrest: Where do we stand? Ann Fr Anesth Reanim 2014; 33: 98-101.

3. Go AS, Mozaffarian D, Roger VL, Benjamin EJ, Berry JD, Blaha MJ, Dai S, Ford ES, Fox CS, Franco S, Fullerton HJ, Gillespie C, Hailpern SM, Heit JA, Howard VJ, Huffman MD, Judd SE, Kissela BM, Kittner SJ, Lackland DT, Lichtman JH, Lisabeth LD, Mackey RH, Magid DJ, Marcus GM, Marelli A, Matchar DB, McGuire DK, Mohler ER 3rd, Moy CS, Mussolino ME, Neumar RW, Nichol G, Pandey DK, Paynter NP, Reeves MJ, Sorlie PD, Stein J, Towfighi A, Turan TN, Virani SS, Wong ND, Woo D, Turner MB. Heart disease and stroke statistics – 2014 update: a report from the American Heart Association. Circulation 2014; 129: e28-e292.

4. Herman ST. Epilepsy after brain insult. Targeting epileptogenesis. Neurology 2002; 59 (Suppl 5): S21-S26.

5. Kawai K, Nitecka L, Reutzler CA, Nagashima G, Joó F, Mies G, Nowak TS, Saito N, Lohr JM, Klatzo I. Global cerebral ischaemia associated with cardiac arrest in the rat: I. Dynamics of early neuronal changes J Cereb Blood Flow Metab 1992; 12: 238-249.

6. Kawai K, Penix LP, Ruetzler CA, Nitecka L, Lohr JM, Klatzo I. Effect of cardiac arrest cerebral ischaemia on the GABA-ergic system and development of audiogenic seizures. In: Pharmacology of Cerebral Ischaemia. Krieglstein J, Oberpichler-Schwenk H (eds.). Wissenschaftliche Verlaggesellschaft, Stuttgart 1992; pp. 195-206.

7. Kawai K, Penix LP, Kawahara N, Ruetzler CA, Klatzo I. Development of susceptibility to audiogenic seizures following cardiac arrest cerebral ischaemia in rats. J Cereb Blood Flow Metab 1995; 15: 248-258.

8. Kiryk A, Pluta R, Figiel I, Mikosz M, Ułamek M, Niewiadomska G, Jabłoński M, Kaczmarek L. Transient brain ischaemia due to cardiac arrest causes irreversible long-lasting cognitive injury. Behav Brain Res 2011; 219: 1-7.

9. Krumholz A, Stern BJ, Weiss HD. Outcome from coma after cardiopulmonary resuscitation: relation to seizures and myoclonus. Neurology 1988; 38: 401-405.

10. Maślińska D, Laure-Kamionowska M, Taraszewska A, Deręgowski K, Maśliński S. Immunodistribution of amyloid beta protein (Aβ) and advanced glycation end-product receptors (RAGE) in choroid plexus and ependyma of resuscitated patients. Folia Neuropathol 2011; 49: 295-300.

11. Moulaert VRMP, Verbunt JA, van Heugten CM, Wade DT. Cognitive impairments in survivors of out-of-hospital cardiac arrest: A systematic review. Resuscitation 2009; 80: 297-305.

12. North BJ, Sinclair DA. The intersection between aging and cardiovascular disease. Circ Res 2012; 110: 1097-1108.

13. O'Reilly SM, Grubb NR, O'Carroll RE. In-hospital cardiac arrest leads to chronic memory impairment. Resuscitation 2003; 58: 73-79.

14. Pluta R. Influence of prostacyclin on early morphological changes in the rabbit brain after complete 20-min ischaemia. J Neurol Sci 1985; 70: 305-316.

15. Pluta R, Salińska E, Puka M, Stafiej A, Łazarewicz JW. Early changes in extracellular amino acids and calcium concentrations in rabbit hippocampus following complete 15-min cerebral ischaemia. Resuscitation 1988; 16: 193-210.

16. Pluta R, Lossinsky AS, Mossakowski MJ, Faso L, Wiśniewski HM. Reassessment of new model of complete cerebral ischaemia in rats. Method of induction of clinical death, pathophysiology and cerebrovascular pathology. Acta Neuropathol 1991; 83: 1-11.

17. Pluta R, Lossinsky AS, Wiśniewski HM, Mossakowski MJ. Early blood-brain barrier changes in the rat following transient complete cerebral ischaemia induced by cardiac arrest. Brain Res 1994; 633: 41-52.

18. Pluta R. The role of apolipoprotein E in the deposition of beta-amyloid peptide during ischaemia-reperfusion brain injury. A model of early Alzheimer's disease. Ann NY Acad Sci 2000; 903: 324-334.

19. Pluta R. Glial expression of the β-amyloid peptide in cardiac arrest. J Neurol Sci 2002; 203-204: 277-280.

20. Pluta R, Ułamek M, Jabłoński M. Alzheimer's mechanisms in ischaemic brain degeneration. Anat Rec 2009; 292: 1863-1881.

21. Pluta R, Ułamek-Kozioł M, Januszewski S, Ściślewska M, Bogucka-Kocka A, Kocki J. Alzheimer's factors in postischaemic dementia. Rom J Morphol Embryol 2012; 53: 461-466.

22. Pluta R, Jabłoński M, Czuczwar SJ. Postischaemic dementia with Alzheimer phenotype: selectively vulnerable versus resistant areas of the brain and neurodegeneration versus β-amyloid peptide. Folia Neuropathol 2012; 50: 101-109.

23. Pluta R, Furmaga-Jabłońska W, Maciejewski R, Ułamek-Kozioł M Jabłoński M. Brain ischaemia activates β- and γ-secretase clea-

vage of amyloid precursor protein: significance in sporadic Alzheimer's disease. Mol Neurobiol 2013; 47: 425-434.

24. Pluta R, Jabłoński M, Ułamek-Kozioł M, Kocki J, Brzozowska J, Januszewski S, Furmana- Jabłońska W, Bogucka-Kocka A, Maciejewski R, Czuczwar SJ. Sporadic Alzheimer's disease begins as episodes of brain ischaemia and ischaemically dysregulated Alzheimer's disease genes. Mol Neurobiol 2013; 48: 500-515.

25. Preston E, Sutherland G, Finsten A. Three openings of the blood-brain barrier produced by forebrain ischaemia in the rat. Neurosci Lett 1993; 149: 75-78.

26. Qi J, Wu H, Yang Y, Wand D, Chen Y, Gu Y, Liu T. Cerebral ischaemia and Alzheimer's disease: The expression of amyloid-β and apolipoprotein E in human hippocampus. J Alzheimer's Dis 2007; 12: 335-341.

27. Saver JL. Time is brain-quantified. Stroke 2006; 37: 263-266.

28. Sekeljic V, Bataveljic D, Stamenkovic S, Ułamek M, Jabłoński M, Radenovic L, Pluta R, Andjus PR. Cellular markers of neuroinflammation and neurogenesis after ischaemic brain injury in the long-term survival rat model. Brain Struct Funct 2012; 217: 411-420.

29. Wijdicks EF, Parisi JE, Sharbrough FW. Prognostic value of myoclonic status in comatose survivors of cardiac arrest. Ann Neurol 1994; 35: 239-243.

30. Young GB. Clinical practice. Neurologic prognosis after cardiac arrest. N Engl J Med 2009; 361: 605-611.

http://rcin.org.pl

Folia
Neuropathologica

Rapamycin protects dopaminergic neurons against rotenone-induced cell death in primary mesencephalic cell culture

Khaled Radad[1], Rudolf Moldzio[2], Wolf-Dieter Rausch[2]

[1]Department of Pathology, Faculty of Veterinary Medicine, Assiut University, Egypt, [2]Institute of Medical Biochemistry, Department for Biomedical Sciences, University of Veterinary Medicine, Vienna, Austria

Abstract

Introduction: *Parkinson's disease is the most common movement disorder, characterized by a progressive and extensive loss of dopaminergic neurons in the substantia nigra pars compacta and their terminals in the striatum. So far, only symptomatic treatment is available, and no cure or disease-modifying drugs exist. The present study was designed to investigate the neuroprotective effect of rapamycin, an autophagy inducer, on dopaminergic neurons against rotenone-induced cell death in primary mesencephalic cell culture.*

Material and methods: *Primary mesencephalic cell cultures were prepared from embryonic mouse mesencephala (OFI/SPF, Vienna, Austria) at gestation day 14. Four sets of cultures were treated as follows: one was run as an untreated control, a second one was treated with 20 nM rotenone on the 10th day in vitro (DIV) for 48 h, a third one was co-treated with 20 nM rotenone and rapamycin (1, 10, 100, 1000 nM) on the 10th DIV for 48 h, and a fourth one was treated with rapamycin alone (1, 10, 100, 1000 nM) on the 10th DIV for 48 h. On the 12th DIV, cultures were subjected to immunohistochemistry against tyrosine hydroxylase and to fluorescence staining using LysoTracker Deep Red, JC-1 and DAPI stains.*

Results: *Exposure of such cultures to 20 nM rotenone on the 10th DIV for 48 h reduced the number of dopaminergic neurons by 41% and increased the release of lactate dehydrogenase (LDH) by 178% above untreated controls. Rapamycin (1, 10, 100, 1000 nM) added together with rotenone from the 10th to 12th DIV spared dopaminergic neurons by 17% and reduced the release of LDH by 64% at the concentration of 100 nM compared to rotenone-treated cultures. Activation of an autophagic process by rapamycin was demonstrated by LysoTracker Deep Red fluorescent dye, as indicated by a shift to increased red fluorescence. Rapamycin also significantly elevated the mitochondrial membrane potential ($\Delta\psi$m), as shown by an increase of the red:green fluorescence ratio of JC-1. Increased apoptotic cell death due to rotenone was lowered by rapamycin, as shown by the blue-fluorescent DAPI nucleic acid stain.*

Conclusions: *Our study indicates for the first time that rapamycin, known as an autophagy inducer, protected dopaminergic neurons against rotenone-induced cell death in primary mesencephalic cell culture.*

Key words: *apoptosis, autophagy, dopaminergic neurons, neuroprotection, Parkinson's disease, rapamycin.*

Communicating author:

Khaled Radad, PhD, Department of Pathology, Faculty of Veterinary Medicine, Assiut University, Egypt,
e-mail: khaledradad@hotmail.com

Introduction

Parkinson's disease (PD) is a common progressive neurodegenerative disorder affecting more than 6 million people worldwide [28]. The disease is characterized clinically by a triad of cardinal motor symptoms including bradykinesia, tremors and rigidity [13], and pathologically by the selective loss of dopamine neurons in the substantia nigra pars compacta (SNpc) and the formation of Lewy bodies [27]. Although the etiology of PD is still unclear, there is growing evidence indicating that intracellularly oxidative stress, mitochondrial damage, lysosomal dysfunction, neuroinflammatory changes and formation of pathologic inclusions contribute to the pathology of the disease [9].

Treatment of PD is generally symptomatic, where levodopa remains the most effective agent [34]. However with disease progression, levodopa medication becomes increasingly inadequate for the management of motor fluctuations and dyskinesias [40]. Levodopa given clinically undergoes autooxidation and forms reactive oxygen species (ROS) which could be toxic to remaining dopamine neurons [20]. Dopamine agonists and monoamine oxidase B inhibitors are also prescribed for the treatment of early PD as in addition to their symptomatic benefits they postpone the onset of levodopa therapy [11].

During the last two decades, researchers have shown increased interest in developing neuroprotective substances that can slow or stop the clinical progression of PD. As a result, significant numbers of compounds have been identified as neuroprotective in preclinical studies [8]. For instance, the D3/D2/D1 dopamine receptor agonist rotigotine was shown to protect dopaminergic neurons against glutamate, MPP+ and rotenone in primary mesencephalic cell culture [23,32]. The active principal of *Nigella sativa* seed thymoquinone protected dopaminergic neurons against MPP+-induced cell death in primary mesencephalic cell culture [30]. Inhibition of sphingosine kinase (Sphk1), a regulator of bioactive sphingolipid homeostasis, by SKI II protected the dopaminergic SH-SY5Y cells through an antiapoptotic pathway [29]. However, to date, there is no drug that has provided neuroprotection against dopaminergic cell loss in clinical trials [4].

Rapamycin is a lipophilic macrocyclic antibiotic produced by the bacterium *Streptomyces hygroscopicus* indigenous to Easter Island [38]. Rapamycin was shown first to exhibit antibacterial, antifungal, immunosuppressive and anticancer effects [33]. Recently, rapamycin has been reported to reduce cytotoxic injury in different models of neurodegenerative disorders [5]. For instance, Park *et al.* [26] reported that rapamycin protected human neuroblastoma SH-SY5Y cells against fipronil-induced apoptotic cell death. Kanno *et al.* [18] found that rapamycin reduced locomotor impairment and neuronal death after spinal cord injury in mice. This effect of rapamycin was reported to be mediated through activation of autophagy by inhibiting the mammalian target of rapamycin (mTOR) signaling pathways [36].

More recently, studies using post-mortem human tissues and genetic and toxin-induced animal and cellular models have implicated autophagy dysfunction as an important issue in PD pathogenesis [1]. For instance, Dehay *et al.* [7] reported that the number of undegraded autophagosomes increased and the number of autophagolysosomes decreased in post-mortem PD brain samples. Park *et al.* [25] showed that MPP+ inhibited autophagosome formation and increased α-synuclein expression in mice. Parganlija *et al.* [24] found that SH-SY5Y cells with PINK1 knockdown showed down-regulation of key autophagic genes including Beclin, LC3 and LAMP-2. Accordingly, our present study was designed to investigate the neuroprotective potential of the autophagy inducer rapamycin against rotenone-induced dopaminergic cell death relevant to PD. To date, there have been no reports describing the potential neuroprotective role of rapamycin on dopamine neurons in primary mesencephalic cell culture relevant to PD.

Material and methods

Preparation of primary mesencephalic cell culture

Primary mesencephalic cell cultures were prepared from OFI/SPF embryos according to Meinel *et al.* [22]. In brief, embryonic mouse mesencephala were dissected on the 14th day of gestation and cut into small pieces in a drop of DPBS (Invitrogen, Germany), 2 ml of 0.2% trypsin solution (Invitrogen, Germany) and 2 ml of 0.02% DNase I solution (Roche, Germany) were added and the tissue was subsequently incubated in a water bath at 37°C for 7 min. Then, 2 ml of trypsin inhibitor (0.125 mg/ml) (Invitrogen, Ger-

many) were added, the tissue was centrifuged at 100 × g for 4 min and the supernatant was aspirated. The tissue pellet was triturated 2-3 times with a fire-polished Pasteur pipette; each time 0.02% DNase I (Invitrogen, Germany) was included in the medium. Dissociated cells were plated at a density of 257 000 cells/cm^2 in DMEM (Sigma, Germany) supplemented with 4 mM glutamine, 10 mM HEPES buffer, 30 mM glucose, 100 IU/ml penicillin, 0.1 mg/ml streptomycin and 10% heat-inactivated fetal calf serum (Sigma, Germany). The medium was exchanged on the 1st day *in vitro* (DIV) and on the 3rd DIV. On the 5th DIV half of the medium was replaced with serum-free DMEM containing 0.02 ml of B-27/ml (Invitrogen, Germany) DMEM. Serum-free supplemented DMEM was used for feeding from the 6th DIV and subsequently replaced every 2nd day.

Treatment of cultures with rapamycin

A stock solution of 1 mM rapamycin (Invitrogen, USA) was prepared in dimethyl sulfoxide (DMSO) and further diluted in DMEM to final concentrations. On the 10th DIV, cultures were treated with rapamycin (1, 10, 100, 1000 nM) for 48 h to investigate its effect on the survival of dopaminergic cells.

Treatment of cultures with rapamycin and rotenone

A stock solution of 1 µM of rotenone (Sigma-Aldrich, Germany) was prepared in DMSO and then diluted in DMEM to final concentrations. For each treatment, fresh rotenone solutions were used to avoid breakdown of rotenone by storage. To investigate the neuroprotective potential of rapamycin against rotenone-induced dopaminergic cell death, cultures were co-administered with both rotenone (20 nM) and rapamycin (1, 10, 100, 1000 nM) on the 10th DIV for 48 h.

Identification of dopaminergic neurons

Dopaminergic neurons were identified immunocytochemically by tyrosine hydroxylase staining. On the 12th DIV, cultures were rinsed carefully with phosphate buffered saline (PBS, pH 7.2) and fixed in 4% paraformaldehyde for 45 min at 4°C. After washing with PBS, cells were permeabilized with 0.4% Triton X-100 for 30 min at room temperature. Cultures were washed 3 times with PBS and incubated with 5% horse serum (Vectastain ABC Elite kit) for 90 min

to block nonspecific binding sites. To determine the number of tyrosine hydroxylase immunoreactive (THir) cells, cultures were sequentially incubated with anti-TH primary antibody overnight at 4°C, biotinylated secondary antibody (Vectastain) and avidin-biotin-horseradish peroxidase complex (Vectastain) for 90 min at room temperature and washed with PBS between stages. The reaction product was developed in a solution of diaminobenzidine (1.4 mM) in PBS containing 3.3 mM hydrogen peroxide (H$_2$O$_2$), and stained cells were counted with a Nikon inverted microscope in 10 randomly selected fields per well at 10× magnification.

Measurement of LDH activity

Cellular injury was quantitatively assessed by measuring the activity of lactate dehydrogenase (LDH) released from damaged cells into the culture medium. The reaction was initiated by mixing 0.2 ml of cell-free supernatant (diluted 1 : 1 with distilled water) with potassium phosphate buffer containing β-nicotinamide adenine dinucleotide (NADH) and sodium pyruvate (0.18 and 0.62 mM in potassium phosphate buffer, respectively) in a final volume of 0.5 ml in 1 ml cuvettes. The decrease of NADH was spectrophotometrically (NOVASPEC1 II) monitored. Reagent blanks were subtracted. LDH activity was calculated from the slope of the decrease in optical density at 334 nm over a 3 min time period. The LDH release is proportional to the number of damaged or destroyed cells [10,19].

Staining of cultured cells with LysoTracker Deep Red fluorescent dye

LysoTracker dye is a highly soluble small molecule that is retained in acidic subcellular organelles such as lysosomes. It is used to investigate the biosynthesis of lysosomes. Here, 100 nM rapamycin (the concentration significantly protected dopaminergic neurons in rotenone-treated cultures) was added together with 20 nM rotenone on the 10th DIV for 48 h. On the 12th DIV, culture media were aspirated and cells were incubated with a new medium containing 100 nM LysoTracker Deep Red fluorescent dye (Life Technologies, Invitrogen, USA) for 15-30 min at 37°C. After washing with DPBS, stained cells were photographed on a Nikon inverted microscope equipped with an epifluorescence attachment using a rhodamine filter set with an excitation wavelength

of 580 and an emission wavelength of 590, G-2A and a Coolpix 990 digital camera (Nikon, Japan). Six photos were taken randomly from each well (24 photos per experiment). All photos were analyzed densitometrically using Adobe Photoshop software.

Measurement of $\Delta\psi$m by JC-1 fluorescent dye

JC-1 is a lipophilic cationic dye that selectively enters mitochondria. In healthy cells with high mitochondrial $\Delta\psi$m, JC-1 spontaneously forms complexes known as J-aggregates with intense red fluorescence. In the case of apoptotic cells the dye remains in its monomeric form with green fluorescence. The JC-1 red:green ratio has been used as a tool to estimate changes in $\Delta\psi$m [39]. JC-1 was dissolved in DMSO and further diluted in DMEM (10 μg/ml final concentration). After removal of the culture medium cells were loaded with JC-1 for 15 min at 37°C, rinsed twice with PBS and photographed on a Nikon inverted microscope equipped with an epifluorescence attachment using a rhodamine filter set with an excitation wavelength of 510 DM and an emission wavelength of 520 BA and a Coolpix 990 digital camera (Nikon, Japan). Six photos were taken randomly from each well (24 photos per experiment). Fluorescence intensity of the red:green ratio was determined semiquantitatively using Adobe Photoshop software.

Counting of apoptotic cells by blue-fluorescent DAPI nucleic acid stain

DAPI is a fluorescent stain that binds strongly to DNA. It passes through intact membranes of live and fixed cells. Cells were fixed with 4% paraformaldehyde for 45 min at 4°C. After washing with PBS (pH 7.2), cells were permeabilized with 0.4% Triton X-100 for 30 min at room temperature. DAPI solution (2 μM final concentration) was added to the cultures at room temperature for 5 min in the dark. After washing with DPBS, six photos were taken randomly from each well (24 photos per experiment) with a Coolpix 990 digital camera connected to an inverted microscope with an epifluorescence attachment using an ultraviolet (UV) filter (Nikon, Japan). Nuclei with condensed and fragmented chromatin were counted when the photos were reviewed with Adobe Photoshop software.

Statistics

Each experiment was run in triplicate with four wells in each treatment. Data were expressed as mean ± standard error of mean (SEM). Comparisons were made using ANOVA and post-hoc Duncan's test using the statistical program SAS 1998. $P < 0.05$ was considered as statistically significant.

Results

Rapamycin did not affect the survival of dopaminergic neurons

Treatment of cultures with rapamycin (1, 10, 100, 1000 nM) on the 10th DIV for 48 h did not affect the survival (Fig. 1) or the morphology of dopaminergic neurons (data not shown).

Rapamycin rescued dopaminergic neurons from rotenone-induced cell death

Treatment of cultures with 20 nM rotenone on the 10th DIV for 48 h decreased the number of dopaminergic neurons by 41% and altered the morphology of surviving neurons compared to untreated controls (Fig. 2A,B). On the other hand, co-administration of rapamycin and rotenone on the 10th DIV for 48 h significantly increased the survival of dopaminergic

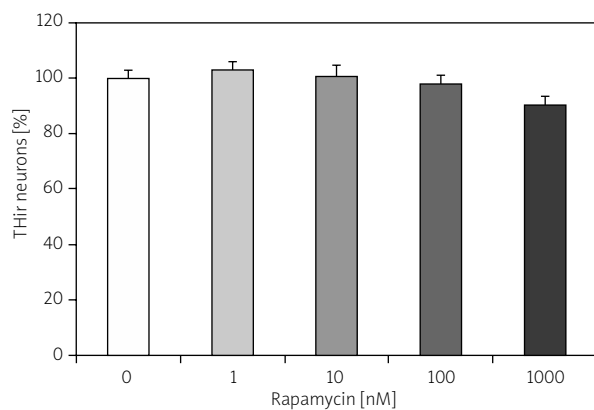**Fig. 1.** Treatment of primary mesencephalic cell cultures with rapamycin on the 10th DIV for 48 h. 100% corresponds to the total number of THir neurons (the average number of THir neurons was 26 cells/field) after 12 DIV in untreated controls. Values represent the mean ± SEM of three independent experiments with four wells in each treatment. In each well THir neurons were counted in ten randomly selected fields.
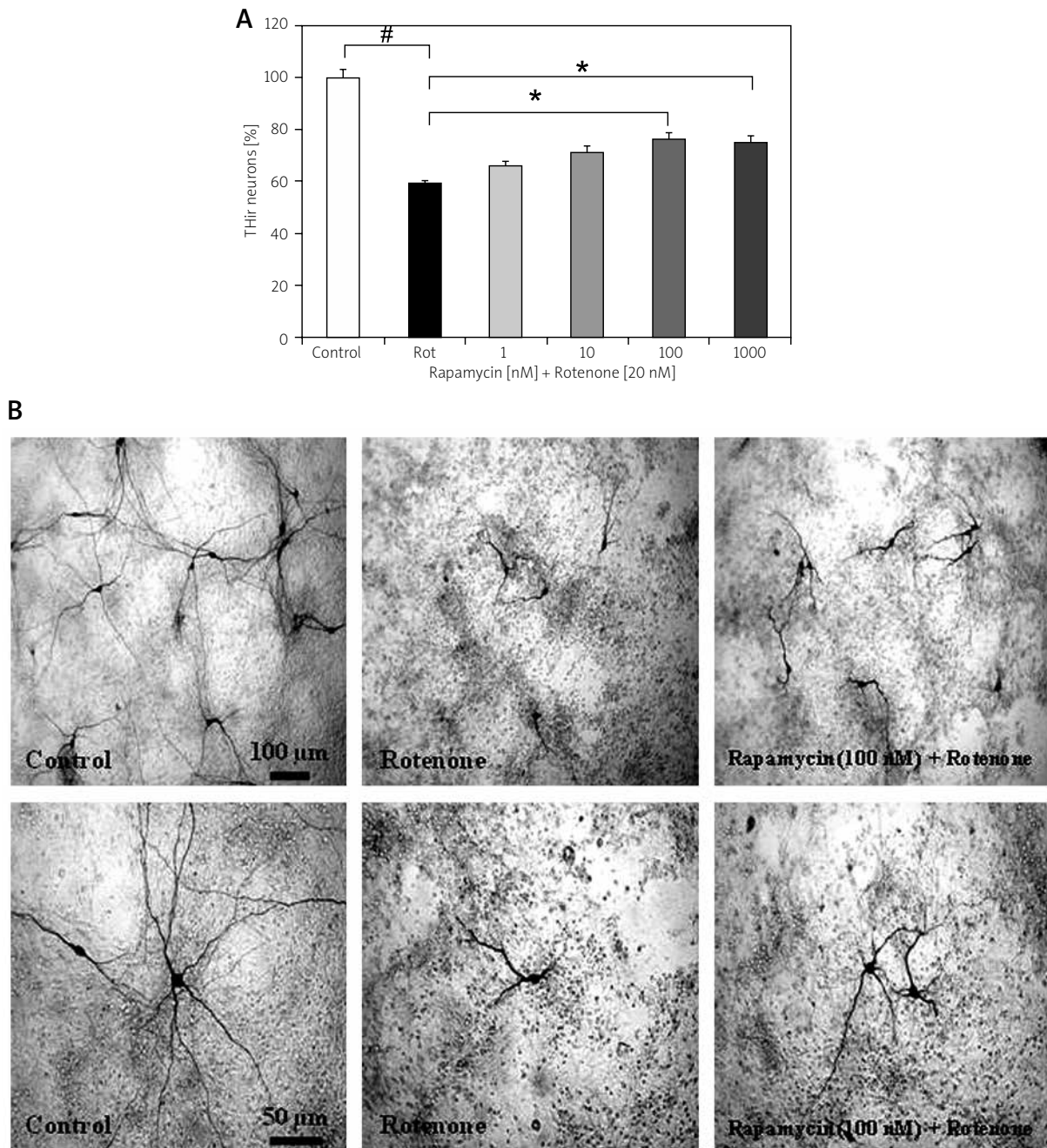
http://rcin.org.pl

A

B

Fig. 2. A) Concomitant treatment of primary mesencephalic cell cultures with rotenone (20 nM) and rapamycin (1, 10, 100, 1000 nM) on the 10th DIV for 48 h. 100% corresponds to the total number of THir neurons (the average number of THir neurons was 23 cells/field) after 12 DIV in untreated controls. Values represent the mean ± SEM of three independent experiments with four wells in each treatment. In each well THir neurons were counted in ten randomly selected fields ([#]$p < 0.001$, [*]$p < 0.001$). **B)** Representative micrographs of THir neurons after 12 DIV. Untreated control cultures showed THir neurons with long and branched processes. Rotenone-treated cultures showed THir neurons with very few, shortened and thickened neurites. Treatment with rapamycin improves the morphology of THir neurons compared to rotenone-treated cultures.
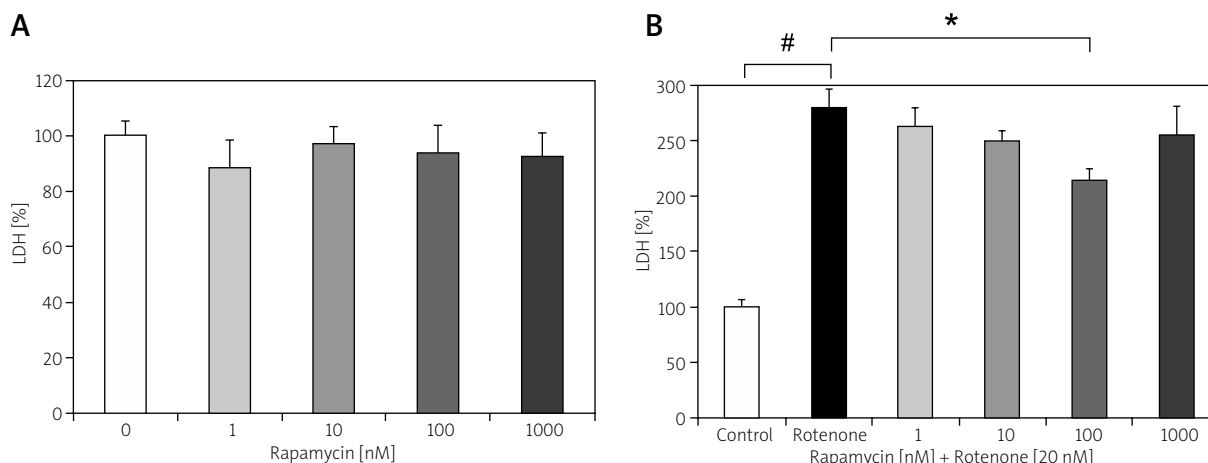
Fig. 3. Release of LDH into the culture medium in primary mesencephalic cell cultures. **A)** Treatment of cultures with rapamycin on the 10th DIV for 48 h. **B)** Concomitant treatment of cultures with rotenone (20 n*M*) and rapamycin (1, 10, 100, 1000 nM) on the 10th DIV for 48 h. 100% corresponds to the amount of LDH in the culture medium after 12 DIV. Values represent the mean ±SEM of three independent experiments with four wells in each treatment ([#]p < 0.001, [*]p < 0.001).

neurons by 17% compared to rotenone-treated cultures (Fig. 2A). Also, rapamycin reduced degenerative changes in dopaminergic neurons seen with rotenone exposure (Fig. 2B).

Rapamycin attenuated rotenone-induced LDH release

Treatment of cultures with rapamycin on the 10th DIV for 48 h did not affect the level of LDH in the culture medium (Fig. 3A). Consistent with the cytotoxic effect of rotenone on dopaminergic neurons, 20 nM rotenone led to an increase in release of LDH into the culture medium by 178% compared to untreated controls (Fig. 4B). Against rotenone, rapamycin (100 nM) reduced the release of LDH by 64% compared to rotenone-treated cultures (Fig. 3B).

Rapamycin increased LysoTracker Deep Red fluorescence

Co-treatment of cultures with rapamycin (100 nM) and rotenone (20 nM) on the 10th DIV for 48 h significantly increased the fluorescent intensity of LysoTracker Deep Red by about 63% compared to rotenone-treated cultures (Fig. 4A). In parallel, Fig. 4B shows higher red fluorescence in the cultures co-treated with rapamycin and rotenone compared to cultures treated with rotenone alone. Rapamycin alone did not produce a significant increase in the

fluorescent intensity of LysoTracker Deep Red compared to untreated control culture (Fig. 4A,B).

Rapamycin increased red: green fluorescence ratio of JC-1

Treatment of cultures with rotenone (20 nM) on the 10th DIV for 48 h decreased the red:green fluorescent ratio of JC-1 by about 29% compared to untreated controls (Fig. 5A). On the other hand, concomitant treatment of cultures with 100 nM rapamycin and 20 nM rotenone on the 10th DIV for 48 h significantly restored the red:green fluorescent ratio of JC-1 by 19% compared to rotenone-treated cultures (Fig. 5A). Figure 5B showed that cultures co-administered with rapamycin and rotenone displayed much higher red fluorescence than the cultures treated with rotenone alone. Rapamycin alone did not significantly affect the red:green fluorescent ratio of JC compared to untreated control culture (Fig. 5A,B).

Rapamycin decreased rotenone-induced apoptotic cell death

Staining of cultured cells with the nuclear fluorescence dye DAPI revealed that rotenone (20 nM on the 10th DIV for 48 h) increased the number of nuclei showing apoptotic features by 119% compared to untreated cultures (Fig. 6A). Against rotenone, rapamycin was found to decrease the number of apoptotic
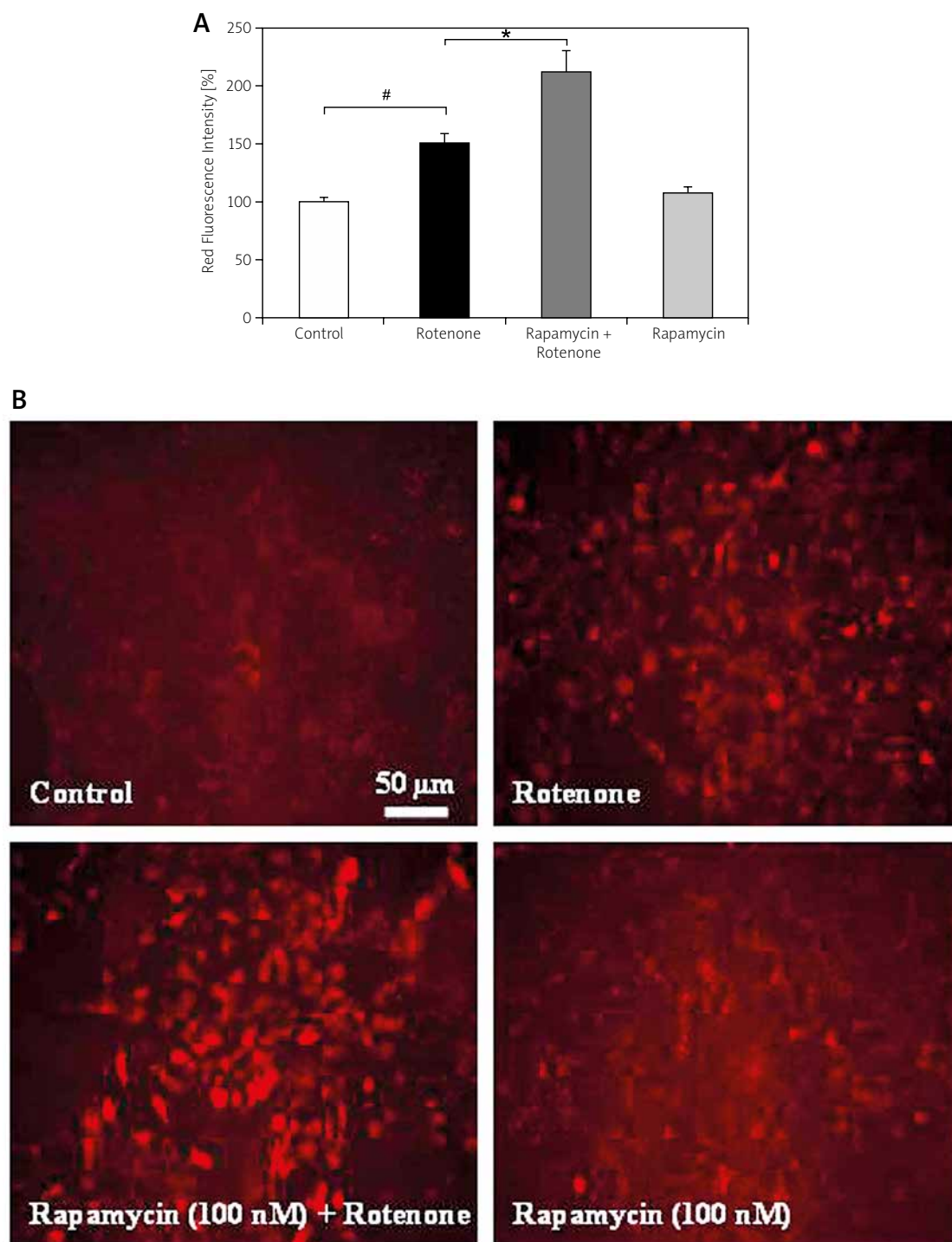
Fig. 4. A) LysoTracker Deep Red fluorescence intensity in primary mesencephalic cell cultures. 100% corresponds to the intensity of LysoTracker Deep Red in primary mesencephalic cell cultures after 12 DIV. Values represent the mean ± SEM of three independent experiments with four wells in each treatment. Fluorescence intensity was determined densitometrically from 24 randomly selected micrographs in each experiment (6 photos from each well) ($^{\#}p < 0.01$, $^{*}p < 0.001$). **B)** Representative micrographs showing that treatment of cultures with rapamycin increased LysoTracker Deep Red fluorescence intensity compared to rotenone-treated cultures.
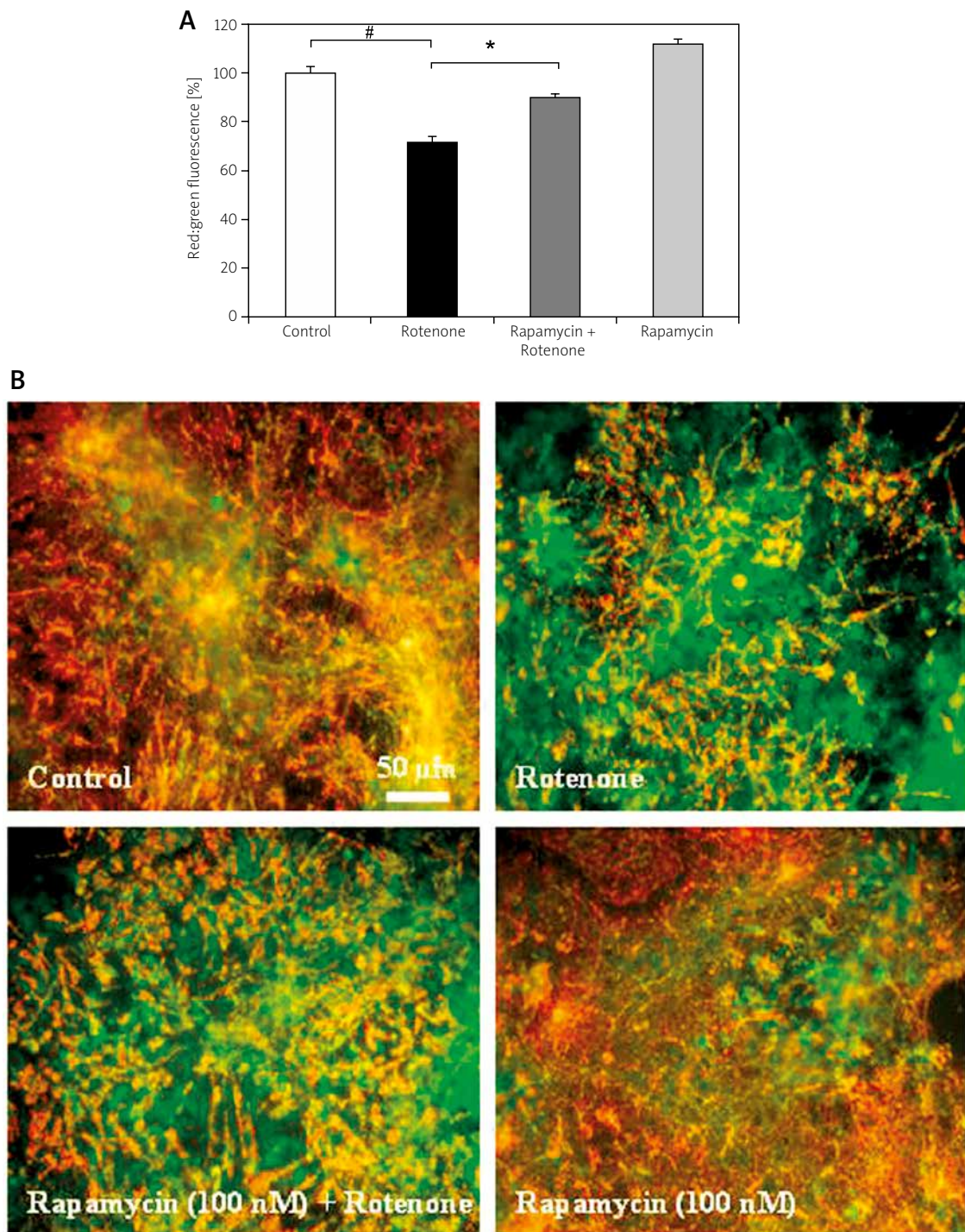
Fig. 5. A) Red:green fluorescence ratio of JC-1 in primary mesencephalic cell cultures. 100% corresponds to the red:green fluorescence ratio of JC-1 in primary mesencephalic cell cultures after 12 DIV. Values represent the mean ± SEM of three independent experiments with four wells in each treatment. Red:green fluorescence ratio of JC-1 was determined densitometrically from 24 randomly selected micrographs in each experiment (6 photos from each well) ($^{\#}p < 0.001$, $^{*}p < 0.001$). **(B)** Representative micrographs showing that treatment of cultures with rapamycin increased red fluorescence compared to rotenone-treated cultures which exhibit marked green fluorescence.
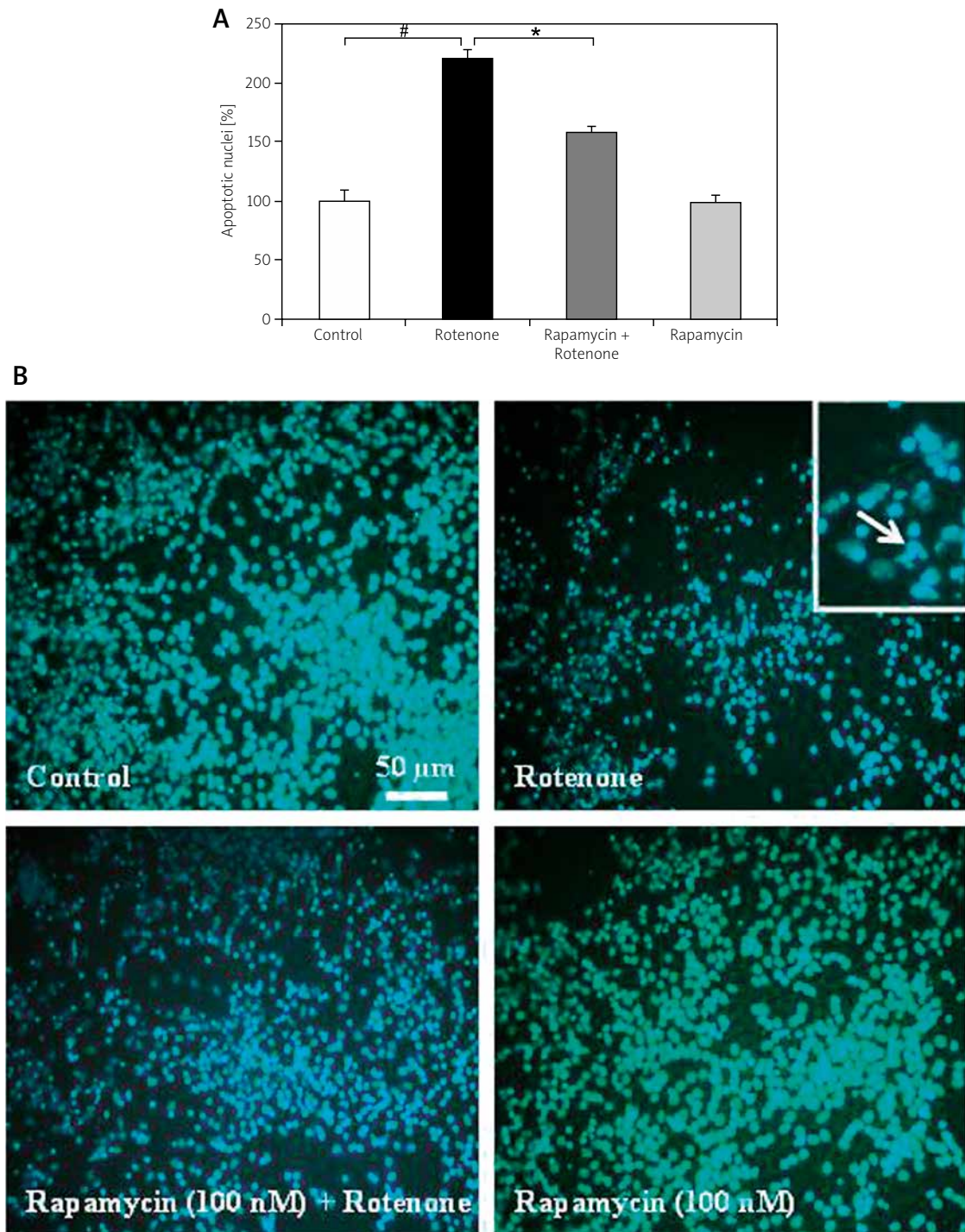
Fig. 6. **(A)** Number of nuclei showing apoptotic features with condensed and fragmented chromatin in primary mesencephalic cell cultures. 100% corresponds to the number of apoptotic nuclei (the average number of apoptotic nuclei was 38 nuclei/photo) in untreated control cultures after 12 DIV. Values represent the mean ± SEM of three independent experiments with four wells in each treatment. Twenty-four photos were taken from each experiment (6 photos from each well) ($^{#}p < 0.001$, $^{*}p < 0.001$). **B)** Representative micrographs showing that treatment of cultures with rapamycin decreased the number of apoptotic nuclei compared to rotenone-treated cultures. Insert shows apoptotic nuclei at 20× magnification.

http://rcin.org.pl

nuclei by about 100% compared to rotenone-treated cultures (Fig. 6A). Apoptotic nuclei showed highly condensed and fragmented chromatin (Fig. 6B). Rapamycin alone did not affect the number of apoptotic nuclei compared to untreated control culture (Fig. 6A,B).

Discussion

In the present study, rotenone-treated primary mesencephalic cell culture was used as a neurotoxicity model to investigate the neuroprotective potential of the autophagy inducer rapamycin on dopaminergic neurons relevant to PD. In summary, rotenone was shown to 1) decrease the survival of dopaminergic neurons; 2) increase the release of LDH into the culture medium; 3) disrupt the mitochondrial $\Delta\psi m$ of cultured cells and 4) increase the features of apoptotic cell death in primary mesencephalic cell culture. This neurotoxic effect of rotenone has been reported in different *in vitro* and *in vivo* models since Betarbet and her colleagues [3] described rotenone as a PD neurotoxin in 2000. For instance, Radad *et al.* [31] found that exposure of primary mesencephalic cell culture to 20 nM rotenone destroyed dopaminergic neurons and resulted in a higher level of LDH in the culture medium. Im *et al.* [15] reported that rotenone decreased the viability and survival of PC12 cells. Tapias *et al.* [37] described a loss of dopamine neurons and nigrostriatal terminals as a result of rotenone treatment in rats. Using JC-1 and DAPI fluorescence dyes we showed that rotenone decreased the $\Delta\psi m$ and induced apoptotic cell death in our mesencephalic cell cultures, as indicated by the decreased red:green fluorescence ratio of JC-1 and increased number of nuclei with condensed and fragmented chromatin, respectively. Similarly, Hu *et al.* [14] demonstrated that rotenone caused a loss of $\Delta\psi m$ and induced apoptotic cell death in SH-SY5Y cells. Mitochondrial damage by rotenone played a central role in apoptotic cell death through interrupting cellular energy metabolism, increasing ROS production and the release of apoptotic factors into the cytosol [2].

Our results showed that rapamycin rescued a significant number of dopaminergic neurons and decreased the release of LDH into the culture medium when concomitantly added with rotenone to primary mesencephalic cell cultures. Likewise, similar neuroprotective effects of rapamycin have been reported in some *in vitro* and *in vivo* models of neurodegeneration. For example, Malagelada *et al.* [21] found that

rapamycin protected PC12 cells from 6-OHDA toxicity. Jiang *et al.* [16] observed that rapamycin provided behavioral improvements and protected against the loss of dopaminergic neurons in a rat model of PD.

Rapamycin increased cellular fluorescence of LysoTracker Deep Red compared to rotenone-treated cultures, indicating that rapamycin upregulated an autophagic process in cultured cells. In line with our results, Chikte *et al.* [6] reported that the signals of LysoTracker Deep Red were increased as the result of rapamycin treatment and could be used as a marker for autophagy in Jurkat T-cell and K562 erythro-myeloid cell lines. He and Klionskey [12] also correlated the fluorescence signals of LysoTracker with the upregulation of autophagy in zebrafish. Staining of cultures co-administered with rapamycin and rotenone with JC-1 fluorescent dye showed that rapamycin enhanced $\Delta\psi m$ as it increased the red:green fluorescence ratio of JC-1 compared to cultures treated with rotenone alone. Rapamycin was similarly reported to enhance $\Delta\psi m$ in the human breast cancer cell line MCF-7, as shown by the JC-1 potentiometric dye [24]. Moreover, rapamycin was reported to ameliorate mitochondrial defects in cells from individuals with the PARK2 mutation through rescuing $\Delta\psi m$ [35]. Counting of apoptotic nuclei using blue-fluorescent DAPI nucleic acid stain indicated that rapamycin decreased rotenone-induced apoptotic cell death in primary mesencephalic cell cultures. Yin *et al.* [41] and Jing *et al.* [17] similarly reported an antiapoptotic effect for rapamycin against transient focal cerebral ischemia/reperfusion and subarachnoid hemorrhage in mice and rats, respectively. The antiapoptotic effect of rapamycin was reported to be mediated by decreasing Bax production and the downstream release of cytochrome c from mitochondria to the cytosol [17]. In addition to aforementioned mechanisms of neuroprotection, rapamycin was found to protect neuronal cells through some other pathways. In this context, Tain *et al.* [35] found that activation of the translation inhibitor 4E-BP protected dopaminergic neurons in parkin and PINK1 mutant *Drosophila*. Jiang *et al.* [16] reported that reduction of oxidative stress is one of the underlying mechanisms that mediate neuroprotection in a 6-OHDA rat model of PD.

Taking all the data together, our study shows that rapamycin protected dopaminergic neurons against rotenone-induced cell death in primary mesencephalic cell culture. This neuroprotection might be attributed to increasing autophagy, enhancing mitochondrial

http://rcin.org.pl

membrane potential and decreasing apoptotic cell death in primary mesencephalic cell culture.

Disclosure

The authors report no conflict of interest.

References

1. Banerjee R, Beal MF, Thomas B. Autophagy in neurodegenerative disorders: pathogenic roles and therapeutic implications. Trends Neurosci 2010; 33: 541-549.
2. Beal MF. Energetics in the pathogenesis of neurodegenerative diseases. Trends Neurosci 2000; 23: 298-304.
3. Betarbet R, Sherer TB, MacKenzie G, Garcia-Osuna M, Panov AV, Greenamyre JT. Chronic systemic pesticide exposure reproduces features of Parkinson's disease. Nat Neurosci 2000; 3: 1301-1306.
4. Boll MC, Alcaraz-Zubeldia M, Rios C. Medical management of Parkinson's disease: focus on neuroprotection. Curr Neuropharmacol 2011; 9: 350-359.
5. Carloni S, Buonocore G, Longini M, Proietti F, Balduini W. Inhibition of rapamycin-induced autophagy causes necrotic cell death associated with Bax/Bad mitochondrial translocation. Neuroscience 2012; 203: 160-169.
6. Chikte S, Panchal N, Warnes G. Use ofLysoTracker dyes: A flow cytometric study of autophagy. Cytometry A 2014; 85: 169-178.
7. Dehay B, Bové J, Rodríguez-Muela N, Perier C, Recasens A, Boya P, Vila M. Pathogenic lysosomal depletion in Parkinson's disease. J Neurosci 2010; 30: 12535-12544.
8. Douna H, Bavelaar BM, Pellikaan H, Olivier B. Neuroprotection in Parkinson's disease: A systemic review of the preclinical data. The Open Pharmacology Journal 2012; 6: 12-26.
9. Eriksen JL, Wszolek Z, Petrucelli L. Molecular pathogenesis of Parkinson disease. Arch Neurol 2005; 62: 353-357.
10. Gwag BJ, Lobner D, Koh JY, Wie MB, Choi DW. Blockade of glutamate receptors unmasks neuronal apoptosis after oxygen-glucose deprivation in vitro. Neuroscience 1995; 68: 615-619.
11. Hauser RA. Early pharmacologic treatment in Parkinson's disease. Am J Manag Care 2010; 16: 100-107.
12. He C, Klionsky DJ. Analyzing autophagy inzebrafish. Autophagy 2010; 6: 642-644.
13. Hirsch EC. Future drug targets for Parkinson's disease. Bull Acad Natl Med 2012; 196: 1369-1377.
14. Hu LF, Lu M, Wu ZY, Wong PT, Bian JS. Hydrogen sulfide inhibits rotenone-induced apoptosis via preservation of mitochondrial function. Mol Pharmacol 2009; 75: 27-34.
15. Im AR, Kim YH, Uddin MR, Chae S, Lee HW, Kim YS, Lee MY. Neuroprotective effects of Lycium chinense Miller against rotenone-induced neurotoxicity in PC12 Cells. Am J Chin Med 2013; 41: 1343-1359.
16. Jiang J, Jiang J, Zuo Y, Gu Z. Rapamycin protects the mitochondria against oxidative stress and apoptosis in a rat model of Parkinson's disease. Int J Mol Med 2013; 31: 825-832.
17. Jing CH, Wang L, Liu PP, Wu C, Ruan D, Chen G. Autophagy activation is associated with neuroprotection against apoptosis via a mitochondrial pathway in a rat model of subarachnoid hemorrhage. Neuroscience 2012; 213: 144-153.
18. Kanno H, Ozawa H, Sekiguchi A, Yamaya S, Tateda S, Yahata K, Itoi E. The role of mTOR signaling pathway in spinal cord injury. Cell Cycle 2012; 11: 3175-3179.
19. Koh JY, Choi DW. Quantitative determination of glutamate mediatedcortical neuronal injury in cell culture by lactate dehydrogenase efflux assay. J Neurosci Methods 1987; 20: 83-90.
20. Lipski J, Nistico R, Berretta N, Guatteo E, Bernardi G, Mercuri NB. L-DOPA: a scapegoat for accelerated neurodegeneration in Parkinson's disease? Prog Neurobiol 2011; 94: 389-407.
21. Malagelada C, Jin ZH, Jackson-Lewis V, Przedborski S, Greene LA. Rapamycin protects against neuron death in in vitro and in vivo models of Parkinson's disease. J Neurosci 2010; 30: 1166-11675.
22. Meinel J, Radad R, Rausch WD, Reichman H, Gille G. Cabergoline protects dopaminergic neurons against rotenone-induced cell death in primary mesencephalic cell culture. Folia Neuropathologica 2015; 53: 29-40.
23. Oster S, Radad K, Scheller D, Hesse M, Balanzew W, Reichmann H, Gille G. Rotigotine protects against glutamate toxicity in primary dopaminergic cell culture. Eur J Pharmacol 2014; 724: 31-42.
24. Parganlija D, Klinkenberg M, Domínguez-Bautista J, Hetzel M, Gispert S, Chimi MA, Dröse S, Mai S, Brandt U, Auburger G, Jendrach M. Loss of PINK1 Impairs Stress-Induced Autophagy and Cell Survival. PLoS One 2014; 21: e95288.
25. Park HJ, Shin JY, Kim HN, Oh SH, Lee PH. Neuroprotective effects of mesenchymal stem cells through autophagy modulation in a parkinsonian model. Neurobiol Aging 2014; 35: 1920-1928.
26. Park JH, Lee JE, Lee SJ, Park SJ, Park KH, Jeong M, Koh HC. Potential autophagy enhancers protect against fipronil-induced apoptosis in SH-SY5Y cells. Toxicol Lett 2013; 223: 25-34.
27. Park SS, Lee D. Selective loss of dopaminergic neurons and formation of Lewy body-like aggregations in alpha-synuclein transgenic fly neuronal cultures. Eur J Neurosci 2006; 23: 2908-2914.
28. Prakash KM, Tan EK. Development of Parkinson's disease biomarkers. Expert Rev Neurother 2010; 10: 1811-1825.
29. Pyszko JA, Strosznajder JB. The key role of sphingosine kinases in the molecular mechanism of neuronal cell survival and death in an experimental model of Parkinson's disease. Folia Neuropathol 2014; 52: 260-269.
30. Radad KS, Al-Shraim MM, Moustafa MF, Rausch WD. Neuroprotective role of thymoquinone against 1-methyl-4-phenylpyridinium-induced dopaminergic cell death in primary mesencephalic cell culture. Neurosciences (Riyadh) 2015; 20: 10-16.
31. Radad K, Gille G, Rausch WD. Dopaminergic neurons are preferentially sensitive to long-term rotenone toxicity in primary cell culture. Toxicol In Vitro 2008; 22: 68-74.
32. Radad K, Scheller D, Rausch WD, Reichmann H, Gille G. Neuroprotective effect of rotigotine against complex I inhibitors, MPP+ and rotenone, in primary mesencephalic cell culture. Folia Neuropathol 2014; 52: 179-186.
33. Seto B. Rapamycin and mTOR: a serendipitous discovery and implications for breast cancer. Clin Transl Med 2012; 1: 29.
34. Singer C. Managing the patient with newly diagnosed Parkinson disease. Cleve Clin J Med 2012; 9: 3-7.

http://rcin.org.pl

35. Tain LS, Mortiboys H, Tao RN, Ziviani E, Bandmann O, Whitworth AJ. Rapamycin activation of 4E-BP prevents parkinsonian dopaminergic neuron loss. Nat Neurosci 2009; 12: 1129-1135.

36. Tang P, Hou H, Zhang L, Lan X, Mao Z, Liu D, He C, Du H, Zhang L. Autophagy reduces neuronal damage and promotes locomotorrecovery via inhibition of apoptosis after spinal cord injury in rats. Mol Neurobiol 2014; 49: 276-287.

37. Tapias V, Cannon JR, Greenamyre JT. Pomegranate juice exacerbates oxidative stress and nigrostriatal degeneration in Parkinson's disease. Neurobiol Aging 2014; 35: 1169-1176.

38. Vézina C, Kudelski A, Sehgal SN. Rapamycin (AY-22,989), a new antifungal antibiotic. I. Taxonomy of the producing streptomycete and isolation of the active principle. J Antibiot (Tokyo) 1975; 28: 721-726.

39. White RJ, Reynolds IJ. Mitochondrial depolarization in glutamate-stimulated neurons: an early signal specific to excitotoxin exposure. J Neurosci 1996; 16: 5688-5697.

40. Worth PF. How to treat Parkinson's disease in 2013. Clin Med 2013; 13: 93-96.

41. Yin L, Ye S, Chen Z, Zeng Y. Rapamycin preconditioning attenuates transient focal cerebral ischemia/reperfusion injury in mice. Int J Neurosci 2012; 122: 748-756.

http://rcin.org.pl

Investigation of iron's neurotoxicity during cerebral maturation in the neonatal rat model of haemolysis

Ebru Akar[1], Aycan Ünalp[2], Gulden Diniz[3], Ragip Ortac[3], Banu Senturk[4], Osman Yilmaz[5], Muge Kiray[6], Merve Tepetam[7], Canan Coker[8], Sukru Cangar[1]

[1]Department of Pediatrics, Dr. Behçet Uz Child Disease and Pediatric Surgery Training and Research Hospital, Izmir, [2]Department of Pediatric Neurology, Dr. Behçet Uz Child Disease and Pediatric Surgery Training and Research Hospital, Izmir, [3]Department of Pathology, Dr. Behçet Uz Child Disease and Pediatric Surgery Training and Research Hospital, Izmir, [4]Department of Biochemistry, Ataturk Training and Research Hospital, Izmir, [5]Department of Animal Experimentation, Faculty of Medicine, Dokuz Eylul University, Izmir, [6]9 Eylul University Faculty of Medicine, Balçova, Izmir, [7]Department of Thoracic Medicine, Faculty of Medicine, Meram University, Konya, [8]Department of Biochemistry, Faculty of Medicine, Dokuz Eylul University, Izmir, [9]Department of Pediatrics, Dr. Behçet Uz Child Disease and Pediatric Surgery Training and Research Hospital, Izmir, Turkey

Abstract

Introduction: Haemolytic disease of newborns due to rhesus and AB0 incompatibility is encountered frequently in neonatal clinics and may lead to severe haemolysis. In this study, it is suggested that important amounts of iron released with haemolysis may have a toxic effect on the brain parenchymal tissue, and the severity of the toxic effect can be correlated with the maturation of the brain barrier systems. To demonstrate the accumulation and the neurotoxic effects of free iron (Fe) in the brain an experimental haemolysis model with various maturation phases was performed.

Material and methods: The study was composed of 48 Wistar rats with the following ages: five days old (Group A), 10 days old (Group B), and 19 days old (Group C). Each group was divided into three experimental subgroups and three control groups. Experimental groups were treated with intraperitoneal 75 mg/kg/day phenyl hydrazine hydrochloride for haemolysis.

Results: We demonstrated that the blood brain barrier (BBB) is permeable in five-day-old newborn rats and is mature in 10- and 19-day-old rats. Iron staining and neuronal damage were detected in group A and group B rats. No damage was detected in the brain tissue of group C animals. The presence of iron staining and neuronal damage in group B with mature BBB may suggest the existence of other incomplete barrier systems different from BBB that lead to iron accumulation in the brain.

Conclusions: Blood brain barrier has a partial role in Fe transport, and the alternative barrier systems may also be involved. It could be supposed that after maturation of all barrier systems, excessive Fe penetration to the brain cannot occur. Our findings showed that the toxic amounts of iron may penetrate into the brain parenchyma of newborns despite the BBB preservation and cause neuronal damage in newborns, but the mature brain is not affected by the same magnitude blood levels.

Key words: haemolysis, neurotoxic, free iron, brain barrier systems, newborn.

Communicating author:

Assoc. Prof. Aycan Ünalp, Department of Pediatric Neurology, Dr. Behcet Uz Child Diseases and Pediatric Surgery Training and Research Hospital, Montro, Izmir, Turkey, phone: +90 232 2387097, e-mail: aycanunalp@mynet.com

Introduction

In neonates, isoimmune and non-immune haemolytic diseases, including Rh, ABO, and subgroup incompatibility disorders, result in toxic heme metabolites, such as bilirubin and iron (Fe). Bilirubin encephalopathy, known as kernicterus, is one of the severe complications of neonatal hyperbilirubinaemia [12,22] and is caused by deposition of unconjugated bilirubin in specific regions of the brain. Blood-brain barrier (BBB) permeability is primarily responsible for exposing the brain to toxic doses of bilirubin; however, the mechanism by which toxic levels of Fe are passed to the brain is poorly understood.

Recent evidence has revealed a connection between Fe and a number of diseases with previously unclear pathogeneses such as Hallervorden-Spatz disease, Friedreich's ataxia, and Huntington chorea. These neurodegenerative diseases are reported to coincide with Fe metabolism disorders and abnormal Fe accumulation [5,7,14]. Severe iron toxicity is thought to result from reactive oxygen radicals and lipid peroxidation [18]. Cerebral tissue has high amounts of lipid molecules, so the brain is the most susceptible organ to peroxidation injury [11,12]. Studies of babies with Rh incompatibility have revealed increased byproducts of ferritin and lipid peroxidation. These results support the hypothesis that a high Fe load generates free oxygen radicals and causes cerebral damage [1,11,17]. Fe transportation is strictly regulated by the BBB and other barriers with unclear mechanisms [3]. For instance, rats with congenital BBB defects were shown to have abnormal perivascular Fe deposition [4]. High or low Fe transport rates in critical phases cause cerebral dysfunction in adulthood. The most important phase is the early postnatal period, during which the standard distribution of normal quantities of Fe is necessary for normal myelinisation [24].

The present study creates a rat model of haemolysis with various maturation phases and investigates Fe accumulation and related neuronal damage in the brain.

Material and methods

To demonstrate the accumulation and the neurotoxic effects of free iron in the brain, we performed experimental haemolysis model in 5-day-old (Group A), 10-day-old rats (Group B), and 19-day-old rats (Group C). Forty-two male Wistar rats from Dokuz Eylul University Faculty of Medicine Experimental Animal Laboratory were used in this study, following Institutional Ethical Committee approval. According to Vannucci et al. [28], the development of the brain of 7-day-old rat is histologically similar to that of a 32-34-week gestation human premature newborn infant. The brain maturation of 12-13-day-old rats resembles term human neonates. Also, 21-day-old rat brains represent the human prepubertal period, when brain development has been completed. Each group of rats was divided into three experimental subgroups and three control groups of seven rats each.

As indicated in previous studies [13,20], a 75-mg/kg/day dose of intraperitoneal (IP) phenyl hydrazine hydrochloride (PHZCI) was injected for two days to create the rat model of haemolysis. Phenyl hydrazine immediately reacts with the carbonyl groups of different important biomolecules. It interacts with haemoglobin (Hb) and cytochrome p450 through an oxidation reaction, leading to the generation of destructive free radicals, which are responsible for subsequent haemolysis [15]. During sacrification, ether was used as a general anaesthetic [20]. Blood samples were studied as the indicator of haemolysis. Iron accumulation and the neuronal damage were evaluated by the pathologists.

Control groups received the same volume of 0.9% NaCl IP on the first and the second days of the study. Half of the animals of both groups were used for histological studies and the other half for biochemical indicators. In the trial groups haemolysis was induced by IP administration of 75 mg/kg/day PHZCI for two consecutive days based on previous data [13]. On the third day, under general anaesthesia, blood samples were taken for haematological and biochemical tests. Following ventricular perfusion, rats were sacrificed by decapitation, and brain tissue was evaluated histopathologically.

In order to verify the BBB permeability, intracardiac Evans Blue was administered under general anaesthesia to four mature newborn rats (10 days old) and four adult rats (19 days old) and sacrificed after 20 minutes. Frozen sections of brain tissue were evaluated by the Department of Pathology to observe the effects of PHZCI on the BBB.

Haematological and biochemical tests

Haemoglobin and Htc levels were evaluated using a hemocounter device and the spectrophotometric method. For biochemical tests, the Diazo and Jendrasik-Grof methods were used to detect plasma

http://rcin.org.pl

Ebru Akar, Aycan Ünalp, Gulden Diniz, Ragip Ortac, Banu Senturk, Osman Yilmaz, Muge Kiray, Merve Tepetam, Canan Coker, Sukru Cangar

direct (d.bill) and total (t.bill) bilirubin, respectively. Hyperbilirubinaemia was indicated by a total bilirubin measurement of more than 3 mg/dl [8]. Aspartate transaminase (AST) and lactate dehydrogenase (LDH) levels were determined. The following methods were also used: the chemiluminescence method for plasma ferritin measurements, the immunoturbidimetric

method for transferrin, and the Ferrozine method for Fe and total iron binding capacity (TIBC) measurements (Beckman Synchron Kit).

During pathologic evaluation, the brains of the animals were fixed in 10% formalin/0.1 M phosphate buffer, pH 7.2, and were embedded in paraffin. After these procedures slices 5 μm thick were prepared from the frontoparietal cerebral cortex, cerebellar cortex, hypothalamus, thalamus, and choroid plexus. The two samples composed of the same slice were obtained and the first sample was stained using haematoxylin and eosin to show neuronal damage. Two expert pathologists, blinded to the slides observed, evaluated the stained sections to observe the presence of neuronal damage (angular retraction, cell fragmentation, neuronophagia) as well as acidophilia and reactive gliosis in different sections of the brain. Neuronal damage level was evaluated as no damage (0), mild (+), moderate (++), or severe damage (+++) [20]. The second sample stained with Pearl's Prussian blue was evaluated as the absence (–) or presence (+) of intra- and extracellular iron.

Table I. Comparison of the biochemical parameters of the A control group with the A trial group

Group A – biochemical parameters	Control group	Trial group	p
Hb	12.6 ± 0.97	5.4 ± 1.62	0.002
Htc	37.2 ± 2.84	13.8 ± 4.2	0.002
t.bill	0.54 ± 0.19	2.28 ± 0.56	0.002
d.bill	0.41 ± 0.21	1.2 ± 0.51	0.004
AST	59.14 ± 28.5	223 ± 79.5	0.002
LDH	247 ± 66.3	1403 ± 706	0.002
Fe	125.4 ± 15.8	332.1 ± 134.9	0.002
TIBC	246 ± 80.9	440.5 ± 66.8	0.002
Ferritin	22.6 ± 3.8	37.2 ± 9.6	0.04
Transferrin	139.2 ± 16.9	182.8 ± 33.3	0.05

Hb – haemoglobin, Htc – hematocrit, t.bill – total bilirubin, d.bill – direct bilirubin, AST – aspartate transaminase, LDH – lactate dehydrogenase, Fe – iron, TIBC – total iron binding capacity

Table II. Comparison of the biochemical parameters of the B control group with the B trial group

Group B – biochemical parameters	Control group	Trial group	p
Hb	10 ± 0.8	6.11 ± 0.64	0.002
Htc	28.6 ± 2.1	14.7 ± 2.29	0.002
t.bill	0.37 ± 0.13	1.37 ± 0.36	0.002
d.bill	0.3 ± 0.11	0.7 ± 0.58	0.008
AST	54.8 ± 24	175 ± 25.9	0.002
LDH	293 ± 81	1143 ± 343	0.002
Fe	135 ± 41.3	527.7 ± 178	0.002
TIBC	373.7 ± 36.1	645.7 ± 111	0.002
Ferritin	23.17 ± 5.2	34.1 ± 8.4	0.004
Transferrin	156 ± 16.9	179.7 ± 15.7	0.18

Hb – haemoglobin, Htc – hematocrit, t.bill – total bilirubin, d.bill – direct bilirubin, AST – aspartate transaminase, LDH – lactate dehydrogenase, Fe – iron, TIBC – total iron binding capacity

Statistical analysis

The distribution of data is represented using median, minimum, and maximum values. The Kruskal-Wallis and Mann-Whitney U tests were performed for intergroup comparisons of categorical variables. The χ^2 and Fisher exact tests were also performed for dichotomous findings. A p-value of less than 0.05 was considered statistically significant.

Results

As a consequence of the induction of haemolysis Hb, Htc, t.bill, d.bill, AST, and LDH levels were significantly different in the study and control groups, as biochemical parameters. A statistically significant difference was observed for the concentration of Fe, TIBC, and ferritin in the study and control groups ($p < 0.05$), but transferrin concentrations were not significantly different ($p > 0.05$) (Tables I-III).

A statistically significant difference was found in Hb and Htc levels for control A group as compared to control B and C groups (Mann Whitney U Test) ($p < 0.05$). Bilirubin levels were at physiological levels in the studied groups. Significantly increased AST and LDH levels were observed in the experimental group. Although iron and TIBC were significantly increased in the group of haemolysis, ferritin and transferrin levels did not increase.

Table III. Comparison of the biochemical parameters of the C control group with the C trial group

Group C – biochemical parameters	Control group	Trial group	p
Hb	10.8 ± 0.48	6.7 ± 1.25	0.002
Htc	30.6 ± 2.62	18 ± 3.1	0.002
t.bill	0.3 ± 0.11	0.8 ± 0.25	0.002
d.bill	0.21 ± 0.06	0.42 ± 0.17	0.014
AST	65.7 ± 30.1	228.1 ± 59.8	0.002
LDH	241.8 ± 49.4	1727 ± 274	0.002
Fe	161.1 ± 72.7	406 ± 109.7	0.002
TIBC	390.57 ± 53.8	650 ± 108	0.002
Ferritin	11.6 ± 2.51	23.8 ± 7.5	0.002
Transferrin	153.4 ± 14.1	172.4 ± 12	0.21

Hb – haemoglobin, Htc – hematocrit, t.bill – total bilirubin, d.bill – direct bilirubin, AST – aspartate transaminase, LDH – lactate dehydrogenase, Fe – iron, TIBC – total iron binding capacity

Both iron accumulation and neuronal damage were evaluated in the control and study groups. The neuronal tissues demonstrate the same degenerative changes

Table IV. Comparison of the neuronal damage in the brain areas between the study groups

Area of the brain	Study Group A	Study Group B	Study Group C
Amygdala	–	–	–
Frontoparietal cortex	+++	++	–
Hypothalamus	–	–	–
Thalamus	–	–	–
Choroid plexus	–	–	–
Cerebellum	++	+	–

such as vacuolisation, pyknosis, and cavitations. Herein, these changes were graded as semi-quantified. There was no neuronal damage in the control groups. Neuronal damage was less in the B study group than in the A study group. No damage was detected in the brain parenchyma of the C study group. There was no damage in the hypothalamus, thalamus, or choroid plexus in any of the trial groups (Table IV, Fig. 1).

No Fe accumulation was observed in the control groups. PHZCI-induced haemolysis seemed to cause Fe accumulation in some cerebral regions of some of the trial groups. In fact, there was very little iron
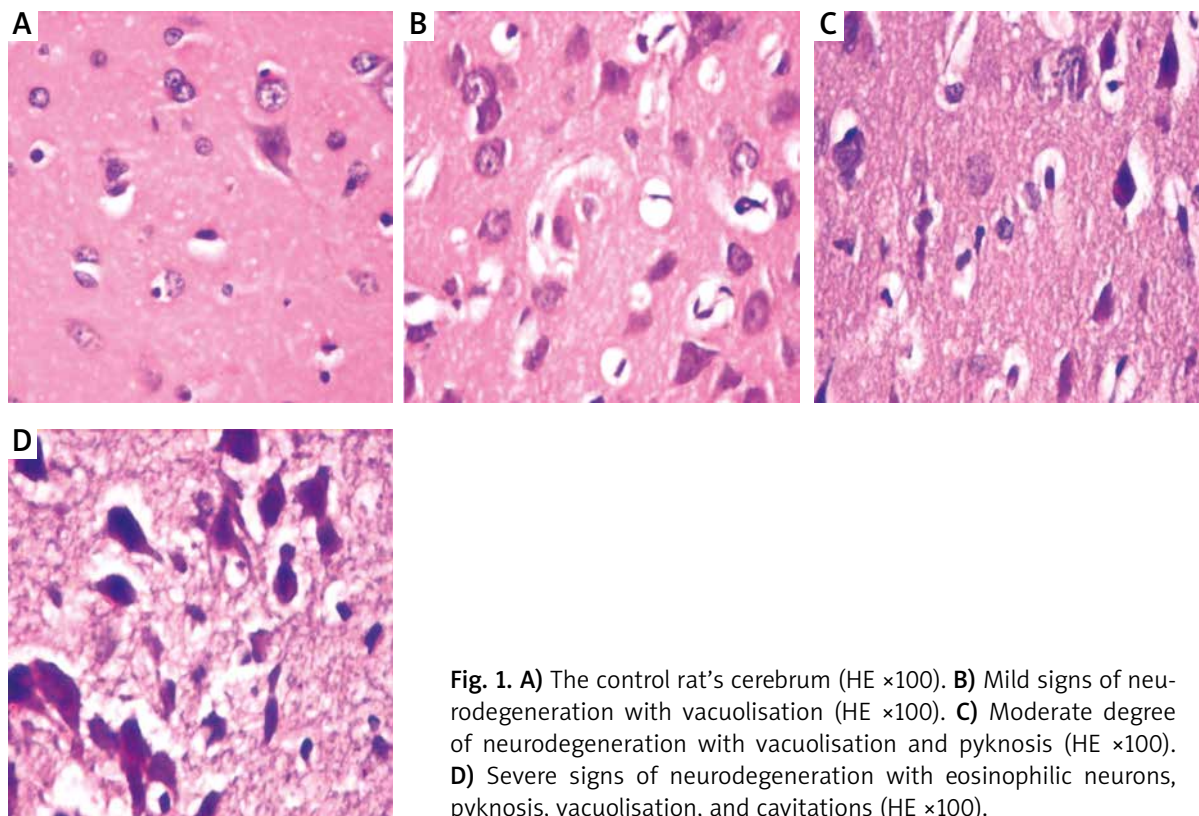

Fig. 1. A) The control rat's cerebrum (HE ×100). **B)** Mild signs of neurodegeneration with vacuolisation (HE ×100). **C)** Moderate degree of neurodegeneration with vacuolisation and pyknosis (HE ×100). **D)** Severe signs of neurodegeneration with eosinophilic neurons, pyknosis, vacuolisation, and cavitations (HE ×100).
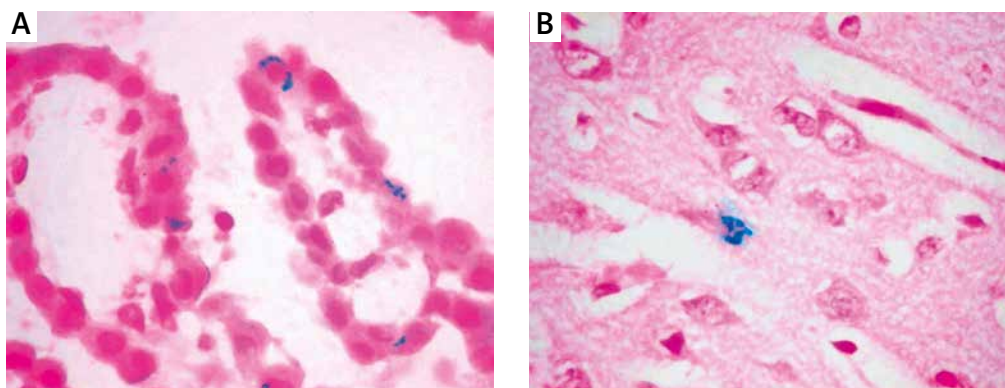
Ebru Akar, Aycan Ünalp, Gulden Diniz, Ragip Ortac, Banu Senturk, Osman Yilmaz, Muge Kiray, Merve Tepetam, Canan Coker, Sukru Cangar

Fig. 2. Intracellular iron deposits in choroid plexus **(A)** and cerebrum **(B)** (Pearl's Prussian Blue ×400).

Table V. Comparison of the iron accumulation in the brain areas of the study groups

Brain areas	Study Group A	Study Group B	Study Group C
Amygdala	–	–	–
Frontoparietal cortex	+	+	–
Hypothalamus	–	–	–
Thalamus	–	–	–
Choroid plexus	+	+	–
Cerebellum	+	+	–

accumulation. Therefore, we did not need grading of iron accumulation and we graded iron as being absent or present (Table V, Fig. 2). The presence of iron staining and neuronal damage in B study group with mature BBB supposed the presence of other incomplete barrier systems different from the BBB that lead to iron accumulation in the brain.

The Evans Blue staining did not pass over the vascular walls of the B and C groups. We demonstrated that BBB was permeable in fibe-day-old newborn rats and was mature in 10- and 19-day-old mature rats (Fig. 3).

Discussion

Isoimmune haemolytic anaemia related to blood type incompatibility (especially Rh alloimmunisation) is the most common cause of excessive haemolysis and increased heme catabolism. Heme catabolism generates two toxic by-products: bilirubin and heme. Albumin binds free bilirubin, whereas ferritin and transferrin bind Fe, thus minimising the risk of toxicity. However, these "buffer mechanisms" fall short during haemolysis. Increased free bilirubin penetrates the brain during the early neonatal period, when the BBB is immature, and causes kernicterus. Bilirubin is thought to interfere with oxidative phosphorylation, and protein and glucose metabolism, resulting in neu-
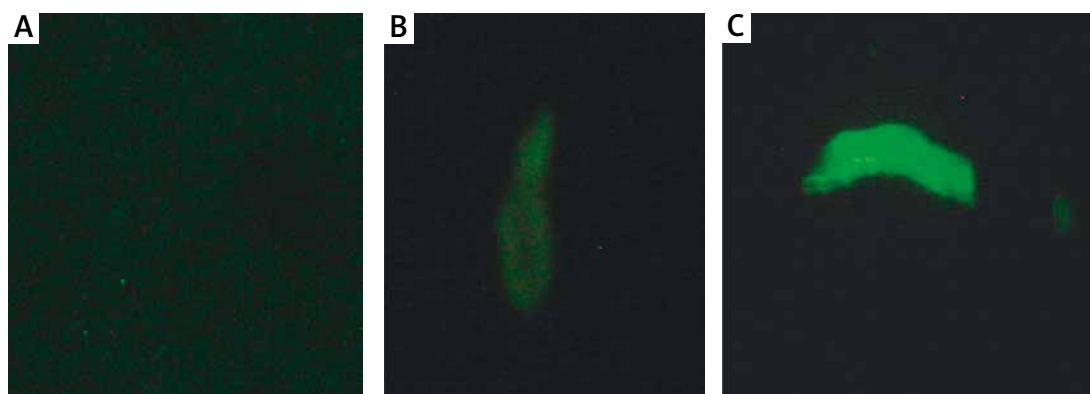

Fig. 3. Evans Blue staining was passed over the vascular wall in Group A **(A)**, B **(B)**, C **(C)**. Evans Blue staining was not passed over the vascular walls of the B and C study groups.

rotoxic damage [6,19]. Iron causes peroxidation injury in lipid rich tissues and may play a critical role in bilirubin encephalopathy (its pathophysiology is still unclear) and neuronal damage. Iron accumulation and Fe metabolism disorders have been correlated with a number of neurodegenerative diseases; therefore, Fe produced by haemolysis might cause neurologic disorders [9,29]. Although hyperbilirubinaemia and its toxic effects during the neonatal period have been well studied, few studies have focused on Fe. In addition, the role of BBB permeability in Fe transportation to the brain is unclear.

In this study, we demonstrated Fe accumulation in special cerebral regions, induced by haemolysis. We also investigated the role of BBB permeability in Fe transportation into the brain. We used semi-quantitative methods to evaluate the degree of neuronal damage in different cerebral regions of rats of different postnatal ages.

To evaluate haemolysis, we evaluated the decrease in Hb and Htc levels, the increase in t.bill, d.bill, and LDH, as well as peripheral blood smears. No statistical difference was observed between either the Hb or Htc levels of trial groups A, B, and C ($p > 0.05$). However, within the control groups, Hb and Htc levels were statistically different in Group A compared to Group B and C. We predicted that the normal ranges of Hb and Htc levels would increase when neonatal maturation was decreased. Therefore, this result has clinical significance as well as statistical significance.

Bilirubin levels were statistically higher in some groups but were still within normal ranges, so no clinical hyperbilirubinaemia occurred. Even with haemolysis, an insufficient increase in bilirubin levels occurred in the Wistar rat model. On the other hand, AST and LDH levels, indicators of cell lysis, were higher in the trial groups than in the control groups ($p < 0.05$). It was concluded that glucuronidation of the bilirubin occurring in the renal and intestinal tissues of the rat is as important as that of the hepatic tissue [16,20,21]. Therefore, it might not be possible to establish the higher indirect bilirubin levels necessary to create kernicterus in Wistar rats. Based on this information, we chose to use Wistar rats in order to isolate the effects of Fe from bilirubin. Conversely, use of PHZ caused extremely high t.bill levels in Gunn rats because they have a glucuronyl transferase gene deficiency [25].

Similarly to the study of Mejia *et al*. [20], the trial groups had significantly increased serum Fe; the

increase was clinically consistent. We also investigated ferritin, transferrin, and TIBC in our study, none of which was assessed by Mejia *et al*. Although TIBC levels were significantly higher, ferritin was higher but still within the normal physiological range in the trial groups. There was no statistically significant increase in transferrin levels. In contrast, Aygun *et al*. monitored Fe accumulation in Rh alloimmunisation starting from the intrauterine period and found significantly higher levels of ferritin [1]. Similarly, Berger *et al*. [2] reported that cord blood samples of babies with Rh alloimmunisation had increased ferritin levels, decreased TIBC, normal Fe levels, and increased lipid peroxidation metabolites. The chronic haemolytic process started during the intrauterine period and continued through the postpartum period; moreover, to compensate for increased Fe, ferritin synthesis was increased. In our study, serum Fe levels were increased; however, ferritin levels were in the normal range. Our haemolysis model is limited to acute courses (48 hours), which may explain the lack of increase in ferritin levels. Ferritin synthesis requires additional time and so may fail to compensate for the sudden Fe increase. In addition, other adaptation mechanisms for buffering excessive Fe followed by haemolysis may be ineffective and slow. This also may explain why serum Fe increases, but ferritin and transferrin levels were not increased in our haemolysis model.

The babies with Rh incompatibility, hyperbilirubinaemia and anaemia were treated prenatally and postnatally, but the clinical significance of the increased Fe load is unknown. However, Berger *et al*. [2] found that increased ferritin coincided with increased lipid peroxidation metabolites. Mejia *et al*. [20] also reported that Fe and lipid peroxidation metabolites were increased after haemolysis. Excessive Fe loads may predispose cells to free radical damage in neonatal haemolytic diseases. Neonates have limited TIBC and poor antioxidant mechanisms, so they may be susceptible to free radical damage [23]. The neurodegeneration observed in our five- and 10-day old rats, all of which had immature brains, may be explained by this hypothesis.

Frederikson *et al*. [10] administered an Fe enriched diet to 3-5-, 10-12-, and 19-21-day-old rats. They monitored the rats' behavioural alterations and motor functions and reported that 10-12-day-old rats were more affected than other rats, 19-21-day-old rats were not affected, and 3-5-day old rats

http://rcin.org.pl

Ebru Akar, Aycan Ünalp, Gulden Diniz, Ragip Ortac, Banu Senturk, Osman Yilmaz, Muge Kiray, Merve Tepetam, Canan Coker, Sukru Cangar

were mildly affected. These results may indicate a critical period of Fe susceptibility in the brain. The critical period seems to have occurred during an intermediate period, instead of when the brain was least mature. Cerebral Fe uptake in rats peaks between birth and the 15th postnatal day [27]. In this peak period, differentiation in the thresholds of regulatory mechanisms might be responsible for increased cerebral Fe uptake, which may explain why 10-12-day-old rats were most affected by the Fe-enriched diet. Mejia *et al.* [20] used Evans Blue staining in seven-day-old rats and determined that the BBB was permeable. We showed that 10-day-old rats (representative of 38-40th week foetal brains) and 19-day-old rats (brain maturation was completed) had impermeable BBBs, which may suggest that the BBB does not play a primary role in Fe transportation. In our study, the five-day-old rats with permeable BBBs and the 10-day-old rats with impermeable BBBs had similar Fe accumulation and neuronal damage. No Fe accumulation or neuronal damage occurred in the 19-day-old group. We suggest that the BBB does not have a primary role in Fe transfer; however, immature brains are susceptible to excessive Fe penetration and neurotoxic damage, and mature brains prevent excessive Fe transfer. These results are consistent with those of Frederikson *et al.* [10].

Mejia *et al.* evaluated the neurotoxic effects of Fe in seven-day-old rats with permeable BBBs using semi-quantitative methods. The most damage and Fe accumulation were observed in the frontoparietal cortex. Dense Fe accumulation occurred in the choroid plexus, but the damage was mild [20]. The choroid plexus lacks a BBB, as well as neurons, which may explain these results. Similar to Mejia *et al.,* we observed that five-day-old rats had Fe accumulation in the frontoparietal cortex and choroid plexus. The frontoparietal cortex also had neuronal damage, while the choroid plexus did not. The 10-day-old rats had similar results. Rice *et al.* [25] reported that in the rat model of hyperbilirubinaemia, some histopathological findings secondary to hyperbilirubinaemia were observed in the cerebellum in 15-day-old Gunn rats. Similarly, we found Fe accumulation and neuronal damage in the cerebellum, but our findings were related to the bilirubin-independent effects of Fe. Iron may predispose rats to the toxic effects of hyperbilirubinaemia.

Castelnau *et al.* reported that rats with congenital BBB defects had abnormal perivascular Fe accumulation, which supports the hypothesis that the BBB is primarily responsible for Fe transfer [4]. In haemochromatosis, intense Fe deposition occurs in the choroid plexus and pituitary gland, where there is no BBB, also suggesting a primary role for the BBB [26]. However, despite intact BBBs, the 10-day-old rats in our study had Fe accumulation and neuronal damage. Our study proposes that there are other immature barriers, besides the BBB, that may have a role in Fe transfer. Several cerebral regions have higher Fe concentrations on the physiological conditions, including the substantia nigra and the cerebellar nuclei, suggesting that the brain has various regulatory mechanisms and barriers. For instance, cerebrospinal fluid (CSF) helps transport Fe to the brain parenchyma. An hour after Fe injection, Fe is seen in the choroid plexus. Even with low levels of transferrin in circulation, normal Fe uptake levels are observed in the choroid plexus, thus there may also be alternative transport systems between the choroid plexus (that exempts from BBB) and CSF.

The BBB has a major role in bilirubin transport to the brain, and in babies with mature BBBs toxic levels of bilirubin never penetrate into the brain. Our study demonstrates that, unlike with bilirubin, the BBB is not the only determinant for Fe transfer. We observed that rats with permeable BBBs (trial Group A) had Fe accumulation and the most severe neuronal damage. Some rats with impermeable BBBs (trial Group B) also had damage and accumulation and still seemed to experience toxic effects. Trial Group C had neither damage nor accumulation. Per these findings, we propose that the BBB has a partial role in Fe transport, but alternative barrier systems may also be involved, and after the maturation of all barrier systems, excessive Fe penetration to the brain may not occur.

Disclosure

Authors report no conflict of ineterst.

References

1. Aygun C, Tekinalp G, Gurgey A. Increased fetal iron load in rhesus hemolytic disease. Pediatr Hematol Oncol 2004; 21: 329-333.
2. Berger HM, Lindeman JH, van Zoeren-Grobben D, Houdkamp E, Schrijver J, Kanhai HH. Iron overload, free radical damage and rhesus hemolytic disease. Lancet 1990; 335: 933-936.
3. Burdo JR, Simpson IA, Menzies SL, Beard J, Connor JR. Regulation of the profile of iron-management proteins in brain microvasculature. J Cerebral Blood Flow Metab 2004; 24: 67-74.

4. Castelnau PA, Garrett RS, Palinski W, Witztum JL, Campbell IL, Powell HC. Abnormal iron deposition associated with lipid peroxidation in transgenic mice expressing interleukin-6 in the brain. J Neuropathol Exp Neurol 1998; 57: 268-282.

5. Connor JR, Menzies SL, St. Martin SM, Mufson EJ. A histochemical study of iron, transferrin, and ferritin in Alzheimer's diseased brains. J Neurosci Res 1992; 31: 75-83.

6. Conolly AM, Volpe JJ. Clinical features of bilirubin encephalopathy. Clin Perinatol 1990; 17: 371-379.

7. Dexter DT, Carayon A, Javoy-Agid F, Agid Y, Wells FR, Daniel SE, Lees AJ, Jenner P, Marsden CD. Alterations in the levels of iron, ferritin and other trace metals in Parkinson's disease and other neurodegenerative diseases affecting the basal ganglia. Brain 1991; 114: 1953-1975.

8. Dominguez F, Gonzales G, Cedars M, Calvo J. Apertura reversible de la barrera hemato-encefalica inducida por hipercapnia en hiperbilurrubinemia experimental. Ann Espanoles Pediatr 1997; 46: 374-377.

9. Faucheux BA, Nillesse N, Damier P, Spik G, Mouatt-Prigent A, Pierce A, Leveugle B, Kubis N, Hauw JJ, Agid Y, Hirsch EC. Expression of lactoferrin receptors is increased in the mesencephalon of patients with Parkinson disease. Proc Natl Acad Sci USA 1995; 92: 9603-9607.

10. Fredriksson A, Schröder N, Eriksson P, Izquierdo I, Archer T. Maze learning and motor activity deficits in adult mice induced by iron exposure during a critical postnatal period. Brain Res Dev Brain Res 2000; 119: 65-74.

11. Gutteridge JM, Halliwell B. Free radicals and antioxidants in the year 2000. A historical look to the future. Ann N Y Acad Sci 2000; 899: 136-147.

12. Halliwell B. Iron and damage to biomolecules. In: Iron and Human Disease. Lauffer RB (ed.). CRC Press, Boca Raton 1992; pp. 210-230.

13. Hansen TW, Allen JW. Hemolytic anemia does not increase entry into, nor alter rate of clearace of bilirubin from rat brain. Biol Neonate 1996; 69: 268-274.

14. Kienzl E, Puchinger L, Jellinger K, Linert W, Stachelberger H, Jameson RF. The role of transition metals in the pathogenesis of Parkinson's disease. J Neurol Sci 1995; 134 Suppl: 69-78.

15. Latunde-Dada GO, McKie AT, Simpson RJ. Animal models with enhanced erythropoiesis and iron absorption. Biochim Biophys Acta 2006; 1762: 414-423.

16. Li XD, Xia SQ, Lv Y, He P, Han J, Wu MC. Conjugation metabolism of acetaminophen and bilirubin in extrahepatic tissues of rats. Life Sci 2004; 74: 1307-1315.

17. Lindeman JH, van Zoeren-Grobben D, Schrijver J, Speek AJ, Poorthuis BJ, Berger HM. The total free radical trapping ability of cord blood plasma in preterm and term babies. Pediatr Res 1989; 26: 20-24.

18. Malecki EA, Devenyi AG, Beard JL, Connor JR. Existing and emerging mechanisms for transport of iron and manganese to the brain. J Neurosci Res 1999; 56: 113-122.

19. Martinez JC, Garcio HO, Otheguy LE, Drummond GS, Kappas A. Control of severe hyperbilirubinemia in full-term newborns with the inhibitor of bilirubin production Sn-mesoporphyrin. Pediatrics 1999; 103: 1-5.

20. Mejia GB, Sanz CR, Avila MM, Peraza AV, Guzmán DC, Olguín HJ, Ramírez AM, Cruz EG. Experimental hemolysis model to study bilirubin encephalopathy in rat brain. J Neurosci Methods 2008; 15; 168: 35-41.

21. Mottino AD, Pellegrino JM, Guibert EE, Roma MG, Rodriguez Garay EA. Comparison of hepatic, renal and intestinal bilirubin UDP-glucuronyl transferase activities in rat microsomes. Int J Biochem 1988; 20: 1113-1116.

22. Odell GB, Schutta HS. Bilirubin encephalopathy. In: Cerebral Energy Metabolism and Metabolic Encephalopathy. Mc Candles DW (ed.). Plenum, New York 1985; pp. 229-261.

23. Otani H, Engelman RM, Rousou JA, Breyer RH, Das DK. Enhanced susceptibility of immature hearts to free radical mediated reperfusion injury. In: Medical, Biochemical and Chemical Aspects of Free Radicals. Hayaishi O, Niki E, Kondo M, Yoshikawa T (eds.). Elsevier Science Publishers, Amsterdam 1989; pp. 1181-1184.

24. Rakic P, Goldman-Rakic PS. The development and modifiability of the cerebral cortex. Overview. Neurosci Res Program Bull 1982; 20: 433-438.

25. Rice AC, Shapiro SM. A new animal model of hemolytic hyperbilirubinemia-induced bilirubin encephalopathy (kernicterus). Pediatr Res 2008; 64: 265-269.

26. Russfield A. Diseases of the pituitary. In: Pathology of the nervous system. Minckler J (ed.). Vol 1. McGraw-Hill Book Co, New York 1968; pp. 619-638.

27. Taylor EM, Morgan EH. Developmental changes in transferin and iron uptake by the brain in the rat. Brain Res Dev Brain Res 1990; 55: 35-42.

28. Vannucci RC, Connor JR, Mauger DT, Palmer C, Smith MB, Towfighi J, Vannucci SJ. Rat model of perinatal hypoxic-ischemic brain damage. J Neurosci Res 1999; 55: 158-163.

29. Yokel RA. Blood-brain barrier flux of aluminum, manganese, iron and other metals suspected to contribute to metal-induced neurodegeneration. J Alzheimers Dis 2006; 10: 223-253.

http://rcin.org.pl

Folia
Neuropathologica

Emery-Dreifuss muscular dystrophy type 2 associated (?) with mild peripheral polyneuropathy

Agnieszka Madej-Pilarczyk[1], Katarzyna Kotruchow[1], Dagmara Kabzinska[1], Joanna Cegielska[2], Andrzej Kochanski[1], Irena Hausmanowa-Petrusewicz[1]

[1]Neuromuscular Unit, Mossakowski Medical Research Centre, Polish Academy of Sciences, Warsaw, [2]Department of Neurology, Medical University of Warsaw, Bielanski Hospital, Warsaw, Poland

To our deepest regret Prof. Irena Hausmanowa-Petrusewicz passed away on July 07, 2015.

Abstract

In recent years numerous mutations in the LMNA gene encoding lamin A/C were shown to segregate with a wide spectrum of phenotypes. A recurrent p.R377H mutation in the LMNA gene was reported in patients with Emery-Dreifuss dystrophy (EDMD2) with various ethnic backgrounds. We present a patient with EDMD2 caused by a p.R377H mutation, associated with mild peripheral polyneuropathy. The analysis of peripheral myelin protein 22 (PMP22), ganglioside-induced differentiation-associated protein 1 (GDAP1), gap junction β-1 protein (GJB1), and myelin protein zero (MPZ) genes did not reveal mutations; however, we identified a new sequence intronic variant in the mitofusin 2 (MFN2) gene of unknown pathogenic significance. A complex phenotype in the presented patient might depend either on single mutation in the LMNA gene or on bigenic defect; therefore, a wide genetic investigation is needed to elucidate the molecular background of EDMD2/polyneuropathy in this case.

Key words: *Emery-Dreifuss muscular dystrophy, Charcot-Marie-Tooth neuropathy, LMNA, lamin A/C, mitofusin 2.*

Introduction

Mutations in the *LMNA* gene have been shown to segregate with a wide spectrum of phenotypes, known as lamiopathies [10], which might manifest as muscular dystrophy, cardiomyopathy, peripheral neuropathy, lipodystrophy, or premature ageing syndromes. In a large cohort of patients with *LMNA* mutations reported to date, only in few patients a "double" phenotype of axonal neuropathy coexisting with muscular dystrophy [1,5] or dilated cardiomyopathy [4] was reported. In this study we present a patient with genetically confirmed Emery-Drei-

fuss dystrophy type 2 (EDMD2), who additionally had late-onset mild, distal, axonal neuropathy. The coexistence of axonal neuropathy and EDMD2 might either result from a single *LMNA* mutation or have a bigenic background. By analyzing of five genes involved in pathogenesis of polyneuropathy, i.e. peripheral myelin protein 22 (*PMP22*), ganglioside-induced differentiation-associated protein 1 (*GDAP1*), gap junction β-1 protein (*GJB1*), myelin protein zero (*MPZ*) and mitofusin 2 (*MFN2*) genes, we attempted to elucidate the molecular background of axonal polyneuropathy in our EDMD2 patient.

Communicating author:

Dr Agnieszka Madej-Pilarczyk, Neuromuscular Unit, Mossakowski Medical Research Centre, Polish Academy of Sciences, 5 Pawińskiego St., 02-106 Warsaw, Poland, e-mail: agamadpil@gmail.com

Case report

A thirty-four-year-old female (III:6) presented because of slowly progressing walking difficulties and weakness and atrophy of arms and thigh muscles. Since childhood she had been very slim, physically weaker, and less agile than her peers (Fig. 1). During adolescence frequent fainting occurred. Similar clumsy walking was seen in the proband's father (II:4) and her grandmother (I:1); however, they were not examined neurologically. In addition, both relatives had a pacemaker implanted due to conduction disturbances, and the same cardiac problem occurred in the patient's uncle (II:2), who otherwise did not have any skeletal muscle disease. All three of these persons died suddenly at the age of 58 years (II:4), 62 years (II:2), and 66 years (I:1), respectively. Awareness of positive family history for a life-threatening cardiac disease and muscle symptoms being a cause of progressive physical disability were the main reasons for the proband to seek medical attention. Neurological examination revealed atrophy of arms, thighs, and calf muscles, weakness of proximal muscles with Gowers' sign, iliac asymmetry, absence of knee and ankle reflexes, spine rigidity with lumbar hyperlordosis, and slight elbow, knee, and ankle contractures. Superficial sensation was decreased in distal parts of lower limbs ("short socks"), while vibration sensation was normal. 24-hour electrocardiogram (ECG) monitoring revealed numerous episodes of supraventricular tachycardia and periodical atrioventricular block grade I. Echocardiogram was normal. On electroneurography (ENG) the stimulation of the left peroneal nerve revealed trace response in the distal point (0.1 mV; velocity not recordable) with no response near the fibula head; the stimulation of the right peroneal nerve revealed prolongation of the motor response latency (10.4 ms). Nerve conduction velocities were slightly decreased in the motor fibres of tibial and sural nerves, being 42.5 m/s and 45.2 m/s, respectively. Clinically affected members (I:1, II:2, II:4) were unavailable for ENG/electromyography (EMG), but the examination was normal in the patient's aunt (II:6) and mother (II:3). Once written informed consent and Bioethical Committee approval had been received, we performed genetic analysis in the proband and in her unaffected mother (II:3) and aunt (II:6). Genomic DNA was extracted from peripheral blood lymphocytes using a salting-out procedure. All 12 exons of *LMNA* and exon-intron

Fig. 1. Thirty four years old patient with Emery-Dreifuss dystrophy and mild axonal neuropathy; note atrophy of proximal muscles and slight elbow, knee and ankle contractures.
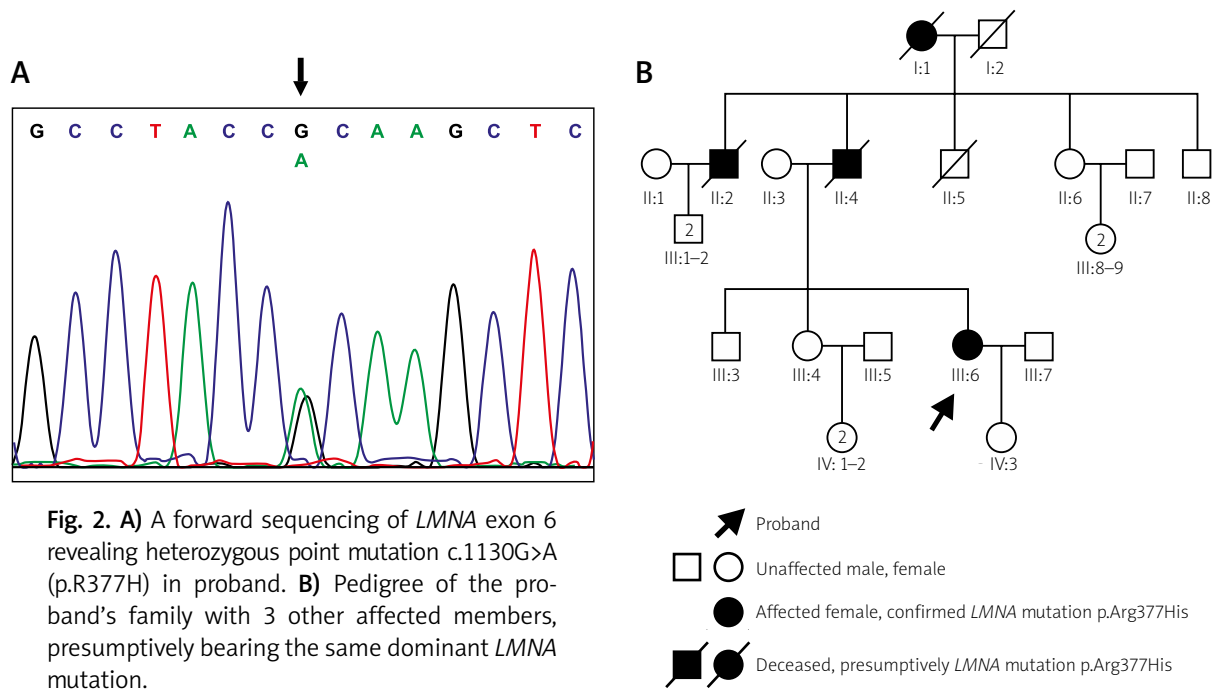
http://rcin.org.pl

Agnieszka Madej-Pilarczyk, Katarzyna Kotruchow, Dagmara Kabzinska, Joanna Cegielska, Andrzej Kochanski, Irena Hausmanowa-Petrusewicz

Fig. 2. A) A forward sequencing of *LMNA* exon 6 revealing heterozygous point mutation c.1130G>A (p.R377H) in proband. **B)** Pedigree of the proband's family with 3 other affected members, presumptively bearing the same dominant *LMNA* mutation.
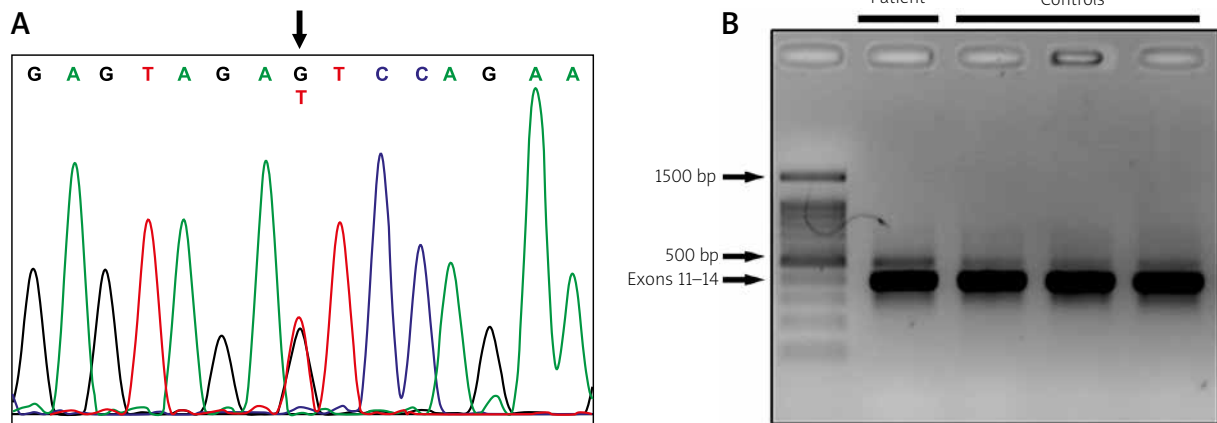

Fig. 3. A) Heterozygous mutation c.1468+50G>T in *MFN2* gene. **B)** PCR amplification of proband's cDNA and control cDNA showing no visible difference in products' length.

junctions were amplified by PCR, sequenced using the Big Dye Terminator Sequencing Ready Reaction kit (Applied Biosystems), and analysed on an ABI PRISM 373 fluorescent DNA sequencer (Applied Biosystems). Analysis of the *LMNA* gene revealed a heterozygous missense mutation c.1130G>A (p.R377H) (Fig. 2). Analysis of *PMP22* did not reveal deletion/ duplication. Direct sequencing of *GDAP1*, *GJB1*, and *MPZ* did not reveal mutations. Sequence analysis of *MFN2* showed a single nucleotide substitution

c.1469+50G>T within the twelfth intron, not found either in the proband's unaffected mother (II:3) and aunt (II:6) nor in 100 healthy controls. To check whether it affects splicing, we extracted mRNA from blood lymphocytes and then obtained cDNA from mRNA, encompassing exons 12-13 of *MFN2* gene. Polymerase chain reaction (PCR) with the designed primers: forward in 11 exon and reverse in 14 exon, resulted in synthesis of the 391 bp oligonucleotide, which had the same length in the proband and in

3 healthy controls. This might indicate that *MFN2* variant c.1469+50G>T does not affect splicing (Fig. 3).

Discussion

The coexistence of axonal polyneuropathy with muscular dystrophy/dilated cardiomyopathy has been shown only in a few patients [1,4,5]. Laminopathy with peripheral nerve involvement, associated with homozygous *LMNA* mutation p.R298C, was first described by De Sandre-Giovannoli *et al.* in 2002 [3]. There have been several reports of laminopathies with overlapping phenotype of axonal neuropathy and muscular dystrophy and/or cardiac involvement with autosomal dominant trait of inheritance. In 2004 Goizet *et al.* described a 55-year-old man and his 13-year-old daughter presenting axonal neuropathy, muscular dystrophy, cardiac involvement, and leukonychia, in whom *LMNA* mutation p.E33D was found [5]. Both patients had sensory abnormalities in distal lower limbs, while pes cavus, pelvic and distal muscle weakness was seen only in the older one. In 2005 Benedetti *et al.* reported a boy with *LMNA* mutation c.1711C>T, who had progressive distal and proximal muscle atrophy/weakness, causing him to be wheelchair bound; as well as pes equinovarus, which was corrected surgically, mildly impaired proprioceptive sensation and fat accumulation in the face and neck were seen [1]. A cardio-neurological form of laminopathy, associated with *LMNA* mutation c.1496delC, has been described in a 40-year-old man by Duparc *et al.* [4]. In addition to heart disease atrophy of quadriceps muscle, lack of reflexes, and contracted feet were found and ENG showed moderate axonal neuropathy. However, no molecular basis of EDMD2/Charcot-Marie-Tooth neuropathy (CMT) coexistence has been identified. The question remains unanswered: whether the phenotype in the presented case results from a single mutation within the *LMNA* gene or rather represents an overlapping syndrome associated with mutations in at least two genes. Our patient harbours a mutation in *LMNA*, c.1130G>A (p.R377H). This has been shown to segregate with phenotypes affecting skeletal and cardiac muscles, i.e. EDMD2 [8], limb-girdle muscular dystrophy 1B (LGMD1B) [6], isolated cardiomyopathy with conduction defects (DCM-CD) [7], or quadriceps myopathy with DCM-CD [2]. No axonal neuropathy in EDMD2 was reported as being caused by R377H mutation in the *LMNA* gene. To elucidate

the genetic background of the disease in our patient we analysed five genes: *PMP22*, *GDAP1*, *GJB1*, *MPZ*, and *MFN2*, causative for CMT disease. Heterozygous mutations in *GDAP1* segregate with a mild form of axonal neuropathy with slow progression, resembling the clinical course observed in our patient [11]. Analysis of the *GDAP1* gene in our patient did not reveal mutations. Also, no mutations in the coding sequence of *PMP22*, *GJB1*, and *MPZ* genes were found. The *MFN2* gene is the most commonly mutated gene in autosomal dominant CMT2. Late onset, milder phenotype is associated either with intronic mutations or with mutations at the end of the coding sequence of the *MFN2* gene [9]. We attempted to investigate the pathogenic status of the sequence variant c.1469+50G>T in *MFN2*; the analysis of cDNA showed that it probably did not affect splicing (Fig. 2). We cannot definitively exclude that another unknown mutation caused the peripheral neuropathy observed in our patient. Polyneuropathy has never been reported in the context of the *LMNA* mutation p.R377H; therefore, bigenic molecular pathogenesis seems more likely in the presented case of EDMD2/CMT2. Initially we decided to sequence the late onset-CMT2-associated genes instead of exome sequencing analysis because hundreds of NGS-generated variants of unknown clinical relevance might be difficult to interpret. Since no mutations were detected in the analysed genes responsible for neuropathy, it seems that only wide genetic analysis could help to clarify the genetic basis of this case.

Acknowledgements

Disclosure

Authors report no conflict of interest.

References

1. Benedetti S, Bertini E, Iannaccone S, Angelini C, Trisciani M, Toniolo D, Sferrazza B, Carrera P, Comi G, Ferrari M, Quattrini A, Previtali SC. Dominant LMNA mutations can cause combined muscular dystrophy and peripheral neuropathy. J Neurol Neurosurg Psychiatry 2005; 76: 1019-1021.

2. Charniot JC, Desnos M, Zerhouni K, Bonnefont-Rousselot D, Albertini JP, Salama JZ, Bassez G, Komajda M, Artigou JY. Severe

http://rcin.org.pl

Agnieszka Madej-Pilarczyk, Katarzyna Kotruchow, Dagmara Kabzinska, Joanna Cegielska, Andrzej Kochanski, Irena Hausmanowa-Petrusewicz

dilated cardiomyopathy and quadriceps myopathy due to lamin A/C gene mutation: a phenotypic study. Eur J Heart Fail 2006; 8: 249-256.

3. De Sandre-Giovannoli A, Chaouch M, Kozlov S, Vallat JM, Tazir M, Kassouri N, Szepetowski P, Hammadouche T, Vandenberghe A, Stewart CL, Grid D, Lévy N. Homozygous defects in LMNA, encoding lamin A/C nuclear-envelope proteins, cause autosomal recessive axonal neuropathy in human. Am J Hum Genet 2002; 70: 726-736.

4. Duparc A, Cintas P, Somody E, Bieth E, Richard P, Maury P, Delay M. A cardio-neurological form of laminopathy: dilated cardiomyopathy with permanent partial atrial standstill and axonal neuropathy. Pacing Clin Electrophysiol 2009; 32: 410-415.

5. Goizet C, Yaou RB, Demay L, Richard P, Bouillot S, Rouanet M, Hermosilla E, Le Masson G, Lagueny A, Bonne G, Ferrer X. A new mutation of the lamin A/C gene leading to autosomal dominant axonal neuropathy, muscular dystrophy, cardiac disease, and leuconychia. Med Genet 2004; 41: e29.

6. Muchir A, Bonne G, van der Kooi AJ, van Meegen M, Baas F, Bolhuis PA, de Visser M, Schwartz K. Identification of mutations in the gene encoding lamins A/C in autosomal dominant limb girdle muscular dystrophy with atrioventricular conduction disturbances (LGMD1B). Hum Mol Genet 2000; 9: 1453-1459.

7. Perrot A, Sigusch HH, Nägele H, Genschel J, Lehmkuhl H, Hetzer R, Geier C, Leon Perez V, Reinhard D, Dietz R, Josef Osterziel K, Schmidt HH. Genetic and phenotypic analysis of dilated cardiomyopathy with conduction system disease: demand for strategies in the management of presymptomatic lamin A/C mutant carriers. Eur J Heart Fail 2006; 8: 484-493.

8. van Tintelen JP, Hofstra RM, Katerberg H, Rossenbacker T, Wiesfeld AC, du Marchie Sarvaas GJ, Wilde AA, van Langen IM, Nannenberg EA, van der Kooi AJ, Kraak M, van Gelder IC, van Veldhuisen DJ, Vos Y, van den Berg MP; Working Group on Inherited Cardiac Disorders, line 27/50, Interuniversity Cardiology Institute of The Netherlands. High yield of LMNA mutations in patients with dilated cardiomyopathy and/or conduction disease referred to cardiogenetics outpatient clinics. Am Heart J 2007; 154: 1130-1139.

9. Verhoeven K, Claeys KG, Züchner S, Schröder JM, Weis J, Ceuterick C, Jordanova A, Nelis E, De Vriendt E, Van Hul M, Seeman P, Mazanec R, Saifi GM, Szigeti K, Mancias P, Butler IJ, Kochanski A, Ryniewicz B, De Bleecker J, Van den Bergh P, Verellen C, Van Coster R, Goemans N, Auer-Grumbach M, Robberecht W, Milic Rasic V, Nevo Y, Tournev I, Guergueltcheva V, Roelens F, Vieregge P, Vinci P, Moreno MT, Christen HJ, Shy ME, Lupski JR, Vance JM, De Jonghe P, Timmerman V. MFN2 mutation distribution and genotype/phenotype correlation in Charcot-Marie-Tooth type 2. Brain 2006; 129: 2093-2102.

10. Worman HJ, Bonne G. "Laminopathies": a wide spectrum of human diseases. Exp Cell Res 2007; 313: 2121-2123.

11. Zimon M, Baets J, Fabrizi GM, Jaakkola E, Kabzińska D, Pilch J, Schindler AB, Cornblath DR, Fischbeck KH, Auer-Grumbach M, Guelly C, Huber N, De Vriendt E, Timmerman V, Suter U, Hausmanowa-Petrusewicz I, Niemann A, Kochański A, De Jonghe P, Jordanova A. Dominant GDAP1 mutations cause predominantly mild CMT phenotypes. Neurology 2011; 77: 540-548.

Schwannoma of the medial cutaneous nerve of the arm: a rare location with concomitant compression neuropathy of the ulnar nerve

Jerzy Gosk[1], Olga Gutkowska[1], Jacek Martynkiewicz[1], Michał Bąk[1], Agnieszka Hałoń[2]

[1]Department of Traumatology, Clinic of Traumatology and Hand Surgery, Wroclaw Medical University
[2]Division of Pathomorphology and Oncological Cytology, Wroclaw Medical University

Abstract

The objective of this paper is to present a case of rare location of schwannoma in the medial cutaneous nerve of the arm at the level of the axilla. Preliminary diagnostic examination of the tumour was carried out in another hospital by means of open biopsy. In the preoperative period symptoms of ulnar nerve dysfunction (paraesthesias, positive Hoffmann-Tinel sign) dominated the clinical picture. After having performed imaging studies and electromyographic (EMG) examination, the patient was scheduled for an operation. The tumour, measuring 3.5 × 3.0 × 1.5 cm, was resected without damage to the fascicular structure. Presence of paraesthesias in the distribution of the medial cutaneous nerve of the arm, which was first noted in the postoperative period, persists in moderate severity until now. As a result of the performed operative treatment, such symptoms as palpable tumour mass, pain, paraesthesias in the ulnar nerve distribution and positive Hoffmann-Tinel sign resolved. On the basis of histopathological examination results the final diagnosis of classical schwannoma was established.

Key words: *schwannoma, nerve compression, tumour, medial cutaneous nerve of the arm.*

Introduction

The medial cutaneous nerve of the arm is one of the smallest branches of the brachial plexus [20]. It is a nerve arising from the medial cord (C8, Th1) [16,20]. The medial cutaneous nerve of the arm passes through the axilla, crossing posterior to the axillary vein and lying medially to it. In its further course it is located medially to the brachial artery and the basilic vein [16,20]. At the mid-length of the arm the nerve pierces the deep fascia and runs toward the skin [16,20]. The medial cutaneous nerve of the arm supplies the skin of the medial aspect of the arm (the anterior aspect of the distal third of the arm and most of the posteromedial aspect) [16]. This nerve can communicate with the intercostobrachial nerve and medial cutaneous nerve of the forearm [2].

The medial cutaneous nerve of the arm can be subjected to damage due to trauma (including that of iatrogenic aetiology), inflammatory factors or as a result of development of neoplastic lesions affecting the nerve or adjacent structures [9].

Communicating author:

Jerzy Gosk, Department of Traumatology, Clinic of Traumatology and Hand Surgery, Wroclaw Medical University, ul. Borowska 213, 50-556 Wrocław, phone: +48 71 734 38 00, fax: +48 71 734 38 09, e-mail: chiruraz@umed.wroc.pl

Jerzy Gosk, Olga Gutkowska, Jacek Martynkiewicz, Michał Bąk, Agnieszka Hałoń

Case report

A 51-year-old woman was admitted to our unit for surgical treatment of a tumour located in her left axillary fossa. The tumour was first noticed by the patient about 6 months earlier. There was no history
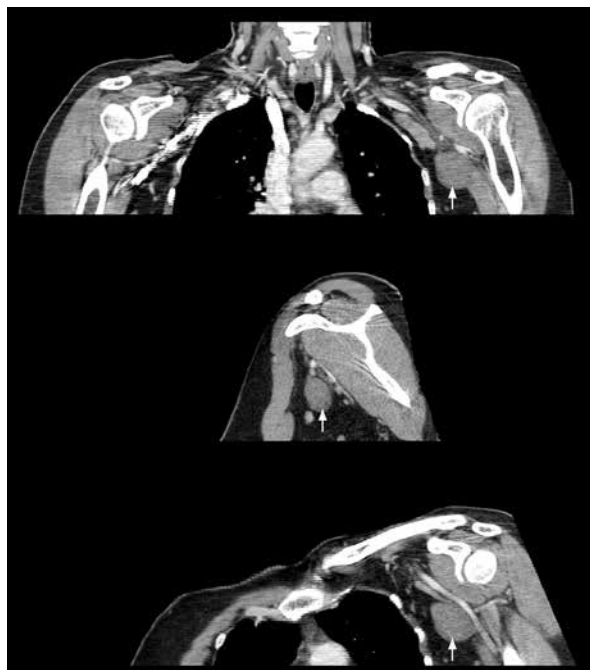

Fig. 1. Computed tomography scans of the chest and left shoulder showing the tumour (white arrows) located in the left axillary fossa.

of trauma or inflammation of the affected area. On anamnesis, the patient reported pain, aggravated by applying pressure to the tumour mass and by overstraining the upper limb, and presence of paraesthesias in the 4th and 5th fingers of her left hand. Before admission to our clinic, the patient had an open biopsy of the tumour performed in another hospital (27.03.2013). On the basis of histopathological analysis of the biopsied material, the diagnosis of schwannoma was established. In the computed tomography (CT) scan performed before the biopsy (08.07.2013), presence of a smoothly contoured solid tumour measuring 3.2 × 2.8 × 3.6 cm was detected. The tumour was hypo/isodense (20-40 H), with no significant contrast enhancement. Medially and anteriorly it was difficult to determine the boundaries between the tumour and the short head of the biceps brachii muscle and coracobrachialis muscle (Fig. 1). On magnetic resonance imaging (MRI) examination performed after the biopsy (29.08.2014), presence of a tumour measuring 3.7 × 2.3 × 3.5 cm was demonstrated. The tumour had clear outer boundaries and did not compress the blood vessels of the axillary fossa. After administration of contrast agent, homogeneous signal enhancement was noted (Fig. 2).

On EMG examination performed on 29.08.2013 no characteristics of significant function impairment of the median, ulnar and radial nerves were detect-
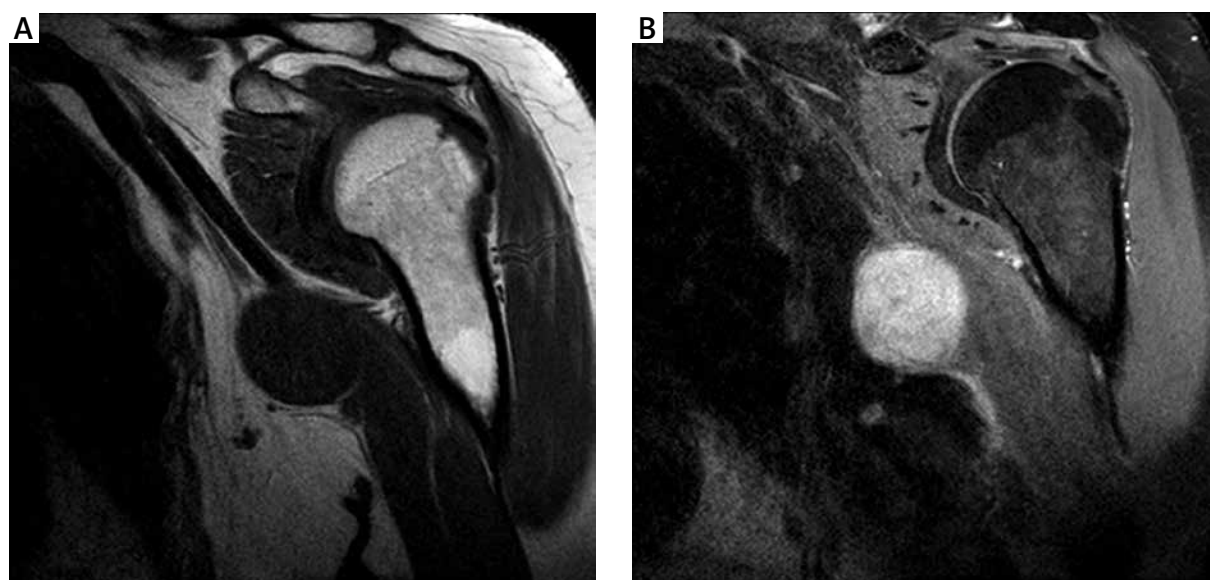

Fig. 2. Magnetic resonance imaging scans demonstrating: **A)** the tumour location in the left axillary fossa; **B)** signal enhancement of the lesion after administration of contrast agent.
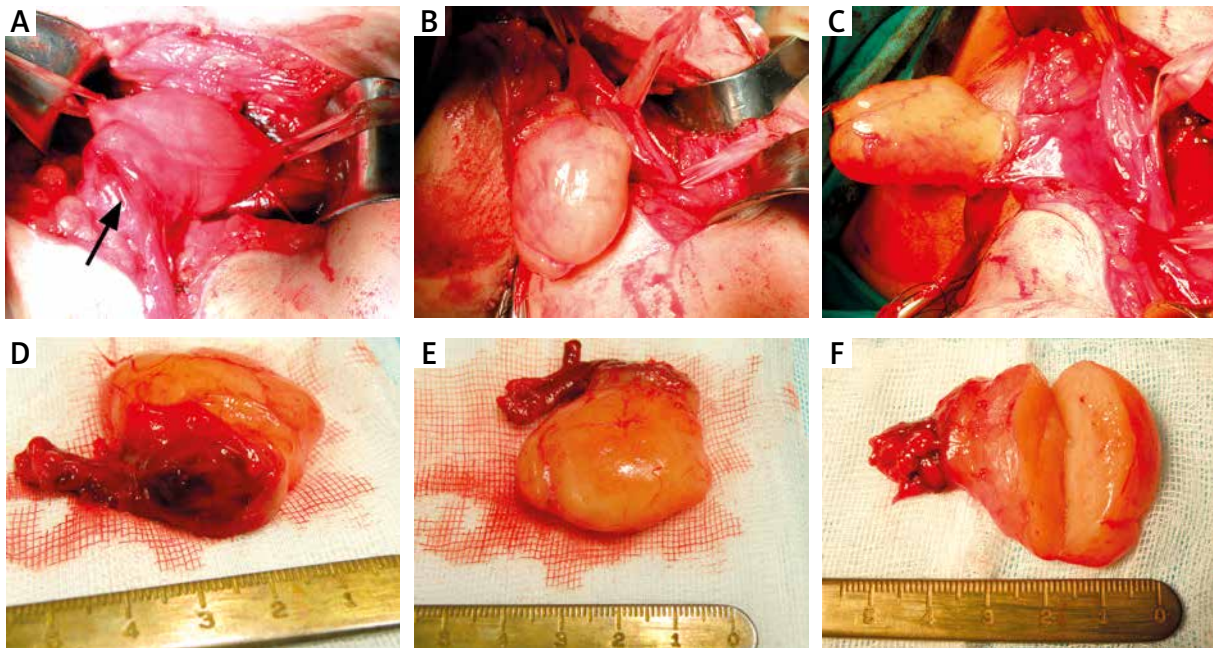
Fig. 3. Removal of the tumour from the medial cutaneous nerve of the arm: **A)** intraoperative view: exposure of the tumour (the site of previously performed biopsy is visible – black arrow); **B, C)** intraoperative view: status after dissection of the tumour; **D, E)** postoperative view: appearance of the tumour after resection; **F)** cross-section of the tumour.

ed. The medial cutaneous nerve of the arm was not subjected to assessment.

On clinical examination a palpable tumour mass was present in the left axillary fossa. Pain was triggered by applying pressure to the tumour. On percussion of the tumour, a positive Hoffmann-Tinel sign was elicited, with the presence of paraesthesias in the 4th and 5th fingers of the patient's left hand. Superficial sensory function examination (static and dynamic sensory discrimination) of this area did not reveal significant impairment in comparison to the opposite side. No muscle atrophy was observed in the patient's left upper limb.

The patient was scheduled for an operation. Surgery was performed on 18.11.2013. After exposure of the tumour mass and identification of the adjacent neural structures, it was determined that the tumour originated from the medial cutaneous nerve of the arm. The tumour, measuring 3.5 × 3.0 × 1.5 cm, was dissected from the nerve without damage to the fascicular structure. The operation was performed with the use of microsurgical instruments and an operating microscope. Marked hardening and scarring of tissues at the site of previously performed

open biopsy significantly hindered the dissection and enucleation of the tumour (Fig. 3).

Classical schwannoma was diagnosed on the basis of postoperative histopathological examination results – no. 33695 from 03.12.2013 (Fig. 4). In the early postoperative period, onset of paraesthesias in the distribution of the medial cutaneous nerve of the arm was observed. During the follow-up period of one year, no symptoms of tumour recurrence were detected, and the pain and paraesthesias in the ulnar nerve distribution resolved. Hoffmann-Tinel sign is negative. Paraesthesias of moderate severity in the distribution of the medial cutaneous nerve of the arm still persist.

Discussion

The case of schwannoma located in the medial cutaneous nerve of the arm presented in this paper is interesting for a number of reasons. Firstly, this location of schwannoma is extremely rare in clinical practice. In the upper limb, these tumours are most commonly located in the ulnar, median and radial nerves, being significantly rarer in the musculocutaneous and axillary nerves [1,3,5,6,18]. In our
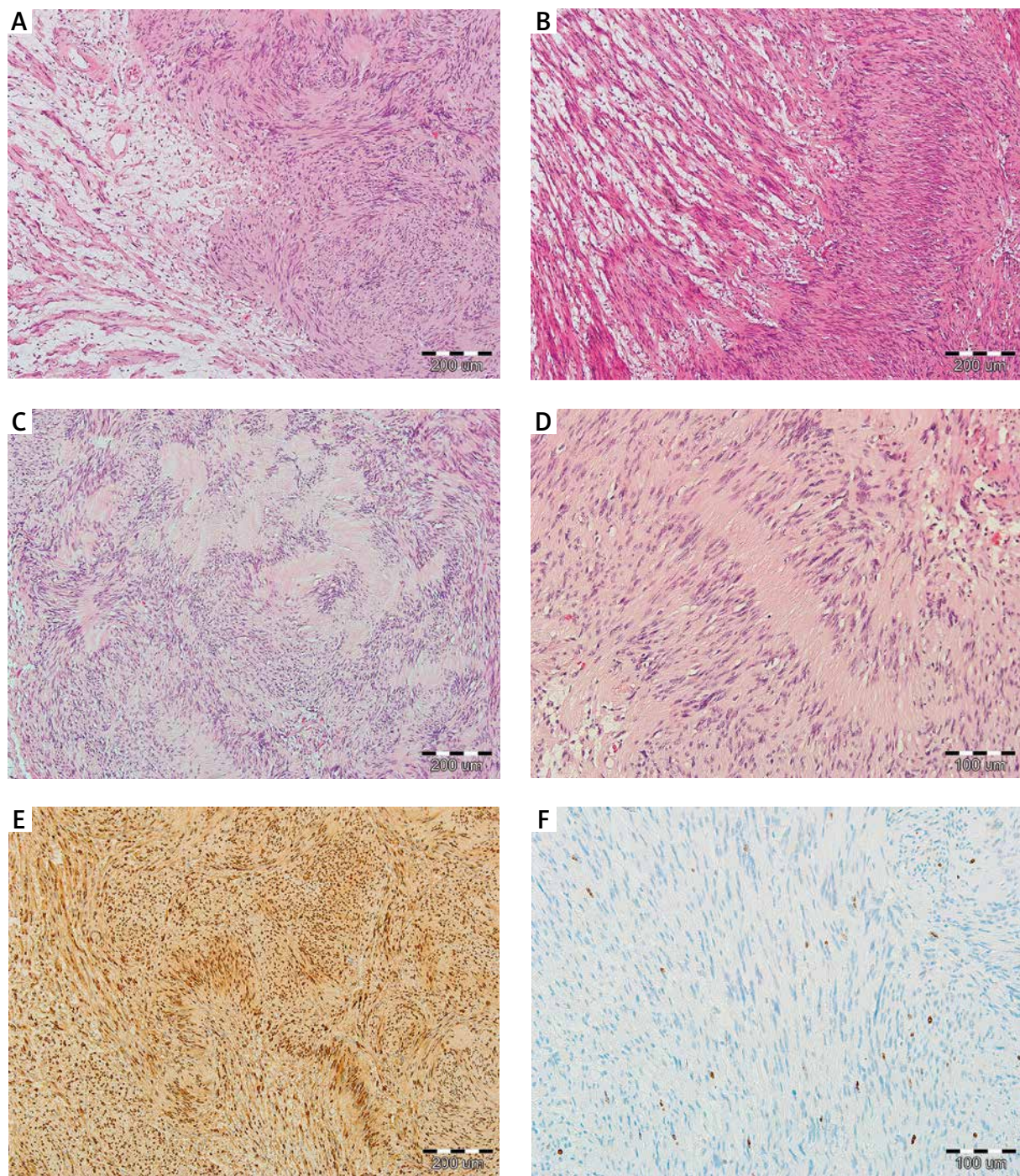
http://rcin.org.pl

Jerzy Gosk, Olga Gutkowska, Jacek Martynkiewicz, Michał Bąk, Agnieszka Hałoń

Fig. 4. Histological features of classical schwannoma: **A)** two typical histological patterns: Antoni A pattern – Verocay bodies as cellular areas surrounded by nuclear palisades (right side of the image) opposed to less cellular Antoni B pattern (left side of the image); **B)** cellular Antoni A area (right side of the image) and loose paucicellular Antoni B area with sharp border between them; **C)** typical Verocay bodies (Antoni A pattern); **D)** prominent nuclear palisading; **E)** diffuse positive immunostaining for S-100 protein; **F)** proliferative index Ki-67 positive, low (1%).

http://rcin.org.pl

material comprising 101 cases of peripheral nerve tumours treated operatively between the years 1983 and 2012, we observed only one case of schwannoma located in the medial cutaneous nerve of the arm in a 24-year-old male patient [6]. We have not found a single case report describing a schwannoma in this location in the available literature. Secondly, symptoms observed in the preoperative period suggested location of the tumour in the ulnar nerve. Positive Hoffmann-Tinel sign and presence of paraesthesias in the 4th and 5th fingers of the patient's left hand were detected on clinical examination. The above symptoms resulted from compression of the adjacent ulnar nerve, also originating from the medial cord of the brachial plexus, by the tumour mass. At the same time, less evident symptoms of dysfunction of the nerve being the site of tumour origin can result from the less important role of the medial cutaneous nerve of the arm in innervation of the upper limb. The medial cutaneous nerve of the arm is purely sensory. Impairment of its function does not affect the functionality of the upper limb. For this reason, dysfunction of the medial cutaneous nerve of the arm does not cause evident discomfort in patients, in contrast to impairment of function of other nerves [2,16,20]. Detection of its potential pathologies is also difficult due to the fact that this nerve is rarely subjected to assessment during electrodiagnostic testing [9].

Thirdly, difficulties in tumour dissection resulting from previously performed open biopsy of the tumour made us wonder whether it is necessary and useful to perform a biopsy of a peripheral nerve tumour preoperatively. Tumour biopsy can be performed as percutaneous fine-needle or core needle biopsy or as an open biopsy [17]. Closed biopsy techniques of a soft tissue mass are highly diagnostic, with a low complication rate [13,21]. However, biopsy of a nerve tumour is connected with the risk of certain complications. The possibility of haemorrhage and damage to viable fascicles has been highlighted [3,11,18]. It may lead to secondary intraneural scarring and aggravation of neuropathic pain [3,10,11]. Some authors emphasise increased risk of development of new, postoperative neurological deficits in patients who underwent a previous invasive procedure at the surgical site [4,10,12,15]. Levi *et al.* observed new, postoperative neurological deficits in 41% of their patients who had previously been subjected to such procedures (biopsy or oper-

ation) at the surgical site [12]. It is also important to be aware that the results obtained after biopsy are not always identical to the results of histopathological examination of the surgically removed tumour [1,17-19]. It has been suggested that biopsy is recommended in case of a suspected malignant lesion [3,14]. At the same time, the possibility of spread of malignant neoplastic cells as a result of tumour biopsy has been emphasised [7,18].

In the above-described case, the patient underwent an open tumour biopsy in another hospital before definitive operative treatment. Histopathological examination of the removed sample revealed a schwannoma. This result, obtained after the first operation, neither changed further management nor made it possible to determine the site of tumour origin.

In order to remove the entire tumour, another operation was required, which was performed in conditions altered by the previous surgery and therefore technically more demanding. In our opinion, incisional biopsy is only recommended in cases in which presence of a large tumour with focal necrosis, haemorrhage and infiltration of surrounding tissues is observed intraoperatively. This is compatible with observations made by other authors [7,8]. In the above-described case an increase in intensity of paraesthesias in the distribution of the medial cutaneous nerve of the arm was seen in the postoperative period. This observation may to some extent confirm suggestions regarding the risk connected with performing preoperative tumour biopsy.

Conclusions

A case of very rare location of classical schwannoma in the medial cutaneous nerve of the arm with concomitant symptoms of ulnar nerve irritation has been presented in this paper. Preoperative open biopsy of the tumour constituted grounds for questioning the appropriateness and the risk connected with this type of management of peripheral nerve tumours.

Acknowledgements

Disclosure

Authors report no conflict of interest.

http://rcin.org.pl

Jerzy Gosk, Olga Gutkowska, Jacek Martynkiewicz, Michał Bąk, Agnieszka Hałoń

References

1. Adani R, Baccarani A, Guidi E, Tarallo L. Schwannomas of the upper extremity: diagnosis and treatment. Chir Organi Mov 2008; 92: 85-88.

2. Blanco R, Jiménez Gómez BM, López González JM. Ultrasound Appearance of the Cutaneous Nerves of the Upper Limb: A Novel Description in Pain Management. J Pain Relief 2012; 1: 2.

3. Date R, Muramatsu K, Ihara K, Taguchi T. Advantages of intracapsular micro-enucleation of schwannoma arising from extremities. Acta Neurochir (Wien) 2012; 154: 173-178; discussion 178.

4. Donner TR, Voorhies RM, Kline DG. Neural sheath tumors of major nerves. J Neurosurg 1994; 81: 362-373.

5. El Andaloussi Y, Abkari I, Bleton R. Schwannome du nerf axillaire (à propos d'un cas) [Axillary nerve schwannoma (case report)]. Chir Main 2008; 27: 232-234.

6. Gosk J, Rutowski R, Rabczyński J. Peripheral nerve tumours in own material. Folia Neuropathol 2004; 42: 203-207.

7. Gupta G, Mammis A, Maniker A. Malignant peripheral nerve sheath tumors. Neurosurg Clin N Am 2008; 19: 533-543.

8. July J, Guha A. Treatment of the peripheral nerve tumors. CDK 185 2011; 38: 257-262.

9. Jung MJ, Byun HY, Lee CH, Moon SW, Oh MK, Shin H. Medial antebrachial cutaneous nerve injury after brachial plexus block: two case reports. Ann Rehabil Med 2013; 37: 913-918.

10. Knight DM, Birch R, Pringle J. Benign solitary schwannomas: a review of 234 cases. J Bone Joint Surg Br 2007; 89: 382-387.

11. Kubiena H, Entner T, Schmidt M, Frey M. Peripheral neural sheath tumors (PNST) – what a radiologist should know. Eur J Radiol 2013; 82: 51-55.

12. Levi AD, Ross AL, Cuartas E, Qadir R, Temple HT. The surgical management of symptomatic peripheral nerve sheath tumors. Neurosurg 2010; 66: 833-840.

13. Malizos K, Ioannou M, Kontogeorgakos V. Ancient schwannoma involving the median nerve: a case report and review of the literature. Strat Trauma Limb Recon 2013; 8: 63-66.

14. Matejcik V. Our experience with surgical treatment of the schwannomas of peripheral nerves. Bratisl Lek Listy 2002; 103: 477-479.

15. Miles S-J, Amirfeyz R, Bhatia R, Leslie I. Benign soft tissue tumours of the hand. Orthop Trauma 2010; 24: 181-185.

16. Race CM, Saldana MJ. Anatomic course of the medial cutaneous nerves of the arm. J Hand Surg Am 1991; 16: 48-52.

17. Resnick JM, Fanning CV, Caraway NP, Varma DG, Johnson M. Percutaneous needle biopsy diagnosis of benign neurogenic neoplasms. Diagn Cytopathol 1997; 16: 17-25.

18. Siqueira MG, Socolovsky M, Martins RS, Robla-Costales J, Di Masi G, Heise CO, Cosamalón JG. Surgical treatment of typical peripheral schwannomas: the risk of new postoperative deficits. Acta Neurochir (Wien) 2013; 155: 1745-1749.

19. Sohn YM, Kim SY, Kim EK. Sonographic appearance of a schwannoma mimicking an axillary lymphadenopathy. J Clin Ultrasound 2011; 39: 477-479.

20. Tubbs RS, Jones VL, Loukas M, Cömert A, Shoja MM, Wellons JC 3rd, Cohen-Gadol AA. Anatomy and landmarks for branches of the brachial plexus: a vade mecum. Surg Radiol Anat 2010; 32: 261-270.

21. Welker JA, Henshaw RM, Jelinek J, Shmookler BM, Malawer MM. The percutaneous needle biopsy is safe and recommended in the diagnosis of musculoskeletal masses. Cancer 2000; 89: 2677-2686.

Instructions to Authors

This instruction is based upon *Uniform Requirements for Manuscripts Submitted to Biomedical Reviews* (the complete document appears in N Engl J Med 1997; 336, 309-315).

Aims and scope

Folia Neuropathologica is an official journal of the Mossakowski Medical Research Centre Polish Academy of Sciences and the Polish Association of Neuropathologists. The journal publishes original articles and reviews that deal with all aspects of clinical and experimental neuropathology and related fields of neuroscience research. The scope of journal includes surgical and experimental pathomorphology, ultrastructure, immunohistochemistry, biochemistry and molecular biology of the nervous tissue. Papers on surgical neuropathology and neuroimaging are also welcome. The reports in other fields relevant to the understanding of human neuropathology might be considered.

Ethical consideration

Papers describing animal experiments can be accepted for publication only if the experiment conforms to the legal requirements in Poland as well as with the European Communities Council Directive of November 24, 1986 or the National Institute of Health Guide (National Institute of Health Publications No. 80-23, Revised 1978) for the care and use of Laboratory Animals for experimental procedure. Authors must provide a full description of their anesthetics and surgical procedures. Papers describing experiments on human subjects must include a statement that experiments were performed with the understanding and consent of each subject, with the approval of the appropriate local ethics committee.

Submission of manuscripts

Articles should be written in English. All new manuscripts should be submitted through the online submission at http://panel2.termedia.pl/fn

For authors unable to submit their manuscript online, please contact with Prof. E. Matyja, Editor-in-Chief of *Folia Neuropathologica*, ematyja@imdik.pan.pl

The Editorial Board reserves the right to reject a paper without reviewers' opinion if the content or the form of the paper does not meet minimum acceptance criteria or if the subject of the paper is beyond the aims and scope of the journal.

Legal aspects

In sending the manuscript the author(s) confirm(s) that (s)he has (they have) not previously submitted it to another journal (except for abstracts of no more than 400 words) or published it elsewhere. The author(s) also agree(s), if and when the manuscript is accepted for publication, to automatic and free transfer of copyright to the Publisher allowing for the publication and distribution of the material submitted in all available forms and fields of exploitation. The author(s) accept(s) that the manuscript will not be published elsewhere in any language without the written consent of the copyright holder, i.e. the Publisher.

All manuscripts submitted should be accompanied by an authors' statement including signed confirmation of the above and confirming that this publication has been approved by all co-authors (if any), as well as by the responsible authorities at the institution where the work has been carried out. The authors' statement should be signed by ALL co-authors. Additionally, the author(s) confirm(s) that (s)he is (they are) familiar with and will observe the "Instruction to Authors" included in *Folia Neuropathologica* and also that all sources of financial support have been fully disclosed. Materials previously published should be accompanied by written consent for reprinting from the relevant Publishers. In the case of photographs of identifiable persons, their written consent should also be provided. Any potential conflict of interest will be dealt with by the local court specific to the Publisher. Legal relations between the Publisher and the author(s) are in accordance with Polish law and with international conventions binding on Poland.

Authors agree to waive their royalties.

Anonymous review

All manuscripts will be subject to a process of anonymous editorial review.

Preparation of manuscripts

Articles must be written in English, with British spelling used consistently throughout. Authors not entirely familiar with English are advised to correct the style by professional language editors or native English speakers.
- The length of original article should not exceed 20 printed pages including text, illustrations, tables, and references.
- Manuscripts should be typed using 12pts.font, double-spaced, and fully corrected. Allow a margin at least 2.5 cm at the top, bottom and left side of the page. Text should not be justified.

- The title page should contain: the author's full names, title of the paper, all authors' affiliations, full name and address of the communicating author (including e-mail address and fax number), running title (not exceed 40 characters including spaces).
- The abstract should not exceed 350 words. A list of 3–10 key words is recommended below the abstract.
- The manuscript body should be organized in a standard form with separate sections: Introduction, Material and Methods, Results, Discussion, and References. Review articles should be divided into sections and subsections as appropriate without numbering.
- Do not underline in the text. Avoid footnotes.
- All dimensions and measurements must be specified in the metric system.
- The source of any drug and special reagent should be identified.
- Particular attention needs to be paid to the selection of appropriate analysis of data and the results of statistical test should be incorporated in the results section.
- The nomenclature used should conform to the current edition of the Nomina Anatomica or Nomina Anatomica Veterinaria.
- Acknowledgements should be made in a separate sheet following Discussion and before References. These should contain a list of dedications, acknowledgements, and funding sources.
- Legends of figures and tables should be typed on separate pages.
- The editor reserves the right to make corrections.

Tables

- Tables numbered in Roman numerals require a brief but descriptive heading.
- The major divisions of the table should be indicated by horizontal rules.
- Explanatory matter should be included in footnotes, indicated in the body of the table in order of their appearance.
- Tables must not duplicate material in the text or in illustration.

Illustrations

All figures should be supplied electronically at resolution 300dpi in all standard formats (tiff, jpg, Adobe Photoshop, Corel Draw, and EPS). Name your figure files with "Fig" and the figure number, e.g., Fig1.tif
- The maximum figure size is 84 mm or 174 mm for use in a single or double column width, respectively.
- When possible, group several illustrations on one block for reproduction. Like all other figures, block should be prepared within a rectangular frame to fit within a single or double column width of 84 and 174 mm, respectively, and a maximum page height of 226 mm.
- Each figure should include scale magnification bar; do not use magnification factors in the figure legends.
- All figures, whether photographs, graphs or diagrams, should be numbered using Arabic numerals and cited in the text in consecutive numerical order
- **Immunohistochemical study requires color illustrations of very good quality. The papers with white and black immunohistochemistry will not be accepted.**
- **The expense of color illustrations must be borne by the authors.** The cost of color print for every successive 8 pages is 200 euro irrespective of the number of color pages, i.e., the price remains the same whether there is one or eight pages. The Publisher makes out the bill to the communicating Author.

References

The list of references (written on a separate page) should include only those publications that are cited in the text. Avoid citation of academic books, manuals and atlases. References may be arranged alphabetically and numbered consecutively. References should be given in square brackets with no space between the comma and the consecutive number, e.g. [3,4,6-12].
References should be written as follows:
Journal papers: initials and names of all authors, full title of paper, journal abbreviation (according to Index Medicus), year of publication, volume (in Arabic numerals), first and last page (example below):
1. Valverde F. The organization of area 18 in the monkey. Anat Embryol 1978; 154: 305-334.
2. Uray NJ, Gona AG. Calbindin immunoreactivity in the auricular lobe and interauricular granular band of the cerebellum in bullfrogs. Brain Behav Evol 1999; 53: 10-19.
Book and monographs: initials and names of all authors, full title, edition, publisher, place, year (examples below):
1. Pollack RS. Tumor surgery of the head and neck. Karger, Basel 1975.
2. Amaral DG, Price JL, Pitkänen A, Carmichael ST. Anatomical organization of the primate amygdaloid complex. In: Aggleton JP (ed.). The amygdala. Wiley-Liss, New York 1992; pp. 1-66.
Reference to articles that are accepted for publication may be cited as „in press" or Epub.

Proofs

Corrections to the proofs should be restricted to printer's errors only; other alterations will be charged to the authors. In order to maintain rapid publication, proofs should be returned within 48 hours, preferably by e-mail, fax or courier mail. If the Publisher receives no response from the authors after 10 days, it will be assumed that there are no errors to correct and the article will be published.

Subscription information

The journal is published in one volume per year consisting of four numbers. The annual subscription price is 160 PLN for Institutions from Poland and 80 PLN for individual subscribers from Poland and 140 Euro for foreign Institutions and 70 Euro for foreign individual subscribers.
Payment should be made to:
Termedia sp. z o.o., ul. Kleeberga 8, 61-615 Poznan
BZ WBK III O/Poznań PL 61 1090 1359 0000 0000 3505 2645
SWIFT: WBKPPLPP

The publisher must be notified of a cancellation of a subscription not later than two months before the end of the calendar year. After that date the subscription is automatically prolonged for another year.
Publishing, Subscription and Advertising Office:
TERMEDIA Publishing House
ul. Kleeberga 2
61-615 Poznan, Poland
phone/fax +48 61 822 77 81
e-mail: termedia@termedia.pl
http://www.folianeuro.termedia.pl

Folia
Neuropathologica

AUTHOR'S STATEMENT

Title of the article

....

....

....

The author(s) hereby confirm(s) that:

☐ The above-mentioned work has not previously been published and that it has not been submitted to the Publishers of any other journal (with the exception of abstracts not exceeding 400 words).

☐ All co-authors named and the relevant authorities of the scientific institutions at which the work has been carried out are familiar with the contents of this work and have agreed to its publication.

☐ In sending the manuscript together with illustrations and tables agree(s) to automatic and free transfer of copyright to the Publisher allowing for the publication and distribution of the material submitted in all available forms and fields of exploitation, without limits of territory or language, provided that the material is accepted for publication. At the same time the author(s) accept(s) that the submitted work will not be published elsewhere and in whatever language without the earlier written permission of the copyright holder, i.e. the Publisher.

☐ (S)he (they) agree to waive his(her)(their) royalties (fees).

☐ (S)he (they) empower(s) the Publisher to make any necessary editorial changes to the submitted manuscript.

☐ All sources of funding of the work have been fully disclosed.

☐ The manuscript has been prepared in accordance with the Publisher's requirements.

☐ (S)he (they) is (are) familiar with the regulations governing the acceptance of works as published in *Folia Neuropathologica* and agree(s) to follow them.

☐ (S)he (they) agree to accept appropriate invoice from the Publisher in case colour illustrations are implemented.

Date   *Signatures of **all authors***

The covering letter formula can be found at: www.folianeuro.termedia.pl
-The covering letter should be sent to Associate Editor:
Milena Laure-Kamionowska
-Editorial Office of Folia Neuropathologica
Mossakowski Medical Research Centre, Polish Academy of Sciences
Poland Medical Research Centre
ul. Pawinskiego 5
02-106 Warszawa, Poland

CONTENTS